

**A STUDY OF UPWARD-GOING MUONS IN ICAL
DETECTOR AT INDIA-BASED NEUTRINO
OBSERVATORY**

A THESIS

submitted to the

FACULTY OF SCIENCE

PANJAB UNIVERSITY, CHANDIGARH

for the degree of

DOCTOR OF PHILOSOPHY

2015

KANISHKA

DEPARTMENT OF PHYSICS

CENTRE OF ADVANCED STUDY IN PHYSICS

PANJAB UNIVERSITY, CHANDIGARH

Dedicated to my loving family

Acknowledgements

Though only my name appears on the cover of this thesis, a great many people have contributed to its production. I owe my gratitude to all those people who have made this thesis possible and because of whom my graduate experience has been one that I will cherish forever.

Foremost, I would like to express my sincere gratitude to my supervisor Prof. Vipin Bhatnagar for the continuous support for Ph.D and research, for his patience, motivation, enthusiasm, and immense knowledge. He always encouraged me to discuss my work with various collaborators in INO. It was him who introduced me to my co-supervisor that helped me to further my research. His guidance helped me in all the time of research and writing of this thesis. I am thankful to him for carefully reading and commenting on countless revisions of this thesis. I have discussed even small issues that he always listens patiently, which can not be expressed in words. His helping hand whether it is on a physics related matter or financial issues motivated me to even spend more time in my research. He has always let his students enjoy the freedom and has never pressurised them for anything which makes the student relaxed even in hard times and is really appreciable. Peace of mind is essential for every research student and that I have learned from him, not to lose the calm even if you are in extreme pressure. Whenever we had attended the conferences or INO collaboration meetings he always introduced me to great people who are currently working with international collaborations. I could not have imagined having a better advisor and mentor for my Ph.D study. His code writing skills, understanding of software and the hardware lab experience made me learn the techniques that will help me throughout my life.

I gratefully acknowledge my co-supervisor Prof. D. Indumathi for her advice, supervision, insight and crucial guidance, which made her a backbone of this research and so to this thesis. Her involvement with her originality has triggered and nourished my intellectual maturity that I will benefit from, for a long time to come. She encouraged me to present my work in the collaboration and to participate in different research activities. I am deeply grateful to her for the long discussions that helped me sort out the technical details of my work. She has fascinated me with her ability to solve physics problems but has also given me detailed discussions on physics theory. Sometimes I have observed her giving solutions to very small things like how to guess the length of say, a page without using scale which

would be helpful to me in the real life too. I have discussed even very minor issues with her and that was possible because she made me feel comfortable just like a friend. She always handled me calmly because she knows that I used to get tensed quickly. The lectures given by her during my IMSc visit helped me in understanding the topic. She recognized my research capability and the area where I can focus and progress. I am grateful to her in every possible way.

I am thankful to Chairman, Department of Physics, Panjab University for providing adequate facilities to work in the department. Many thanks and regards go in particular to Prof. J. B. Singh, Prof. M. Kaur and Prof. S. B. Beri for their continuous support and efforts to provide us adequate facility in PU-EHEP lab. I would like to thank Dr. Ashok and Dr. Shahi for their help whenever needed. I also thank Mr. V. K. Bhandari, Mr. Baljinder Singh, Mr. Subhash, Mr. Shiv, Mr. Amarjeet and Mr. Navjot for their support in hardware lab. I am thankful to Mr. Ajit, Mr. Gyan and members of purchase section in the department who were always there to help me in my official works. I would also like to thank CIL, cyclotron facility at Panjab University and NTTTR, sector 26 for providing me facilities to characterise glass samples for hardware work.

I am heartily thankful to Prof. Nita Sinha, Prof. M.V.N. Murthy, IMSc, Chennai and Prof.G. Rajasekaran, IMSc and CMI, Chennai for their help and guidance during my Chennai visit. I would like to thank K.K. Meghna for having discussions on INO-ICAL simulations of muon which helped me in understanding the detector part of INO-ICAL code.

I would like to thank professors, scientists and my colleagues of INO collaboration. First of all, the director and spokesperson of INO collaboration Prof. Naba K Mondal for his suggestions and support. I would also like to thank Dr. Satyanarayana Bheesete for his help while working with him in the TIFR-RPC lab during my TIFR visit. I thank Shir. R. Shindhe and Mr. M. Saraf also for their help while working at TIFR-RPC lab. I thank Prof. Gobinda Majumder, TIFR and Asmita Redij (former member of INO) for code related discussions. I would like to thank INO members Prof. Sandhya Choubey, Prof. Amol Dighe, Prof. Srubabati Goswami, Prof. Prafulla Behera, Prof. Sanjib Agarwalla, Prof. Md. Naimuddin, Dr. Ashok Kumar, Dr. Kolahal Bhattacharya, Dr. Sudeshna, Dr. Deepak Samuel, Dr. Sumanta Pal, Dr. Tarak Thakore, Dr. Anushree Ghosh, Ankit, Nitali, Neha, Mathi, Shiba, Aleena, Animesh, Susnata, Raveendra, Varchaswi and Rajesh for many discussions during INO collaboration meetings.

This research has been supported by various organizations including University Grants Commission (UGC) and Department of Atomic Energy (DAE) and Department of Science and Technology (DST). I am thankful to all of them for their confidence in me.

Many friends have helped me stay sane through these difficult years. Their support and care helped me overcome setbacks and stay focused on my research. I greatly value their friendship and I deeply appreciate their belief in me. One of them is my friend and colleague Ms. Bhawandeep Uppal (BU) who has always constantly supported me. We have been friends since M.Phil (2008). I have no words to express the depth and gratitude of our friendship. Even then I will say that she was always with me in my good/bad times and she is/will be the one to appreciate my success and stand with me when I am in trouble. Whenever we were frustrated with some hurdles we tried to make each other relax so that we can work. We motivated each other to spend our time more in research which speaks about our true friendship. I am lucky to have her as my best friend and wish we will be together always. May we go through life together and our friendship last forever. We have enjoyed these 7 years together. Even if we are from different experiments we helped each other in understanding the topics of our respective fields. People in her experiment know me because of her and vice-versa. She cared for me a lot. Whenever she visited CERN, Geneva she used to ask me daily about my well-being even if she was extremely busy. I remember how we used to spend our free time at student centre (STU-C). Our endless stimulating discussions during our lunch or tea time is unforgettable. We always tried to remain calm during lab hours but the moment we come out of the lab we used to have fun. I have enjoyed her company for shopping because I always appreciate her choice. I remember how we used to work stressfully before deadlines especially when we had conferences. I recall enjoying lunch after finishing the rather stressful poster session in one of the conferences. Since last one year we have been unfortunately staying away, when I am in the department then she is away or vice-versa. I wish we will be together sometimes possibly at our marriages and spend time together again. I also wish we were in same experiment so that we had travelled together to some new place and enjoyed more. But even then we have lot of memories to remind each other forever. We have always thought of staying together even after marriage, atleast in the same city but god knows where our destiny will take us to. It would be painful to separate from her. I have lot of wonderful moments to write here but now I can only recall them in my mind to miss her and her company.

I would like to thank my friend Dr. Seema also who always listened to me. We trio (me, Bhawan and Seema) have enjoyed these 7 years together. Our trio company rocked everywhere. Whenever we three were together we had great times. The jokes we crack are so funny that could make anyone laugh. I can never forget the birthday parties we had in Gopal's restaurant. The time spent with we three together is unforgettable.

I would like to thank my friends Vishalli and Heena for being together sharing unforgettable moments during the Ph.D journey.

I would like to thank my friend and colleague Ms. Lakshmi S Mohan (LSM) from IMSc, Chennai whose immense help throughout the Ph.D journey was wonderful. When I visited Chennai for the first time then she was the first person who helped me in settling there. Whenever I visited IMSc I got the accommodation with her. I have seen her running and managing to catch the IMSc shuttle everytime either she used to missed it. I always felt good to have evening walk around the C.I.T campus with her after evening tea and discussing endlessly. When we used to go back to our flat by night shuttle bus she always cooked food for me. I can never forget dosa, curry and rice made by her that was far better than any restaurant food. I miss the food cooked by her and she always instructed me for cooking. She used to accompany me everywhere whether it was to campus canteen, hospital, shopping mall, beach, theatre or A2B restaurant (our favorite). I still remember I caught cold one day and she was busy with her thesis work during my 2014-2015 Chennai visit. But she managed to spare time for me and accompanied me to visit the doctor. Her jolly nature has always made everyone laugh even if she is giving talk in a conference. Because of her jolly nature I always felt relieved from the burden of my work. I still remember when there was venus transit, we managed to wake up early and went to Marina beach to watch it. However, both of us are evening girls i.e., we wake up late. One of our visits was from Chennai to Shantiniketan to present our work in DAE symposium at Visva Bharati university. Both of us have a habit of collecting accessories and the very first moment itself both of us noticed that so many accessories were readily available at Shantiniketan. During all the six days we did a lot of shopping, collecting different accessories and no doubt all the shopkeepers were so happy because of this reason. We went to our friend Debasmita's home, whom I call Debby and had great time there. My last year's IMSc visit was one of the memorable visit because of her. Whether it was our code-related or physics discussions, I can not forget that time. I always appreciate her writing skills and photography. We had a nice and fun photo-session last Christmas till 5 am in the

morning. Last day with her was extremely sad that I broke into tears but could not cry in front of her despite knowing that we may or may not meet again. I have a lot of beautiful memories to recall here and I am just left with pictures taken with her that will always remind me about her and I will miss her for forever.

I would also like to thank my friend Daljeet Kaur (DJ) from Delhi university for sharing amazing moments during Ph.D. Her company during train or flight journeys, in collaboration meeting or any conference made me feel relaxed. Whenever we had journey together I used to catch cold, sore throat infection and fever and she always helped me to during that time. I remember our worst journey from Delhi to Mumbai (TIFR) when our train tickets could not get confirmed. We managed to take general compartment tickets and shared one sleeper berth. We were fined and slept one by one in a single berth and managed to reach Mumbai. Even if it was worst journey when I recall it now it seems to me the best journey. I cannot forget our code related discussions even while sitting in any conference at the back. I have many nice moments to recall but due to time limit I am not writing anymore. I also thank Geetika and Shivali too for making me comfortable whenever I visited Delhi university.

I am deeply thankful to all my friends in PU-EHEP lab Dr. Archana, Dr. Nishu, Dr. Vishal, Dr. Sunil, Dr. Monika, Dr. Nitish, Dr. Jyoti, Dr. Ritu, Dr. Manuk, Dr. Sonam, Dr. Richa, Dr. Ruchi, Dr. Anu, Monika, Deepika, Kuldeep, Anwinder, Manisha, Daisy, Jyoti, Aman, Ankita, Genius, Ridhi, Anter, Sandeep, Manbir, Arshpreet, Abhimanyu and Priyanka for helping me out from all kind of problems and creating enjoyable environment in the lab.

I have learned many new things while doing Ph.D like cooking, swimming and salsa dance which is a wonderful experience for me for the lifetime. My special thanks to Abhishek for his teachings and encouraging me always, making me feel always motivated. Whether its salsa dance or any personal advice I feel grateful towards him for sharing his wonderful experience. I would also like to thank Vinu John and Matangi for making me learn salsa dance. I have learned a lot from these people and a lot need to be learn from them.

I would like to thank my rakhi brother Harsh and his wife Chetali Shah for encouraging me towards the research and always listening to my sufferings. If I had a real brother he would not have been as great as Harsh.

My deepest gratitude goes to my family for their persistent love and non-stop support throughout my life. This thesis would have been simply impossible without them. Lot

of people criticized me when I joined BSc, that it is a boring field and moreover is not professional, so it's of no use. Later when I joined Ph.D many people criticised me that it's of long duration and will eat up many years of mine but my family always supported me in an incredible manner. I am indebted to my father, S. S. Rawat, for his love and care. He had never complained inspite of all the hardships in his life. I always seek his advice before I opt for something. I love his teachings, his knowledge in any field is immense. I cannot ask for more from my mother, B. Rawat, as she is simply perfect. I have no suitable word that can fully describe her everlasting love to me. I remember her constant support when I encountered difficulties. Whenever I travelled anywhere her inexplicable care extended despite the distance. The sacrifice and love offered by my parents is commendable. They always kept my priorities above anything else. They always tried to fulfill my needs even at the time of financial crisis. Even if I had committed any mistake they always poured their love on me, forgiving them. Their generosity is highly respectful. I am lucky to have them and I wish everyone to have such parents. I feel proud of my elder sisters Sushma and Rashmi and I am the one whom they always supported. They let me know about the other activities other than just Physics so that I may not get isolated from the social world. I am lucky to have such sisters who always supported me to focus on my research. I also thank my elder brother in law Dharmendra and second elder brother in law Dharampal whom I call "bade jiju" and "chote jiju". They always cared for me, whether I worked late hours in the lab or travelled they always took pain and dropped me to the destination. I loved the company of my niece Aarna and nephew Aaryaman in the stressing hours. I am simply thankful to my sisters' families too. This completes my family and I belong to them.

Last but not least, thanks to almighty God for making me learn and experience through the tests in my life. You have made my life more versatile. May you be honored everywhere. Finally, I would like to thank everybody who was important to the successful realization of this thesis and helping me directly or indirectly, as well as expressing my apology that I could not mention personally everyone.

Dated:

Chandigarh

(Kanishka)

Abstract

The Standard Model (SM) of Particle Physics has been able to explain many important physics results but failed to dwell light on some fundamental problems like unification of fundamental forces, neutrino mass hierarchy and few more. According to SM, neutrinos possess three distinct flavours ν_e , ν_μ , ν_τ and are massless. That further implies neutrino flavour and mass eigenstates do not mix and hence mass hierarchy could not be observed. Later the experiments like Super-Kamiokande (Super-K) and the Sudbury Neutrino Observatory (SNO) have shown that neutrino flavours oscillate and hence possess mass. These experiments provided information on neutrinos and motivated to explore more about them. Many recent developments have been done in neutrino physics. Lot of experiments are running currently and have planned to search for neutrino properties.

Indian researchers have contributed a lot in the field of neutrino physics. The first evidence of neutrinos produced by cosmic ray interactions was provided by Kolar Gold Fields (KGF), the southern part of India in 1965. This is one of the main motivations for the Indian researchers to form an inter-institutional collaboration called India-based Neutrino Observatory (INO). It was established in order to continue our studies on atmospheric neutrinos. This underground laboratory is proposed to be build at Bodi west hills in Theni district of south India. The main aim of this experiment is to determine neutrino oscillations, mass hierarchy and probe CPT violation using atmospheric neutrinos with a magnetised Iron CALorimeter (ICAL) detector. INO will also host a neutrino less double beta decay (TinTin) and dark matter searches experiments (DINO) at the same site. The magnetised ICAL serves as the target for the neutrino interactions to happen whereas the Resistive Plate Chambers (RPCs) act as an active detector element in it. The ICAL with its good energy, direction, time resolution as well as reconstruction and charge identification efficiencies will be able to track muons (detected by RPCs) very well. Around 30,000 RPCs will be needed with each one across the area of $200 \text{ cm} \times 200 \text{ cm}$ having an active area of about 4 m^2 . The ICAL with around 1.3–1.5 T magnetic field will be capable of distinguishing μ^- and μ^+ and hence can sort mass hierarchy problem.

In this thesis, we have worked on three different problems and these analyses are related to each other. As in general, in any detector, we need to check first detector's performance, detector's response and then perform some physics analysis. Here we have used upward-going muons for our physics analysis. Our first analysis is the optimisation

and characterization of glass RPC parameters. In order to choose the best glass electrode we procured various glass samples from the local manufacturers, namely, Asahi, Saint Gobain and Modi. We characterized these glass samples and compared their physical, optical, electrical, surface properties and elemental composition. On the basis of these properties we conclude that Asahi and Saint Gobain are better than Modi glass sample. We measured efficiency and cross-talk using different strip widths of pick-up panel and different RPCs, we conclude that Asahi and Saint Gobain glass with strip width 2.8 and 3.8 cm gave the best results (cross-talk measurements) in avalanche mode (three gases) than Modi glass RPC.

Second part of our analysis is the response of ICAL to muons. A reconstruction efficiency of about 60–70% and a correct charge identification of about 97% was obtained for $P_{\text{in}} \geq 4$ GeV/c and this decreased to about 90% for higher momenta $P_{\text{in}} \sim 50$ GeV/c in both peripheral and side regions. A good angular resolution of better than a degree for incident momentum, $P_{\text{in}} \geq 4$ GeV/c is obtained in the peripheral and side regions and is almost same in all the regions. All these estimates of detector response and various efficiencies would help in solving the mass hierarchy problem and determine precision results very well.

Third part of our analysis focuses on oscillation sensitivity of upward-going muons in ICAL detector. The determination of oscillation parameters of upward-going muons will provide an independent check over the sensitivity and improves further the overall measurement of oscillation parameters. Upward-going muons actually comes from the usual interactions of atmospheric neutrinos with the rock material covering the detector, having signatures of oscillation. The resolutions and efficiencies has been obtained with vertex taken at the bottom part of the detector. The three neutrino flavor mixing with earth matter effect has been applied and done marginalised $\Delta\chi^2$ analysis. The different sets of systematic uncertainties has been taken and the results are compared with Super-K detector for 4.5 years of data. For 10 years with 50 kt exposure of detector, the sensitivity improves with 10 systematic uncertainties along with one constraint. Further the addition of upward-going muons to the atmospheric muons improves the sensitivity of ICAL.

Glossary

AC	Accelerator neutrino
AFM	Atomic Force Microscopy
AGN	Active galactic nuclei neutrino
μ^+	Anti-muon
ASIC	Application-Specific Integrated Circuit
ATM	Atmospheric neutrino
β	Attachment coefficient
ϕ	Azimuthal angle
CAMAC	Computer Automated Measurement and Control
CC	Charged-Current (interaction)
CP	Charge conjugation and Parity (symmetry)
CPT	Charge conjugation, Parity and Time reversal (symmetry)
CR	Cosmic ray neutrino
ϵ_{cid}	Charge identification efficiency
DAQ	Data Acquisition
L	Distance travelled by the neutrino
e^-	Electron
ν_e	Electron neutrino
$\bar{\nu}_e$	Electron anti-neutrino
eV	Electron Volt
E_μ	Energy of muon
E_ν	Energy of the neutrino
HV	High Voltage
P_{in}	Input momenta
LS	Low-energy solar neutrino
LSN	Low-energy supernova neutrino
Δm_{32}^2	Mass-squared difference
μ^-	Muon
ν_μ	Muon neutrino
$\bar{\nu}_\mu$	Muon anti-neutrino
n	Neutron
ν_1, ν_2, ν_3	Neutrino mass eigenstates

$\theta_{12}, \theta_{13}, \theta_{23}$	Neutrino mixing angles
NC	Neutral-Current (interaction)
NIM	Nuclear Instrumentation Module
ndf	Number of degrees of freedom
N_{hits}	Number of hits in the event
$ntrkt$	Number of muon tracks
$P_{\alpha\beta}$	Oscillation probability of $\nu_\alpha \rightarrow \nu_\beta$ channel
π	Pion
e^+	Positron
p	Proton
PID	Proportional Integral Derivative
PIXE	Proton Induced X-ray Emission spectroscopy
ϵ_{rec}	Reconstruction efficiency
P_{rec}	Reconstructed momenta
R & D	Research & Development
RTD	Resistance Temperature Detectors
RMS	Root mean square
R	Reactor neutrino
SEM	Scanning Electron Microscopy
S	Solar neutrino
$P_{\mu\mu}$	Survival probability
SN	Supernova neutrino
T	Terrestrial neutrino
ν_τ	Tau neutrino
α	Townsend coefficient
UV/VIS/NIR	Ultra-Violet/Visible/Near-Infrared
WD-XRF	Wavelength Dispersive X-ray Spectroscopy
WIMP	Weakly Interacting Massive Particles
F_x, F_y, F_z	x, y, z components of force
B_x, B_y, B_z	x, y, z components of magnetic field
θ_z	Zenith angle

Contents

List of Tables	xv
List of Figures	xvii
1 Introduction	1
1.1 Standard Model	1
1.1.1 Particle Interactions	3
1.2 Neutrinos and their Interactions	5
1.2.1 History of Neutrinos	5
1.2.2 Properties of Neutrinos	6
1.2.3 Neutrino Oscillations	8
1.2.4 Non-oscillation Neutrino Experiments	11
1.3 Uses of Neutrinos	12
1.4 Sources of Neutrinos	13
1.4.1 Atmospheric Neutrino Problem	16
1.5 Neutrino Experiments and their Goals	18
1.5.1 Detector types	19
1.5.2 Open Issues in Neutrino Physics	21
1.6 Overview of Thesis Content	23
2 ICAL Detector at INO	27
2.1 Future Goals of INO	29
2.1.1 Choice of the Detector	30
2.2 History of Particle Detectors	32
2.3 The Magnetised Iron CALorimeter (ICAL) Detector	34
2.3.1 Magnet	34
2.3.2 Resistive Plate Chambers (RPCs)	37
2.3.3 Detector Readout Scheme	45
2.4 Goals of the ICAL Detector	46
3 Optimisation and Characterisation of Glass RPC	51
3.1 Motivation for the Study	52
3.1.1 Aging of Resistive Plate Chambers	53
3.2 Characterisation of Glass Electrode	54
3.3 Gas System and Mixing Unit	63

3.4	Scintillator Paddles	69
3.4.1	Fabrication of Scintillator Paddles	70
3.4.2	Characterisation of Scintillator Paddles	71
3.5	Fabrication and Characterisation of glass RPCs	75
3.5.1	Fabrication of RPCs	75
3.5.2	V-I Characteristics of RPC	81
3.5.3	Efficiency and Cross-talk of RPCs	84
3.5.4	Efficiency and Cross-talk of RPC stack	93
4	Response of ICAL to Muons	97
4.1	The ICAL Detector Simulation Framework	98
4.1.1	The Magnetic Field	98
4.1.2	Event Reconstruction	99
4.2	General Feature of Muon Response in the Peripheral and Side Regions . .	100
4.3	Selection Criteria Used	106
4.3.1	Effect of Selection Criteria	107
4.4	Muon Response in the Peripheral and Side Regions	110
4.4.1	Reconstruction Efficiency	110
4.4.2	Relative Charge Identification Efficiency	112
4.4.3	Direction (up/down) Reconstruction	113
4.4.4	Zenith Angle Resolution	115
4.4.5	Muon Momentum Response	118
4.4.6	Momentum Resolution as a Function of (θ, ϕ)	120
4.5	Comparison of Muon Response in Different Regions of ICAL	124
5	Oscillation Analysis with Upward-going Muons	129
5.1	Upward-going Muons at ICAL Detector	129
5.2	Methodology	130
5.2.1	Data Generation	131
5.2.2	Nuance Event Generator	132
5.2.3	Detector Response for Muons	133
5.2.4	Theoretical Considerations	138
5.2.5	χ^2 Analysis	146
5.3	Results of the Simulations Analyses	150
5.3.1	Sensitivity to Individual Parameters	151
5.3.2	Precision Measurements	153
5.3.3	Combining with Atmospheric Neutrino Analysis	154
6	Summary and Conclusions	157
	Appendices	163
	Bibliography	171
	Bibliography	171
	List of Publications	187

List of Tables

1.1	Three generations of charged leptons with their corresponding neutrinos. . .	2
1.2	Quarks with their six different flavours.	2
1.3	Properties of the force mediators.	3
1.4	Current best known values of neutrino oscillation parameters.	10
1.5	Three cases of neutrino mass ordering.	10
1.6	List of neutrino experiments across the globe.	19
2.1	ICAL detector specifications.	28
2.2	Specifications of INO caverns and access tunnel.	29
2.3	An overview of the RPCs used in the past and current experiments (Area is given in m^2 , while the gap (width) is in mm).	45
3.1	Density Measurements.	54
3.2	Composition of samples.	62
3.3	Comparison of Asahi, Saint Gobain and Modi glass samples based on the properties studied.	64
3.4	PMTs with different operating voltage ranges.	71
3.5	Noise rate of Asahi, Saint Gobain and Modi glass RPC in avalanche (two and three gases) and streamer mode with strip width = 2.8 cm at 10 kV. . .	87
3.6	Efficiencies of all the RPCs operated in different modes with different strip widths at their operating voltages.	92
3.7	Cross-talk measurements (approximate values) for all RPCs operated in different modes with different strip widths at their operating voltages. . . .	93
4.1	Momentum and angular resolution, reconstruction and cid efficiency in peripheral and side regions (9 and 10).	121
5.1	Energy and $\cos\theta$ bins of observed (smeared) muons for 2-flavour analysis. .	139
5.2	Energy and $\cos\theta$ bins of observed (smeared) muons for 3-flavour analysis. .	140
5.3	Oscillated and unoscillated events for the observed energy bin and $0 <$ $\cos\theta < 0.15$ bin.	141
5.4	Oscillated and unoscillated events for the observed energy bin and 0.15 $< \cos\theta < 0.3$ bin.	143
5.5	Oscillated and unoscillated events for the observed energy bin and $0.3 <$ $\cos\theta < 0.45$ bin.	143

5.6	Oscillated and unoscillated events for the observed energy bin and $0.45 < \cos \theta < 0.6$ bin.	144
5.7	Oscillated and unoscillated events for the observed energy bin and $0.6 < \cos \theta < 0.75$ bin.	144
5.8	Oscillated and unoscillated events for the observed energy bin and $0.75 < \cos \theta < 0.9$ bin.	145
5.9	3σ range of $\sin \theta_{23}$, Δm_{32}^2 and θ_{13} for marginalisation.	149
5.10	ICAL's capability for measuring the atmospheric mixing angle $\sin^2 \theta_{23}$ with a precision of at 1σ , 2σ and 3σ confidence levels respectively.	154
5.11	ICAL's capability for measuring the atmospheric mass squared difference Δm_{32}^2 with a precision of at 1σ , 2σ and 3σ confidence levels respectively.	154

List of Figures

1.1	Three generations of matter.	3
1.2	Neutrino spectrum from different sources as a function of energy.	6
1.3	Feynman diagram of neutrino interactions.	7
1.4	Primary cosmic particle collides with a molecule of atmosphere.	14
1.5	The energy spectrum of atmospheric neutrino flux.	17
1.6	The flux intensity of cosmic rays as a function of energy.	23
2.1	A schematic of the proposed INO-ICAL detector.	28
2.2	A sketch of the proposed INO main cavern (left); detail showing how the three modules of ICAL will be positioned in that cavern (right).	29
2.3	One module of the magnet with the coil inserted (side view).	37
2.4	Magnetic field map as generated by the MAGNET6 software. Points A = (0, -650, 0) cm, B = (300, -650, 0) cm, C = (-2270, 0, 0) cm (in the 1 st module of ICAL), are defined for later use. Notice that C is actually in the left-most module of the detector and is marked here for convenience.	38
2.5	A schematic of RPC detector.	40
2.6	Gaseous ionisation detection regions.	41
2.7	Schematic of the development of avalanche in an RPC.	43
2.8	Schematic of the development of streamer in an RPC.	43
2.9	Schematic diagram of RPC read out scheme.	46
3.1	UV-VIS transmittance of Asahi, Saint Gobain and Modi glass samples.	55
3.2	Experimental set-up for two-probe method.	55
3.3	Bulk resistivity of Asahi, Saint Gobain and Modi glass samples.	56
3.4	A schematic of atomic force microscope connected to computer.	57
3.5	A schematic of scanning electron microscope.	59
3.6	AFM scans of Asahi, Saint Gobain and Modi glass samples respectively.	60
3.7	SEM scans of Asahi, Saint Gobain and Modi glass samples respectively.	60
3.8	WD-XRF analysis of Asahi, Saint Gobain and Modi glass samples respectively, where x-axis denotes KeV and y-axis denotes KCps.	62
3.9	PIXE analysis of Asahi, Saint Gobain and Modi glass samples respectively.	64
3.10	Top figure is the block diagram of the gas mixing system. (Below-left) figure shows the gas distribution system and (below-right) figure shows the gas cylinders used.	65

3.11	(b) (Top-left) plot shows calibration of freon gas, (top-right) plot shows calibration of isobutane gas. (Bottom-left) plot shows calibration of SF_6 gas and (bottom-right) plot shows calibration of argon gas.	68
3.12	Components of Scintillator detector.	70
3.13	(Top-left) figure shows the paddle of 1.8 cm width and cookie before making scintillator detector. (Top-right) figure shows the paddle glued to the cookie. (Bottom-left) figure shows paddle wrapped with Aluminium for the shield from light. (Bottom-right) figure shows paddle wrapped with black paper and masked with black tape to avoid any light passing through the paddle.	72
3.14	The fabricated scintillator detectors of width 1.8, 2.5 and 3.8 cm respectively.	72
3.15	Circuit diagram of the coincidence of scintillator paddles.	73
3.16	The plots (top) show the plateau region study of the scintillator paddles of width = 1.8, 2.5 cm respectively. The plots (middle) show the plateau region study of scintillator paddles of width = 3.8, 5 cm respectively. The two plots (bottom) show the plateau region study of scintillator paddles of same width = 21.5 cm. Note that the y-axis is different due to the different number of counts.	74
3.17	Left figure shows the efficiency of scintillator paddle of width = 2.5 cm. Right figure shows the efficiency of scintillator paddle of width = 3.8 cm. .	75
3.18	The fabricated RPCs, before graphite coating (left) and after graphite coating (right).	76
3.19	(b) Surface resistivity measurements of Asahi, Saint Gobain and Modi glass RPC respectively. Left plots show X side, Right plots show Y side of Asahi, Saint Gobain and Modi RPC respectively.	77
3.20	Circuit diagram for gas leakage test.	78
3.21	Gas leakage test of Asahi, Saint Gobain and Modi glass RPCs respectively.	79
3.22	Gas leakage test after re-glue. Left plot shows the gas leakage test of Asahi, Saint Gobain and Modi glass RPCs respectively. Right plot shows the button test of Asahi, Saint Gobain and Modi glass RPCs respectively. .	80
3.23	The three figures are of the fabricated pick-up panels for 30 cm \times 30 cm RPC, with the strip width size of 1.8, 2.8 and 3.8 cm respectively.	81
3.24	(b) RPC mounted on a wooden stand before putting it into the test stand for the testing.	82
3.25	V-I characteristics of Asahi with two gases, three gases in avalanche mode and streamer mode respectively.	83
3.26	V-I characteristics of SG with two gases, three gases in avalanche mode and streamer mode respectively.	83
3.27	V-I characteristics of Modi with two gases, three gases in avalanche mode and streamer mode respectively.	84
3.28	Right figure shows stand with the CAMAC controller, logic gates, CRO, power supply. Left figure shows RPC in the cosmic ray muon stand.	85
3.29	Trigger scheme circuit diagram for testing RPCs.	86

3.30	Efficiency and cross-talk of Asahi glass RPC with the strip width size = 1.8 cm in avalanche mode (two gases), avalanche mode (three gases) and streamer mode respectively.	88
3.31	Efficiency and cross-talk of Asahi glass RPC with the strip width size = 2.8 cm in avalanche mode (two gases), avalanche mode (three gases) and streamer mode respectively.	89
3.32	Efficiency and cross-talk of Asahi glass RPC with the strip width size = 3.8 cm in avalanche mode (two gases), avalanche mode (three gases) and streamer mode respectively.	89
3.33	Efficiency and cross-talk of Saint Gobain glass RPC with the strip width size = 1.8 cm in avalanche mode (two gases), avalanche mode (three gases) and streamer mode respectively.	90
3.34	Efficiency and cross-talk of Saint Gobain glass RPC with the strip width size = 2.8 cm in avalanche mode (two gases), avalanche mode (three gases) and streamer mode respectively.	90
3.35	Efficiency and cross-talk of Saint Gobain glass RPC with the strip width size = 3.8 cm in avalanche mode (two gases), avalanche mode (three gases) and streamer mode respectively.	91
3.36	Efficiency and cross-talk of Modi glass RPC with the strip width size = 1.8 cm in avalanche mode (two gases), avalanche mode (three gases) and streamer mode respectively.	91
3.37	Efficiency and cross-talk of Modi glass RPC with the strip width size = 2.8 cm in avalanche mode (two gases), avalanche mode (three gases) and streamer mode respectively.	92
3.38	Efficiency and cross-talk of Modi glass RPC with the strip width size = 3.8 cm in avalanche mode (two gases), avalanche mode (three gases) and streamer mode respectively.	92
3.39	Comparison plot of efficiency (left) and cross-talk (right) of Asahi, Saint Gobain and Modi glass RPC with the strip width size = 2.8 cm in avalanche mode (three gases).	93
3.40	Top plot shows surface resistivity measurements of Asahi glass RPC_1 and Bottom plot shows surface resistivity measurements of Asahi glass RPC_2 . Left plots show X side of Asahi glass RPC_1 and RPC_2 and Right plots show Y side of Asahi glass RPC_1 and RPC_2	94
3.41	V-I characteristics of Asahi glass RPC_1 with two gases and three gases in avalanche mode and streamer mode respectively.	94
3.42	V-I characteristics of Asahi glass RPC_2 with two gases and three gases in avalanche mode and streamer mode respectively.	95
3.43	Trigger scheme circuit diagram for testing RPC stack.	95
3.44	Efficiency and cross-talk of three Asahi glass RPC stack with the strip width size = 2.8 cm (in the center of stack) in avalanche mode (two gases), avalanche mode (three gases) and streamer mode respectively.	96
4.1	Muon tracks (μ^-) in the x-z plane with same values of ($P_{in}, \cos\theta$) but for $ \phi < \pi/2$ and $> \pi/2$	102

4.2	Magnetic field map with the net force directions in the peripheral and side region. The thick black arrows indicate the direction of the magnetic field with labels $B(i, j)$, $i = +, -$, that denote the sign of the B_x, B_y components in each region. The small coloured circles indicate the direction of F_z in each region, with purple (cyan) denoting $F_z > 0 (< 0)$. The brown arrows indicate the direction of F_x or F_y force components that will act on a negatively charged upward-going muon. (Note that side regions 9 and 10 are in the 1 st and 3 rd modules of the detector respectively and are shown together in the same module for convenience.) [176]	103
4.3	The choice of ϕ bins in the peripheral (left) and side (right) regions.	103
4.4	The reconstructed momenta P_{rec} with χ^2/ndf cut. The red (blue) curve represents $\chi^2/\text{ndf} \leq 2$ (10).	106
4.5	Top (bottom) figures show the reconstructed momenta P_{rec} using selection criteria $N_{hits} > n_0$ for partially contained events in the peripheral region with $(P_{in}, \cos\theta) = (5 \text{ GeV}/c, 0.65)$ (top) and $(9 \text{ GeV}/c, 0.85)$ (bottom) with $n_0 = 15$ (20) in the left (right) figure. Fully contained events have no N_{hits} constraint. In each figure, the black curve is without constraints on N_{hits} , red is with $N_{hits}/\cos\theta > n_0$ and blue is for $N_{hits} > n_0$	108
4.6	Top (bottom) figures show the N_{hits} distributions using selection criteria $N_{hits} > n_0$ for partially contained events in the peripheral region with $(P_{in}, \cos\theta) = (5 \text{ GeV}/c, 0.65)$ (top) and $(9 \text{ GeV}/c, 0.85)$ (bottom) with $n_0 = 15$ (20) in the left (right) figure. Fully contained events have no N_{hits} constraint. In each figure, the black curve is without constraints on N_{hits} , red is with $N_{hits}/\cos\theta > n_0$ and blue is for $N_{hits} > n_0$	109
4.7	The figures show the reconstructed momenta P_{rec} using the selection criteria $N_{hits} > n_0$ for partially contained events in the side regions 9 (left) and 10 (right) for $(P_{in}, \cos\theta) = (5 \text{ GeV}/c, 0.65)$ with $n_0 = 15$. Fully contained events have no N_{hits} constraint. In each figure, the black curve is without constraints on N_{hits} , red is with $N_{hits}/\cos\theta > n_0$ and blue is for $N_{hits} > n_0$	110
4.8	Reconstruction efficiency averaged over all ϕ bins as a function of the input momentum P_{in} (GeV/c) for different zenith angles $\cos\theta$ in the peripheral (above), side 9 (below-left) and side 10 (below-right) regions.	111
4.9	Charge identification (cid) efficiency averaged over all ϕ bins as a function of the input momentum P_{in} (GeV/c) for different zenith angles $\cos\theta$ in the peripheral (above), side 9 (below-left) and side 10 (below-right) regions respectively.	113
4.10	Reconstructed zenith angle distributions for $P_{in} = 1 \text{ GeV}/c$ at $\cos\theta = 0.35$ (left) and 0.85 (right) respectively, in the peripheral region. Note that the y-axis scales are different for the two plots.	114
4.11	Reconstructed zenith angle distributions for $P_{in} = 1 \text{ GeV}/c$ at $\cos\theta = 0.35$ (left) and 0.85 (right) respectively, in the side region 9. Note that the y-axis scales are different for the two plots.	114
4.12	Reconstructed zenith angle distributions for $P_{in} = 1 \text{ GeV}/c$ at $\cos\theta = 0.35$ (left) and 0.85 (right) respectively, in the side region 10. Note that the y-axis scales are different for the two plots.	115

4.13	Reconstructed distribution θ_{rec} for input $(P_{in}, \cos\theta) = (5 \text{ GeV}/c, 0.65)$ in the peripheral region (above), side region 9 (below-left) and side region 10 (below-right) respectively.	116
4.14	Resolution, σ_θ , of reconstructed angle θ_{rec} as a function of the input momentum P_{in} (GeV/c) for different values of input $\cos\theta$ in the peripheral region (above), side region 9 (below-left) and side region 10 (below-right) respectively.	117
4.15	Gaussian fits to reconstructed momentum distributions P_{rec} (GeV/c) for muons with fixed energy $(P_{in}, \cos\theta) = (5 \text{ GeV}/c, 0.65)$ in four different bins of azimuthal angle in the peripheral region.	118
4.16	Gaussian fits to reconstructed momentum distributions P_{rec} (GeV/c) for muons with fixed energy $(P_{in}, \cos\theta) = (5 \text{ GeV}/c, 0.65)$ in four different bins of azimuthal angle in the side region 9.	119
4.17	Gaussian fits to reconstructed momentum distributions P_{rec} (GeV/c) for muons with fixed energy $(P_{in}, \cos\theta) = (5 \text{ GeV}/c, 0.65)$ in four different bins of azimuthal angle in the side region 10.	120
4.18	Muon resolution in the peripheral region as a function of input momentum P_{in} (GeV/c) for $\cos\theta = 0.65$ in different bins of ϕ with $N_{hits}/\cos\theta > n_0$ cut, where $n_0 = 15$ (20) left (right).	120
4.19	Muon resolution in the peripheral region as a function of input momentum P_{in} (GeV/c) for different values of $\cos\theta$ in different bins of ϕ	122
4.20	Muon resolution in the side region 9 as a function of input momentum P_{in} (GeV/c) for different values of $\cos\theta$ in different bins of ϕ	122
4.21	Muon resolution in the side region 10 as a function of input momentum P_{in} (GeV/c) for different values of $\cos\theta$ in different bins of ϕ	123
4.22	Comparison of reconstruction (left) and cid efficiency (right) of central, peripheral and side regions as a function of P_{in} (GeV/c) at $\cos\theta = 0.65$. Note that the y-axis scales are different for the two plots.	125
4.23	Comparison of resolutions in peripheral and side region 9 as a function of the input momentum P_{in} (GeV/c) along with earlier results in the central region [173] for different values of $\cos\theta = 0.45, 0.65, 0.85$	125
5.1	Production of upward-going muons at ICAL.	131
5.2	E_μ calculated from formula Equation 5.2 vs. E_μ as calculated by the NUANCE neutrino generator at the ICAL detector.	134
5.3	The reconstructed momenta P_{rec} using selection criteria $N_{hits} > n_0$ for partially contained events in the bottom region of ICAL at $(P_{in}, \cos\theta) = (5 \text{ GeV}/c, 0.65)$ (left) and $(P_{in}, \cos\theta) = (15 \text{ GeV}/c, 0.65)$ (right). In both figures, the black curve is without constraints on N_{hits} , red is with $N_{hits}/\cos\theta > n_0$ and blue is for $N_{hits} > n_0$; $n_0 = 15$	135
5.4	The reconstructed momenta P_{rec} with and without $ntrkt == 1$ cut in the bottom region of ICAL at $(P_{in}, \cos\theta) = (5 \text{ GeV}/c, 0.65)$ (left) and $(P_{in}, \cos\theta) = (9 \text{ GeV}/c, 0.65)$ (right). In both figures, the red (blue) curves are with (without) $ntrkt == 1$ cut.	135

5.5	Left figure shows Gaussian fit to reconstructed momentum distribution P_{rec} (GeV/c) for muons with fixed energy $(P_{in}, \cos \theta) = (5 \text{ GeV/c}, 0.65)$ bin for $N_{hits}/\cos \theta > 15$. Right figure shows Gaussian fit to θ distribution for muons with fixed energy $(P_{in}, \cos \theta) = (5\text{GeV/c}, 0.65)$ for $N_{hits}/\cos \theta > 15$. In both cases ϕ is uniformly distributed over $-\pi \leq \phi \leq \pi$ (scale is different).	136
5.6	Left figure shows muon resolution as a function of input momentum and $\cos \theta$ for $N_{hits}/\cos \theta > 15$. Right figure shows the θ resolution as a function of input momentum and $\cos \theta$. In both cases ϕ is uniformly distributed over $-\pi \leq \phi \leq \pi$ (scale is different).	137
5.7	Left figure shows reconstruction efficiency for $N_{hits}/\cos \theta > 15$. Right figure shows the charge identification efficiency as a function of P_{in} for different values of $\cos \theta$ and ϕ is uniform over $-\pi \leq \phi \leq \pi$ (scale is different).	137
5.8	Energy distribution of muons (E_{μ}) for different $\cos \theta$ bins with and without 2-flavour oscillations.	141
5.9	Energy distribution of muons (E_{μ^-}) for different $\cos \theta$ bins with and without 3-flavour oscillations.	142
5.10	Energy profile of the neutrinos surviving 3-flavour oscillations for 10 years of data.	145
5.11	90 % CL allowed contour of ICAL with 4.5 years of simulated data in comparison with the same contour obtained from 4.5 years data at Super-K, in the $\Delta m_{32}^2 - \sin^2 2\theta_{23}$ parameter space of 2-flavour oscillation analysis.	150
5.12	Left plot shows the allowed parameter space as a function of Δm_{32}^2 and $\sin^2 2\theta_{23}$ for simulations at ICAL with input values $\Delta m_{32}^2 = 2.4 \times 10^{-3} \text{ eV}^2$ and $\sin \theta_{23} = 0.707$. Right plot shows the precision reach expected at ICAL in the $\sin^2 \theta_{23} - \Delta m_{32}^2$ plane for 4.5-years running of the 50 kton detector.	152
5.13	The precision reach expected at ICAL in the $\sin^2 \theta_{23} - \Delta m_{32}^2$ plane for 10-years with 50 kton detector. The left plot shows the comparison of precision results when μ^+ and μ^- events are combined and analysed (so no cid capability is assumed) and when they are kept separate. The latter shows better sensitivity. The right plot compares the effect of including the additional constraint on the μ^+/μ^- charge ratio. The sensitivity, especially on θ_{23} marginally improves.	152
5.14	Left plot shows comparison of 5 systematic (black) with 10 systematic (red) for $\Delta\chi^2$ as a function of Δm_{32}^2 . Right plot shows comparison of 5 systematic (black) with 10 systematic (red) for $\Delta\chi^2$ as a function of $\sin^2 \theta_{23}$.	153
5.15	Sensitivity to Δm_{32}^2 (left) and $\sin^2 \theta_{23}$ (right) with different analysis: combining μ^+ and μ^- data so without cid is done (black curve), retaining them separately, with cid (red curve) and further including the 11 th pull (blue curve).	154

5.16 Left plot shows comparison of atmospheric muons (black) with combined atmospheric and upward-going muons (red), upward-going muons (blue) with 10 systematic uncertainties for $\Delta\chi^2$ as a function of Δm_{32}^2 . Right plot shows comparison of atmospheric muons (black) with combined atmospheric and upward-going muons (red), upward-going muons (blue) with 10 systematic uncertainties for $\Delta\chi^2$ as a function of $\sin^2\theta_{23}$ 155

Chapter 1

Introduction

High energy Physics or Particle Physics aims to study the fundamental particles and the nature of the interactions between them. The explanation behind using the term “high energy” is that the search for such fundamental particles requires very high resolution probes, a consequence of Heisenberg’s Uncertainty relation, where small objects (with small spatial uncertainty Δx) require large kinetic energies or momenta (Δp) to detect them. Also, many fundamental particles are amazingly massive and the energy (mc^2) needed to generate them is correspondingly large. Different theories and discoveries led to the formation of a framework of the particles and their interactions that we now know as the Standard Model (SM). The Standard Model is very important for particle physics as it concerns particles and their interactions and is well tested by several collider and non-collider experiments. But SM fails to explain certain phenomena like neutrino mass problem. In this chapter we begin with the Standard Model starting with the description of the particles and their interactions, followed by importance of neutrinos and the related physics and the experiments.

1.1 Standard Model

The Standard Model [1] is a theoretical picture that depicts the fundamental particles and their interaction with one another. The SM gives an effective hypothesis of the strong,

electromagnetic and weak interactions. The electromagnetic and weak interactions have been unified together into the electroweak interaction that is depicted by the Glashow-Weinberg-Salam (GWS) model [2]. The Quantum Chromodynamics (QCD) portrays the theory of strong interactions. The GWS model and the QCD together form the Standard Model. In Standard model [3, 4], the particles are classified as fermions with spin $s = 1/2$ or bosons with spin $s = 0, 1$. Fermions are further classified as quarks and leptons, each of which come in three generations as listed in Tables 1.1 and 1.2. Quarks carry an additional quantum number, the color, which is of three types red, blue and green [5]. Quarks must always belong to bound states because of the property of color confinement [6]. These bound states are called hadrons and are further classified as baryons and mesons. The baryons are fermions, which are made of three quarks, qqq . The mesons are bosons made of one quark and one anti-quark. On the other hand, the gauge particles which mediate the interactions are bosons of spin $s = 1$ listed in Table 1.3. One of the big missing pieces of the SM, the Higgs boson, was discovered at CERN's LHC in 2012 [7, 8]. The Figure 1.1 summarizes the particles of the Standard Model [9]. Now we describe the fundamental particle interactions and limitations of Standard Model in the following subsection.

Generation	First	Second	Third
Electric Charge = 0	ν_e	ν_μ	ν_τ
Electric Charge = -e	e^-	μ^-	τ^-

Table 1.1: Three generations of charged leptons with their corresponding neutrinos.

Generation	First	Second	Third
Electric Charge $+\frac{2}{3}e$	up (u)	charm (c)	top (t)
Electric Charge $-\frac{1}{3}e$	down (d)	strange (s)	bottom(b)

Table 1.2: Quarks with their six different flavours.

Force	Gauge Boson	Charge	Spin	Mass (GeV/c^2)	Range	Rel. Strength
Gravity	Graviton (G)	0	2	0	∞	10^{-38}
Weak	W^\pm, Z^0	$\pm 1, 0$	1, 1	$80.423 \pm 0.039, 91.188 \pm 0.002$	10^{-18}m	10^{-5}
EM	Photon (γ)	0	1	0	∞	10^{-2}
Strong	Gluon (g)	0	1	0	10^{-15}m	1

Table 1.3: Properties of the force mediators.

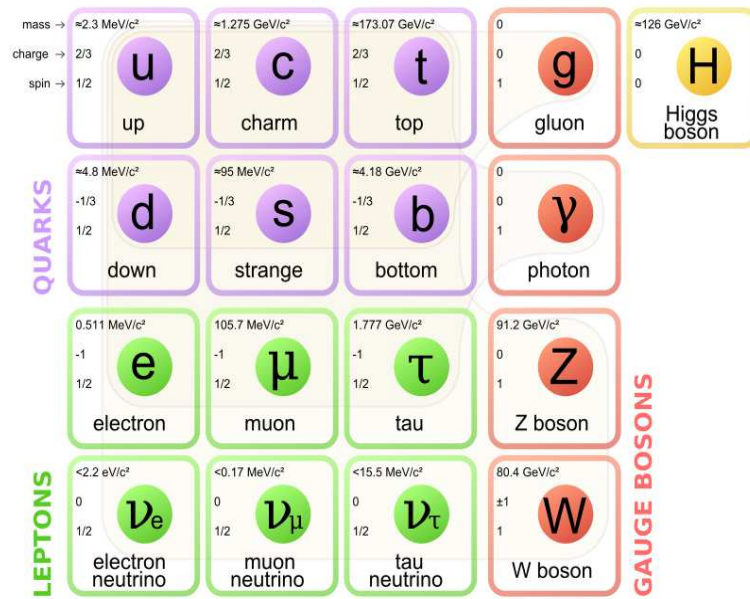


Figure 1.1: Three generations of matter.

1.1.1 Particle Interactions

There are four fundamental interactions (or forces) in nature: gravitational, weak, electromagnetic and strong, with which we can explain all the natural processes. These are mediated by fundamental particles called gauge bosons. All the fundamental interactions [10] conserve certain quantum numbers. For instance baryonic quantum number which portray the baryon families, is conserved in all the four interactions. Similarly, the lepton quantum numbers L_e, L_μ, L_τ are always conserved. We now describe these interactions one by one.

The *Gravitational interactions* act between a wide range of particles. These are mediated by the exchange of massless boson with spin 2, the graviton. At atomic and subatomic

levels the gravitational interaction is extremely feeble and can be ignored, moreover Standard Model does not include it.

The *Weak interactions* have shortest range among all the interactions and are responsible for flavour change interactions between quarks. The mediators of the weak interactions are the W^\pm and Z^0 bosons. These particles have large masses and interact with both leptons and quarks as well as with the Higgs boson. These interactions violate parity, charge conjugation and time reversal individually but have never been observed to violate combined CPT operation [11].

The *Electromagnetic (EM) interactions* are mediated by massless photons which are spin 1 gauge bosons. They account for most of the observed atomic and chemical phenomena. They have infinite range and much stronger than gravitational force.

The *Strong interactions* are responsible for binding the quarks in the protons and neutrons within the nuclei. The mediators of the strong interactions are gluons. They have short range and force between two particles increases as they move apart. These interactions conserve the strangeness, charge conjugation, parity and time reversal, just like electromagnetic interactions. More details of these fundamental forces are given in Table 1.3.

So the Standard Model explained the structure of matter and the interactions between them very well. Despite being mathematically self-consistent and also verified by many experiments, the model has some limitations. One of the major limitation of SM was Higgs boson, (discovered in 2012) which gives masses to the gauge bosons. The SM failed to explain, why the weak interactions should be mediated by massive gauge bosons while the electromagnetic and strong forces are mediated by massless gauge bosons. The SM does not complete the unification of three interactions because the strengths of these interactions are not related by the model. In Standard Model, the three neutrinos with their anti-particles are taken as massless and a neutrino cannot change its flavour [12]. This was proved wrong by a series of experiments starting with the Homestake experiment [13] – [21] observed a deficit in the flux of solar neutrinos which also showed

evidence for the phenomenon of neutrino oscillation. Non-zero neutrino masses and their oscillations are critical issues and need lots of studies to explore more about them. In the next section we describe the history of neutrinos with their interactions and properties.

1.2 Neutrinos and their Interactions

1.2.1 History of Neutrinos

Neutrinos were initially proposed by Pauli in 1930 in order to explain the spectrum of electrons from beta decay [22, 23]. The vast spread of energies raised a doubt about the conservation of energy, since no other particle were seen to be emitted [24] and Pauli hypothesised that a small, massless, neutral particle must be accompanying the beta particle and called these neutrinos (actually these are the electron neutrinos). Lederman, Schwartz and Steinburger found the muon neutrino in 1962, by demonstrating that the neutrinos in the process $\pi \rightarrow \mu\nu$ act differently from those generated from beta decay [25]. The discovery of tau in 1975 made the scientists think that tau neutrino (ν_τ) was accompanying the tau and it was confirmed directly by the Direct Observation of Nu-Tau (DONuT) experiment at Fermilab in 2000 [26].

The neutrinos found in nature are both terrestrial [27] and extraterrestrial [28]. They are generated in the laboratory too. The information provided by these sources is needed to understand the essential properties of the neutrinos. The energy spectrum of naturally occurring neutrinos starts from some fractions of electron-volts and spans an impressive range. Figure 1.2 shows the spectra of neutrinos [29] from different sources. Some of the spectra as shown in the figure are based on just observation while others, especially at high energies, are based on model calculations. No single detector can possess such a large range in detection capability. Neutrinos produced over such a wide energy range make it challenging to detect and understand them.

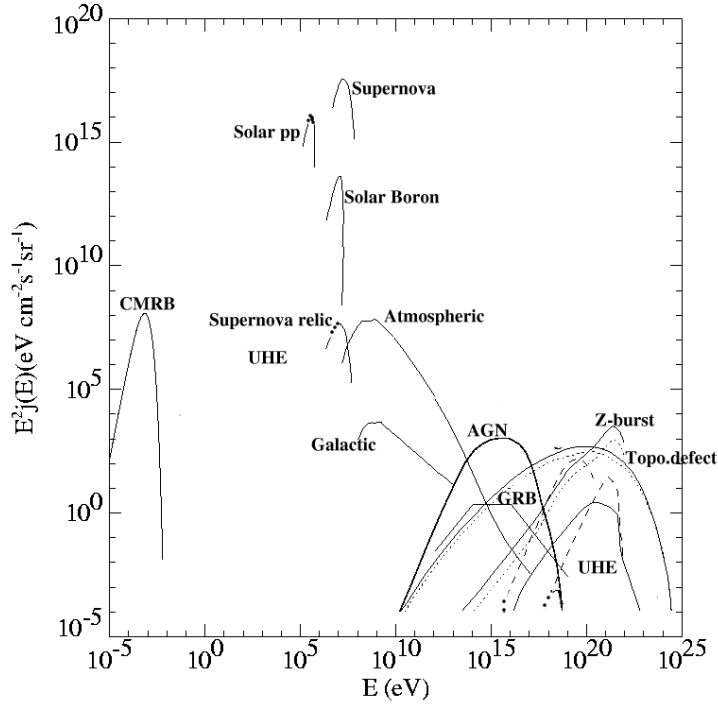


Figure 1.2: Neutrino spectrum from different sources as a function of energy.

1.2.2 Properties of Neutrinos

Neutrinos, the second most abundant particles in the Universe after light, are electrically neutral and interact only via the weak interaction. They exist in (at least) three different flavors (electron, muon and tau) and are almost massless i.e., they have very small masses compared to the other fermions. They are extremely elusive, i.e., they have very tiny cross-sections with matter.

Neutrino Interactions

Depending on the energy range the neutrino interactions with matter (here we restrict to nucleons as these are of interest to us) are classified as follows:

Quasi-elastic charge current (QECC) interactions : Quasi-elastic scattering comprises both charged and neutral current two-body neutrino reactions with nucleons. Below

1 GeV, quasi-elastic charge current interactions dominate and produce associated leptons, as given by:

$$\nu_{\mu}n \rightarrow \mu^{-}p; \quad \bar{\nu}_{\mu}p \rightarrow \mu^{+}n .$$

Charge current resonance interactions (RI) : For neutrino energies around 1 GeV and above, baryon resonances may be excited and subsequently decay into a nucleon and one or more mesons. The production of single pion events takes place and is given by:

$$\nu_{\mu}N \rightarrow \mu^{-}N^{*}; \quad N^{*} \rightarrow \pi N .$$

Charge current deep-inelastic scattering (DIS) : Deep-inelastic scattering is unique as it is modeled as an inclusive, rather than exclusive, reaction between a neutrino and the parton constituents of the nucleon. Above a few GeV, this process dominates and produces leptons and associated hadrons collectively labelled X , as given by:

$$\nu_{\mu}N \rightarrow \mu^{-}X; \quad \bar{\nu}_{\mu}N \rightarrow \mu^{+}X .$$

where we have specified only the muon-type neutrinos, although all flavours can undergo these interactions. All these processes are explained in Feynman diagrams as shown in Figure 1.3.

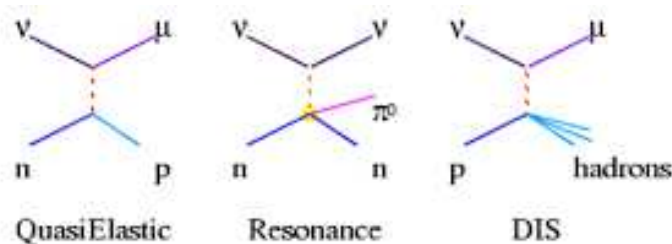


Figure 1.3: Feynman diagram of neutrino interactions.

One of the most interesting properties of neutrinos is the observation of neutrino oscillations, which we describe in a separate subsection below.

1.2.3 Neutrino Oscillations

The first experimental clue of neutrino oscillations was observed by Davis in 1967 in the reaction $^{37}\text{Cl} + \nu_e \rightarrow ^{37}\text{Ar} + e^-$ initiated by solar neutrinos. A finite rate of this reaction was observed but with significant deficit as compared to the solar model predictions [30]. It was not clear for a long time, whether the inconsistency is in the solar model, in the neutrinos, or in the experiment. Similar deficits were observed in atmospheric showers from cosmic rays. Source of atmospheric neutrinos is the pion decay by means of $\pi \rightarrow \mu \nu_\mu \rightarrow (e \nu_e \nu_\mu) \nu_\mu$. It is expected that there should be two muon neutrinos for each electron neutrino in these showers. Experiments in the 1960s tried to measure these atmospheric neutrinos. After gathering adequate statistics, it started to be obvious that there was an inclination for both the $\nu_\mu : \nu_e$ proportion and the ν_μ flux to be deficient. Probably the first strong insight towards the oscillation theory came in the 1980s at the Irvine-Michigan-Brookhaven (IMB) experiment, which observed a 2.5σ deficit in the number of low energy muons decaying in the detector [31]. In 1988, a critical deficit was observed in both the ratio and the absolute ν_μ flux by the Kamiokande collaboration [32]. In 1998, Super-Kamiokande reported a complete evidence of $\nu_\mu \leftrightarrow \nu_\tau$ neutrino oscillations [33] – [37] which was confirmed by Soudan 2 experiment [38]. The (KEK to Kamioka) K2K observed the same impact with an accelerator produced beam of ν_μ [39]. Many reactor neutrino experiments such as KamLAND [40] also showed evidence for oscillations.

The solar neutrino problem was sorted out in 2001 by the Sudbury Neutrino Observatory (SNO) [41] experiment and showed that there is a part of non- ν_e neutrinos in the solar flux and the aggregate flux agrees with the standard solar model prediction [42, 43]. This completed the case for neutrino flavour oscillations.

Pontecorvo [44] was the first to propose neutrino oscillations in 1957. He considered the oscillation $\nu \leftrightarrow \bar{\nu}$ as only electron neutrinos were known that time. Later, Maki, Nakagawa and Sakata (MNS), proposed the mixing between ν_e and ν_μ in 1962 [45]

and it was extended to three neutrino mixing after the discovery of tau particle [46]. The neutrino mixing matrix is actually known from their names as the Pontecorvo-Maki-Nakagawa-Sakata (PMNS) matrix [47].

According to the theory of oscillations, neutrinos have non-zero masses (or rather mass-squared differences) and the flavour states which participate in the weak interactions are mixtures (quantum mechanical superpositions) of mass eigenstates with different masses (m_1 , m_2 and m_3). Within the Standard Model, this mixing cannot occur but it has been seen in nature and is the 1st evidence of physics beyond the Standard Model. In general the two bases - flavour and mass states, are connected by a unitary matrix i.e., Pontecorvo-Maki-Nakagawa-Sakata (PMNS) matrix which is given by:

$$\begin{pmatrix} \nu_e \\ \nu_\mu \\ \nu_\tau \end{pmatrix} = \begin{pmatrix} U_{e1} & U_{e2} & U_{e3} \\ U_{\mu1} & U_{\mu2} & U_{\mu3} \\ U_{\tau1} & U_{\tau2} & U_{\tau3} \end{pmatrix} \begin{pmatrix} \nu_1 \\ \nu_2 \\ \nu_3 \end{pmatrix}$$

where the vector containing ν_e , ν_μ , ν_τ represents the flavour eigen states and that containing ν_1 , ν_2 , ν_3 represents the mass eigen states (There is another possibility, called Sterile neutrino ν_s [48], which is a hypothetical type of neutrino that does not interact via any of the fundamental interactions of the Standard Model except gravity, but we do not consider this here).

For instance one flavour eigenstate when propagating a macroscopic distance can be detected as a different flavour eigenstate. This phenomenon is interpreted as neutrino oscillation [12] and arises from a mixture between the flavour and mass eigenstates of neutrinos, which are the indirect proof for the existence of the non-zero mass of neutrinos. The probability of an initial neutrino ν_α of flavour α and energy E being detected as a neutrino ν_β of the same energy but with flavour β after travelling a distance L in vacuum is given by,

$$P_{\alpha\beta} = \delta_{\alpha\beta} - 4 \sum_{i>j} \text{Re}[U_{\alpha i} U_{\beta i}^* U_{\alpha j}^* U_{\beta j}] \sin^2 \frac{\pi L}{\lambda_{ij}} + 2 \sum_{i>j} \text{Im}[U_{\alpha i} U_{\beta i}^* U_{\alpha j}^* U_{\beta j}] \sin \frac{2\pi L}{\lambda_{ij}} \quad (1.1)$$

where $\lambda_{ij} = 2.47 \text{ km}(E/\text{GeV})(eV^2/\delta_{ij})$, L is also expressed in km, and $\delta_{ij} = m_i^2 - m_j^2$. More details for survival probability ($P_{\mu\mu}$), in vacuum or in matter are given in [49]. The currently known values (and 3σ ranges) of the mixing parameters are shown in Table 1.4.

Parameter	Central value	3σ range
\sin_{12}^2	0.304	–
Δm_{21}^2	$7.6 \times 10^{-5} \text{ eV}^2$	–
θ_{13}	8.729°	$[7.671^\circ, 9.685^\circ]$
$\sin^2 \theta_{23}$	0.5	$[0.36, 0.66]$
$ \Delta m_{32}^2 $	$2.4 \times 10^{-3} \text{ eV}^2$	$[2.1, 2.6] \times 10^{-3} \text{ eV}^2$
δ_{CP}	–	Unknown

Table 1.4: Current best known values of neutrino oscillation parameters.

While the parameters in the 1–2 sector (which are mostly determined by solar neutrino experiments) are rather well known, those in the 2–3 sector are not as well known; in fact, the *sign* of the 2–3 mass squared difference Δm_{32}^2 is not known; this is referred to as the neutrino mass ordering problem [50]. The mass ordering problem is also related to the mass hierarchy problem as listed in Table 1.5 below. In addition, the across-generation mixing angle θ_{13} was only recently found to be different from zero, as per some results from RENO [51] and DAYA-BAY [52] experiments; this has made the challenge of determining the neutrino mass hierarchy easier. More details are in chapter 5 in section 5.1. This thesis contains the simulations studies of atmospheric neutrino interactions and will therefore focus on determining parameters in the 2–3 sector.

Normal hierarchy $m_3 \simeq \sqrt{ \Delta m_{32}^2 } \simeq 0.03 - 0.07 \text{ eV}$	$m_1 < m_2 \ll m_3$	$\Delta m_{32}^2 \equiv m_3^2 - m_2^2 > 0$	two lighter levels involved
Inverted hierarchy $m_{1,2} \simeq \sqrt{ \Delta m_{32}^2 } \simeq 0.03 - 0.07 \text{ eV}$	$m_1 \simeq m_2 \gg m_3$	$\Delta m_{32}^2 \equiv m_3^2 - m_2^2 < 0$	two heavier levels involved
Degenerate neutrinos	$m_1 \simeq m_2 \simeq m_3$	–	–

Table 1.5: Three cases of neutrino mass ordering.

Many experiments are involved in the precise measurement of the oscillation studies. The proposed up-coming experiment India-based Neutrino Observatory (INO) with magnetised Iron CALorimeter (ICAL) detector will do precision measurements of neu-

trino oscillation using atmospheric neutrinos. Simulations shows that the detector will gave good muon energy and direction resolution as well as excellent charge identification (cid) capability. In addition, R & D has shown that the Resistive Plate Chambers (RPCs) which are the active detector elements, have good timing resolution and ease of construction; more details on RPC studies will be given later in chapter 2. Hence ICAL will be able to detect muon neutrinos very well. It will be able to discriminate between upward-going and downward-coming muons also (as we will discuss in chapters 2, 5).

1.2.4 Non-oscillation Neutrino Experiments

This issue is beyond the scope of this thesis, which focuses on neutrino oscillation physics alone. A short account is included for completeness here.

Oscillation experiments cannot tell us about the overall scale of masses. Hence, it is important to find the absolute values of the masses. A sensitive probe for the absolute scale of the neutrino masses is the search for neutrino-less double beta decay, $\beta\beta 0\nu$, whose rate is potentially measurable if the neutrinos are Majorana fermions [53] (i.e., they are their own anti-particles) and m_{ν_e} is large enough. The TinTin detector at INO aims to search for the nature of neutrinos i.e., whether they are Dirac or Majorana (whether or not it is its own antiparticle).

The presence of a neutrino mass suggests the presence of its magnetic moment of the order of 10^{-19} Bohr magneton implying that neutrinos may interact electromagnetically also.

Some experiments show that neutrinos possess left-handed helicities [54, 55], which is defined as the spin projection along the direction of motion of the particle. On the other hand anti neutrinos possess right-handed helicities. It indicates that only one of the two possible helicities is observed for either particle.

In the next section we describe uses and even exotic applications of neutrinos.

1.3 Uses of Neutrinos

The neutral charge and the low mass of neutrinos makes them interact weakly with other particles and fields. This further interests the scientists as the neutrinos can be used to probe environments where the other radiation such as light or radio waves cannot penetrate.

It was first proposed in the mid-20th century to use neutrinos as a probe in order to detect conditions at the core of the Sun. As the electromagnetic radiation is diffused by huge amount and density of matter surrounding the core, the solar core cannot be imaged directly. But neutrinos on the other hand pass through the Sun with few interactions. The emitted photons from the solar core may require 40,000 years to diffuse to the outer layers of the Sun, neutrinos created in stellar fusion reactions at the core cross this distance practically unobstructed at almost the speed of light.

Neutrinos are additionally helpful for probing astrophysical sources beyond the Solar system because they are not significantly attenuated by their travel through the interstellar medium. Whereas optical photons can be obscured or diffused by gas, dust and background radiation and high-energy cosmic rays, are unable to travel more than around 100 megaparsecs due to the Greisen-Zatsepin-Kuzmin limit [56] (GZK cutoff). Neutrinos, interestingly, can travel much more distances and get barely attenuated.

The galactic core of the Milky Way is completely obscured by dense gas and numerous bright objects. Neutrinos generated in the galactic core may be measurable by Earth-based neutrino telescopes.

One more important use of the neutrino is in the observation of supernovae, the explosions in which the life of a highly massive star ends. The core collapse phase of a supernova is greatly dense and energetic event. It is dense to the extent that no known particles have the capacity to escape from the advancing core front with the exception of neutrinos. Thus, supernovae release approximately 99% of their radiant energy in a short

(10-second) burst of neutrinos and these neutrinos are extremely useful probes for core collapse studies.

Neutrinos can also be used for studying quantum gravity effects. As they are neither affected by the strong interaction nor by electromagnetism, also they are neither found in composite particles nor prone to near instantaneous decay. It may be possible to isolate and measure gravitational effects on neutrinos at a quantum level.

Neutrinos with their lowest mass are examples of the lowest-energy particles and are categorized in the beyond Standard Model physics and hence are important.

In November 2012 American scientists sent a coherent neutrino message using a particle accelerator through 780 feet of rock [57]. Hence this was the first attempt to use neutrinos for communication, and it is probable that in future binary neutrino messages will be send to immense distances through even the densest materials, such as the Earth's core. In the following section we discuss about the various sources of neutrinos.

1.4 Sources of Neutrinos

Each source of neutrinos provide information, sometimes overlapping, that is crucial in understanding the intrinsic properties of the neutrinos and their sources. The various neutrino sources are described below:

1. **Solar neutrinos:** Solar neutrinos arise from the nuclear fusion powering the Sun and other stars. As per the Standard Solar Model, four protons fuse to become one helium nucleus, two of them have to convert into neutrons, and each such conversion releases one electron neutrino. The Sun sends huge amount of neutrinos in all directions with about 65 billion (6.5×10^{10}) solar neutrinos passing through every square centimeter per second on the part of the Earth facing the Sun. Since neutrinos are hardly absorbed by the mass of the Earth, the surface area on the side of the Earth opposite the Sun gets about the same number of neutrinos as the side confronting the Sun.

2. **Atmospheric neutrinos:** They are formed by the interaction of cosmic rays with atomic nuclei (protons) in the Earth's atmosphere, creating showers of particles called hadrons. Most of them are unstable (pions) and produce neutrinos when they decay [58] as shown in Figure 1.4. We will discuss this further in detail in the next subsection 1.4.1. Experiments performed at Kolar Gold Fields (KGF) in India in 1965 recorded the first cosmic ray neutrino interaction [59].

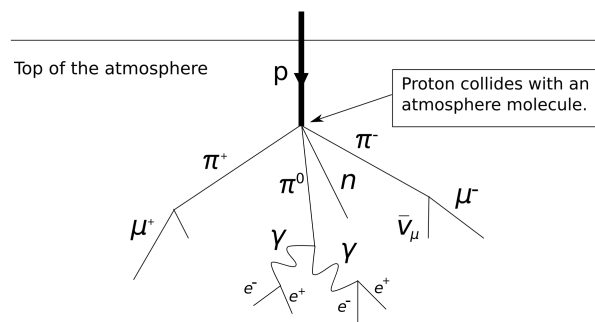


Figure 1.4: Primary cosmic particle collides with a molecule of atmosphere.

3. **Geologically produced neutrinos:** Neutrinos are also produced from natural radioactivity. Particularly, the decay chains of ^{238}U , ^{232}Th and ^{40}K , including beta decays which emit anti-neutrinos. These geoneutrinos can provide crucial information on the Earth's interior. In 2005, KamLAND provided a first prediction for geoneutrinos. The main background in KamLAND's detection of the geoneutrinos are the anti-neutrinos coming from reactors. Several future experiments will improve the geoneutrino measurement and need to be done far away from the reactors.
4. **Supernovae:** The energy produced in supernovae is mostly radiated away in the form of an immense burst of neutrinos. Because neutrinos interact weakly with matter, it is believed that a supernova neutrinos carry information about the innermost regions of the explosion. One more important neutrino source is the thermal energy of the newly formed neutron core, which gets dissipated via the formation

of neutrino-anti neutrino pairs of all flavors, as explained below:



Approximate neutrino flux observed from the SN1987a supernova was $10^{12}/m^2/s$.

5. **Big Bang:** It is thought that, just like the cosmic microwave background radiation left over from the Big Bang, there is a background of low-energy neutrinos in our Universe. Despite their being very numerous - about 330 neutrinos per cm^3 , their energy is so small (about 0.0004 eV), that no experiment has been able to detect them as yet.
6. **Reactor neutrinos:** Nuclear reactors [60] are the biggest source of neutrinos generated by humans. Anti-neutrinos are generated in the beta-decay of neutron-rich daughter fragments in the fission process. The average nuclear fission releases about 200 MeV of energy, of which roughly 4.5% is radiated away as anti-neutrinos. An average nuclear power plant produces about 10^{20} anti-neutrinos per second.
7. **Accelerator neutrinos:** Neutrino beams [61] can be produced using the particle accelerators. They are formed by colliding protons with a fixed target, generating charged pions or kaons. The unstable particles formed are then magnetically focused into a long tunnel where they decay while in flight and the relativistic boost of the decaying particles causes the neutrinos to be produced as a beam rather than isotropically. Neutrinos can also be generated from muon decays in a neutrino factory. High precision studies can be conducted with such neutrinos although no such facility exists so far.
8. **Nuclear bombs:** They also generate large amount of neutrinos. Fission bombs produce anti-neutrinos and fusion bombs produce both neutrinos (from the fusion process) and anti-neutrinos (from the initiating fission explosion).

1.4.1 Atmospheric Neutrino Problem

The primary cosmic ray particles coming from Earth's atmosphere, mainly contain protons and alpha particles. After interacting with air nuclei they create secondary mesons, mainly pions and kaons which further decay to produce neutrinos (atmospheric neutrinos):

$$\begin{aligned}\pi^\pm &\rightarrow \mu^\pm + \nu_\mu(\bar{\nu}_\mu) \\ \mu^\pm &\rightarrow e^\pm + \nu_e(\bar{\nu}_e) + \nu_\mu(\bar{\nu}_\mu) \\ K^\pm &\rightarrow \mu^\pm + \nu_\mu(\bar{\nu}_\mu) \\ \mu^\pm &\rightarrow e^\pm + \nu_e(\bar{\nu}_e) + \nu_\mu(\bar{\nu}_\mu)\end{aligned}$$

The decay chain indicates that the expected ratio of number of $(\nu_\mu + \bar{\nu}_\mu)/(\nu_e + \bar{\nu}_e)$, or simply ν_μ/ν_e , should be about two at the lower energy region ($\sim 1\text{GeV}$). Whereas at higher neutrino energy, this ratio becomes greater than two because flight distances of pions and muons become longer and there is less chance for the muons to decay into electron neutrinos. Further, neutrinos easily traverse the entire Earth without getting attenuated, as their cross-section is too small.

As downward-coming neutrinos are produced directly above the detector and upward-going are produced underground, neutrino flight distances vary from 15 km to 13,000 km. Atmospheric neutrino measurement can be sensitive to the neutrino oscillation parameter Δm_ν^2 down to $10^{-4}eV^2$.

Atmospheric neutrinos [62] – [67] cover all possible energy ranges (~ 100 MeV to > 1 TeV). Energy spectra for atmospheric neutrino fluxes have been calculated by Honda [68], Bartol [69], Volkova [70] and Butkevitch [71] and are shown in Figure 1.5 [72]. These neutrinos can interact with the material of the detector. These are called contained events and are dominated by the lowest energy neutrinos. The response of ICAL to these neutrinos are discussed in chapter 4. A simulations study of the sensitivity of these neutrinos to oscillations has been studied elsewhere [73, 74].

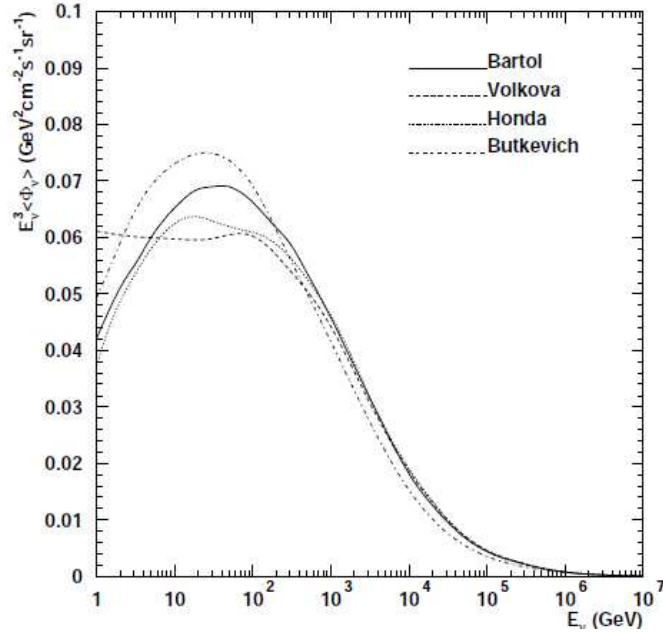


Figure 1.5: The energy spectrum of atmospheric neutrino flux.

Sometimes these neutrinos interact with the rock surrounding the detector and produce rock muons. They usually come from all the directions in an underground detector and can be separated from the cosmic ray muon background only in the upward direction as these background muons can still penetrate down to the detector about 1000 m underground. These rock muons when they reach the detector are called the *Upward-going muons*. The effective target volume for interactions involving upward-going muons is larger than the size of the detector. The muon produced needs to have sufficiently high energy so that it can travel through rock to reach the detector. Thus, upward-going muon analysis deals with higher energy neutrinos than the contained events analysis and also carries significant amount of oscillation information. In chapter 5, we discuss the oscillation analysis using upward-going muons and its importance in ICAL detector.

1.5 Neutrino Experiments and their Goals

Several neutrino experiments have provided many new and significant results. Some of the main results are summarized as follows:

- **Solar and Atmospheric neutrinos:** The Solar Neutrino problem is the deficit in electron neutrinos from the Sun relative to the what is expected from the Standard Solar Model. A mixture of deficit in charged current interactions and the identification of all the anticipated number of neutrinos in neutral current interactions demonstrates that the solution to this problem lies in neutrino oscillations. The other problem includes the atmospheric ν_μ with the deficit relative to the atmospheric ν_e and is represented by a mass squared difference. The magnitude of mass squared difference relevant to atmospheric data is larger than the mass squared difference relevant to solar neutrino data, but then there is another large mixing between states. These observations accordingly suggest the presence of at least two non-zero masses for neutrino mass eigenstates.
- **Cosmological data:** Cosmological experiments, beside restricting the number of light neutrino flavour, set an upper limit on the sum of all the active neutrino masses [75].
- **Beta decay and double beta decay:** As compared to neutrino oscillation sensitive experiments, these are effective in putting direct mass limits. An upper limit of 2.2 eV [76, 77] is achieved on the dominant mass eigenstate for electron neutrinos included in tritium beta decay. KATRIN [78] experiment, will either improve this limit or discover the actual mass. The limits from experiments including muon and tau-type neutrinos are much higher and can be neglected.

Neutrino-less beta decay experiments searches for the nature of neutrino, whether its Majorana or Dirac particle. In case neutrinos are Majorana particles, a limit less

1.5. Neutrino Experiments and their Goals

than 0.2 eV [79] could be put on the effective mass parameter related to neutrino masses and mixing.

- **Neutrinos from Supernova:** Supernova SN1987a [80] has confirmed so many qualitative features of the stellar collapse scenario. But due to the low statistics of observed events, it is difficult to conclude on the neutrinos' properties.
- **Other neutrino properties:** Stringent upper limits exist for neutrino decay rates, magnetic moments and other such properties.

Some important characteristics of the on-going and future detectors are mentioned in Table 1.6. We describe the various detectors in the neutrino experiments in the following subsection.

Experiment	Location	Type of detector	Sensitivity	Operation
BOREXINO	Italy	Scintillator	LS	May 2007-
Daya Bay	China	Scintillator	R	2011-
Double Chooz [81]	France	Scintillator	R	2011-
GALLEX	Italy	Radiochemical	LS	1991-1997
GNO	Italy	Radiochemical	LS	May 1998-Jan 2002
HOMESTAKE-CHLORINE	South Dakota	Radiochemical	S	1967-1998
ICARUS	Italy	Liq. Ar Cherenkov	S	2010-
IceCube	Antarctica	Water Cherenkov	ATM, CR, AGN	2006-
INO	India	Mag. Iron CAL	ATM	future
JUNO	China	Scintillator	R	2014- (construction)
Kamiokande	Japan	Water Cherenkov	S, ATM	1986-1995
KamLAND	Japan	Liq. scintillator	R	2002-
LBNE [82]	South Dakota	Cherenkov	AC, ATM, S	future
MicroBooNE	USA	Liq. Ar TPC	AC, SN	2014
MINERvA	USA	Scintillator	AC	2009-
MiniBooNE	USA	Cherenkov	AC	2002-
MINOS	USA	Solid scintillator	AC, ATM	2005-2012
MINOS+	USA	Solid scintillator	AC, ATM	2013-
NOvA [83]	USA	Liq. scintillator	AC	2011-
OPERA	Italy	Lead emulsion	AC	2008-
RENO	South Korea	Scintillator	R	2011-
SNO	Ontario	Water Cherenkov	S, ATM, GSN	1999-2006
SNO+	Ontario	SNO with liquid scintillator	S,LS,R,T,SN,LSN	2014-
Super-K	Japan	Water Cherenkov	S, ATM, GSN	1996-
UNO	Colorado	Water Cherenkov	S, ATM, GSN, RSN	future

Table 1.6: List of neutrino experiments across the globe.

1.5.1 Detector types

A brief description of the types of detectors with their properties are given below:

- **Water Cherenkov Detector:** The detecting element is highly purified water. When high energy charged particles go through the water they produce Cherenkov light which is then detected by Photo Multiplier Tubes (PMTs) that surround the water. Taking into account of the pattern of emission of Cherenkov light, these detectors can distinguish both electrons, positrons and muons. A large number of particles in the hadron shower produced in the deep inelastic scattering causes a problem in the energy reconstruction of very high energy neutrinos ($E_\nu \geq 5\text{GeV}$), as many particles will be below their Cherenkov threshold. Due to the absence of a magnetic field in these detectors the charge of a particle cannot be identified. The heavy water or mineral oil can replace the pure water.
- **Liquid Argon Detector:** The detecting medium here is liquid Argon. The charged particles' tracks are identified in the liquid and the pattern of their tracks makes it easier for the particle to be identified. Along with good calorimetry the detector has excellent capability to identify the particles. Due to the absence of a magnetic field it is incapable of distinguishing particles and anti-particles.
- **Emulsion Detector:** Emulsion films ($50\ \mu\text{m}$ thick) are placed to detect the trajectories of τ and its decay products. In order to get a large target mass (1.8 kton) these films are sandwiched between 1 mm thick lead plates. Additionally, a magnetic spectrometer is placed which measures the momentum and charge of muons going through it.
- **Iron Calorimeter:** The MINOS [84] detector uses 5 kton iron with scintillators as the active detector elements. On the other hand, the proposed Iron Calorimeter (ICAL) detector at the India-based Neutrino Observatory (INO) will comprise iron (steel) modules blended with sensitive elements such as Resistive Plate Chambers (RPCs) in which charged particles deposit energy (described in chapter 2). These detectors can detect ν_μ and $\bar{\nu}_\mu$ and are not as sensitive to electron-type neutrinos.

The presence of magnetic field makes the distinction of ν_μ and $\bar{\nu}_\mu$ possible. In chapter 2 we will discuss about ICAL and RPCs at INO. The R & D of RPC is necessary and hence their fabrication and characterization will be discussed in detail in chapter 3.

1.5.2 Open Issues in Neutrino Physics

Regardless of the significant results that have been obtained by experiments so far, there are some extraordinary issues of great importance which form the major motivation for establishing a neutrino experiment in India:

- Results from several experiments predict the neutrino oscillation and precision measurements. A re-confirmation and improvement in these results will be the challenge for the several future experiments.
- Matter effects help to determine both the magnitude and sign of the mass squared difference (Δm_{21}^2 is positive) in the solar neutrino problem.

The atmospheric neutrino and reactor or accelerator based experiments are till now insensitive to the sign of the mass squared difference between the participating neutrinos i.e., sign of Δm_{32}^2 is not yet known. Precision experiments sensitive to matter effects with the neutrino propagation through the earth will be able to predict it.

- Is there CP violation in the leptonic sector? Though these effects are small but this problem will be solved by future long-baseline neutrino experiments.
- What is the absolute scale of neutrino mass? Direct mass measurements from beta decay put an upper limit of around 2.2 eV. Model dependent interpretation of the astrophysical results limits the sum of the neutrino masses to around 0.5 eV. Neutrino-less double beta decay, will also determine the mass scale.

- Are the neutrinos Dirac or Majorana particles? Hypothetical assumption reveals that neutrinos are Majorana particles, that is, they are their own anti-particles. As only charge-neutral fermions can be Majorana thus neutrinos are the only candidates inside the Standard Model. Subsequently there is an extraordinary enthusiasm for predicting the nature of neutrinos by an unambiguous perception of neutrino-less twofold beta decay.
- Do neutrinos decay? This is improbable as a predominant situation to clarify the known data. On the other hand, they might still be allowed in combination with dominant neutrino oscillations.
- How many species of neutrinos exist? The LEP experiments [85] predicts the number of active species with masses less than half the mass of Z boson, are three. Results from the LSND [86] experiment depicts the presence of one more relatively light species, which has to be sterile i.e., it cannot interact via weak interactions, as there cannot be more than three light active species.
- Whether neutrinos have a non-zero magnetic moment? As neutrinos are massive so a non-zero magnetic moment is possible. The magnitude determination is of great fundamental significance and can impact on the solar neutrino problem.
- The composition and energy spectrum of primary cosmic rays (CR) can provide critical information to both particle physics and astrophysics. The observed *knee and ankle* [87] features of the CR spectrum are yet to be understood. The knee and ankle features are shown in Figure 1.6 [88]. The source and mechanism responsible for the highest energy CR will open new windows to our understanding of many important processes in our Universe. It will lead to production of very high energy neutrinos, and then the study of them may provide the vital clues to resolve *knee and ankle* features.

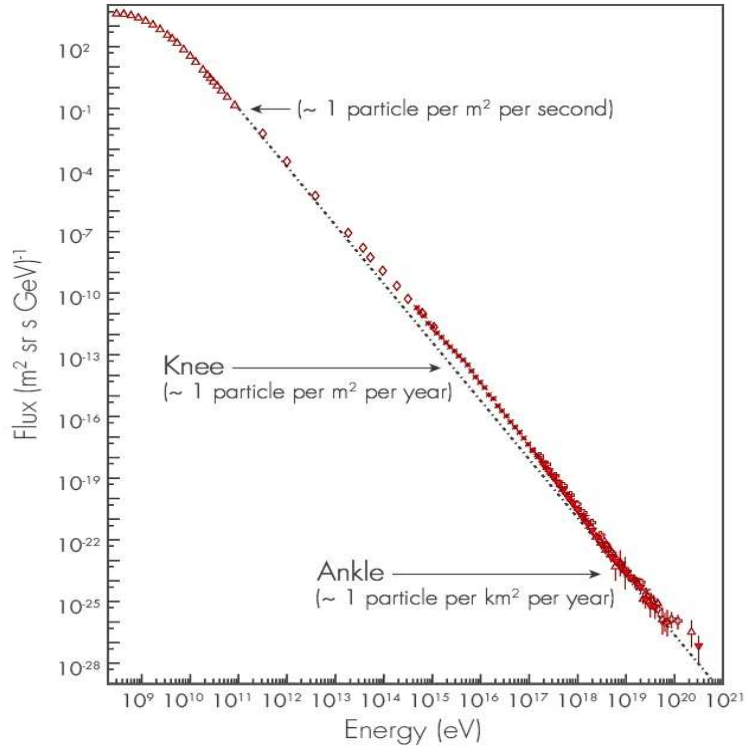


Figure 1.6: The flux intensity of cosmic rays as a function of energy.

Many of these issues will be addressed at on-going and future planned experiments. The proposed Iron CALorimeter detector at INO will be able to sort out some of the above described issues using atmospheric neutrinos by providing complimentary data to other experiments.

1.6 Overview of Thesis Content

To summarize, the elusive particles neutrinos were proposed by Pauli to explain observed beta decay spectrum. They interact only via weak interactions and their cross sections with nucleons are dominated by quasi-elastic, resonance and deep-inelastic interactions. Neutrinos are important in the cosmological and astrophysical fields. Neutrinos are generated from various sources like reactor, accelerator, geoneutrinos, solar, supernovae, big bang, atmospheric, etc. Accordingly, neutrino detectors are made to study the neutrinos

from different sources.

The Standard Model (SM) of particle physics predicted neutrinos to be massless while experiments discovered that neutrinos exhibit flavour oscillations and hence possess mass. For this the Nobel Prize in Physics 2015 was awarded jointly to Takaaki Kajita (Super-K) and Arthur B. McDonald (SNO) [89]. Many neutrino properties are not known till now, such as mass hierarchy, nature of neutrinos, existence of sterile neutrinos, CPT violation in the neutrino sector using atmospheric neutrinos, etc. In the coming years, neutrino studies are going to be interesting as the future experiments like INO will study neutrino mass hierarchy problem which will help us understand the mass ordering of neutrinos. The layout of thesis is given below:

In the next chapter, we discuss in detail about INO and its goals. The history of particle detectors is described briefly. Then we describe the components of the magnetised Iron CALorimeter detector (ICAL): details of magnet to be used, RPCs with its modes of operation, types of RPCs and applications and detector readout scheme. Then, we describe the goals of ICAL detector and its related neutrino physics.

In Chapter 3, we present a study of RPCs. We begin with the motivation to do this study and discuss the aging factor. Then, we describe the characterisation of various glass samples. We discuss their physical, optical, electrical, surface properties along with elemental and compositional studies. We then explain the gas system and mixing unit used for our study and a procedure to do MFC calibration with results. The fabrication and characterisation of three scintillator paddles with different widths is discussed in the next section. The fabrication and characterisation of various glass RPCs is discussed in detail in the later section. We describe the methodology to find the efficiency and cross-talk of various glass RPCs. Efficiency and cross-talk of RPC stack is discussed in the last section.

Chapter 4 begins with the brief description of ICAL detector simulated using the GEANT4 [90] and the INO-ICAL reconstruction software [91]. The magnetic field in

the different regions of ICAL is described along with details of input used to generate the muons in the Geant-based INO-ICAL code. Effect of different forces and choice of angular bins is explained in the next section. The choice of selection criteria with its effects is also described. Muon response–reconstruction efficiency, relative charge identification efficiency, direction reconstruction, zenith angle resolution and momentum resolution—along with the results is described for peripheral and side regions of the simulated ICAL detector. Momentum resolution as a function of the zenith and azimuthal angles, (θ, ϕ) , with results is also shown. Chapter 4 concludes with a comparison of muon response in different regions of ICAL.

Chapter 5 describes the simulations study of upward-going rock muons analysis in ICAL detector. Details about the detector response for muons (selection criteria, resolutions and efficiencies specifically obtained to use for upward-going muons), brief description of neutrino event generator (NUANCE) and data generation for upward-going muons are presented. The systematic uncertainties and χ^2 analysis along with the oscillation results and sensitivity to the 2–3 oscillation parameters is also discussed there.

In chapter 6, the work presented in this thesis is summarized and conclusions are discussed.

Chapter 2

ICAL Detector at INO

The magnetised Iron CALorimeter (ICAL) [29], along with Neutrino-less Double Beta Decay (NDBD) experiment and Dark matter at INO (DINO), are the proposed underground experiments to be placed in the India-based Neutrino Observatory (INO) laboratory to be build at Bodi West hills of Theni District in Tamil Nadu, located at $9^{\circ}39'$ and $10^{\circ}30'$ North latitude and between $77^{\circ}00'$ and $78^{\circ}30'$ of East longitude and Central location: $10^{\circ} 04'N 77^{\circ} 45'E$. The ICAL is an experiment which is aimed to study atmospheric neutrinos. The atmospheric neutrinos interact inside the detector through different processes. We focus here on the charged current (CC) interactions of the muon-type neutrinos (and anti-neutrinos) giving muons and hadrons. Hence, the neutrino energy is given by,

$$E_{\nu} = E_{\mu} + E_{hadrons} , \quad (2.1)$$

where the different processes are described in Section 1.2.2.

The ICAL detector's primary detection mechanism for the atmospheric neutrinos is via detection of muons produced in the CC interactions. The detector will consist of 3 modules of total 50 ktms of iron layers having an inhomogeneous magnetic field of 1.3–1.5 T and interleaved with the active detector elements which are Resistive Plate Chambers (RPCs). The specifications of ICAL detector are given in Table 2.1. It is proposed that it will have a good charge identification, tracking and energy resolution, especially for

muons; the energy of the associated hadrons can be reconstructed as well. Figure 2.1 shows a sketch of the proposed INO-ICAL detector.

ICAL	Dimensions
No. of modules	3
Module dimension	16 m × 16 m × 14.4 m
Detector dimension	48 m × 16 m × 14.4 m
No. of layers	150
Iron plate thickness	5.6 cm
Gap for RPC trays	4 cm
Magnetic field	1.3–1.5 T
RPC	Dimensions
RPC unit dimension	2 m × 2 m × 0.035 m
Read out strip width	3 cm
No. of RPC units/Road/Layer	8
No. of Roads/Layer/Module	8
No. of RPC units/Layer	192
Total no. of RPC units	28800
No. of electronic readout channels	3.6864×10^6

Table 2.1: ICAL detector specifications.

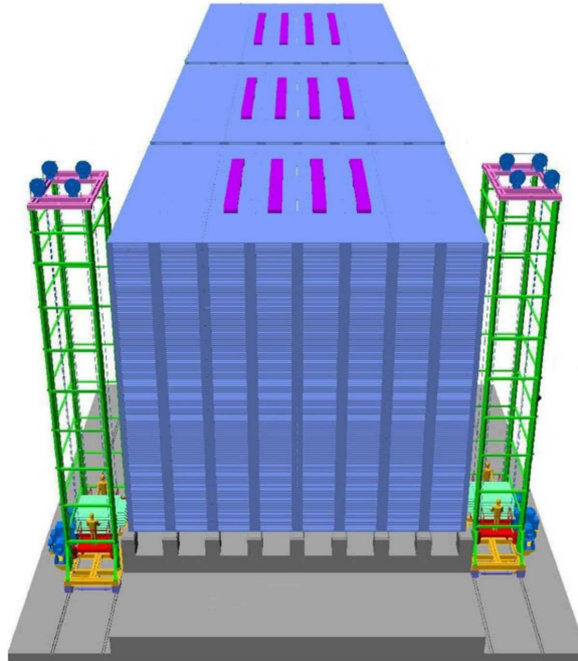


Figure 2.1: A schematic of the proposed INO-ICAL detector.

The NDBD experiment aims to determine the nature of neutrinos i.e., whether

they are Dirac or Majorana particles, using the tin (^{124}Sn) bolometer detector (TinTin). It will also determine the effective neutrino Majorana mass. The DINO experiment will search for low mass WIMPs using silicon as the active detector. Both these experiments will be housed along with ICAL at the underground INO laboratory. Simulations and R&D work is going on and many collaborating institutes are participating in it. Figure 2.2 shows sketch of proposed main INO cavern that will house ICAL and a closer look at how ICAL will be housed in it, whereas the specifications of the cavern are given in Table 2.2.

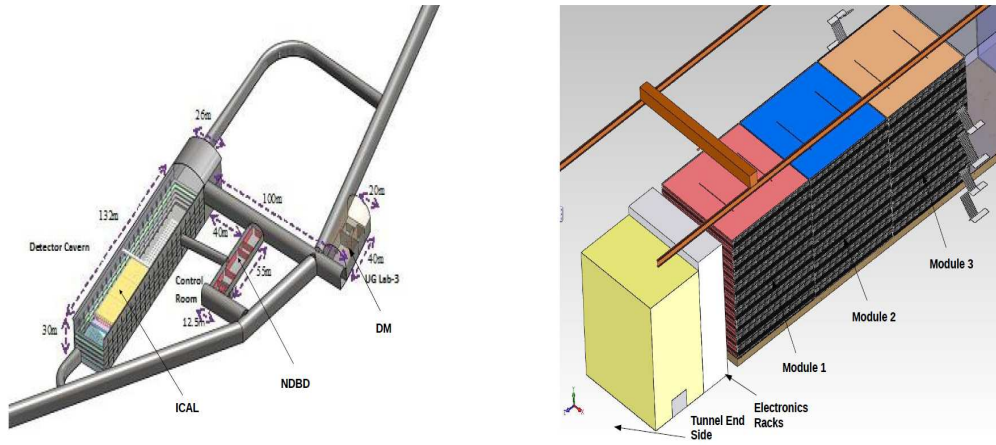


Figure 2.2: A sketch of the proposed INO main cavern (left); detail showing how the three modules of ICAL will be positioned in that cavern (right).

Length of the tunnel	2.1 km (approx.)
Tunnel cross-section	7.5 m (W) \times 7.5 m (H)
Tunnel gradient	1:15
Rock overburden	1300m (4000 mwe)
Rock type and density	Charnockite, 2.7 gm/cc
Number of caverns	3 (one big and two small)
Size of the main cavern	132 m \times 26 m \times 30 m (H)

Table 2.2: Specifications of INO caverns and access tunnel.

2.1 Future Goals of INO

INO will be housed in a low background region with overburden of 1200 m mountain rock which reduces the cosmic ray background to minimum level. It will be the best suitable

place to achieve many physics goals such as:

- The precise determination of oscillation parameters using atmospheric neutrinos.
- A study of matter effects with good charge identification will lead to the determination of the sign of one of the neutrino mass differences.
- To study charge-conjugation and parity (CP) violation in the leptonic sector. The study of possible charge-conjugation, parity, time-reversal (CPT) violation will also be important.
- A study of Kolar type events [59], identification of ultra high energy neutrinos and multi-muon events.

Though INO will start its activity with only atmospheric neutrinos, it is expected that it will ultimately have other neutrino experiments as well under its umbrella. There are several possibilities open for future directions and they are:

- Possible study of dark matter particle (DMP) decaying into leptonic modes.
- Solar, supernova and geoneutrino studies.
- Tomography of the Earth using natural and laboratory neutrino sources.
- Study of magnetic monopoles.
- High-precision measurement of the oscillation parameters after the upgradation of ICAL and its possible use as a far-end detector for a long base-line neutrino oscillation experiment in future.

2.1.1 Choice of the Detector

In order to achieve the above discussed goals the detector must fulfill some basic requirements. The choice of the detector for the INO experiment can be made as follows:

- The target mass should be large to achieve good statistics of significant number of neutrino interactions in a reasonable time-frame (say 5 years) to confirm atmospheric neutrino oscillation,
- Good energy and angular resolution in order to measure the path length travelled to energy ratio L/E with an accuracy better than half of the modulation period (consider neutrino cloud with flattened disc shape and its axis of symmetry inclined with respect to direction of ecliptic plane. In case of neutrino density gradually decreasing to the periphery of the cloud, the Earth in its movement twice a year crosses most and less dense area of the cloud.),
- In order to distinguish between neutrino and anti-neutrino, the charge identification of muons should be good.

The oscillation pattern in the L/E spectrum of atmospheric muon neutrinos can be obtained with good precision when the energy E and direction θ of the incoming neutrino is determined accurately in each event. The properties of the neutrino can be obtained by measuring the energies of muon and the hadrons produced in each event. However, it is found to be convenient to make measurements in terms of the observables which are the muon energy and direction, and the total hadron energy, since it is not easy to determine the hadron direction.

Hence it is essential to find the flight direction (up vs. down) of the muon produced by a neutrino interaction with high efficiency. The techniques like track curvature in a magnetic field and the measurement of timing in successive detector layers can be used to achieve this goal. The time-of-flight technique is the best and allows good up-down discrimination for a detector with a time resolution of 2 ns or better.

Some more factors have also been considered while finalising the choice of detector type and technology. The availability of technological capabilities within the country is an important one. The existence of other neutrino detectors around the world makes

the selection easier. The modularity, the possibility of phasing, compactness and ease of construction are some factors that should be kept in mind while deciding about a detector. The ICAL detector satisfies all the design goals listed above. The ICAL is a big modular detector with 50 kton magnetised iron plates interleaved with layers of RPCs whose time resolution is better than 2 ns and spatial resolution < 1 cm that will be ideal to address the physics goals listed above. Before we describe about the components of ICAL detector especially RPCs we discuss the history of particle detectors in order to have a better understanding.

2.2 History of Particle Detectors

A particle detector is a device which is capable of detecting, tracking and identifying high-energy particles. These particles are produced by cosmic radiation, reactions in a particle accelerator and nuclear decay. Calorimeters have been used since long to measure the energy/momentum, spin, charge of the particles. Detectors used now-a-days are huge in both size and cost. Spark, cloud and bubble chambers are the old detectors technologies in which the particle tracks were photographed. With time and the technology particle detectors have been changed. Detectors like wire or drift chambers [92] have successfully augmented the scintillation counters in experiments, as they require high spatial resolution particularly. Due to the ionisation created inside the active volume of these gaseous detectors they can also be used to determine the charge and velocity of the particle. Most of the gaseous detectors have wire-like anode electrodes which lead to the $1/r$ dependence of the electric field on the distance r from the wire. The amplification in the wire detectors is limited to the region around the wire i.e., of the order of the diameter of wire. Before amplification the electrons need to drift into this region and then the signal generation starts, whereas the electric field near the cathodes is quite low. Thus this geometry allows to achieve very good spatial resolution ($\sim 100\mu\text{m}$). But the time resolution of wire detectors is poor (in ns) due to the fluctuations in the drift time of the primary

electrons. As far as time resolution is concerned, scintillator detectors are better than the wire based gaseous detectors [93]. To improve time resolution, a strong uniform electric field is needed instead of that of a charged wire (to reduce the drift time). The first gas detector having the improved time resolution with strong uniform electric fields was the Keuffel Spark Counter, a gaseous avalanche detector with parallel plate geometry [94].

For instance, spark counters comprise of two planar metal electrodes with a high voltage applied and the gap between the plates is filled with a gas mixture. When the charge particle passes it leaves a trail of free charge carriers (primary ionisation) in the gas, triggering avalanches of charge carriers in the electric field. At a certain size, the avalanches convert into streamers, where photons produced by the recombination process, contribute to the spread of free charge carriers. Later, a conducting plasma filament connecting the two electrodes is formed and the electrodes are discharged forming a spark. Large signals are formed and have a time resolution of around 1 ns which was far better than any of the Geiger-Muller counters which have timing resolution of around 100 ns. But as the area of spark chamber is of the order of a few cm^2 and as the area increases the discharge energy becomes so large as to damage the surface of the counter electrodes. A big disadvantage of spark counter is that they have long dead time ($\sim 1s$) due to switching-off circuit in order to prevent short-circuit of plates [95]. In order to overcome these issues, spark chamber with resistive plate electrodes and special gas mixtures for photon absorption was introduced [96]. The electrodes with resistivity of around $10^9\Omega\text{-cm}$ limits the discharge around the primary avalanche and the remaining counter area is still sensitive to charged particles because the high voltage drops only locally. The recharge of electrodes takes place with a time constant that is much longer than even the time scale of the avalanche development. Thus the multiplication process is self-extinguishing when resistive electrodes are used (more details are provided in section 2.3.2). A big advantage of the use of resistive electrodes is that a higher detection rate can be achieved.

Planar Spark Chamber (PSC), built by Pestov, was the first detector mounting

resistive electrodes. The Pestov Spark Counter [97, 98] with a 0.1 mm gap achieved a time resolution of 25 ps. But a thin gap (0.1 mm) along with the high values of the electric field (500 kV/cm) requires a very good surface smoothness of the electrodes. Also, the detector needs to be operated at a large overpressure of 12 bar ensuring a sufficiently large number of primary electron-ion pairs in the thin gap leading to good detection efficiency. A Parallel Plate Avalanche Chamber (PPAC) [99] is a single gap gaseous detector and is similar to the Spark Counter. However, it is operated in avalanche mode. It comprises of two planar electrodes made of metal, kept apart at a fixed distance of 0.5 to 2 mm by precise spacers. It has a fast response, an increased rate capability of up to 10 MHz/cm^2 , the time resolution is 100 to 250 ps, a gain of 10^3 to 10^4 can be reached, depending on the gas used and low signal-to-noise ratio. In the next section we describe the ICAL detector.

2.3 The Magnetised Iron CALorimeter (ICAL) Detector

The proposed magnetised ICAL detector at INO aims to study atmospheric muon neutrinos and also distinguish muon neutrinos and anti-neutrinos. The ICAL detector is sensitive to the energy, direction and charge of the muons produced in CC interactions of atmospheric muon neutrinos in the detector. The atmospheric neutrinos have large energy range E and path length L ; hence ICAL is capable of studying the neutrino mass hierarchy which is one of the most important parameters to be determined. In order to do precise physics measurements it is important to have each component in good condition. Therefore, to understand each component of ICAL detector we describe them in detail in the next subsections.

2.3.1 Magnet

The ICAL detector provides target nucleons so that neutrino interactions take place and along with that it acts as a medium in which secondary particles like muons can be

separated on the basis of their magnetic rigidity so that their momenta and charge can be estimated. A heap of magnetised iron plates interweaved with position sensitive gas detectors make up the ICAL calorimeter. The total mass of magnetised ICAL needed is 50 kton to begin with, which may be later expanded, thus making it the single largest part in the calorimeter. The magnetised iron calorimeter comprises 50 kton of low carbon steel (carbon percentage should be 0.1% or less) to have good magnetic characteristics. The design criteria for the ICAL magnet are essentially the following:

- **Field uniformity:** The detector will perform best when the magnetic field is uniform. A uniform magnetisation of iron block can be achieved by placing a copper coil so as to encompass the block, but the electric power required for magnetising a 50 kton block will be restrictive. Aside from that, the field will be available in a large air volume outside the magnet. To overcome all these issues we embrace a gap-less toroidal design. The magnetic field in this design is transcendently inside the iron and field leakage outside is negligible.
- **Modularity:** A calorimeter with mass of 50 kton or more of steel can only be realized if a modular structure is adopted from the beginning. The ICAL magnet will have a modular structure indeed. The basic design with 50 kton of steel, the detector and the magnet will be made in three modules and in later stages, more modules can be added.
- **Optimum copper-to-steel ratio:** The ratio of copper to steel decides the expense and the electrical power consumption. For taking a larger ratio, power consumption is low leading to the low running cost but higher fixed cost. Other than the cost, the total permissible power dissipation may be constrained by the cooling capacity of the environment in the tunnel. The heat dissipation in the coil depends on the volume of copper used. For taking a small amount of copper, copper cost is reduced but dissipating a large amount of heat which has to be removed by using

low conductivity water (LCW) flow through hollow copper conductors.

- **Access for maintenance:** Modularity is the most important from the point of view of accessibility for providing maintenance. Hence the overall availability factor of the ICAL detector will be decided by the quick replacement of faulty detectors. The modular design will ensure that the faulty detectors can be easily replaced with the least effort and will lead to minimising the distance that is required to be accessed to reach the faulty detector.

To overcome some of the problems discussed above, the toroidal (gap-less) design will be used. It will have the copper coil going through two rectangular slots in the stack of iron plates. In total, four coils will be installed at the centre of the each detector module as shown in the Figure 2.3. The length, breadth and the positions of the coil slots are chosen to generate a uniform field in as large a volume of iron as could reasonably be expected. The design is such that it is easy to insert and remove the active detector trays. The small cross-section of the copper conductor and of the coil ensures insignificant loss of fiducial volume of the detector. Hollow copper conductors are to be proposed which is cooled by low conductivity water that flows through them. Also, the heat generated by the magnet coil can also be dissipated by conduction through the iron plates and by radiation from the iron surface.

A coil with 40,000 amp-turns is required for generating a field of $\sim 1.3\text{--}1.5$ T in one module. A simulation performed by one of the member groups (BARC) used a 3D commercial code MagNet 6.0 [100] to design the magnet and for computing the magnetic field. The variation of the field over the entire set of plates is expected to be within 0.3% but the field varies by less than 0.15% over a height of ± 5 m from the centre. This variation of the field is quite uniform in the X-direction, varies less than 0.25% but in the Y-direction it starts falling beyond the length of the coil slot (± 4 m) [29]. Figure 2.4 shows the magnetic field map generated by MAGNET6 [100] software in the central iron layer of the central module (more details in chapter 4). This design is used in the simulation

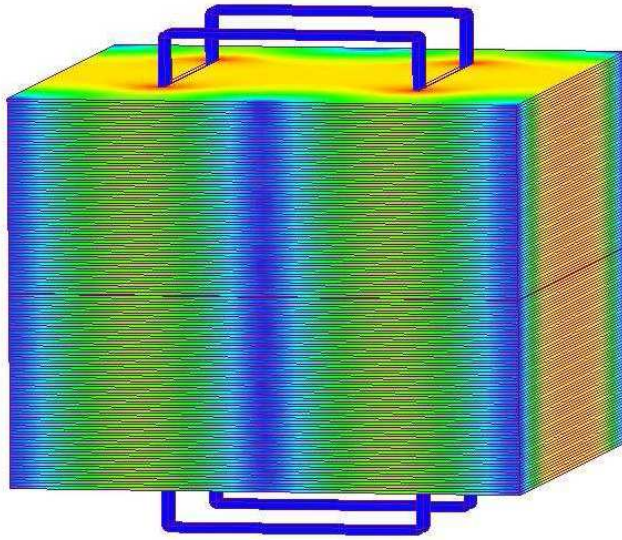


Figure 2.3: One module of the magnet with the coil inserted (side view).

studies for generating resolutions and efficiencies in the peripheral regions and is discussed in detail in chapter 4, section 4.4. Next, we will describe the active detector elements, the resistive plate chambers.

2.3.2 Resistive Plate Chambers (RPCs)

The Resistive Plate Chamber (RPC), introduced in 1981 by R. Santonico and R. Cardarelli [101, 102], is a particle detector that uses a constant and uniform electric field produced by two parallel electrode plates having high bulk resistivity (10^{10} – $10^{12}\Omega\text{-cm}$). A gas mixture of high absorption coefficient meant for ultraviolet light is passed through the gap between the electrodes. The choice of gas mixture depends on the factors like low working voltage, linearity, high gain and high rate capability. Noble gases are usually chosen because they require the lowest electric field intensities for the formation of avalanche. So, at the point when the gas is ionised by a charged particle the free charge carriers that are deposited in the gas gap trigger avalanches of electrons in the externally applied electric field and originate a discharge. Since the resistivity of the electrodes is

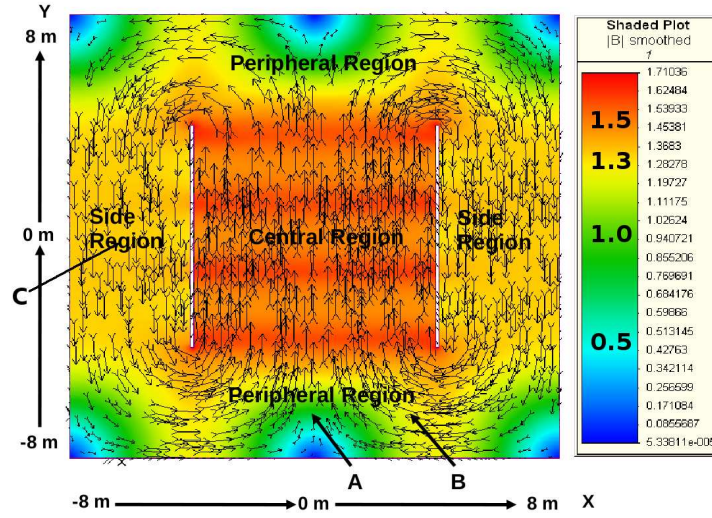


Figure 2.4: Magnetic field map as generated by the MAGNET6 software. Points $A = (0, -650, 0)$ cm, $B = (300, -650, 0)$ cm, $C = (-2270, 0, 0)$ cm (in the 1st module of ICAL), are defined for later use. Notice that C is actually in the left-most module of the detector and is marked here for convenience.

high, the electric field is dropped in a limited portion around the point where the discharge occurred and hence the discharge is not propagated through the whole gas volume. Since the ultra-violet absorbing component is present in the gas mixture, the photons produced by the discharge do not propagate in the gas. Thus secondary discharge is prevented from originating at other points of the detector. The electron propagation induces a current on external strip electrodes. The RPCs possess better time resolution than even the wire chambers.

RPC Fabrication

- Two planar electrodes of around 2 mm thick, either of glass or bakelite with the dimensions: $\sim 2 \text{ m} \times 2 \text{ m}$ or $1 \text{ m} \times 1 \text{ m}$ or $30 \text{ cm} \times 30 \text{ cm}$ are assembled.
- The four corners of electrodes are chamfered at 45° .
- Glass plates, polycarbonate cylindrical spacers (bulk resistivity is around $10^{13} \Omega\text{-cm}$), button spacers and nozzles are cleaned with distilled water, labolene solution

and propanol.

- Polycarbonate cylindrical spacers and nozzles are glued to one glass plate (in our case it is glass electrode) around the four corners, using epoxy adhesive and button spacers are glued at equal distance on the plate.
- After drying for more than 12 hours, glue is applied on the top of each button spacer and the other glass plate is gently placed such that it creates a gap of 2 mm.
- Glue is again applied around all the corners and the whole frame is kept for two days to dry at room temperature.
- The corners of electrodes are masked (~ 1 cm) with masking tape.
- The both sides of RPC is painted with graphite paint (paint:thinner :: 1:1) using spray gun, to make them conducting.
- Two diagonally opposite sides are blocked and tygon tubes are attached to the other two diagonally opposite sides.
- The pick-up panel is made from plastic honeycomb of 5 mm thick with 50 micron aluminium sheet (for grounding) on one side and copper strips of 2.8 cm with gap of 0.2 cm on the other side. Or a foam interleaved between two 50 micron aluminium sheet is etched from one side to make 2.8 cm strips with gap of 0.2 cm.
- Each strip is terminated with a 50Ω impedance to match the characteristic impedance of the preamplifier. Other end of the strip is soldered to wire to connect with electronics.
- The pick-up panels are oriented orthogonally to each other which are separated from RPC by 2-3 insulating mylar sheets and then assembled using kapton tape.

Choice of Gases : For RPC to work, a gas mixture is flowed through the RPC, which are: Argon which acts as a target for ionizing particle. It provides robust first ionisation signal with large avalanche multiplication and is available at low cost. Hence, due to these factors Argon is preferred for streamer mode, but excited Argon atoms in the avalanche formation get de-excited and emit high energy photons. These photons further ionise the gas causing cascade of avalanche, which is undesirable. This problem can be sorted out by adding polyatomic gases like Isobutane. It is an organic gas to absorb photons from the recombination process, limiting the formation of secondary avalanche from primary and is a costly gas. Quenching can be further increased by adding Freon (R134a is its eco-friendly substitute) [103]. It absorbs free charge particles in the gas before any further avalanche is produced and is available at lower cost. SF_6 acts as a quenching gas and should be used in small ratio as small amount of it brings stability to the operation of RPCs [104, 105]. Figure 2.5 represents the schematic of RPC detector with nozzles, polycarbonate cylindrical spacers and button spacers also shown. The pick-up strips are actually aligned to face the graphite coating of the glass plates. In the figure, the pick-up strips on the top of glass plate are aligned opposite for convenience. After fabricating RPCs it is necessary to characterise them so now we describe their operating modes in detail.

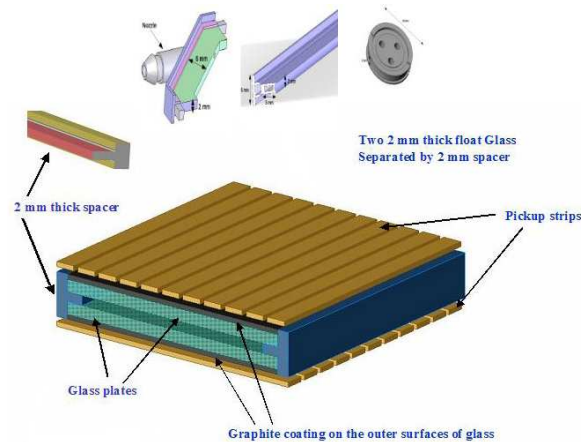


Figure 2.5: A schematic of RPC detector.

Modes of Operation : The two modes of operation of RPCs are *avalanche mode* [103, 106] and *streamer mode* [107, 108]. In the avalanche mode, the primary charge is released by the incoming ionising radiation and is followed by the propagation and multiplication of the electrons corresponding to a Townsend avalanche (refer to Figure 2.6). A change in the gas gain changes the avalanche dynamics. The electric field is influenced by the avalanche charge carriers in the gas gap and hence their propagation and multiplication is also influenced. This is known as the *space charge effect*. Further increase in the gas gain causes photons to contribute to the propagation of the avalanche and a streamer evolves. Later a conductive channel is formed between the two electrodes, through which the local electrode surfaces are discharged, creating a weak spark. In streamer mode, the large current pulses induced by the streamers simplifies the read out of the RPC. The details of development of avalanche and streamer in RPC with their schematic diagrams are explained below:

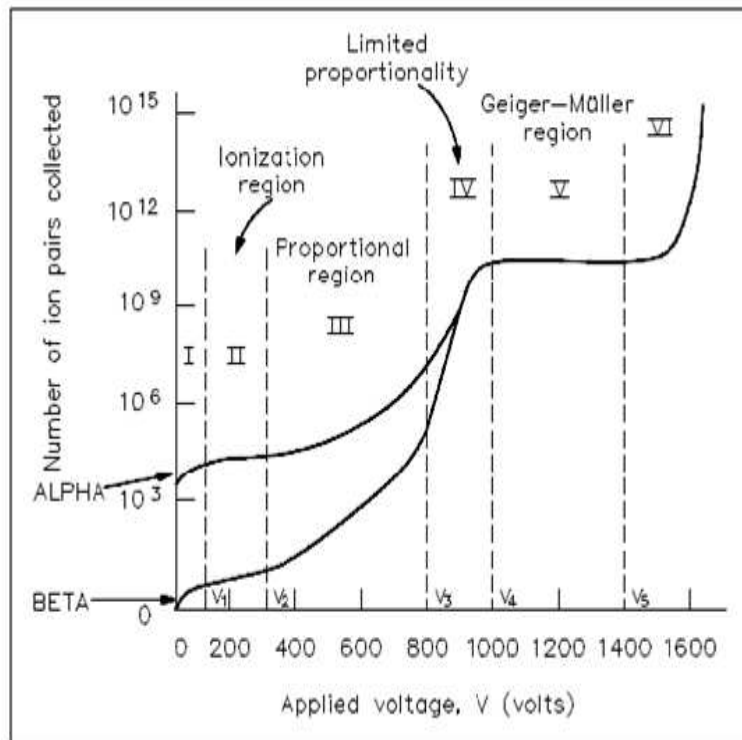


Figure 2.6: Gaseous ionisation detection regions.

The development of an avalanche in an RPC is shown in Figure 2.7. A uniform electric field E_0 is applied across the gas gap. Some of the gas atoms get ionised by the passage of a charged particle through the gas gap and hence an avalanche is started (top-left panel). The size of avalanche is large enough to influence the electric field in the gas gap and is shown in top-right panel. The electrons reach the anode plate, whereas the ions drift much slower due to their lower drift velocities (bottom-left panel). The ions reach the cathode and the charges influence the field in a small portion where an avalanche is developed (bottom-right panel).

The development of a streamer in an RPC is shown in Figure 2.8. It begins with the development of an avalanche, as shown in top-right panel of Figure 2.7. A high field distortion is observed in the gas gap due to the avalanche charges. Altogether high energetic photons start contributing towards the development of avalanche, causing the spread of the avalanche i.e., a streamer emerges (top-right panel). A weak spark is generated and the local electrode area is discharged (bottom-left panel). The electric field decreases around the area where an avalanche is formed and hence a blind spot is developed by the detector (bottom-right panel).

The electric signal formation is essentially based on the electron multiplication process. When an ionising particle is passed through its gas gap it creates certain number of primary electrons; these are grouped into clusters each of them is created by a single ionisation. In a given cluster the n_0 electrons are accelerated by the electric field which further start the multiplication in the gas. This process is characterised by the parameter α (first Townsend coefficient), representing the number of ionisations per unit length, and by β which represents the attachment coefficient, i.e. the number of electrons as captured by the gas per unit length. The parameter β is important when electronegative gases are present. If x is the distance between the anode and the point where the cluster is produced then the number of electrons that reach the anode will be given by [109]:

$$n = n_0 e^{\eta x} , \quad \text{where } \eta = \alpha - \beta . \quad (2.2)$$

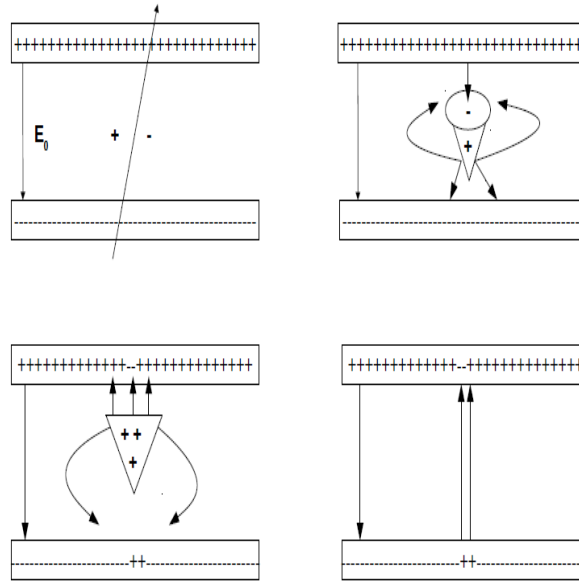


Figure 2.7: Schematic of the development of avalanche in an RPC.

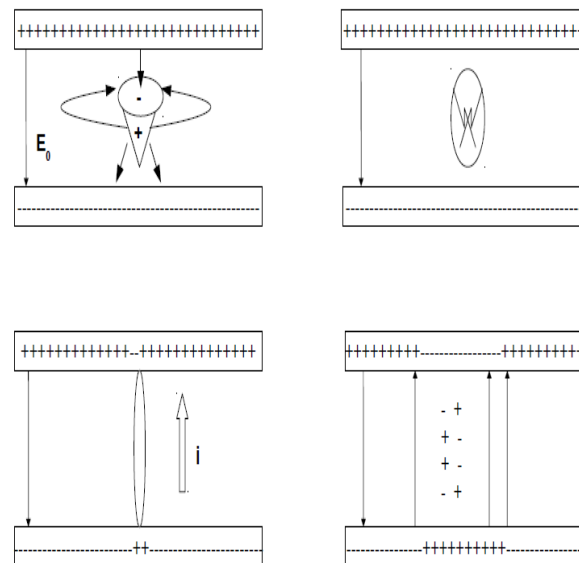


Figure 2.8: Schematic of the development of streamer in an RPC.

Hence the gain factor is defined as:

$$M = \frac{n}{n_0} . \quad (2.3)$$

The operating modes can be distinguished by the value of M . For M greater than 10^8 , then primary ionisations will produce streamers. But for M lower than 10^8 , additional secondary avalanches are prevented from forming and simple charge multiplication occurs. Hence a small amount of charge is created and the detector is said to operate in avalanche mode.

A planar detector with resistive electrodes is modeled as a set of discharge cells, which to the first order can be considered independent of each other. A simple expression of the capacitance of a planar condenser leads to the result that the area of such cells is proportional to the total average charge Q produced in the gas gap [93]:

$$S = \frac{Qd}{\epsilon_0 V}, \quad (2.4)$$

where d is the gap thickness and V is the voltage applied to the electrodes. Smaller the value of Q , smaller the surface of the discharge cells and hence higher the rate capability. The average charge produced in the gas gap for an RPC operating in the avalanche mode is 1 pC, while in the streamer mode the value is about ~ 100 pC. Highly sophisticated front-end electronics is required for avalanche mode whereas no amplification is required for streamer mode and the signals can be discriminated against the detection threshold directly. Thus streamer mode has simplified read out.

Types of RPCs : Depending on their application in an experiment, RPCs are generally classified as trigger or timing devices. The timing RPCs provide much better timing resolution as compared to trigger RPCs and hence the timing RPCs are used as Time-Of-Flight (TOF) detectors [108, 110] in many experiments. On the other hand trigger RPCs are used to detect the passage of Minimum Ionising Particles (MIPs) such as muons and signaling the other co-detectors and their data acquisition systems to record the data.

Applications : RPCs have been used in several major experiments in the past. RPCs of many designs using a variety of materials, construction techniques and operating modes

2.3. The Magnetised Iron CALorimeter (ICAL) Detector

are extensively used in many currently running experiments and are also being used as a prototype for so many future experiments such as ICAL at INO. By goodness of their adaptability in configuration and development, RPC detectors are tunable and adaptable to a variety of applications and environments. Consequently, they are progressively favored over other competing technologies for accelerator as well as cosmic ray experiments, as a trigger or timing detectors. An overview of the organization of RPCs in the past and current experiments [111] –[145] is given in Table 2.3.

Experiment	Application	Area	Electrodes	Gap	Gaps	Mode
ALICE-Muon	Trigger	140	Bakelite	2	1	Streamer
ALICE-TOF	Timing	150	Glass	0.25	10	Avalanche
ATLAS	Trigger	6550	Bakelite	2	1	Avalanche
BaBar	Trigger	2000	Bakelite	2	1	Streamer
Belle	Trigger	2200	Glass	2	2	Streamer
BESIII	Trigger	1200	Bakelite	2	2	Streamer
CBM TOF	Timing	120	Glass	0.25	10	Avalanche
CMS	Trigger	2953	Bakelite	2	2	Avalanche
COVER-PLASTEX	Timing	16	Bakelite	2	1	Streamer
EAS-TOP	Timing	40	Bakelite	2	1	Streamer
FOPI	Timing	6	Glass	0.3	4	Avalanche
HADES	Timing	8	Glass	0.3	4	Avalanche
HARP	Timing	10	Glass	0.3	4	Avalanche
L3	Trigger	300	Bakelite	2	2	Streamer
NeuLAND	Timing	4	Glass	0.6	8	Avalanche
OPERA	Trigger	3200	Bakelite	2	1	Streamer
PHENIX	Trigger	-	Bakelite	2	2	Avalanche
STAR	Timing	50	Glass	0.22	6	Avalanche
YBJ-ARGO	Trigger	5630	Bakelite	2	1	Streamer

Table 2.3: An overview of the RPCs used in the past and current experiments (Area is given in m^2 , while the gap (width) is in mm).

2.3.3 Detector Readout Scheme

The basic RPC detector elements for ICAL will have dimension as $\sim 2 \text{ m} \times 2 \text{ m}$. Eight such elements will cover a road of $16 \text{ m} \times 2 \text{ m}$ and a total of $\sim 28,800$ elements therefore will be required for the entire detector. The readout of the RPCs will be performed by external pick-up strips (X and Y strips) placed orthogonally. Induced pulses will be produced by the charged particles on the strips. These pulses will go to front end ASICs

located near the strip ends having fast discriminators that will be providing a fast timing signal. Presently we use 3 cm wide strips with 2.8 cm strip width and 0.2 cm gap between the adjacent strips. This has been optimised through simulation studies by our group (more details in section 3.5). Thus, each RPC will have 64 strips along the X-direction (2 m) and 512 strips along the Y-direction (16 m). For this, the readout panel is composed of a plastic honeycomb (refer to subsection 2.3.2 for more details). Eight readout boards along a road will be connected to each other. The X strips from individual boards will be connected to one another and will be read out at the edge of the detector whereas the Y-strips from individual boards will also be brought to the edge of the detector using impedance matched cables. All the front end ASICs will be located on boards near the edge of the detector. A schematic of RPC read out scheme is shown in Figure 2.9.

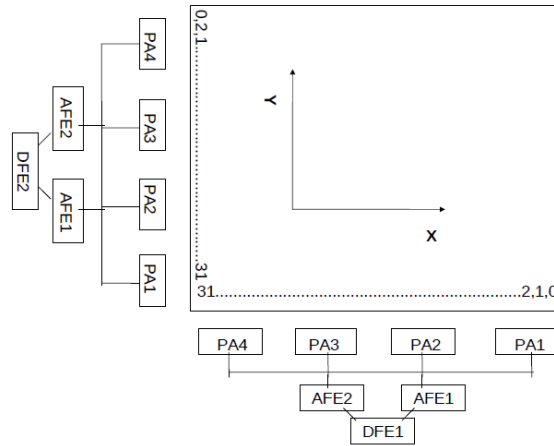


Figure 2.9: Schematic diagram of RPC read out scheme.

2.4 Goals of the ICAL Detector

INO-ICAL will be one of the important neutrino experiments, in the near future, which will be exploring the vast sector of neutrino physics, either by re-confirming the results or establishing new results (in matter effects and mass hierarchy, neutrino and anti-neutrino oscillations, etc). Besides all these, it will establish a world class physics experiment in

India. As already mentioned in the section 2.1 about the main goals of INO, by achieving these goals it will help to find and understand unanswered questions regarding neutrinos. One of the main goal will be to do the oscillation studies of neutrinos. So, oscillation studies with upward-going muons will also be important to have a better understanding of them (will be discussed in chapter 5). Some of these goals are discussed below.

Neutrino Physics with Magnetised Iron Calorimeter

The major physics goals of the ICAL detector are:

To re-confirm the occurrence of oscillation in atmospheric muon neutrinos :

Re-confirmation of oscillation will aim to do a precise measurement of neutrino oscillation parameters such as Δm_{32}^2 and $\sin^2 \theta_{23}$. So, ICAL will have a sensitivity in depicting the evidence of neutrino mass and oscillation by observing dips and peaks in the event rate vs L/E ratio [146]. To measure the oscillations, ICAL will determine the ratio of upward-going and downward-coming neutrinos (R) with their nadir/zenith [29] angles interchanged. This reflects an asymmetry of up-down fluxes due to oscillations and hence will directly measure oscillation probability [49] which for the case of two flavour oscillations is given as,

$$P_{\mu\mu} = 1 - \sin^2 2\theta_{23} \sin^2 \left(1.27 \times \Delta m_{32}^2 \times \frac{L}{E} \right) . \quad (2.5)$$

Hence, a dip in this ratio measures Δm_{32}^2 , whereas the value of it at a minimum measures θ_{23} .

Matter effects in neutrino oscillations : Neutrinos and anti-neutrinos interact differently with matter, which will be important to predict the sign of Δm_{32}^2 and magnitude of θ_{23} . A magnetised ICAL detector at INO has the ability to discriminate between neutrino and anti-neutrino by detecting the charge of produced muons. The matter effects [50] bring changes in the survival and oscillation probabilities and hence the neutrino parameters [147, 148, 149]. For the $\nu_\mu \rightarrow \nu_\mu$ and $\nu_e \rightarrow \nu_\mu$ channel the oscillation probability,

including matter effects, can be written approximately as,

$$\begin{aligned}
 P_{\mu\mu}^m &\approx 1 - \sin^2 2\theta_{23} \left[\sin^2 \theta_{13}^m \sin^2 \Delta_{21}^m + \cos^2 \theta_{13}^m \sin^2 \Delta_{32}^m \right] \\
 &\quad - \sin^4 \theta_{23} \sin^2 2\theta_{13}^m \sin^2 \Delta_{31}^m, \\
 P_{e\mu}^m &\approx \sin^2 \theta_{23} \sin^2 2\theta_{13}^m \sin^2 \Delta_{31}^m,
 \end{aligned} \tag{2.6}$$

where the superscript m to the mixing angles and mass squared differences represent them in matter.

Another factor, known as the mass hierarchy [150, 151], gives sign of the mass-squared difference Δm_{32}^2 involved in atmospheric neutrino oscillations. This mass difference is not known unlike Δm_{21}^2 whose sign is known to be positive from solar neutrino oscillations. Determining mass hierarchy whether normal or inverted is also a main goal of INO.

Deviation from maximality of θ_{23} – octant determination : By using matter effects, ICAL will be able to determine whether the mixing angle θ_{23} is indeed maximal (i.e., $\theta_{23} = \pi/4$), provided θ_{13} is large enough, which indeed appears to be the case: $\theta_{13} \approx 9^\circ$ (from latest results [51]) and, if not then explore how well its octant can be determined [152]. Determining octant discrimination is easier than establishing deviation from maximality for larger θ_{13} and the reverse is true for smaller θ_{13} when islands of allowed parameter space begin to appear near the “wrong octant” solution. Also, values of θ_{23} are more easily distinguished from maximality in the first octant than those in the second octant.

Discrimination between $\nu_\mu \rightarrow \nu_\tau$ and $\nu_\mu \rightarrow \nu_s$: The ICAL detector may also detect whether the muon neutrino deficit observed by previous experiments is due to oscillations of muon neutrinos to tau neutrinos or sterile ones. If the dominant oscillation is $\nu_\mu \rightarrow \nu_\tau$, then τ leptons are produced via CC interactions in the detector, originating from the ν_τ

produced due to these oscillations. At these energies, the τ lepton decays very rapidly, and almost 80% of the time this decay does not produce a muon.

Probing CPT violation in the neutrino sector using atmospheric neutrinos : INO-ICAL aimed at probing CPT violation [153] in the neutrino sector using atmospheric neutrinos and putting bounds [154] on them. The atmospheric neutrino data involve both the particle and the antiparticle channels and are therefore suitable for studying CPT violation. As the atmospheric neutrino experiments are probing mass squared differences and not the absolute neutrino mass, these will be the quantities which might be restricted by the data. The interest in CPT violation arises due to a recently suggested scheme which is capable of solving all neutrino anomalies without the use of a light sterile neutrino [155].

Constraining long range leptonic forces : There are a special class of long range forces which distinguish between leptonic flavours and have far reaching implications for the neutrino oscillations [156, 157]. In turn we may use them as a probe of such forces.

To summarize, the proposed magnetised ICAL experiment at INO facility will study atmospheric neutrinos. Along with that the other two experiments, DINO and TinTin will also be housed at the INO caverns with the aim of understanding the nature of neutrinos and dark matter respectively. The ICAL with large target mass and good L/E determination will be able to achieve many goals like precision measurements, matter effects, mass hierarchy, CPT violation in leptonic sector and many more. It is important to study detector parts, magnet, RPCs and readouts in order to attain these goals. The RPCs due to its good timing and position resolution are effective in low count experiments like INO. Low cost and easy availability of glass electrodes further motivates us to use glass RPCs as active detector element at ICAL. In the next chapter we discuss the details about RPCs characterisation, optimisation and performance.

Chapter 3

Optimisation and Characterisation of Glass RPC

India-based Neutrino Observatory (INO) [29] is going to build a massive 50 kt magnetised Iron CALorimeter (ICAL) detector to study atmospheric neutrinos and their properties. Approximately 30,000 active detector elements called Resistive Plate Chambers (RPCs) [158, 159] of $\sim 2 \text{ m} \times 2 \text{ m}$ size are to be installed in the ICAL detector, where they will be sandwiched between iron plates. In order to execute such a large number of detectors, we need to do a full R & D to develop these detectors and also optimize the production process. It is necessary to fabricate prototype RPCs and do their testing. So, we have fabricated $30 \text{ cm} \times 30 \text{ cm}$ RPCs in the RPC lab at Physics department, Panjab University (PU), Chandigarh, done their testing and analysed the results. Our department has two RPC labs, one lab is for fabricating RPCs and has the setup to characterise $30 \text{ cm} \times 30 \text{ cm}$ RPCs. Other lab is fully equipped with the instruments like gas re-circulation system, VMEs, gas leakage test setup, weather monitoring system, to test $1 \text{ m} \times 1 \text{ m}$ and $2 \text{ m} \times 2 \text{ m}$ RPCs.

In this chapter, first we describe the motivation for the study. Then, we explain the factors such as aging that deteriorate the quality of RPCs. We discuss the characterisation studies undertaken for the glass samples using various techniques like UV-VIS transmission for determining its optical properties, SEM, AFM for its surface properties,

WD-XRF, PIXE for determining the composition of glass samples etc., so that we can choose the best quality glass for better performance of the detectors. We describe the methods to do the calibration of gases used for our study. Before fabricating RPC, we fabricated scintillator paddles of the width of 1.8, 2.5, 3.8 cm and length of 30 cm each and measured their efficiency. We fabricated pick-up panels, with different strip widths of 1.8, 2.8, 3.8 cm, of size 30 cm \times 30 cm. We fabricated RPCs of Asahi, Saint Gobain and Modi glass. Surface resistivity measurement, gas leakage and Voltage-Current (V-I) characterisation was done on each RPC. Then, we describe trigger scheme circuit to find the efficiency and the cross-talk of all the RPCs. Variation of efficiency and cross-talk of all the three RPCs (with different strip widths) is presented. We measured the efficiency and cross-talk of RPC stack fabricated with Asahi glass.

3.1 Motivation for the Study

Selection of electrode material is important for the functioning of the RPC detectors. The electrode material should have high resistivity and high surface smoothness to avoid the localisation of excess charge. Bakelite and glass are the most suitable electrode materials for the RPC detectors. In this chapter we show the optimisation of glass parameters, fabrication and characterisation of glass RPCs. The quality of glass plays a crucial role in long-term stability of RPCs. Factors like aging can deteriorate the glass quality and hence the performance of the RPCs [160]. So, its necessary to study the different properties of glasses. We performed various tests described in the next section on different samples of glass. Based on these tests, three RPCs were fabricated using the Saint Gobain, Asahi, Modi glass samples procured from local market. We performed V-I characterisation and measured efficiency/cross-talk of all the RPCs. Cross-talk studies were done with varying strip width of pick-up panels to check RPCs performance. Strip width study is important for physics analysis, as increase in strip width worsens the detector energy resolution but improves the detector efficiency. Depending on the physics goals—the combination of

good resolution and poor efficiency (or vice-versa)—the strip width can be optimised. We now discuss the factors responsible for aging of the RPCs, which are important before the RPCs are assembled.

3.1.1 Aging of Resistive Plate Chambers

The RPCs usually have a lifetime of around 15 to 20 years and are expected to withstand long term operation in high background conditions. To ensure their efficient working for the given time period, we need to understand the various factors that can affect the performance of RPCs. One of them is aging of the detectors [160]. We describe the reasons for aging of RPCs.

There can be different kinds of aging effects: aging of the materials irrespective of the working conditions, aging due to the integrated dissipated current inside the detector and aging due to irradiation. The main reason for the aging is the possible contamination of the detector gas with impurities and moisture. Moisture contamination to a level of 1000-2000 ppm in the detector gas can damage the RPC even after about two weeks of continuous operation. One more reason is that electron-ion recombinations that produce UV photons cause damage to the electrodes. So, the choice of gases (as described in section 3.3) is also important to prevent aging. One of the plausible chemical reactions causing damage to the electrodes is formation of Hydrogen Fluoride (HF) inside the gas gap. The Freon gas, which is present in the gas mixture, decomposes under electrical discharge and produces a significant concentration of Fluoride radicals. These radicals react with traces of moisture present in the gas mixture to form Hydrogen Fluoride, HF, which is an aggressive acid that causes damage to the inner surfaces of the glass electrodes. The work-function of the electrode surface is reduced and this leads to field emission of electrons from the cathode. This in turn reduces the electric field inside the chamber below the efficiency plateau and causes a permanent efficiency drop. So in order to improve the stability, prevent and understand the aging of RPCs, the characterisation

of electrode material is important. In our case, we have done the characterisation of glass which is used as an electrode in RPCs and we discuss the characterisation of glass in the next section.

3.2 Characterisation of Glass Electrode

The electrode, especially glass, seems to be one of the important components which leads to the aging of RPCs. We have done detailed characterisation studies, using different techniques, on various glass samples of different manufacturers such as Asahi, Saint Gobain and Modi procured from the local market [161, 162].

Physical Properties : After measuring the mass using fractional balance, length and breadth using vernier callipers, we measured the density of all the glass samples. We found no significant difference in the density. The results are given in Table 3.1.

Samples	Volume(cm^3)	Weight(g)	Density(g/cm^3)
Asahi	2.09	5.1179	2.45
Saint Gobain	1.95	4.7664	2.44
Modi	4.82	11.6405	2.42

Table 3.1: Density Measurements.

Optical Properties : We studied optical properties of glass too. UV/VIS spectroscopy was used for the optical characteristics. Transmittance studies for all the glass samples from Ultraviolet to Visible light spectrum was carried out. This will indicate the general bulk quality of the glass and a measure of impurity levels in the glass. This facility was provided by the CIL, Panjab University. It was done using Perkin Elmer's LAMBDA UV/VIS/NIR and UV/VIS spectrophotometers. These spectrophotometers have a resolution of 0.17–5.00 nm in UV and Visible region and 0.20–20.00 nm in the near Infrared region. It uses highly sensitive photomultiplier and Peltier cooled PbS detectors providing

full range UV/VIS/NIR coverage from 190 to 3300 nm. Figure 3.1 shows the optical transmittance for all the glass samples. Asahi and Saint Gobain glass shows better UV-VIS transmittance than Modi glass.

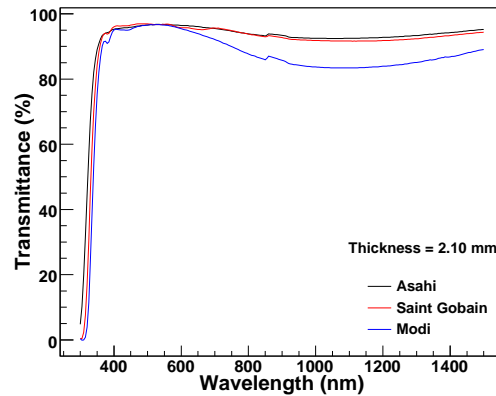


Figure 3.1: UV-VIS transmittance of Asahi, Saint Gobain and Modi glass samples.

Electrical Properties : The bulk resistivity of the glass samples was calculated using Two-Probe method. It is one of the standard and most commonly used method for the measurement of resistivity of highly resistive samples like sheets/films of polymers. Before we discuss the results we explain the experimental set-up of two probe method. Figure 3.2 shows the experimental set-up for two-probe method.



Figure 3.2: Experimental set-up for two-probe method.

The two-probe apparatus has two spring loaded contact probes and these move in a pipe which is insulated by Teflon washers. This probe arrangement is mounted on

a suitable stand, which also holds the sample plate and RTD (Resistance Temperature Detectors) sensor. The stand also serves as the lid of PID (Proportional Integral Derivative) controlled Oven. Teflon coated leads are provided for connecting with High Voltage Power Supply EHT-11 and Digital Picoammeter DPM-111. Secondly, there is a PID Controlled Oven. This is a high quality temperature controlled oven suitable for Four Probe set-up. The oven has been designed for fast heating and cooling rates, which enhances the effectiveness of the controller. It has a good, stable and accurate temperature control.

In order to measure the bulk resistivity, first of all a small piece of Al foil was placed on the base plate below the spring. The glass sample was placed below one of the probes and gently rested on it. One of the probes was in contact with upper surface of the sample, while the other was in contact with lower surface through the Al foil. Leads with connectors were connected to EHT-11 and Digital Picoammeter. The voltage was increased to 10 V and Picoammeter was switched to more sensitive range till some reading was obtained. The voltage was increased gradually and corresponding readings of current were taken. After measuring the dimensions (length, breadth and thickness) of the samples, the resistivity was calculated. Figure 3.3 shows the bulk resistivity of all the glass samples (thickness 2.10 mm) and was found to be of the order of 10^{11} Ω -cm.

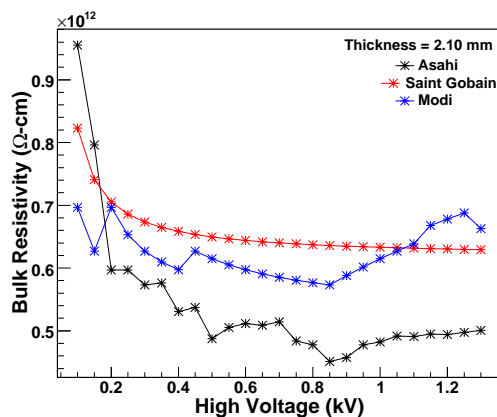


Figure 3.3: Bulk resistivity of Asahi, Saint Gobain and Modi glass samples.

Surface Properties : The surface quality of the electrode is crucial in reducing spontaneous discharges which can affect the rate capability of the detector. Atomic Force Microscopy (AFM) and Scanning Electron Microscopy (SEM) has been used to study and compare the surface quality of various glass samples. Before we discuss the results we describe AFM and SEM briefly.

Atomic Force Microscopy (AFM) is a very high-resolution type of scanning probe microscopy with resolution of the order of fractions of a nanometer. AFMs operate by measuring force between a probe and the sample. Normally, the probe is a sharp tip, which is a 3–6 μm tall pyramid with 15–40 nm end radius. To acquire the image resolution, AFMs can generally measure the vertical and lateral deflections of the cantilever by using the optical lever. The optical lever operates by reflecting a laser beam off the cantilever. The reflected laser beam strikes a position-sensitive photo-detector consisting of four segment photo-detector. The differences between the segments of photo-detector of signals indicate the position of the laser spot on the detector and thus the angular deflections of the cantilever. Figure 3.4 [163] shows the schematic of atomic force microscope.

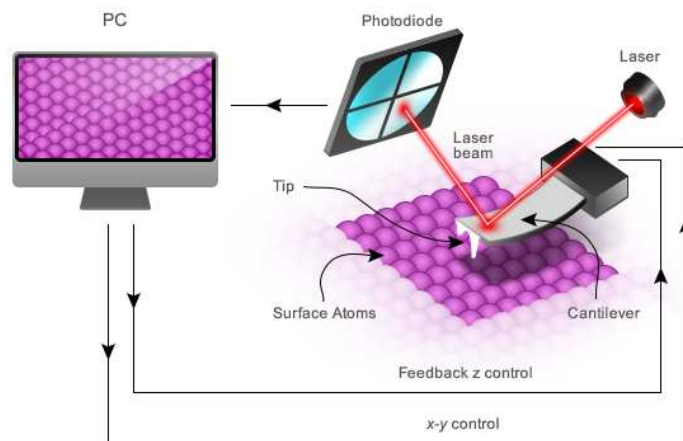


Figure 3.4: A schematic of atomic force microscope connected to computer.

Scanning Electron Microscopy (SEM) uses a focused beam of high-energy electrons to generate a variety of signals at the surface of solid specimens. The signals

that derive from electron sample interactions reveal information about the sample including external morphology (texture), chemical composition, and crystalline structure and orientation of materials making up the sample. Sample is usually coated with an ultra-thin electrically conducting material, deposited either by low-vacuum sputter coating or by high-vacuum evaporation. Conductive materials for specimen coating include gold, gold/palladium alloy, platinum, tungsten, chromium, iridium, and graphite. Then the samples are mounted to the SEM apparatus as shown in Figure 3.5 [164]. Then, an electron beam is thermoionically emitted from an electron gun having energy range from 0.2 keV to 40 keV and is focused by one or two condenser lenses to a spot about 0.4 nm to 5 nm in diameter. The beam then passes through pairs of scanning coils, deflecting the beam in the x and y directions so that it scans in a raster fashion over a rectangular area of the sample surface. The electron loses energy by random scattering when primary electron beam interacts with the sample. The exchange of energy between the electron beam and the sample causes the reflection of high-energy electrons by elastic scattering, emission of secondary electrons by inelastic scattering and the emission of electromagnetic radiation, all of them can be detected by specialized detectors. The most common mode of extraction of information is by secondary electrons. The number of secondary electrons is a function of the angle between the surface and the beam. On a flat surface, the plume of secondary electrons is mostly contained by the sample, but on a tilted surface, the plume is partially exposed and more electrons are emitted. By scanning the sample and detecting the secondary electrons, an image displaying the tilt of the surface is created. Accelerated electrons in an SEM carry significant amounts of kinetic energy, and this energy is dissipated as a variety of signals produced by electron-sample interactions when the incident electrons are decelerated in the solid sample. These signals include secondary electrons (that produce SEM images), Backscattered Electrons (BSE), Diffracted Backscattered Electrons (DBSD that are used to determine crystal structures and orientations of minerals), photons (characteristic X-rays that are used for elemen-

tal analysis and continuum X-rays), visible light (CathodoLuminescence–CL), and heat. Secondary electrons and backscattered electrons are commonly used for imaging samples: secondary electrons are most valuable for showing morphology and topography on samples and backscattered electrons are most valuable for illustrating contrasts in composition in multiphase samples (i.e. for rapid phase discrimination). X-ray generation is produced by inelastic collisions of the incident electrons with electrons in discrete orbitals (shells) of atoms in the sample. As the excited electrons return to lower energy states, they yield X-rays that are of a fixed wavelength.

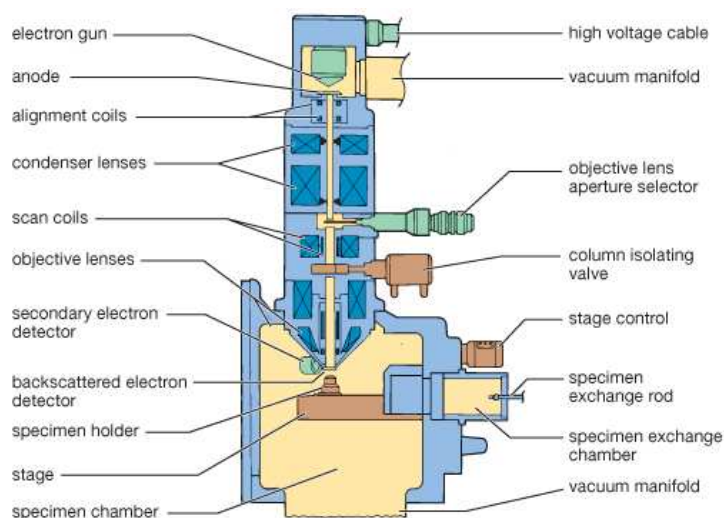


Figure 3.5: A schematic of scanning electron microscope.

AFM was done at NITTTR, Sector 26, Chandigarh. The scanning range was 20 to 50 micron. SEM was done with the help of CIL, Panjab University, using Digital Scanning Electron Microscope - JSM 6100 (JEOL). Glass samples were coated with gold using high-vacuum evaporation technique. The JSM-6100 was equipped with a digital image processor which allowed observation of the entire surface of a specimen upto 150 mm and a tilt of -5 to 90°. Figure 3.6 and 3.7 shows the AFM and SEM of all the glass samples. It was observed that the surface smoothness of Asahi and Saint Gobain were better than Modi sample.

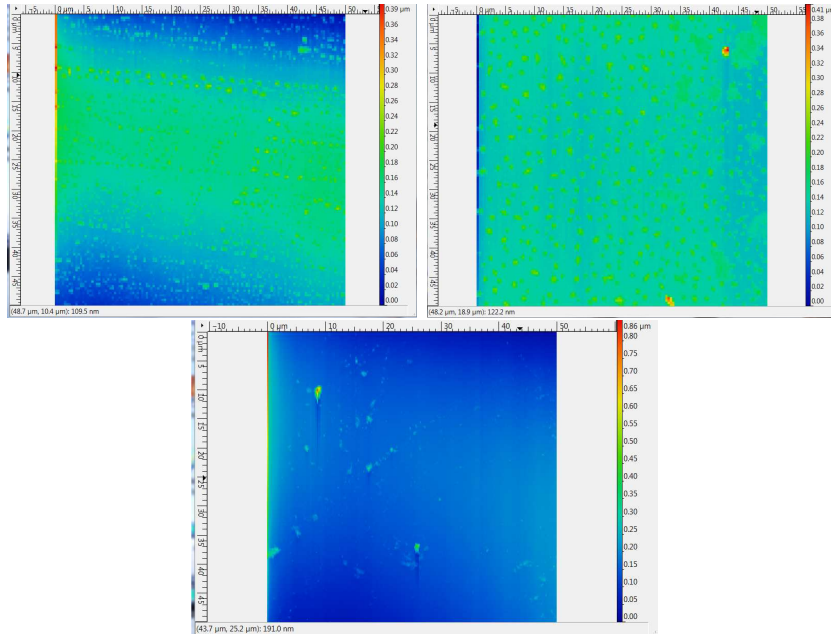


Figure 3.6: AFM scans of Asahi, Saint Gobain and Modi glass samples respectively.

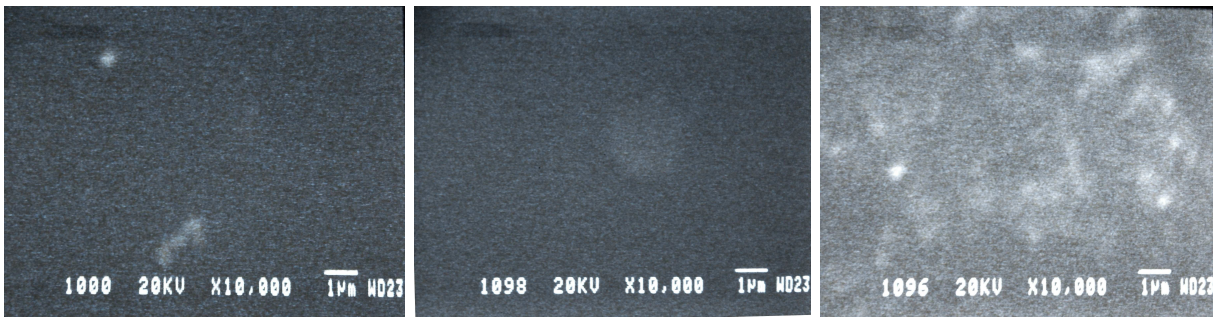


Figure 3.7: SEM scans of Asahi, Saint Gobain and Modi glass samples respectively.

Elemental and Compositional Studies : The glass shows ionic conduction, so it is important to study the composition of the glass in order to get the information of elements or ions in the glass. The fractional percentages of weights of various elements present in the glass samples were obtained using the Wavelength Dispersive X-ray fluorescence Spectroscopy (WD-XRF) technique. Bruker’s S8 tiger WD-XRF spectrometer was used for this purpose, at CIL department, Panjab University. We discuss briefly about XRF technique here. Basically, XRF is an analytical method to determine the chemical composition of all kinds of materials. The materials can be in solid, liquid, powder, filtered or other form. XRF can also sometimes be used to determine the thickness and compo-

sition of layers and coatings. In XRF, X-rays produced by a source irradiate the sample. In most cases, the source is an X-ray tube but alternatively it could be a synchrotron or a radioactive material. The elements present in the sample will emit fluorescent X-ray radiation with discrete energies (equivalent to colors in optical light) that are characteristic for these elements. A different energy is equivalent to a different color. By measuring the energies of the radiation emitted by the sample it is possible to determine which elements are present and is called qualitative analysis. By measuring the intensities of the emitted energies it is possible to determine how much of each element is present in the sample and is called quantitative analysis. The difference between the two systems is found in the detection system. Spectrometer systems can be divided into two main groups, Energy dispersive systems (ED-XRF) and Wavelength dispersive systems (WD-XRF). The ED-XRF spectrometers have a detector that is able to measure the different energies of the characteristic radiation coming directly from the sample. The detector can separate the radiation from the sample into the radiation from the elements in the sample. This separation is called dispersion. The WD-XRF spectrometers use an analyzing crystal to disperse the different energies. All radiation coming from the sample falls on the crystal. The crystal diffracts the different energies in different directions, similar to a prism that disperses different colors in different directions. The WD-XRF is unsurpassed in terms of analytical accuracy and precision. Figure 3.8 shows the WD-XRF of glass samples. Table 3.2 shows the composition of all the samples. We took five different samples for elemental studies. Asahi (1) and Asahi (2), SG (1) and SG (2) are procured from different markets, where X is some local company product. The percentages of SiO_2 and Na_2O are important as they are the main compound of the glass and they show a constant percentage. The presence of compounds like Rb_2O , with high Z Rb, degrades the quality of the glass as in the glass sample X. Similarly, Sc_2O_3 with Sc degrades the quality of Modi sample.

The PIXE (Proton Induced X-ray Emission spectroscopy) technique is used as

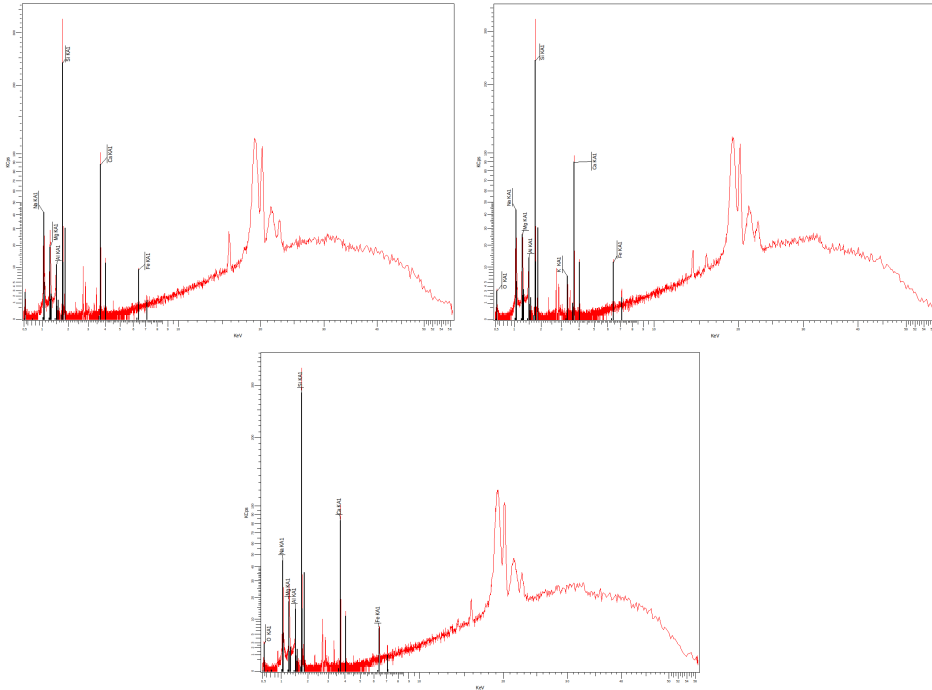


Figure 3.8: WD-XRF analysis of Asahi, Saint Gobain and Modi glass samples respectively, where x-axis denotes KeV and y-axis denotes KCps.

Compound	Modi(%)	SG(1)(%)	SG(2)(%)	Asahi(1)(%)	Asahi(2)(%)	X(%)
SiO_2	72.43	71.85	73.03	71.84	72.39	70.99
Na_2O	13.04	13.15	13.05	14.04	13.51	13.80
CaO	9.13	9.56	8.45	8.96	9.08	9.27
MgO	3.85	3.98	3.72	4.06	3.86	4.09
Al_2O_3	0.94	0.89	0.79	0.69	0.64	0.88
SO_3	0.13	0.16	0.23	0.15	0.16	0.24
Fe_2O_3	0.10	0.15	0.18	0.11	0.14	0.15
K_2O	0.25	0.11	0.48	—	0.07	0.51
TiO_2	0.06	0.08	—	0.09	0.08	—
P_2O_5	—	0.05	—	—	—	0.04
MnO	—	0.02	—	—	—	—
ZrO_2	99 PPM	0.02	40 PPM	0.02	0.02	35 PPM
SrO	—	35 PPM	0.01	—	—	0.01
Sc_2O_3	0.02	—	—	—	—	—
Cl	—	—	0.03	0.03	—	—
Rb_2O	—	—	—	—	—	25 PPM

Table 3.2: Composition of samples.

supplementary to WD-XRF to do elemental analysis. PIXE is an X-ray spectrographic technique, which can be used for the non-destructive, simultaneous elemental analysis of solid, liquid or aerosol filter samples. PIXE is a fast, reliable and—compared to other techniques—very cost efficient analysing method. The X-ray spectrum is initiated by energetic protons exciting the inner shell electrons in the target atoms. The expulsion of

these inner shell electrons results in the production of X-rays. The energies of the X-rays, which are emitted when the created vacancies are filled again, are uniquely characteristic of the elements from which they originate and the number of X-rays emitted is proportional to the mass of that corresponding element in the sample being analyzed. The generation of X-rays in a sample is very strongly influenced by the bombarding proton. The probability of X-ray production depends upon both the total number of incident protons and the proton energy (measured in million electron volts (MeV)). The total number of incident protons can be expressed as proton current (measured in micro amps). The greater the proton current, the greater the probability for X-ray production. As proton energy changes, so does the probability for X-ray production. If quantitative analysis is to be assured, then both of these factors must be accurately known. Protons, while interacting with the sample matrix to produce X-rays, can be envisioned as undergoing collisions, much as a billiard ball on a pool table. Each successive collision will cause a transfer of kinetic energy from the projectile (proton) to the stationary object (target atom). While energy transfer per collision is small, a large number of collisions will eventually reduce proton energy significantly until it comes to rest. As the proton's energy decreases, so does its ability to produce X-rays. This technique was used to study the elemental composition of glass samples using the cyclotron facility at Panjab University, Chandigarh. Figure 3.9 shows the PIXE analysis results.

Table 3.3 shows the comparison of various glass samples based on the properties studied. It was concluded on the basis of optical, surface properties and elemental composition, that Asahi and Saint Gobain were better than Modi glass sample. In the next section, we describe the Gas system, the mixing unit and calibration of gases used.

3.3 Gas System and Mixing Unit

Mixing of gases and their flow should be controlled properly. This was done using a custom built gas mixing and distribution system. It consists of a gas mixing unit, a gas purifier

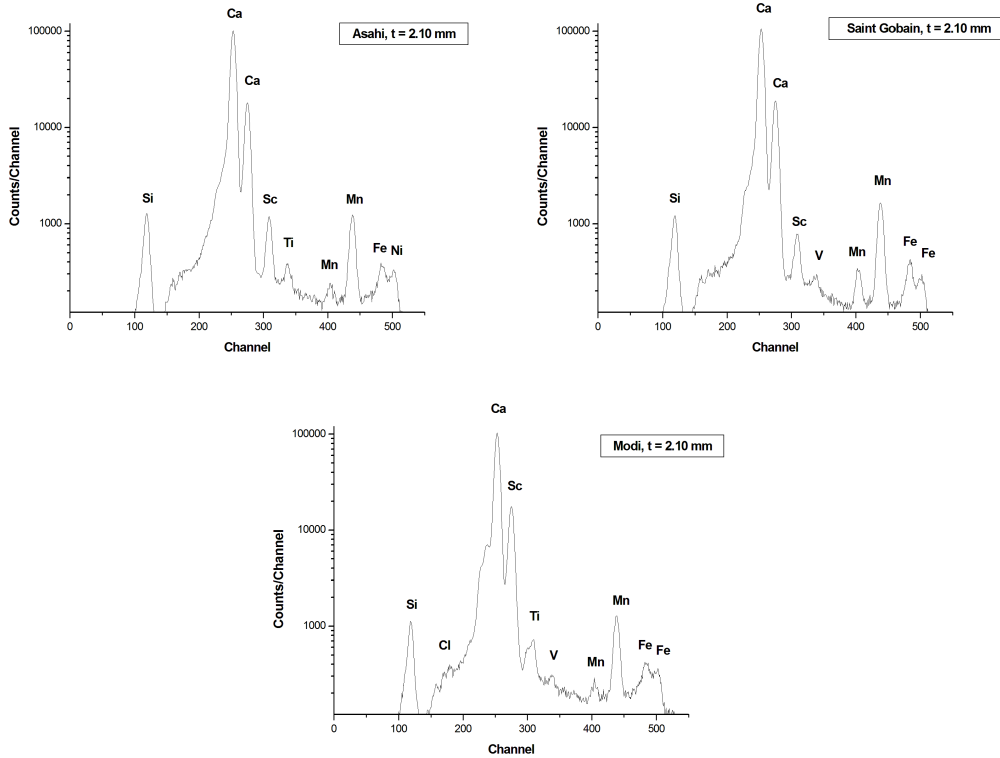


Figure 3.9: PIXE analysis of Asahi, Saint Gobain and Modi glass samples respectively.

Properties studied	Results
Physical	No significant difference
Optical	Asahi, SG shows better UV-VIS transmittance
Electrical	$10^{11} \Omega\text{-cm}$
Surface	Asahi, SG better
Elemental	High Z element in Modi glass

Table 3.3: Comparison of Asahi, Saint Gobain and Modi glass samples based on the properties studied.

column, distribution panel, exhaust manifold, safety and isolation bubblers, moisture meters, controls for monitoring and remote operation, and a set of gas cylinders together with manual and pneumatic valves. A schematic diagram of gas mixing and distribution system are shown in Figure 3.10 along with gas distribution system and gas cylinders. We procured the gases required to test RPCs in cylinders. We used low pressure input regulators of 0 to 5 Kg/cm² for Freon (R134a) (eco-friendly) and Iso-butane whereas 2000 Kg/cm² were used for Argon and SF₆. Depending on the mode of operation, appropriate

3.3. Gas System and Mixing Unit

gas pressure was allowed to flow into the purifier. We describe the design and functioning of each of the components in the gas system.

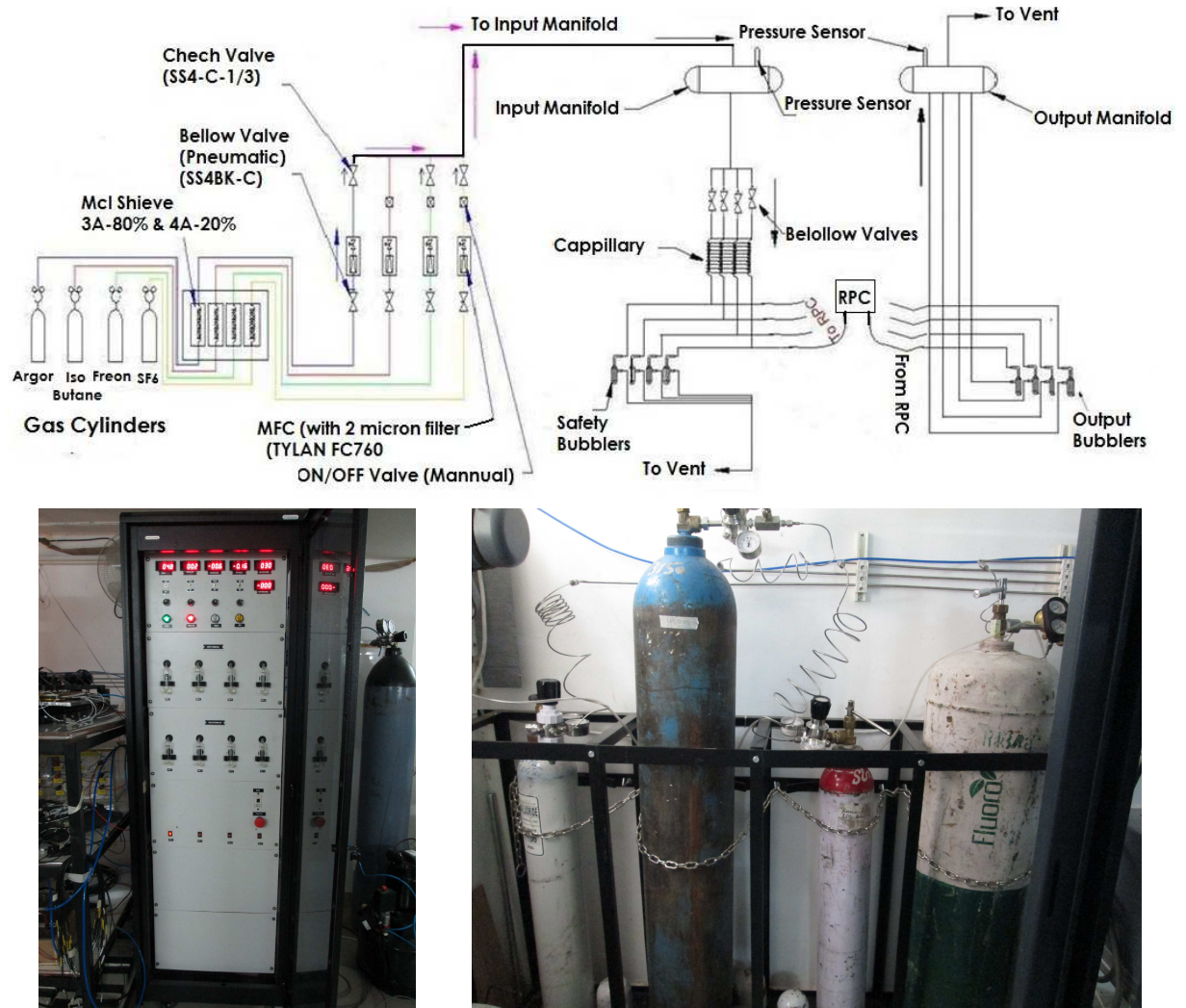


Figure 3.10: Top figure is the block diagram of the gas mixing system. (Below-left) figure shows the gas distribution system and (below-right) figure shows the gas cylinders used.

1. Gas purifier columns: Though the gases we procured were 99.9% pure, but moisture and other impurities may get diffused through valves. Proper storage with moisture free environment is necessary. The arrangement has four in-situ rechargeable molecular sieve based columns (for each input gas) made of stainless steel, attached to the cylinders to absorb moisture, oil and other impurities from the gases. These columns have two built-in heaters of 500 watts each. Each column is charged with

300 grams of molecular sieve absorbents of Type 3⁰A (80%) and Type 4⁰A (20%). Argon column has a 13 type absorbent in addition to these.

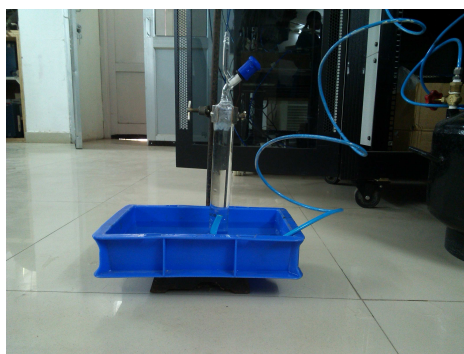
2. Mixing unit: The outputs from purifiers enter the mixing unit, which consists of pneumatic valves, mass flow controllers (MFCs), mixing line, check valves, bellow-sealed valves and a probe for moisture measurement. All the valves used in the system are of normally-closed type.
3. Mass flow controllers (MFCs): These are used to measure and control the flow of gases. These are displayed as SCCM (Standard Cubic Centimeters per Minute) units. The set value is displayed by an LED on the front panel of the system. We will describe MFC calibration in next subsection.
4. Mixing line and moisture measurement probe: It is a microprocessor based capacitive type commercial sensor with dew point display. It measures the moisture content in the gas that is being mixed on-line. The sensitivity range of this device is -800°C to -250°C dew point. Gases get mixed in the sensor volume and further mixing occurs along the stainless steel tubing as the gas flows through it and enters a distribution manifold.
5. Distribution system: It consists of a manifold and pressure transducers. Gas mixture that enters the manifold is further mixed in a small cylinder providing higher cross section and residence time. A pressure transducer-gauge of range $0-1 \text{ kg/cm}^2$ is mounted to indicate the pressure at which the gas mixture is being dispensed. This transducer operates on 15 volts DC giving a current output of 4–20 mA and is displayed on the front panel. The manifold then feeds the gas into four channels, isolated by pneumatically activated valves, with control switches at the bottom front panel. Uniform and approximately equal flow of gas mixture in all chambers is facilitated and ensured by flow resistors. Flow resistors are two meter long stainless steel capillaries having an inner diameter of 300 micron. These capillaries also allow

the gas to mix thoroughly by providing a long residence time. There are four such capillaries wherein one end is connected to one pneumatically controlled valve after the mixing cylinder and other end is connected in parallel to the RPC and safety bubbler.

6. Safety bubblers: These bubblers are made of borosilicate glass and are connected to a stainless steel tube with the help of a Tygon tube. Each bubbler has a 25mm column (typically about 5 ml) of silicone diffusion pump oil (DC704), with a density of 1.08 g/cc and a very low vapour pressure at room temperature. The presence of bubbles in these bubbler might occur due to blockages in the flow path. The gas should not bubble through any safety bubblers.
7. Isolation bubblers: There are four such bubblers in the system. The gas mixture that flows out of each RPC flows through one isolation bubbler. The absence of bubbles in these bubblers implies a leakage in the RPC or a joint or malfunctioning of channel. The output from all bubblers is fed into a output exhaust manifold.
8. Exhaust manifold: The return gas from all connected chambers is collected into this manifold. An output is provided to vent the used gas into the atmosphere.
9. Remote control and monitoring: The flow rates and pressure of the gases can be set and monitored through a PC interface. We describe the calibration of gases now.

MFC Calibration : MFCs are calibrated to control a specific type of gas at a particular range of flow rates. Calibration of the MFCs for different gases, flown through them is important. Two methods for the calibration are downward displacement of water and linear gas flow method. We used downward displacement of water for all the gases, as shown in Figure 3.11. The MFC was set to 0.2 sccm, and the gas under test was passed through it with a pipe into a measuring capillary tube filled with water. This capillary tube was then inverted into a container filled with water. The gas was passed

in the tube from one known level to another known level and the time taken for this was noted. The level difference (volume) divided by the time recorded is the average flow rate. Then MFC was set to 0.6 sccm and again the procedure was repeated (time and level difference were recorded). This procedure was repeated for other gases with different MFCs. When all the MFCs were calibrated, the proportion of various gases in the mixture were decided. Depending on the different modes of RPC operation, these flows were adjusted accordingly.



(a) Setup used to do MFC calibration

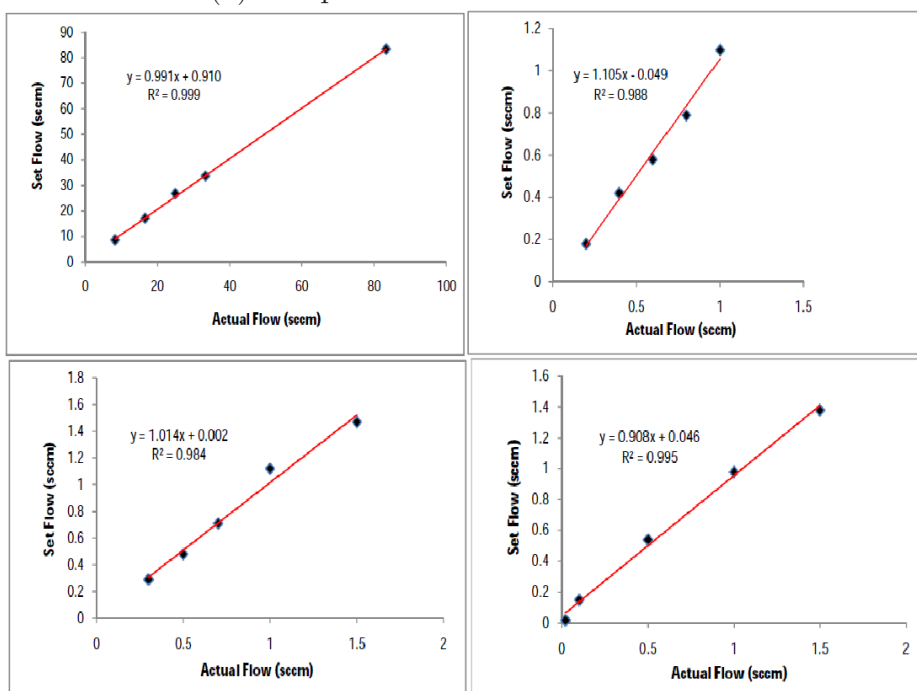


Figure 3.11: (b) (Top-left) plot shows calibration of freon gas, (top-right) plot shows calibration of isobutane gas. (Bottom-left) plot shows calibration of SF₆ gas and (bottom-right) plot shows calibration of argon gas.

We plotted actual flow vs set flow to obtain the calibration curve for the gases we used and we got MFC calibration equations from these plots as shown in Figure 3.11. Basically, we set 5 sccm flow rate for all the gases, but different proportions for different modes. As explained in section 2.3.2, the ratio of the gas mixture depends on the roles performed by these gases, modes used and the cost factor too. For avalanche mode binary mixture of Freon(R134a) and Isobutane is sufficient for RPC operation and traces of SF_6 were added to bring stability in RPC operation. For streamer mode, Argon was used along with other two gases as it provides large avalanche multiplication. In this chapter, we used some terms like two gases for avalanche mode with gas proportion [165] – [169] - Freon(R134a) : Isobutane :: 95.5 : 4.5, three gases for avalanche mode with gas proportion - Freon(R134a) : Isobutane : SF_6 :: 95.15 : 4.51 : 0.34, streamer mode with gas proportion - Freon(R134a) : Isobutane : Argon :: 62 : 8 : 30. After the calibration of MFC our need is to fabricate and characterise scintillator paddles; this is discussed in the next section.

3.4 Scintillator Paddles

In order to perform efficiency and cross-talk studies, we fabricated scintillator paddles using plastic scintillator of different widths. We, first, measured their efficiencies to check their performance in terms of pulse shape and timing.

These scintillation detectors are made of a special piece of plastic called a "scintillator". The basic principle on which scintillator detector works is "scintillation". When a fast moving charged particles such as cosmic ray muons pass through the scintillator they excite the atoms in the plastic by providing them some energy. The excited atoms lose this energy by emitting some photons of light. This light is detected by a photomultiplier tube (PMT) which is coupled to scintillator through a "light guide". The photomultiplier multiplies the small flashes of light into a large electrical signal that can be measured.

Plastic scintillators are mostly used in Nuclear and High Energy Physics exper-

iments. These are solutions of organic scintillators but in a solid plastic form. Plastic scintillators offer an extremely fast signal with decay constant (2-3 ns). They have high light output and are very flexible which can be easily machined by normal means.

3.4.1 Fabrication of Scintillator Paddles

Fabrication of scintillator detector started with cutting of cast scintillator pieces as per our requirement. For our analysis, we needed detectors of 1.8 cm × 30 cm, 2.5 cm × 30 cm, 3.8 cm × 30 cm, 5 cm × 30 cm and two paddles of 21.5 cm × 35 cm. Paddles were cut with 1 cm extra along the length, as 1 cm extra is needed to merge them in the light guide. Figure 3.12 shows the components required for the fabrication of scintillator detector. We required: scintillators cut into rectangular shape of the size mentioned above, light guide (Perspex) cut into fish tail shape (size 1.5 cm × 5.2 cm for small paddles and 3 cm × 10 cm for large paddles), cookie (round) cut into the size of photomultiplier (2" dia), Optical Glue Bicorn 600, white reflecting paper (Tyvek) for wrapping, black paper (tedlar) for 2nd wrapping of whole paddle, Aluminum foil tape. Other requirements were Photomultiplier Tube (PMT), voltage divider for PMT EMI, Aluminum Housing for PMT, Aluminum Housing for voltage divider of PMT, fixed Lemo socket ERA.00.250 CTL, HV Connector/ socket (MHV Type), co-axial cable CCE.99.281.505 (LEMO). The PMTs (positive) connected to the scintillator paddles are of different voltage ranges as given in Table 3.4.

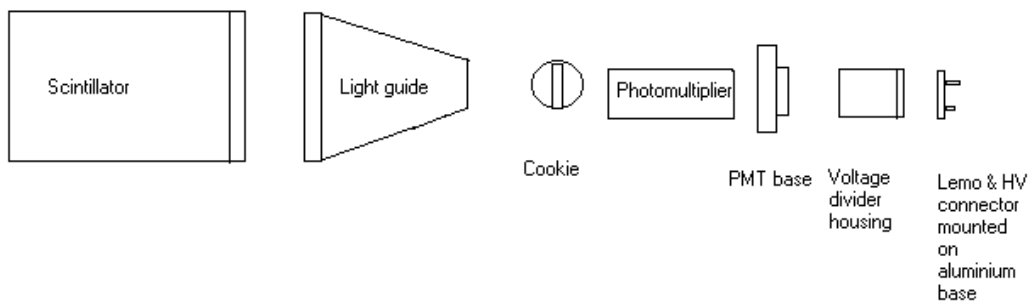


Figure 3.12: Components of Scintillator detector.

Size of scintillator paddles	Voltage range (V)
1.8 cm × 30 cm	1726 - 1996
2.5 cm × 30 cm	1602 - 1843
3.8 cm × 30 cm	1536 - 1755
5 cm × 30 cm	1505 - 1716
21.5 cm × 35 cm	1528 - 1749
21.5 cm × 35 cm	1544 - 1778

Table 3.4: PMTs with different operating voltage ranges.

First of all, we cleaned all the components like scintillator paddles, light guide and cookie with propanol/ethanol. We attached the scintillator with light guide and cookie with the help of optical glue. After completely drying (1-2 days) under room temperature, we applied the aluminium foil tape to all the sides of the scintillator, light guide and cookie. Aluminum tape helps in reflecting back the light into the scintillator and further to PMT through the light guide. We then wrapped the whole detector with Tyvek paper (reflecting paper). Special care was taken to cover the detector properly to avoid the light leaks from the corners and sharp bends. The whole detector was then wrapped with black tedlar paper and black tape in the same fashion. Then, we assembled the voltage divider using Lemo socket and HV socket with help of the aluminium housing. The HV wire and signal wire were soldered with the respective sockets. The EMI Tube was plugged to voltage divider socket. The whole assembled detector was cleaned with propanol/ethanol. We then applied some optical grease to the face of PMT and attached it with cookie of the wrapped scintillator with the help of aluminum coupling. It was wrapped with black tape to fix cookie and PMT with coupling. Figure 3.13 shows the steps followed to make scintillator detector. Figure 3.14 shows the fabricated scintillator detectors of width 1.8, 2.5, 3.8 cm respectively.

3.4.2 Characterisation of Scintillator Paddles

Before measuring efficiency, we did plateauing study of all the scintillator paddles to find their operating voltages for the attached PMTs. Figure 3.15 shows the circuit diagram of



Figure 3.13: (Top-left) figure shows the paddle of 1.8 cm width and cookie before making scintillator detector. (Top-right) figure shows the paddle glued to the cookie. (Bottom-left) figure shows paddle wrapped with Aluminium for the shield from light. (Bottom-right) figure shows paddle wrapped with black paper and masked with black tape to avoid any light passing through the paddle.



Figure 3.14: The fabricated scintillator detectors of width 1.8, 2.5 and 3.8 cm respectively.

the coincidence of scintillator paddles. P_1 and P_2 paddles are connected to the discriminators to make 2-fold coincidence. This 2-fold along with P_3 makes 3-fold coincidence and finally 3-fold and P_4 makes 4-fold coincidence where $P_1 = 1.8 \text{ cm} \times 30 \text{ cm}$, $P_2 = 21.5 \text{ cm} \times 35 \text{ cm}$, $P_3 = 2.5 \text{ cm} \times 30 \text{ cm}$ or $3.8 \text{ cm} \times 30 \text{ cm}$, $P_4 = 21.5 \text{ cm} \times 35 \text{ cm}$. The counters, S_1 to S_7 are connected to count the number of cosmic ray muons passing through the scintillator detectors. Delays were added wherever required due to the longer signal path.

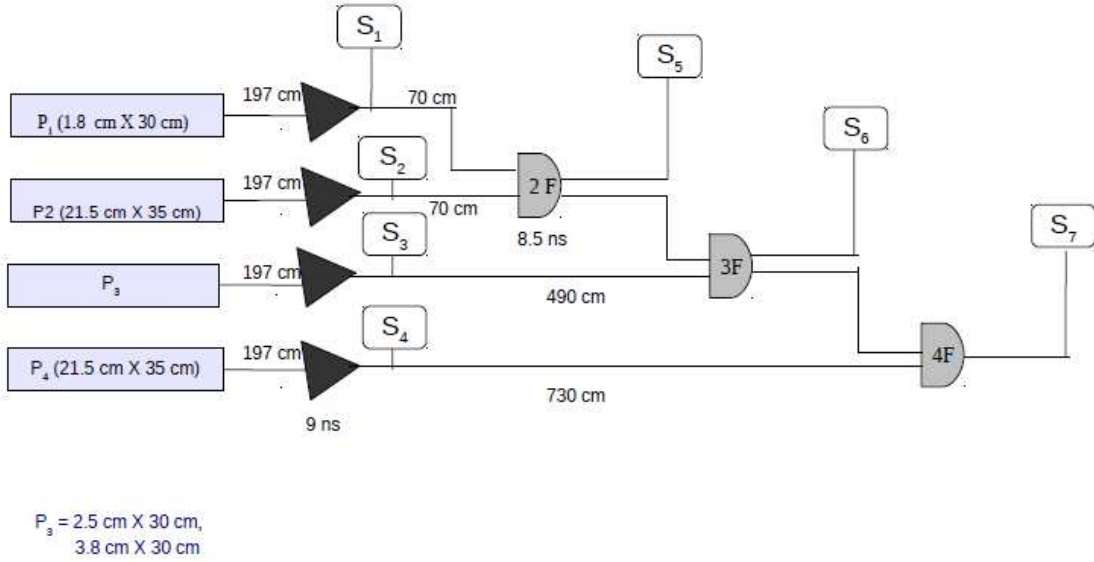


Figure 3.15: Circuit diagram of the coincidence of scintillator paddles.

For finding the operating voltage, we varied the threshold of discriminator while the paddles were kept at their prescribed high voltage (as described earlier, between their voltage range), to set the threshold. Then, the threshold where we got a perfect signal on oscilloscope is kept fixed for overall studies. We varied the voltage that we supplied to the scintillator paddles from 1.5–1.85 kV, to get the operating voltage. Figure 3.16 shows the plateau region study of all the scintillator paddles. From the figure we observed that the point where there is a knee effect is the operating voltage of each scintillator detector and it lies within the prescribed voltage range.

We measured the efficiency of two scintillator paddles using the same coincidence

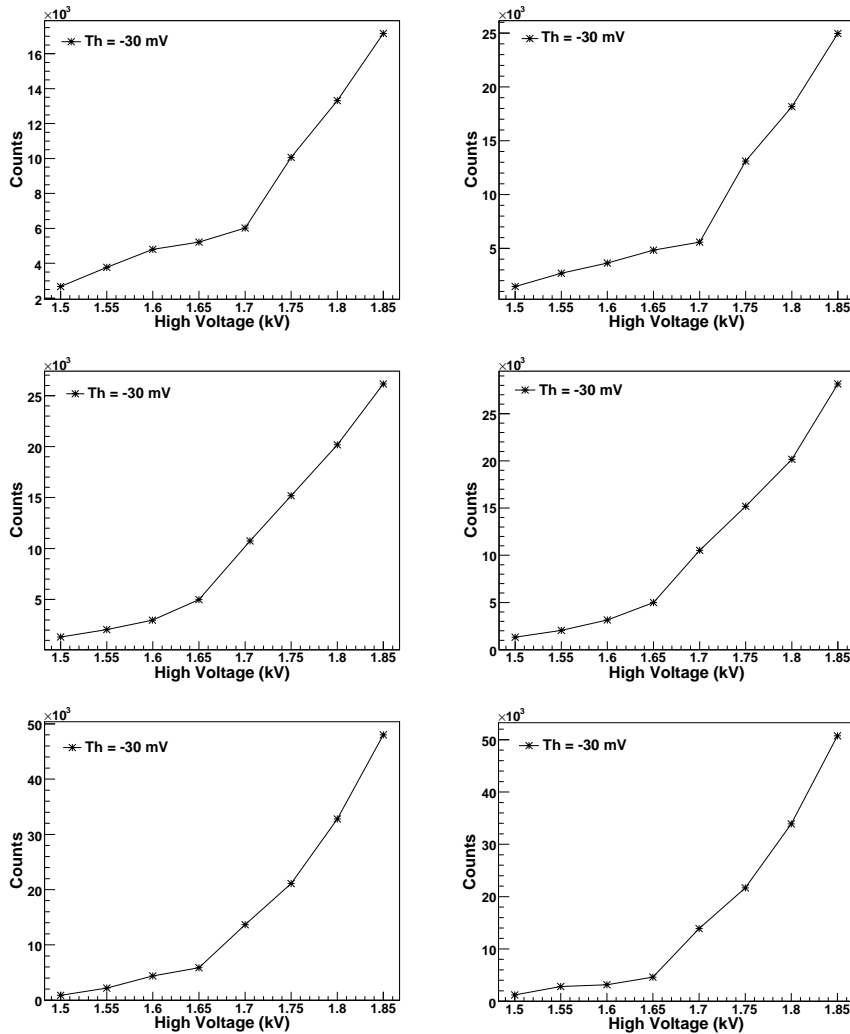


Figure 3.16: The plots (top) show the plateau region study of the scintillator paddles of width = 1.8, 2.5 cm respectively. The plots (middle) show the plateau region study of scintillator paddles of width = 3.8, 5 cm respectively. The two plots (bottom) show the plateau region study of scintillator paddles of same width = 21.5 cm. Note that the y-axis is different due to the different number of counts.

circuit as given in Figure 3.15. We varied the voltage from 1.5–1.85 kV and measured the efficiency of the P_3 paddle, for different threshold values ($\text{Th} = -10$ to -70 mV), while the threshold voltage of P_1 , P_2 and P_4 paddles were kept at -30 mV. Figure 3.17 shows the efficiency of the two scintillator paddles of width 2.5 and 3.8 cm respectively. Efficiency of the scintillator detector increases with the voltage and reaches a plateau at higher voltage. The scintillator detector efficiency is greater than 98% and is suitable to

act as trigger for RPC studies. So, after completing scintillator detector characterisation, we discuss the fabrication and characterisation of glass RPCs.

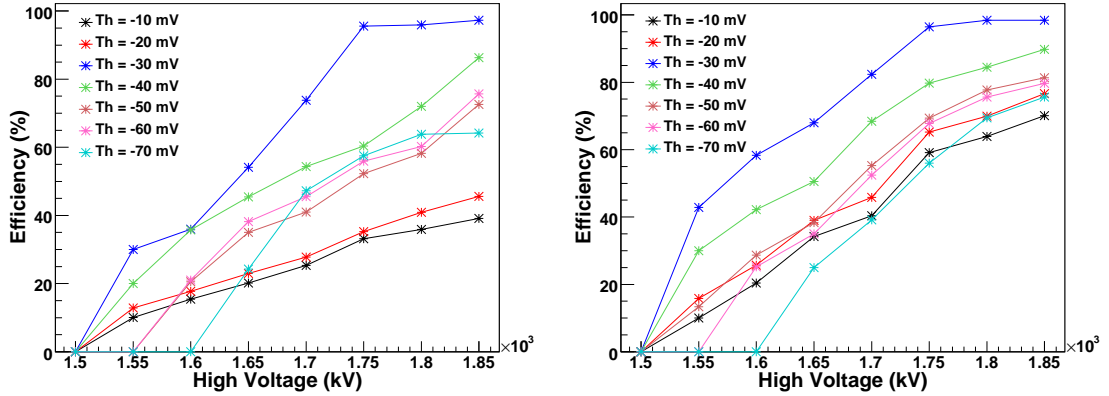


Figure 3.17: Left figure shows the efficiency of scintillator paddle of width = 2.5 cm. Right figure shows the efficiency of scintillator paddle of width = 3.8 cm.

3.5 Fabrication and Characterisation of glass RPCs

After testing the glass samples that we have procured from local market, we have fabricated three RPCs of Asahi, Saint Gobain and Modi glass.

3.5.1 Fabrication of RPCs

We used the float glass of 2.10 mm thickness [170, 171] of Asahi, Saint Gobain and Modi glass to fabricate RPCs of 30 cm \times 30 cm in size with the corners chamfered at 45° . All the glasses, button spacers, side spacers and nozzles were cleaned with distilled water and propanol/ethanol. The glass plate was put on a clean white sheet on a table. A drop of glue (DP 125 grey) was put at four equidistant positions and one at the center and button spacers were placed on the top of each glue drop, and pressed lightly. All the side spacers were cut according to the size of the glass and a frame was made covering all the sides of the glass. Nozzles were kept at the corners in such a manner that the direction of all the

nozzles are in either clockwise direction or anti-clockwise direction. All the side spacers and nozzles were glued with the glass and kept for 12 hours to dry. After drying, again a drop of glue was put on each button spacer and the second glass was placed on top of the button spacers. Special precautions were taken that both top and bottom glass edges were aligned properly to fit in the frame. Glue was applied again on all the sides between side spacers, nozzles and glass. A weight was put on the RPC and the glue allowed to harden for more than 12 hours at room temperature. A standard procedure was adopted to paint the glass. It was spray painted with a spray gun on one side by Nerolac conduction paint, where the paint to thinner ratio is 1:1. The surface resistance was maintained of the order of $1 \text{ M}\Omega \pm 200 \text{ k}\Omega$. Figure 3.18 shows the fabricated RPCs before and after graphite coating. After graphite coating, the surface resistivity measurements were done using a jig and multimeter. Figure 3.19 shows the method used to measure the surface resistivity and surface resistivity measurements of the three glass RPCs. The surface resistivity was of the order of 600–800 $\text{k}\Omega$ for Asahi, Saint Gobain glass RPC and 600–700 $\text{k}\Omega$ for Modi glass RPC. However, the variation in the surface resistivity can be seen which is due to the manual spray painting.



Figure 3.18: The fabricated RPCs, before graphite coating (left) and after graphite coating (right).

Gas leakage test was performed on each RPC to detect the leaks using pico-log meter. Pico-log meter is a versatile instrument that connects to the USB port of any PC. Pico-Log software can be used as a data logger with built-in sensors for light, temperature,

3.5. Fabrication and Characterisation of glass RPCs



(a) RPC with jig and multimeter used to measure surface resistivity.

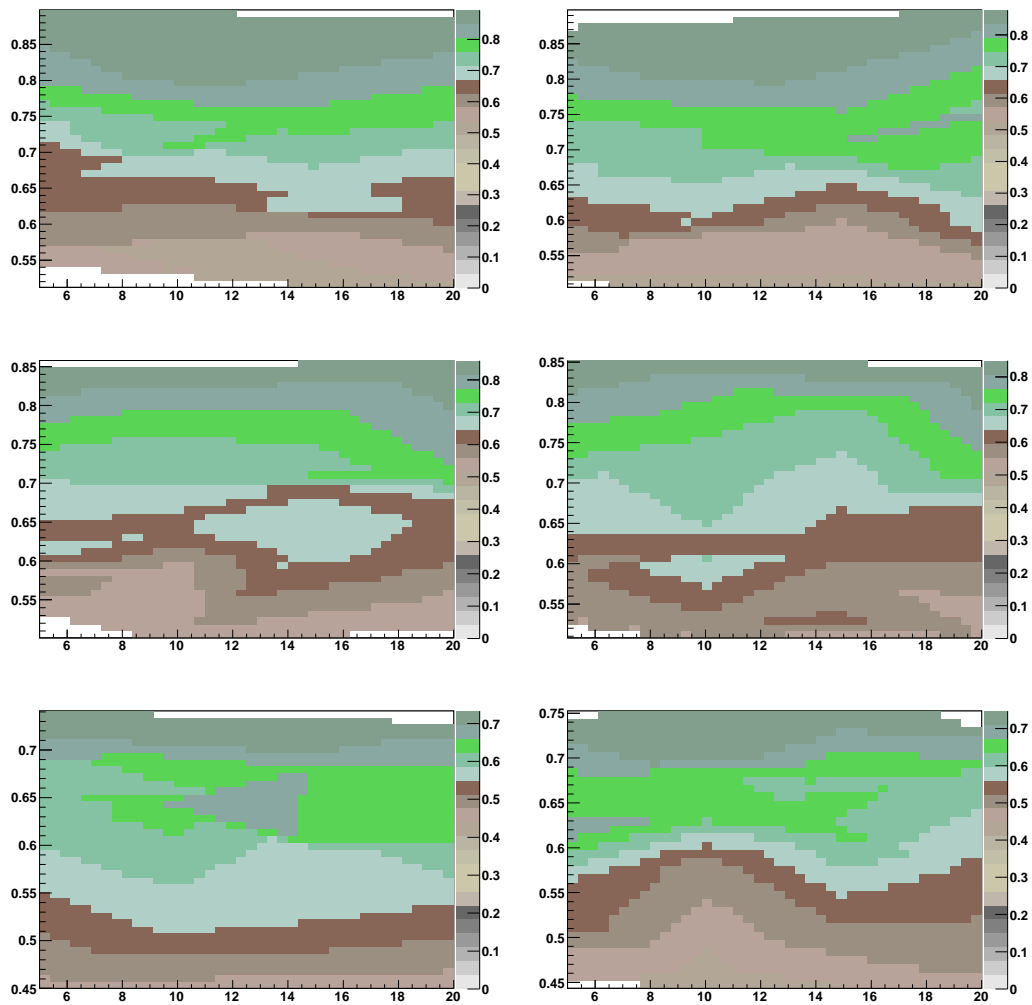


Figure 3.19: (b) Surface resistivity measurements of Asahi, Saint Gobain and Modi glass RPC respectively. Left plots show X side, Right plots show Y side of Asahi, Saint Gobain and Modi RPC respectively.

sound, voltage, resistance, temperature, humidity, pressure and more. Figure 3.20 shows the circuit diagram for gas leakage test. The two diagonally opposite nozzles of RPCs

were blocked, one adjacent nozzle was connected to Argon gas cylinder through tygon pipe and other diagonally opposite nozzle was connected to pico-log meter. Pico-log meter was further connected to power supply, CPU and display unit. Figure 3.21 show gas leakage test of Asahi, Saint Gobain and Modi glass RPCs respectively. The data shown here is for pressure taken over 10 mins and it is seen to be dropping exponentially due to leakage in the RPC.

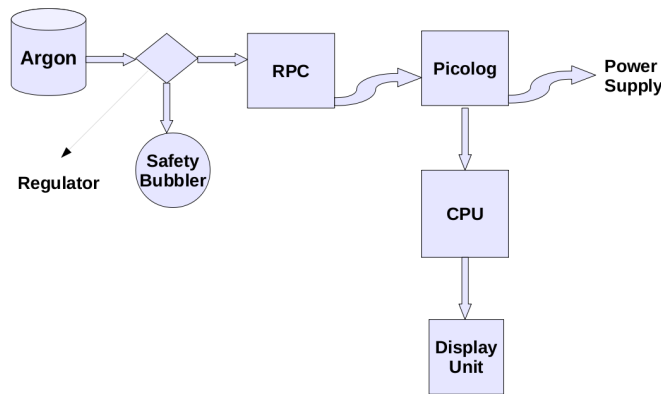


Figure 3.20: Circuit diagram for gas leakage test.

The next step was to fix those leak areas in the RPC, so glue was re-applied to the leaking areas and rechecked for leak after the glue hardened. The data was taken for 10 mins, since the time when we were doing leak tests it was the rainy season and hence humid. The humidity as monitored with a dedicated weather station and was kept under control using the air-conditioning system. Figure 3.22 shows gas leakage test after re-gluing. Left plot shows the gas leakage test of Asahi, Saint Gobain and Modi glass RPCs respectively. The straight line shows there was no further leak in the RPCs. We dipped the sides of the three RPCs in a tub containing water and checked, but we did not find any bubble. The right plot of Figure 3.22 shows the button test of Asahi, Saint Gobain and Modi glass RPCs respectively. We performed button test by pressing those areas with thumb (for 2 sec) where we placed buttons. Those areas were identified with

3.5. Fabrication and Characterisation of glass RPCs

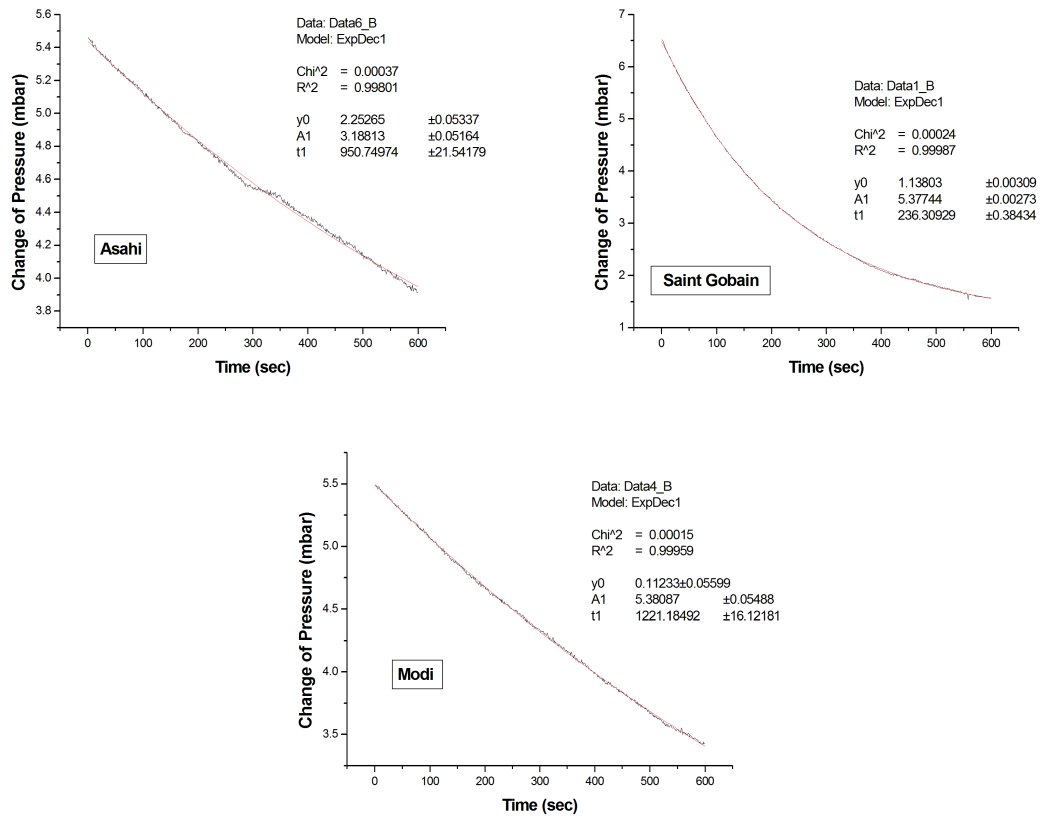


Figure 3.21: Gas leakage test of Asahi, Saint Gobain and Modi glass RPCs respectively.

the help of a mylar sheet with button marks, that was made when we were fabricating RPC. The five peaks of almost equal size shows that the buttons were not popped.

Then the next step was to pack the RPC. Before packing the leak tested RPC, we fabricated pick-up panels with different strip width size, 1.8, 2.8, and 3.8 cm. We took a panel of 30 cm \times 30 cm size, made up of foam and aluminium sheet pasted on both sides of that foam. We marked the size of strips of the panel say for 2.8 cm with the gap between the adjacent strips = 0.2 cm. Then, we peeled off those gaps between each strips. Since soldering on aluminium sheet is not possible, we pasted copper strips above and below, across the two end sides of the panel. The resistance of these strips were measured and it came to be of the order of 50 Ω , so we have terminated each strip with a 50 Ω resistor. On the other end of the pick-up panel, we have connected coaxial cables with lemo connectors soldered to them. These connectors are of the shape to be

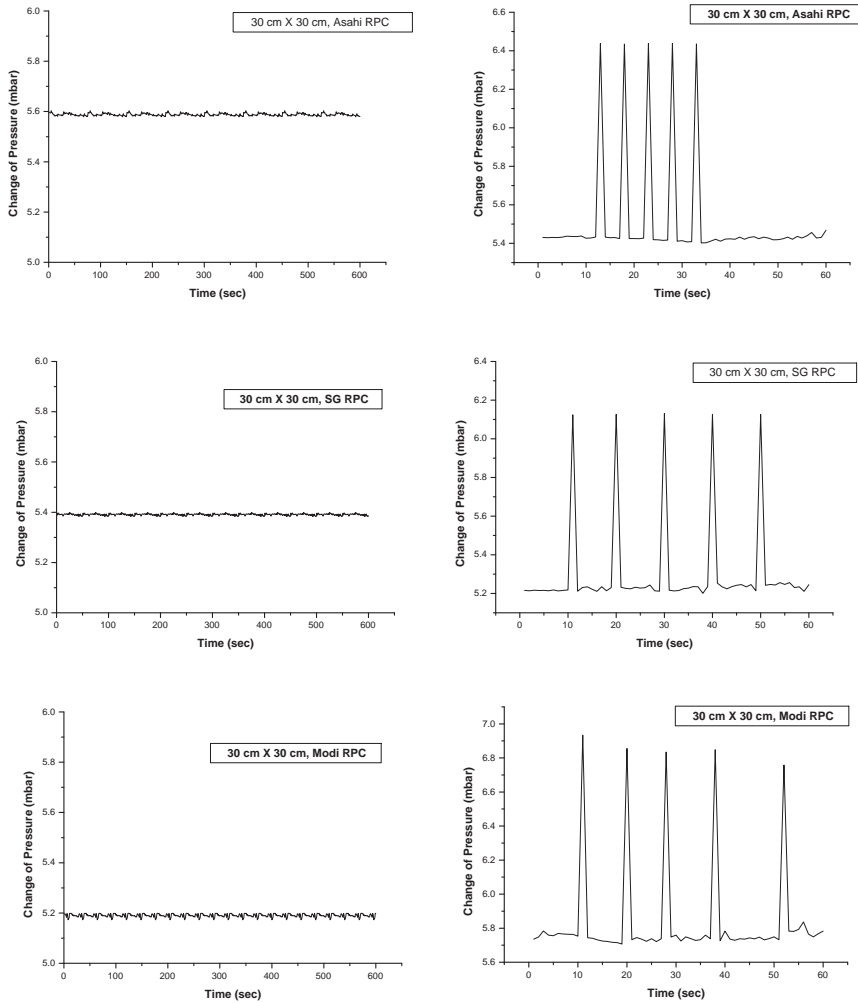


Figure 3.22: Gas leakage test after re-glu. Left plot shows the gas leakage test of Asahi, Saint Gobain and Modi glass RPCs respectively. Right plot shows the button test of Asahi, Saint Gobain and Modi glass RPCs respectively.

fit to the preamplifiers. Figure 3.23 shows the fabricated pick-up panels for 30 cm \times 30 cm RPC, having strip width size of 1.8, 2.8 and 3.8 cm.

Leak tested RPC was packed with the pick-up panels (More details on pick-up panels is provided in subsections 2.3.2 and 2.3.3) on both sides in a manner that they were orthogonal to each other. A small copper strip was pasted on the graphite and high voltage cables were soldered. Positive voltage wire was attached to the upper plate while negative voltage wire was attached to the lower plate. Mylar sheets were placed in between pick-up panels and graphite coating and over the pick-up panel for insulation.

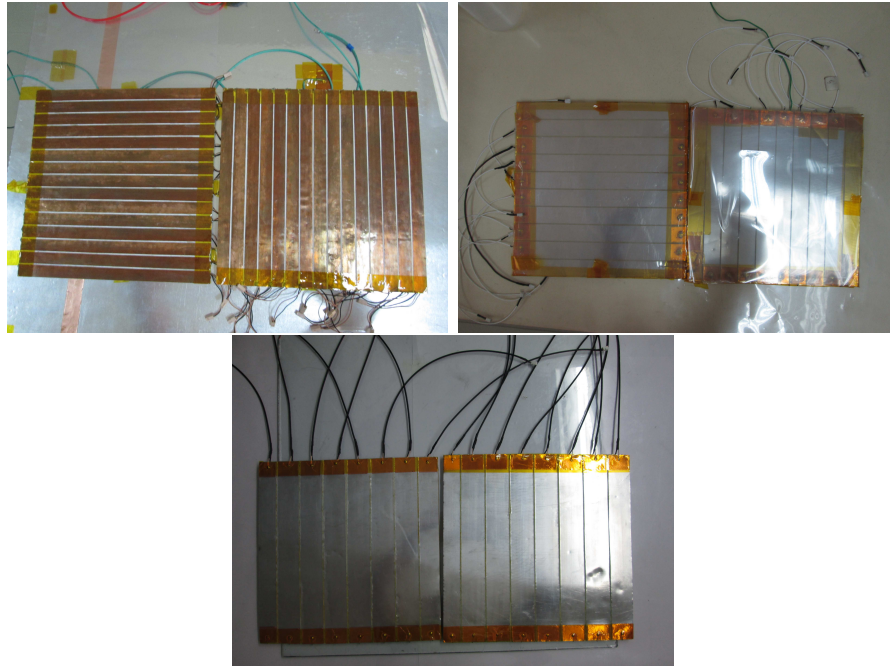


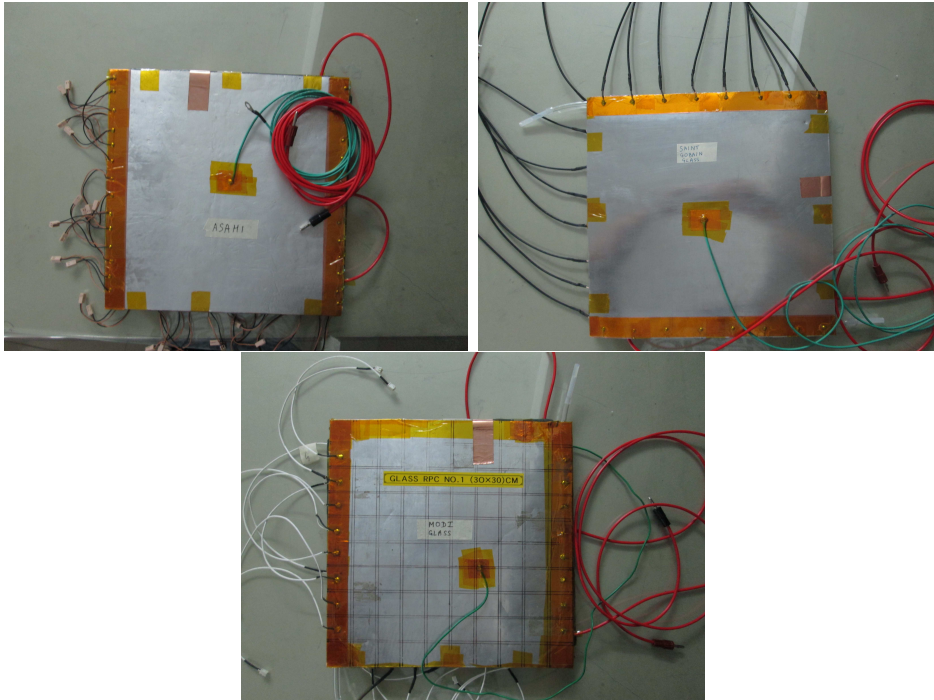
Figure 3.23: The three figures are of the fabricated pick-up panels for 30 cm \times 30 cm RPC, with the strip width size of 1.8, 2.8 and 3.8 cm respectively.

Figure 3.24 shows RPCs fully packed and RPC mounted on a wooden stand. Now we discuss characterisation of fabricated RPCs.

3.5.2 V-I Characteristics of RPC

As described in chapter 2, gaseous detectors like RPCs work on the principle of ionisation of the gas leading to the formation of avalanche and further multiplication of ions takes place. Detectors working in this region are proportional counters and this region is known as *proportional counting region*. Further multiplication leads to secondary avalanche and that's why quenching gas is added to absorb the photons causing multiple avalanche. The detectors working in this region are Geiger-Muller counters and this region is known as *Geiger region* and shows a plateau curve. The gaseous detectors work in both these regimes and that's why we measure V-I characteristics of RPC (refer to Figure 2.6 of chapter 2).

To measure V-I characteristics, we varied the voltage and measured the current



(a) The figures show Asahi, Saint Gobain and Modi glass RPC respectively (fully packed).

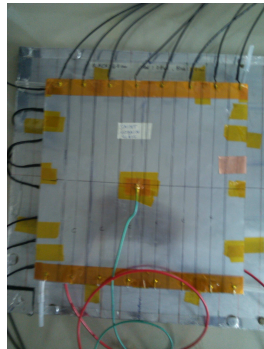


Figure 3.24: (b) RPC mounted on a wooden stand before putting it into the test stand for the testing.

after waiting for 10 mins (when current becomes stable). Figures 3.25, 3.26, 3.27 show V-I characteristics of Asahi, Saint Gobain (SG) and Modi with two gases (avalanche mode), three gases (avalanche mode) and streamer mode. The V-I plot can be divided into two regimes of voltages. At low voltage, the primary ionization does not produce avalanche causing the gas gap impedance to become infinite and the current through the RPC becomes proportional to resistance provided by the spacers which is less than the gap resistance. At high voltage, the production of avalanche cause the drop in gas

3.5. Fabrication and Characterisation of glass RPCs

resistance and the current obtained is due to the resistance from glass plates. We now discuss the efficiency and cross-talk of various glass RPCs.

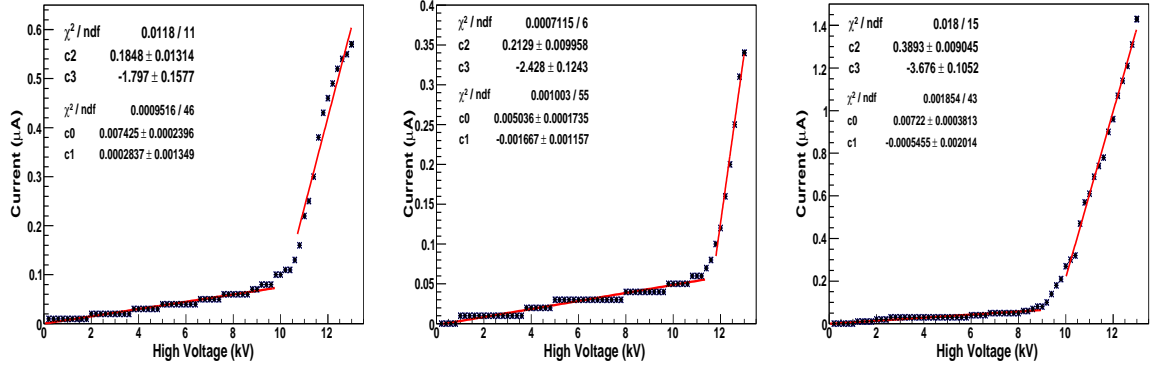


Figure 3.25: V-I characteristics of Asahi with two gases, three gases in avalanche mode and streamer mode respectively.

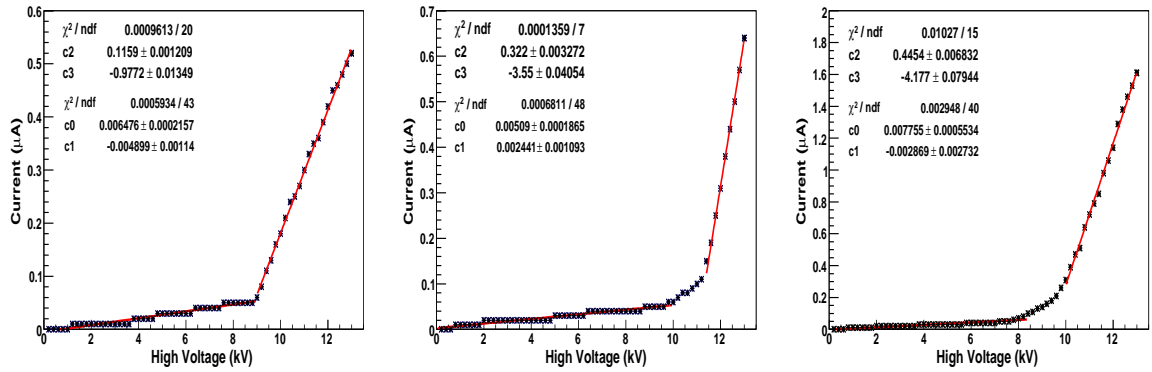


Figure 3.26: V-I characteristics of SG with two gases, three gases in avalanche mode and streamer mode respectively.

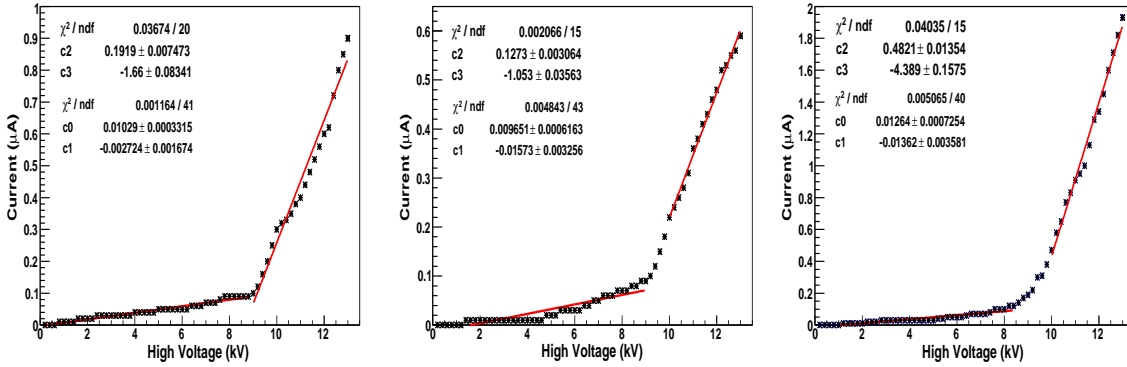


Figure 3.27: V-I characteristics of Modi with two gases, three gases in avalanche mode and streamer mode respectively.

3.5.3 Efficiency and Cross-talk of RPCs

The fabricated RPCs were then tested for their performance using cosmic ray muons. Muons ionize the gas after passing through RPCs and the signal generated in RPC was picked up by copper strips of the pick-up panels. This signal was transmitted to the electronics and amplified by fast preamplifiers in case of avalanche mode, but no preamplifiers were required for streamer mode as the pulses were larger in size. Preamplifiers are of two type mainly: current-sensitive and charge-sensitive. Current-sensitive preamplifier amplifies extremely low currents. Charge-sensitive produces a voltage output proportional to the integrated value of the input current. We used charge-sensitive fast preamplifier *PU_HMCPAN* - 04 (BMC of negative input–negative output used) with gain = 75%. The pre-amplified RPC signals are fed to AFE (analog front-end) boards to convert the amplified analog RPC pulses into logic signals by using a low threshold discriminator circuits. The discriminator signals from the AFE boards are further processed by a DFE (digital front-end) for multiplexing of these signals and actual counting was done by scalars (refer to Figure 2.9).

When a trigger signal from scintillator paddles was received, the processed signals were latched and recorded by the NIM and CAMAC based back-end electronics: control and readout module. All these modules were interfaced to a PC through CAMAC con-

3.5. Fabrication and Characterisation of glass RPCs

troller which regulated the synchronous functioning of all CAMAC modules. Along with that we had few more electronic devices as can be seen from Figure 3.28. On the right hand side of this figure we had (from top to bottom) power supply with zener diode circuit used for scintillator detectors, oscilloscope, multi-channel power supply used for RPCs, NIM modules (with fan-in fan-out, discriminators, logic gates, CAMAC crate, counters). From left hand side of this figure, from bottom to top (ignoring last shelf) we had power supply for preamplifiers, multi-channel box (input from multi-channel power supply is provided to this box and output taken from this box was fed to RPC) and RPC with preamplifiers.

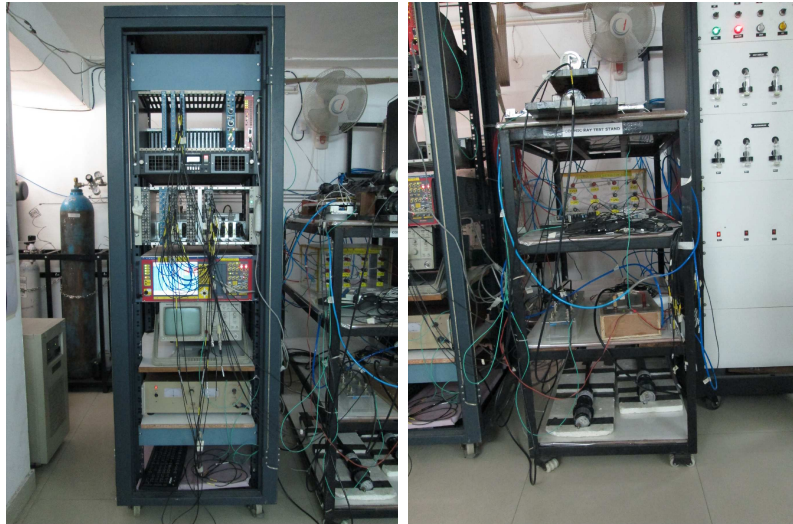


Figure 3.28: Right figure shows stand with the CAMAC controller, logic gates, CRO, power supply. Left figure shows RPC in the cosmic ray muon stand.

In order to study the efficiency of the detector, a cosmic ray telescope was built using four paddles of scintillator detectors (sometimes also referred to as hodoscopes). Figure 3.29 shows the trigger scheme circuit diagram for testing the RPC. P_1 , P_2 , P_3 and P_4 paddles are connected to the discriminators to make 4-fold coincidence (forming trigger signal). This 4-fold along with the different RPC strips form a coincidence. RPC was placed after P_2 , where $P_1 = 1.8 \text{ cm} \times 30 \text{ cm}$, $P_2 = 21.5 \text{ cm} \times 35 \text{ cm}$, $P_3 = 2.5 \text{ cm} \times 30 \text{ cm}$ or $3.8 \text{ cm} \times 30 \text{ cm}$, $P_4 = 21.5 \text{ cm} \times 35 \text{ cm}$. The counters S_1 to S_7 are connected to

count the number of cosmic ray muons passing through the scintillator detectors. Distance between $P_1.P_2$ and RPC was taken as 9 cm. Distance between $P_3.P_4$ and RPC was taken as 2.5 cm. Distance between $P_1.P_2$ and $P_3.P_4$ was taken as 9 cm. P_1 and P_2 were placed one above the other in a manner to create a window of about $14 \text{ cm} \times 1.8 \text{ cm}$ (or 2.5 cm or 3.8 cm depending on the scintillator paddle used). We aligned it with strip number 3 and considered it as “main strip”, whereas 2^{nd} strip was considered as “left strip” and 4^{th} strip was considered as “right strip”. Due to the non-availability of positive output preamplifier, we obtained data for X-strip of RPC. The RPC was placed after P_2 and this ensured that when the muon passed through all the four paddles of the telescope it passed through the RPC too. We tried to maintain temperature at 24.5°C and relative humidity of $RH = 40\%$. But the source of error was the opening and closing of the door which caused moisture level sometimes to go up and affected the efficiency of the RPCs. The pulse width of scintillators were kept at 60 ns and RPCs at 50 ns.

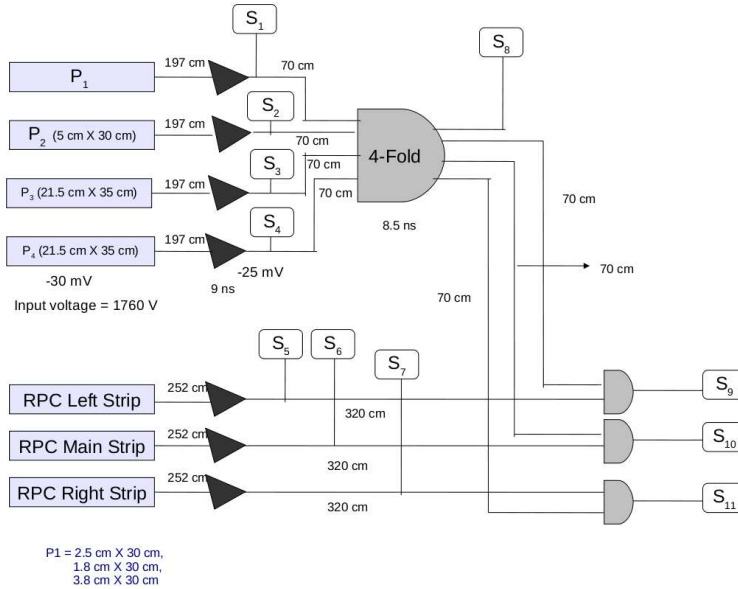


Figure 3.29: Trigger scheme circuit diagram for testing RPCs.

Signals from all the four paddles were passed through a discriminator with threshold voltage of -30 mV , ANDed together to give $P_1.P_2.P_3.P_4$ 4-fold signal. The ANDed signal acted as the trigger pulse. If this ANDed signal was 1 we considered the passage of

3.5. Fabrication and Characterisation of glass RPCs

muon through the set window in the detector. This trigger signal was then ANDed with signal from the main strip of RPC which was aligned to the telescope and also with the signals from adjacent right strip and left strip. Signals from main strip and the adjacent right and left strips were sent to discriminator and delayed before being ANDed with trigger signal. Only when the trigger was 1 and the respective RPC strip signal was 1 then the scalar counter of respective strip incremented its count by one. The number of time the condition was satisfied out of the total trigger signal, gave the efficiency of the RPC. Fluctuations in the efficiency were due to “noise rate”. Noise rate is the rate at which random noise signal hits the RPC strip, which may be due to cosmic ray particles, contributions from electronics, stray radioactivity and dark current in chamber. A comparison of noise rate of Asahi, Saint Gobain and Modi glass RPC in avalanche (two and three gases) and streamer mode with strip width = 2.8 cm at 10 kV is shown in Table 3.5.

RPC and modes	Noise rate Hz/cm ²
Asahi (two gases)	7.4×10^5
Saint Gobain (two gases)	8.9×10^5
Modi (two gases)	5.3×10^6
Asahi (three gases)	6.8×10^4
Saint Gobain (three gases)	7.7×10^4
Modi (three gases)	3.2×10^5
Asahi (streamer)	5.9×10^3
Saint Gobain (streamer)	4.6×10^3
Modi (streamer)	6.3×10^4

Table 3.5: Noise rate of Asahi, Saint Gobain and Modi glass RPC in avalanche (two and three gases) and streamer mode with strip width = 2.8 cm at 10 kV.

When the voltage increases even low energy particles are able to produce signal above threshold, leading to increase in noise. We expected the RPC strip aligned with window set by the cosmic ray telescope to pick up the signal. In case the signal is picked up by adjacent strips, it is called “cross-talk”. Cross-talk can be due to misalignment of strip or due to inadequate amount of quenching gas used which result in spread of discharge. Our effort was to reduce it, in order to improve the performance of the detector. So,

considering all the above facts, the formula for efficiency is given by,

$$\text{Efficiency (strip)} = \frac{(\text{No. of strip hits and Trigger})}{\text{Total no. trigger}} . \quad (3.1)$$

Using this formula and the concept discussed we obtained the efficiency and cross-talks of Asahi, Saint Gobain and Modi glass RPC with strip width of 1.8, 2.8 and 3.8 cm. Figures 3.30, 3.31 and 3.32 show efficiency and cross-talk of Asahi glass RPC in avalanche mode (two gases), avalanche mode (three gases) and streamer mode with the strip width size = 1.8, 2.8, 3.8 cm respectively. From the figures, we see that efficiency of the detector increases with voltage and reaches a plateau at higher voltage with efficiency greater than 90%. The fluctuations may be due to the noise rate, specially in case of two gases. The small strip width size may also add to the fluctuation as the adjacent strips may interfere with each other. The fluctuations in the efficiencies are high with two gases but reduces with the addition of third gas in both avalanche mode and streamer mode.

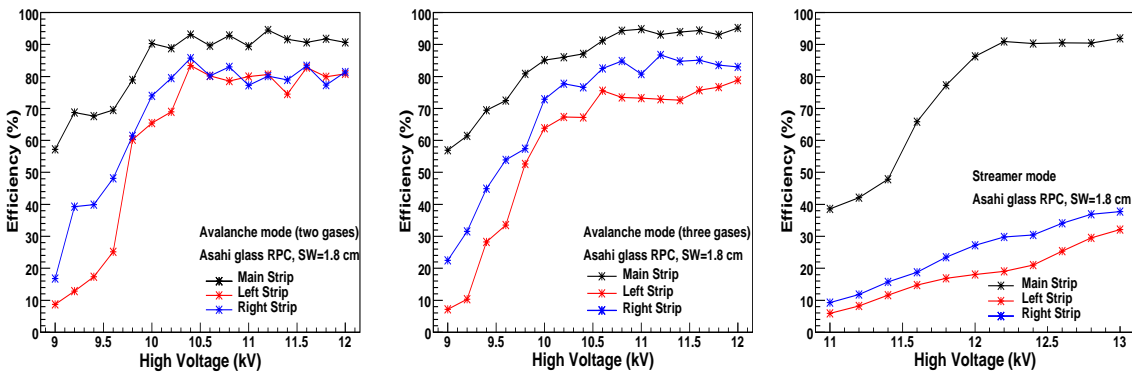


Figure 3.30: Efficiency and cross-talk of Asahi glass RPC with the strip width size = 1.8 cm in avalanche mode (two gases), avalanche mode (three gases) and streamer mode respectively.

Figures 3.33, 3.34 and 3.35 show efficiency and cross-talk of Saint Gobain glass

3.5. Fabrication and Characterisation of glass RPCs

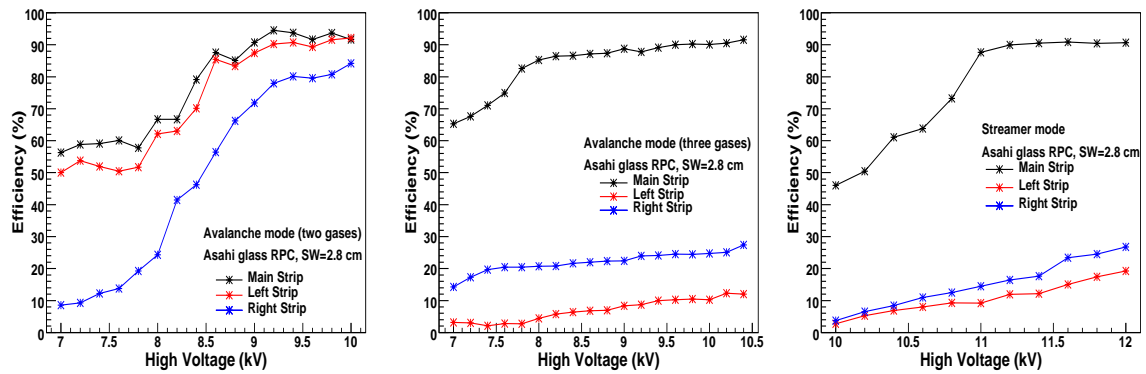


Figure 3.31: Efficiency and cross-talk of Asahi glass RPC with the strip width size = 2.8 cm in avalanche mode (two gases), avalanche mode (three gases) and streamer mode respectively.

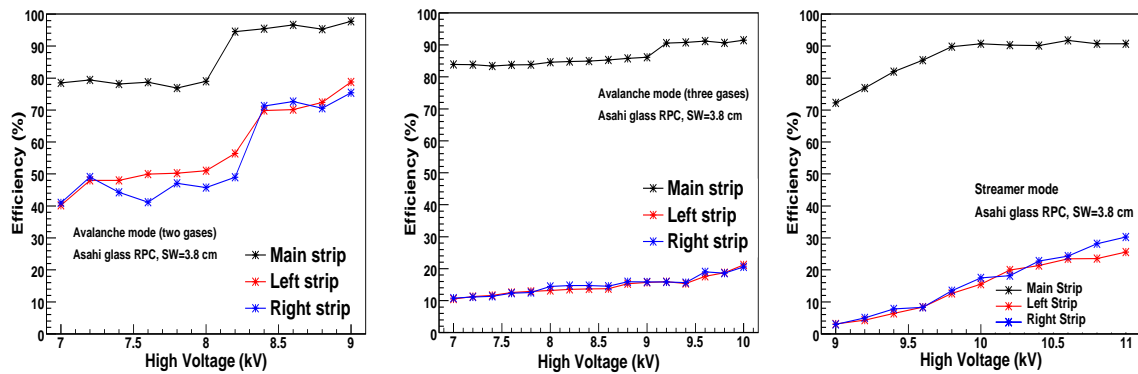


Figure 3.32: Efficiency and cross-talk of Asahi glass RPC with the strip width size = 3.8 cm in avalanche mode (two gases), avalanche mode (three gases) and streamer mode respectively.

RPC in avalanche mode (two gases), avalanche mode (three gases) and streamer mode with the strip width size = 1.8, 2.8, 3.8 cm respectively.

Figures 3.36, 3.37 and 3.38 show efficiency and cross-talk of Modi glass RPC in avalanche mode (two gases), avalanche mode (three gases) and streamer mode with the strip width size = 1.8, 2.8, 3.8 cm respectively.

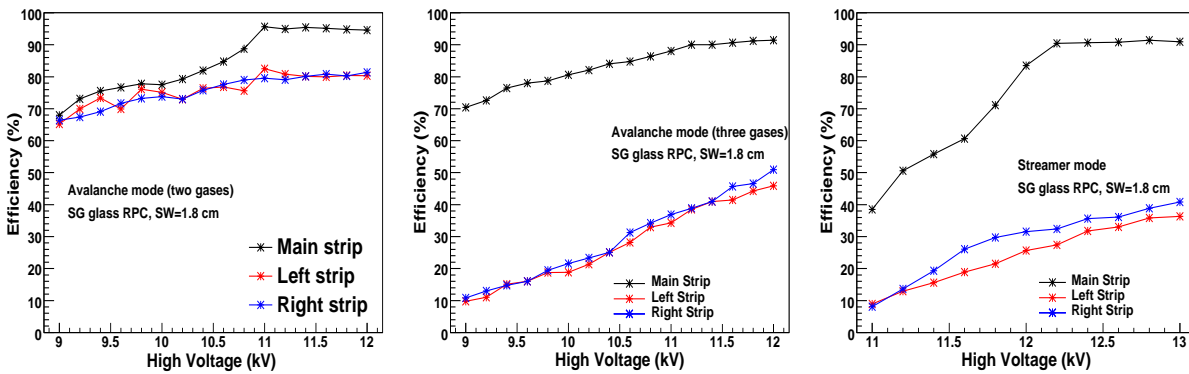


Figure 3.33: Efficiency and cross-talk of Saint Gobain glass RPC with the strip width size = 1.8 cm in avalanche mode (two gases), avalanche mode (three gases) and streamer mode respectively.

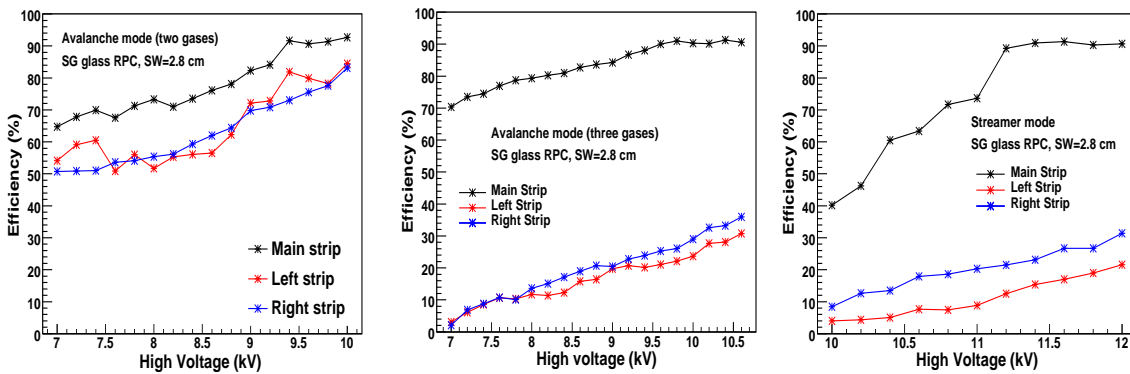


Figure 3.34: Efficiency and cross-talk of Saint Gobain glass RPC with the strip width size = 2.8 cm in avalanche mode (two gases), avalanche mode (three gases) and streamer mode respectively.

3.5. Fabrication and Characterisation of glass RPCs

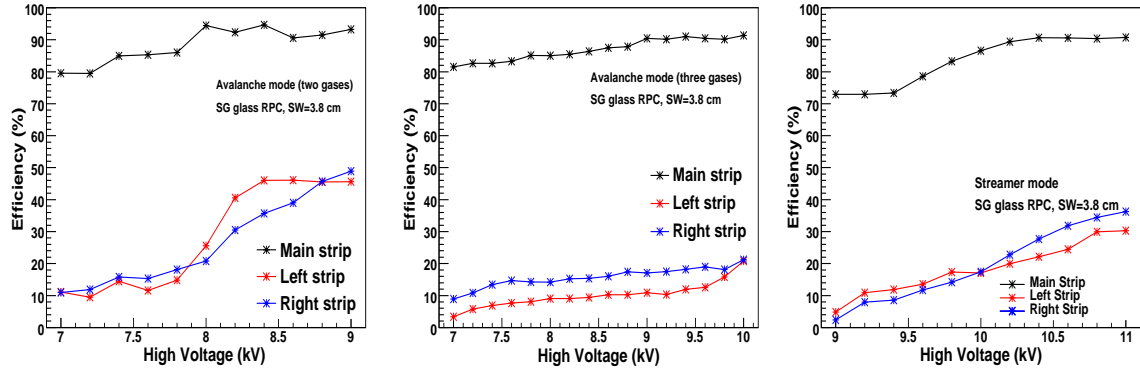


Figure 3.35: Efficiency and cross-talk of Saint Gobain glass RPC with the strip width size = 3.8 cm in avalanche mode (two gases), avalanche mode (three gases) and streamer mode respectively.

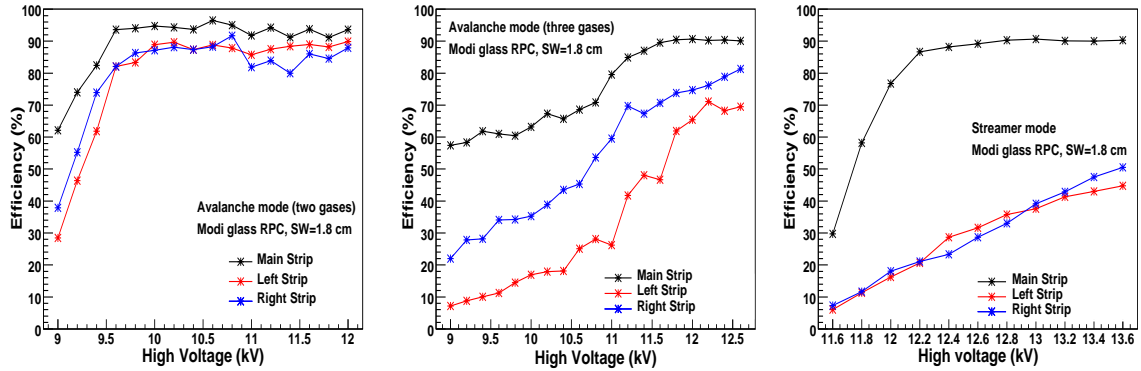


Figure 3.36: Efficiency and cross-talk of Modi glass RPC with the strip width size = 1.8 cm in avalanche mode (two gases), avalanche mode (three gases) and streamer mode respectively.

Tables 3.6 and 3.7 shows efficiency and cross-talk measurements (approximate values) for all RPCs operated in different modes with different strip widths at their operating voltages.

From all the plots and table it is observed that high cross-talk was caused when we used two gases only (avalanche mode). High cross-talk was observed in Modi glass RPC. It may be due to the factors like temperature, humidity and noise rate. Efficiency and cross-talk improves with the addition of SF_6 and argon gas. Shift of threshold voltage was observed with the decrease in the strip width size.

Finally, a comparison plot of three glass RPCs of strip width size = 2.8 cm in

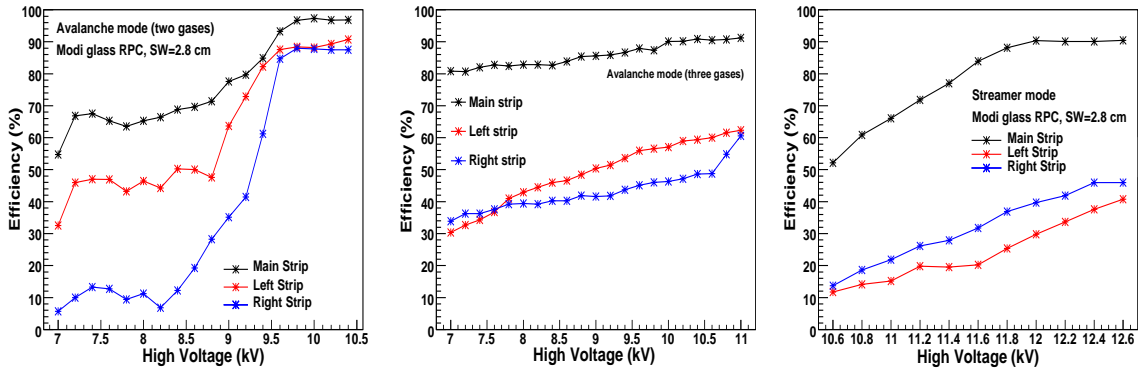


Figure 3.37: Efficiency and cross-talk of Modi glass RPC with the strip width size = 2.8 cm in avalanche mode (two gases), avalanche mode (three gases) and streamer mode respectively.

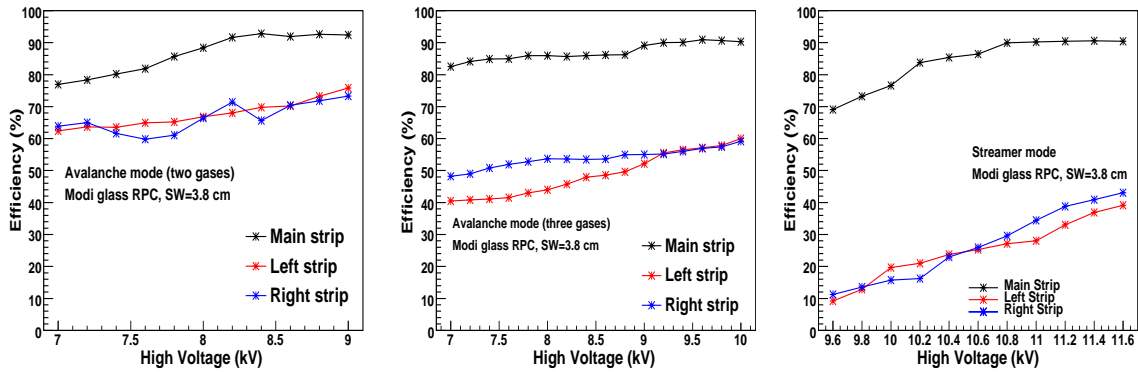


Figure 3.38: Efficiency and cross-talk of Modi glass RPC with the strip width size = 3.8 cm in avalanche mode (two gases), avalanche mode (three gases) and streamer mode respectively.

Modes	Strip width (cm)	Asahi (%)	SG (%)	Modi (%)
Two gases (avalanche)	1.8	90	94	93
Three gases (avalanche)		95	91	90
Streamer		91	90	90
Two gases (avalanche)	2.8	91	92	96
Three gases (avalanche)		91	90	91
Streamer		90	90	90
Two gases (avalanche)	3.8	97	93	92
Three gases (avalanche)		91	91	90
Streamer		90	90	90

Table 3.6: Efficiencies of all the RPCs operated in different modes with different strip widths at their operating voltages.

3.5. Fabrication and Characterisation of glass RPCs

Modes	Strip width (cm)	Asahi (%)	SG (%)	Modi (%)
Two gases (avalanche)	1.8	80	80	89
Three gases (avalanche)		78	45	69
Streamer		32	36	44
Two gases (avalanche)	2.8	84	84	87
Three gases (avalanche)		12	30	60
Streamer		19	21	43
Two gases (avalanche)	3.8	75	45	76
Three gases (avalanche)		20	20	60
Streamer		25	30	39

Table 3.7: Cross-talk measurements (approximate values) for all RPCs operated in different modes with different strip widths at their operating voltages.

avalanche mode (three gases) is shown in Figure 3.39. Asahi and Saint Gobain glass RPCs show best results with strip width size = 2.8 and 3.8 cm with efficiency greater than 90%. Cross-talk for Asahi glass RPC is $\approx 12\%$ and 20% for strip widths 2.8 and 3.8 cm respectively and $\approx 30\%$ and 20% for Saint Gobain glass RPC with strip widths 2.8 and 3.8 cm respectively. We now discuss efficiency and cross-talk of RPC stack.

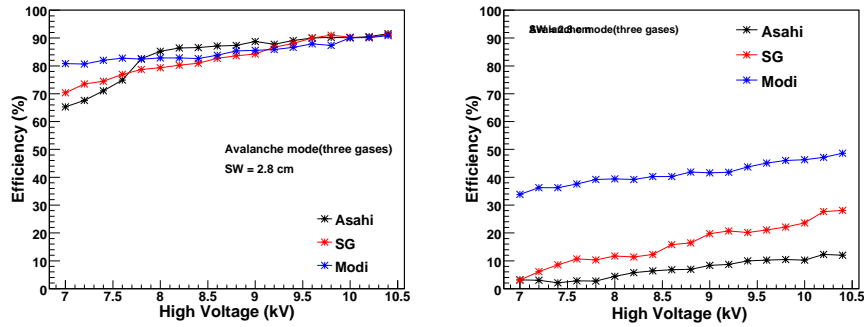


Figure 3.39: Comparison plot of efficiency (left) and cross-talk (right) of Asahi, Saint Gobain and Modi glass RPC with the strip width size = 2.8 cm in avalanche mode (three gases).

3.5.4 Efficiency and Cross-talk of RPC stack

For testing the RPC stack, we fabricated two more Asahi glass RPCs with same procedure as discussed earlier; we named them as RPC_1 and RPC_2 . The third RPC (RPC_3) to form the stack is the same tested Asahi RPC used in subsection 3.5.3. We measured the

surface resistivity of both RPCs to be 600–800 k Ω for Asahi glass RPC_1 and 600–700 k Ω for Asahi glass RPC_2 as shown in Figure 3.40. Figures 3.41, 3.42 show V-I characteristics of Asahi glass RPC_1 and RPC_2 with two gases and three gases in avalanche mode and streamer mode, separating them into two voltage regimes.

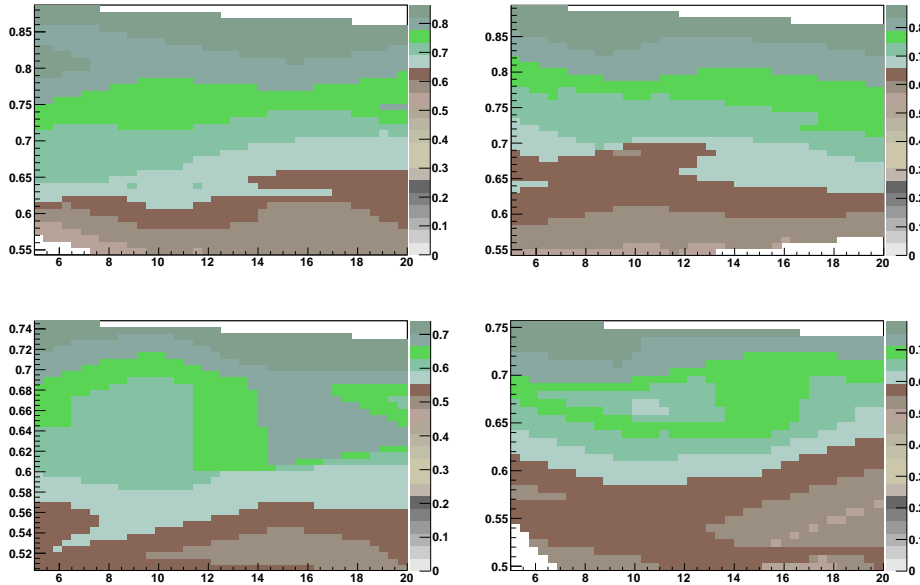


Figure 3.40: Top plot shows surface resistivity measurements of Asahi glass RPC_1 and Bottom plot shows surface resistivity measurements of Asahi glass RPC_2 . Left plots show X side of Asahi glass RPC_1 and RPC_2 and Right plots show Y side of Asahi glass RPC_1 and RPC_2 .

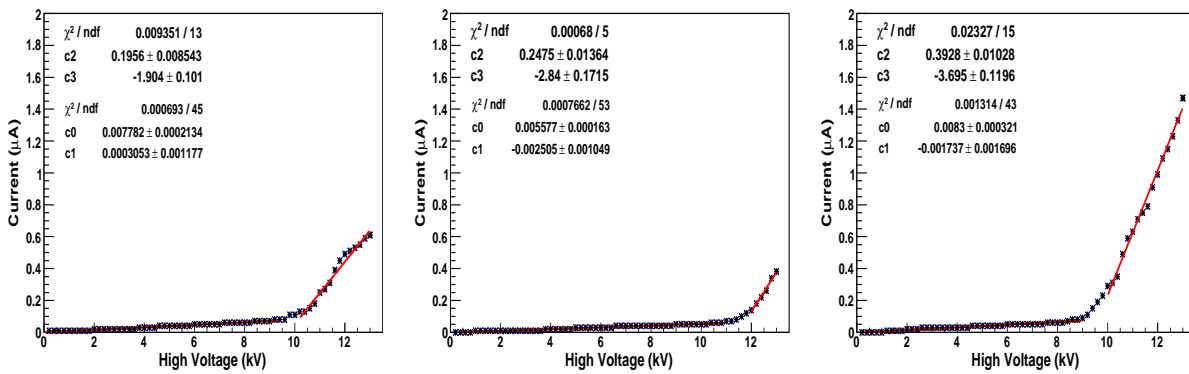


Figure 3.41: V-I characteristics of Asahi glass RPC_1 with two gases and three gases in avalanche mode and streamer mode respectively.

3.5. Fabrication and Characterisation of glass RPCs

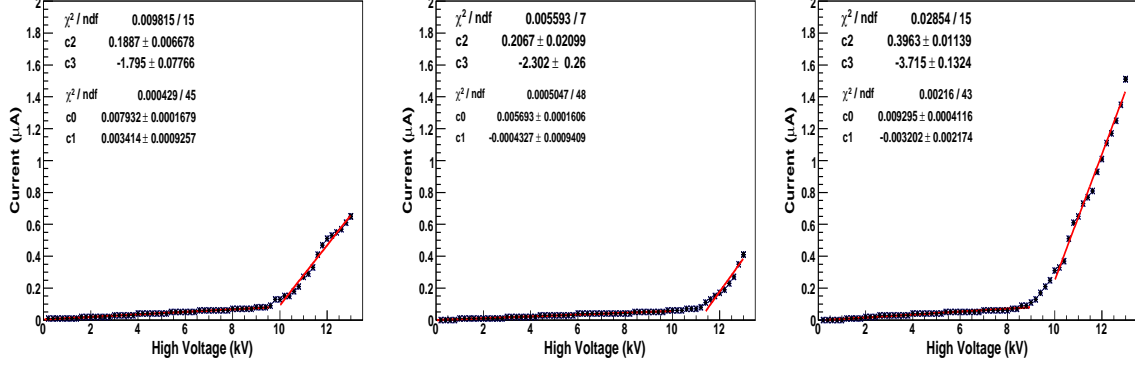


Figure 3.42: V-I characteristics of Asahi glass RPC_2 with two gases and three gases in avalanche mode and streamer mode respectively.

Figure 3.43 shows the trigger scheme circuit diagram for testing the RPC stack. P_1 paddle and RPC_1 with same width $1.8 \text{ cm} \times 30 \text{ cm}$ are connected to the discriminators to make 2-fold coincidence and form a trigger. This 2-fold output along with the different RPC_3 strips (with width $2.8 \text{ cm} \times 30 \text{ cm}$) form a coincidence. RPC_2 (with width $3.8 \text{ cm} \times 30 \text{ cm}$) placed at the bottom and RPC_3 form another coincidence. Input voltage provided to P_1 paddle was -1760 V . The counters, S_1 to S_{11} are connected to count the number of cosmic ray muons passed through the scintillator detectors.

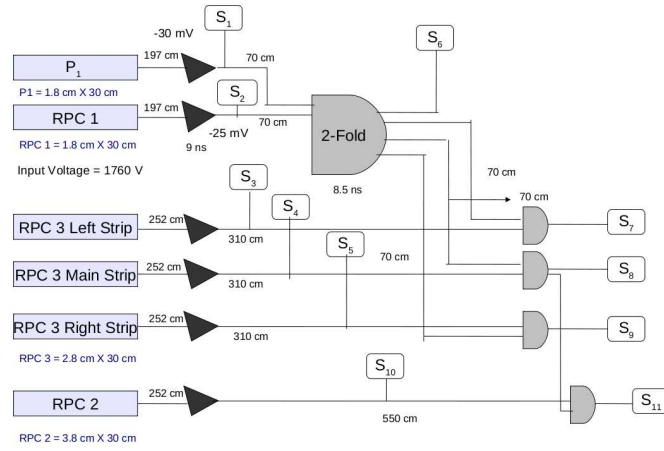


Figure 3.43: Trigger scheme circuit diagram for testing RPC stack.

Figure 3.44 shows efficiency and cross-talk of three Asahi glass RPC stack with the strip width size of 2.8 cm (in the center of stack) in avalanche mode (two gases), avalanche mode (three gases) and streamer mode respectively. Efficiency of the RPC increases with voltage and reach a plateau at higher voltage with efficiency greater than 90%. The cross-talk is higher with two gases (avalanche mode), about 80% and reduces to 10% with the addition of third gas SF_6 (avalanche mode) and argon (streamer mode).

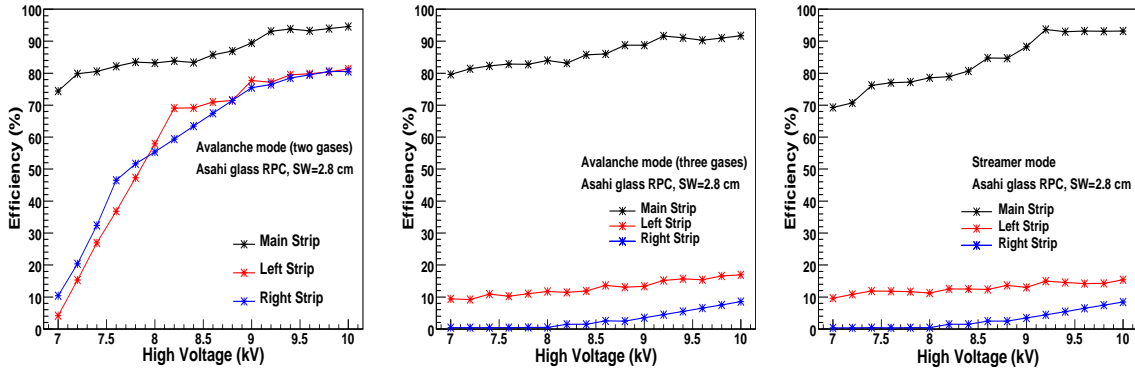


Figure 3.44: Efficiency and cross-talk of three Asahi glass RPC stack with the strip width size = 2.8 cm (in the center of stack) in avalanche mode (two gases), avalanche mode (three gases) and streamer mode respectively.

In this chapter, we presented characterisation of the glass samples and compared them on the basis of their physical properties, optical properties, surface characteristics, elemental composition and electrical properties. It was concluded that Asahi and Saint Gobain were better than Modi glass on the basis of the studied properties. We calibrated four gases used for our analysis. We fabricated scintillator detectors and did their characterisation. We fabricated RPCs and performed their full characterisation. On the basis of that it was concluded that Asahi and Saint Gobain glass RPC with strip width 2.8 and 3.8 cm gave better results than Modi glass RPC (refer to Figure 3.39 and Tables 3.7, 3.6). We obtained results for RPC stack too. After hardware studies, it is necessary to study detector resolution and efficiencies to understand the performance of ICAL detector; this we will discuss in the next chapter.

Chapter 4

Response of ICAL to Muons

The role of muons from the atmospheric neutrinos in the proposed Iron CALorimeter detector is extremely important. The ICAL will specifically concentrate on precision measurements and the sign of the 2-3 mass eigenstate-squared difference Δm_{32}^2 ($= m_3^2 - m_2^2$) and consequently help to determine the neutrino mass hierarchy through earth matter effects [29]. These oscillation parameters are sensitive to the momentum P and the zenith angle $\cos \theta$ (through path length travelled) of neutrinos. Their reconstruction further depends on the energy and direction of muons and hadrons [172] produced in charge-current interactions of the neutrinos in the ICAL detector. So, the studies of energy and direction of muon resolutions are important. The neutrino mass ordering requires the separation of ν s from $\bar{\nu}$ s and hence it is crucial to also determine the sign of the muon charge.

The chapter is organized as follows: in section 4.1 we take a look into the GEANT4-based detector simulations, magnetic field, geometry, and additionally the technique of hit and track generation and track reconstruction. In section 4.2, we describe the general features of muon propagation in the different regions of ICAL. In section 4.3, we describe the choice of the constraints we applied on momentum. In section 4.4 we discuss the results taking into account the selection criteria for the muon efficiencies and resolutions in the peripheral region of ICAL. A comparison of the response in all the

regions of ICAL (central and peripheral) is given in section 4.5 and the summary of this study is presented at the end.

4.1 The ICAL Detector Simulation Framework

The GEANT4 [90] software framework and toolkit is used to simulate [173] ICAL detector geometry. It consist of three modules of same size each having dimensions of $16\text{ m} \times 16\text{ m} \times 14.45\text{ m}$ (height). The x -axis is along the direction in which the modules are placed (and is marked with the azimuthal edge $\phi = 0$ on the co-ordinate system of ICAL). The direction perpendicular to the x -axis in the horizontal plane is the y -direction. From Figure 2.1 of chapter 2, the vertical direction is the z -direction (pointing upwards), hence the polar angle is also the zenith angle. Each module embodies a stack of 150 layers of 5.6 cm thick magnetised iron, isolated by a 4 cm air gap in which the active detector elements, the RPCs, are placed. The y -direction is in the plane of the iron plates and parallel to the slots of the magnet coil, as shown in Figure 2.4. The origin of the co-ordinate system is the centre of the central module.

Coil slots are actually thin 8 m long slots centred around $y = 0$ at $x = x_0 \pm 4$ m, where x_0 is at the centre of each module. Besides the coil slots, there are vertical steel support structures, placed at every 2 m along the whole detector in both x and y directions. They are placed to maintain the air gap between plates and are the dead spaces that affect the muon reconstruction. The non-uniform nature of the magnetic field also affects the quality of reconstruction. So, the location of event affects the reconstruction.

4.1.1 The Magnetic Field

The simulation of magnetic field has been done in a single iron plate using the MAGNET6 software [100]. It is assumed that the magnetic field map generated at the centre ($z = 0$) of the plate is uniform over the full thickness of the plate. The magnetic field lines in a single iron plate in the central module are shown in Figure 2.4 (refer to chapter 2)

with specifications mentioned in the figure. The magnetic field is produced by current passing in copper coils that further pass through the slots. The thin white vertical lines at $x_0 - x = \pm 4$ m in the figure represent the slots, where x_0 is the x-coordinate of the centre of each module. The direction and length of arrows signify the direction and magnitude of the magnetic field.

The “central region” is characterized by the volume contained inside the region $|x - x_0| \leq 4$ m, $|y| \leq 4$ m with z unconstrained, that is, the region inside the coils slots in each module with highest and uniform (in both magnitude and direction (B_y)) magnetic field. The “peripheral region” (outside the central region in the y direction with $|y| > 4$ m) has the most changing magnetic field in both magnitude and direction, with the field value going to zero at the corners of the module. Apart from the changing magnetic field, the peripheral region suffers from edge effects, since particles produced in interactions here can exit the detector from the sides.

Also, there are two small regions in the x direction, outside the coil slots ($|x_0 - x| > 4$ m), labelled as the “side region” in Figure 2.4. Here, the magnetic field is about 15% smaller than in the central region and in the direction opposite to it. The side regions in the central module are contiguous with the side regions in the adjacent modules, so the quality of reconstruction is expected to be similar to that in the central region. But the left (right) side region of the left (right)-most module will suffer from edge effects and we shall consider them separately in the study.

4.1.2 Event Reconstruction

10,000 muons are generated for each analysis using inbuilt gun inside the INO-ICAL geant code (details of detector simulation framework are given in Appendix A). These muons are propagated in the detector with fixed momenta and direction and taking their starting point in any of the regions of the detector. The muon momenta range is taken from 1–50 GeV/c, because the higher energies are of interest for upward-going muon studies. The

tracks of muons are reconstructed using a Kalman filter [174] algorithm as part of the INO-ICAL geant code. The RPCs have a position resolution of about ± 1 cm in the x - and y -directions (the RPC strip width taken as 1.96 cm) and about ± 1 mm in the z -direction (the gas gap in the RPCs taken as 2 mm). In addition, “hits” can be generated in adjoining RPC strips as well. The RPC efficiency and time resolution are about 95% and 1 ns respectively [160] which are incorporated in INO-ICAL geant code for generating muons. More details on the generation of hits, tracks and their reconstruction is given in Appendix B. A detailed study of the muon reconstruction characteristics was first carried out in the central region of ICAL [173]. Given the uniform nature of the magnetic field in this region, it was the simplest to analyse. It was found that the sensitivity to reconstruct both momentum and direction, as well as sign of the charge of the muon was good, in the few GeV region. Here we focus our attention on reconstruction of events in the peripheral and side regions of ICAL. These are particularly relevant for the “upward-going muon” studies that will be taken up in the next chapter. They are also useful to understand the cosmic ray muon background that has been studied elsewhere [175]. The combination of changing magnetic field and edge effects make reconstruction in this region non-trivial compared to that in the central region. Before we begin the detailed study, we make a few remarks about the muon response in such a ϕ -asymmetric geometry.

4.2 General Feature of Muon Response in the Peripheral and Side Regions

We describe the different cases to have a better understanding of the effects of detector geometry and orientation of the magnetic field on muons.

The Lorentz force equation is given by: $\vec{F} = q(\vec{v} \times \vec{B})$. Here, \vec{B} is the magnetic field confined to the x - y plane, q is the charge of the particle having momentum \vec{P} and energy E so that its velocity \vec{v} is directed along the momentum with magnitude $v = Pc^2/E$. Since $q = -1$ for μ^- , the components of force in the peripheral region for an

4.2. General Feature of Muon Response in the Peripheral and Side Regions

upward-going muon, momentarily ignoring energy loss, are given by,

$$\begin{aligned}
 F_x &= v_z B_y ; \\
 F_y &= -v_z B_x ; \\
 F_z &= v_y B_x - v_x B_y ,
 \end{aligned}
 \tag{4.1}$$

whereas the analogous components of force in the side region are given as:

$$\begin{aligned}
 F_x &= -v_z B_y ; \\
 F_y &= 0 ; \\
 F_z &= v_x B_y .
 \end{aligned}
 \tag{4.2}$$

Both F_x and F_y are independent of ϕ (azimuthal angle) in both regions (that is, independent of the momentum components in the plane of the field) but depend upon P_z (i.e., on the zenith angle θ alone), whereas F_z depends upon both θ and ϕ . Depending on the two components of magnetic field B_x and B_y , Equations 4.1 and 4.2 produce the net force in the different regions of ICAL. Consider the in-plane (x, y components) forces in the regions labelled as 1–10 in Figure 4.2. It is noticed that in regions 1, 2, 7, 8, F_y causes an upward-going muon ($\cos \theta > 0$) to bend in a direction exiting the detector, thus the reconstruction efficiency will be lowered and this effect is just the opposite in regions 3, 4, 5, 6. If $F_z > 0$, then upward-going muon traverses more iron layers giving good resolution, as discussed below:

When a muon is directed along the y -axis, it experiences less bending as the momentum component in the plane of the iron plates is parallel to the magnetic field. Also, those upward-going muons which are in the positive (negative) x direction experience a force in the negative (positive) z direction (the opposite is true for μ^+). Hence, muons directed with $|\phi| > \pi/2$ traverse more layers than those with the same energy and zenith

angle but with $|\phi| < \pi/2$ and so they are better reconstructed. This is shown in the schematic in Figure 4.1 which illustrates that two muons (μ^-) directed at the origin with the same momentum magnitude and zenith angle, but one with negative momentum component in the x direction, $P_x < 0$ and the other with positive x momentum component. The muon with $P_x > 0$ bends differently than the one with $P_x < 0$ so they traverse different number of layers, but having the same path length. Hence, muons with different ϕ have different detector response.

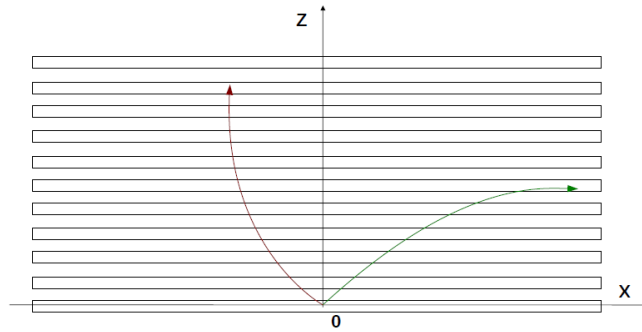


Figure 4.1: Muon tracks (μ^-) in the x-z plane with same values of $(P_{in}, \cos \theta)$ but for $|\phi| < \pi/2$ and $> \pi/2$.

Hence, F_y affects the reconstruction efficiency while F_z determines the quality of reconstruction. As F_z depends on both (θ, ϕ) and magnetic field, the sign of F_z is shown in Figure 4.2, inside a circle of ϕ in each of regions 1, 2, 3, 4 (for negatively charged upward-going muons), for $|B_x| \sim |B_y|$ with purple (cyan) regions as denoted by $F_z > (<)0$ ($F_z > or < 0$).

So, the magnetic field that depicts the quality of reconstruction breaks the azimuthal symmetry, hence muons in different ϕ directions (for the same momenta and polar angle $\cos \theta$) have different detector response [173] (as discussed above). It is therefore convenient to analyse the muon response in the peripheral region in four different set of ϕ bins as shown in the left schematic of Figure 4.3: bin I: $|\phi| \leq \pi/4$, bin II: $\pi/4 \leq \phi < 3\pi/4$, bin III: $-3\pi/4 \leq \phi < -\pi/4$, and bin IV: $3\pi/4 < |\phi| \leq \pi$.

Muons propagating in the negative y peripheral region (regions marked 1, 2, 3, 4

4.2. General Feature of Muon Response in the Peripheral and Side Regions

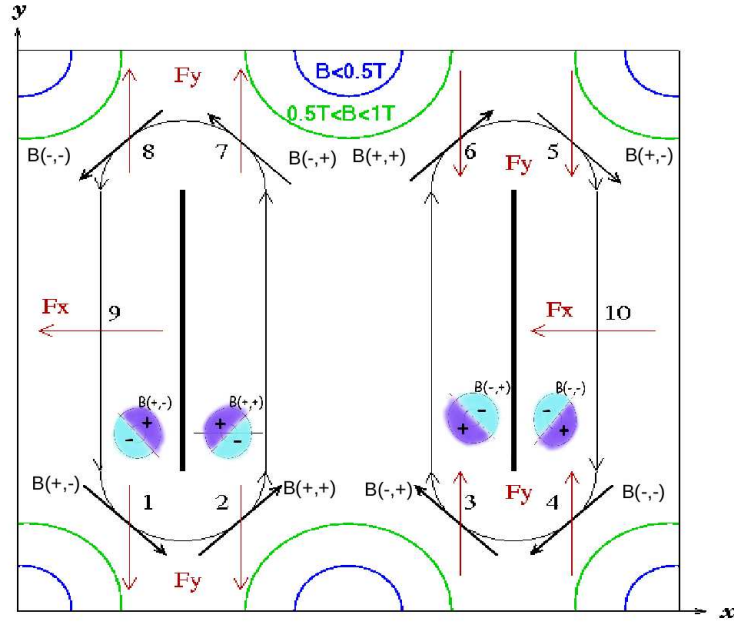


Figure 4.2: Magnetic field map with the net force directions in the peripheral and side region. The thick black arrows indicate the direction of the magnetic field with labels $B(i, j)$, $i = +, -$, that denote the sign of the B_x, B_y components in each region. The small coloured circles indicate the direction of F_z in each region, with purple (cyan) denoting $F_z > 0 (< 0)$. The brown arrows indicate the direction of F_x or F_y force components that will act on a negatively charged upward-going muon. (Note that side regions 9 and 10 are in the 1st and 3rd modules of the detector respectively and are shown together in the same module for convenience.) [176]

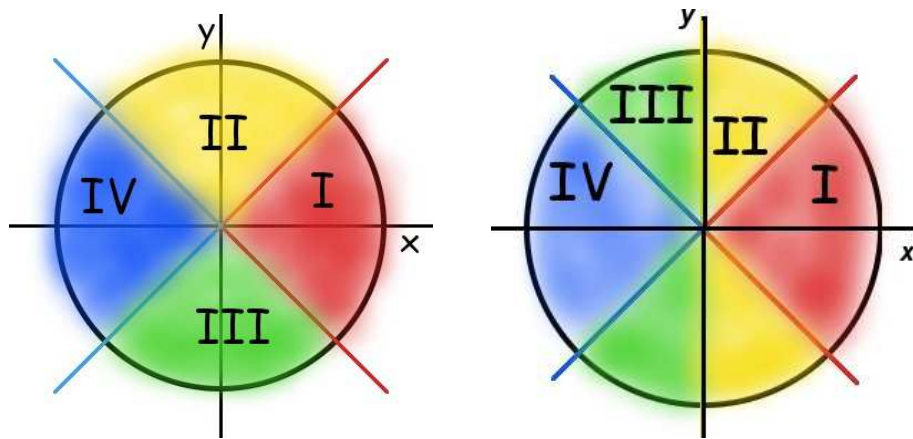


Figure 4.3: The choice of ϕ bins in the peripheral (left) and side (right) regions.

in Figure 4.2) with the ϕ in bin III, but otherwise having same momentum magnitude and $\cos \theta$ are prone to exit the detector from the side. But, the quality of reconstruction

between regions (1, 2) and (3, 4) is different, due to the different F_y force that bends the track back into the detector in regions 3, 4. Hence the average detector response in this region is an average over these two different behaviours. Furthermore, $F_z > 0$ (< 0) for muons with bin II in regions 1, 2 (3, 4) helps to improve the reconstruction in regions 1, 2. So, bin II muons can be expected to have the best quality of reconstruction of the regions 1–4. A similar analysis can be done for muons propagating in the positive y peripheral region (regions marked 5, 6, 7, 8). Obviously, those tracks which are at the edge of a region or of higher energy muons may move from one region to another depending further on the magnetic field. However, we simply bin the events depending on the original co-ordinates of the muon.

In the side region 9, F_x causes the particle to exit the detector, since $F_z > 0$ so this region has good resolution but worse efficiency. For side region 10, the results are just opposite, as $B_y < 0$. Hence, we define the ϕ bins for the side region as, bin I: $|\phi| \leq \pi/4$, bin II: $\pi/4 < |\phi| \leq \pi/2$, bin III: $\pi/2 < |\phi| \leq 3\pi/4$, and bin IV: $3\pi/4 < |\phi| \leq \pi$. These are the same as were used in the analysis for the central region. The difference in side and peripheral region lies in the definition of the second and third bins, as shown in Figure 4.3, and is more appropriate from the point of view of the geometrical configuration in these regions. Side region 9 (10) will have the worst reconstruction in ϕ bin IV (I). But, the direction of the F_x force is expected to improve the results in side region 10, as in the case of regions 3, 4.

The results will be the same for downward-coming μ^+ (with $\cos \theta < 0$), whereas the results for downward-coming muons or upward-going anti-muons can be determined by symmetry. Therefore, we study the muon response in the peripheral regions 1–4 and the side region 9 and 10 for our analysis.

It is to be noted that the coil gaps and support structures also break this azimuthal symmetry in a non-trivial way and the effects of the geometry may further alter the trends of the distributions as discussed above. Their effect can be seen in the next

4.2. General Feature of Muon Response in the Peripheral and Side Regions

section in the muon resolutions and efficiencies.

Fixed Vertex Analysis: Initially, 10,000 events were generated at fixed origin in order to understand the effect of the magnetic field. The starting point in the peripheral region was chosen to be either at point A (in a region of nearly zero magnetic field) or B (large magnetic field with both x - and y -components non-zero). For the side region, a generic point C was studied (refer to Figure 2.4). This analysis showed that a large fraction of events with their truncated tracks were due to the particle exiting the detector (so-called partially contained events) and were relatively poorly reconstructed whenever the portion of track in the detector was too small. They could not be removed by tighter constraints on χ^2 of the fits; but they could be removed by applying a condition of a minimum number of hits, such that either $N_{hits} > n_0$ or $N_{hits}/\cos\theta > n_0$ (note that there may be multiple hits per layer), where n_0 is the minimum no. of hits which needs to be carefully optimised. Clearly, for a given momentum and direction of the muon, n_0 needed to be larger in regions where the magnetic field strength is small and vice-versa. Those muons that do not exit the detector have tracks contained in the detector (fully contained events); for them no constraint on N_{hits} was needed. With this understanding, the generic peripheral and side region response was studied.

Peripheral Region: In this region, 10,000 muons (μ^-) were propagated with fixed input momenta P_{in} and direction $\cos\theta$ (and smeared over the entire azimuthal angle ϕ i.e., $-\pi \leq \phi \leq \pi$) (refer to Appendix C for smearing details). Their starting point is uniformly smeared over the region centred at $(0, -600, 0)$ cm and extending upto $\pm (2400, 200, 720)$ cm from it. This consists of the whole peripheral region along the three modules of the detector in the *negative y region* and the magnetic field is non-uniform here.

Side Region: Same procedure was applied in the side region but the origin smeared in a region centred around $(-2200, 0, 0)$ cm and $(2200, 0, 0)$ cm (which are in the 1st and 3rd modules of the detector respectively) and smeared uniformly in \pm

(200, 400, 720) cm around these.

4.3 Selection Criteria Used

Due to the factors that were responsible for poor reconstruction, we applied a selection criteria in order to get the good reconstructed events and hence good resolutions and efficiencies. We used those tracks which satisfy the loose selection criterion $\chi^2/\text{ndf} \leq 10$, where χ^2 is the standard χ -squared of the fit and ndf are the number of degrees of freedom, $\text{ndf} = 2 \times N_{\text{hits}} - 5$, where N_{hits} are the number of hits in the event, $N_{\text{hits}} \geq 5$ and the Kalman filter involves the fitting of 5 parameters (refer to Appendix B for more details). The χ^2/ndf cut removes the random events at higher energies which are very few in number and not visible in the plots (discussed in next subsections). The Figure 4.4 demonstrates reconstructed momenta P_{rec} with $\chi^2/\text{ndf} \leq 2$ (10). As it can be seen that there is no visible difference in the plots for the two different values, but $\chi^2/\text{ndf} \leq 2$ eliminated lots of desirable events, so $\chi^2/\text{ndf} \leq 10$ is sufficient.

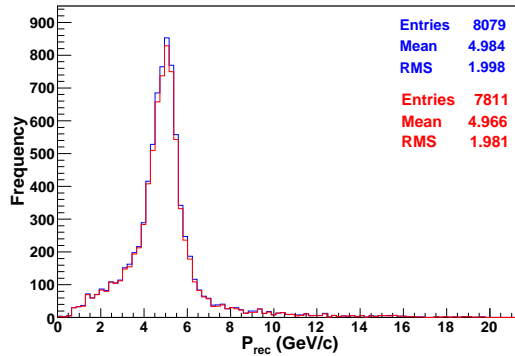


Figure 4.4: The reconstructed momenta P_{rec} with χ^2/ndf cut. The red (blue) curve represents $\chi^2/\text{ndf} \leq 2$ (10).

In order to get reasonable fits and hence resolutions, a fine selection criteria was used. Mainly, two constraints were applied in both regions to eliminate low energy tails (discussed in the next subsection). The first one is the generation of more than one track due to Kalman filter algorithm [173]. This is a problem for single muon analysis and

emerges due to detector's dead space (for instance, two portions of a track on either side of a support structure may be reconstructed as two different tracks). The identification of a vertex in a genuine neutrino interaction can sort this problem. So, here we use a constraint and analyse only those events for which only one track is reconstructed, leading to the worsening in reconstruction efficiency. The second selection criterion is particularly relevant for the peripheral and side regions and is previously discussed (in the fixed vertex analysis).

4.3.1 Effect of Selection Criteria

The impact of $N_{hits} > n_0$ or $N_{hits}/\cos\theta > n_0$ can be noticed from Figure 4.5 for the peripheral region, where the histogram in the magnitude of the reconstructed momentum P_{rec} is plotted. For fully contained events, there is no constraint on N_{hits} ; the effect of $n_0 = 15(20)$ is shown in the left-hand (right-hand) side of Figure 4.5 for $(P_{in}, \cos\theta) = (5 \text{ GeV}/c, 0.65)$ and $(9 \text{ GeV}/c, 0.85)$. It can be seen that for $P_{in} = 5 \text{ GeV}/c$, the N_{hits} constraint does not affect the P_{rec} momentum distribution much, as most of the events are fully contained. So, it reduces the low-energy tail thus giving a better (more symmetrical) shape to the distribution. On the other hand, for $P_{in} = 9 \text{ GeV}/c$ the effect is stronger, with the hump as shown in bottom plots of Figure 4.5 at lower P_{rec} being removed with the N_{hits} selection criteria. Figure 4.6 shows the effect of $N_{hits} > n_0$ or $N_{hits}/\cos\theta > n_0$ on N_{hits} distributions in the peripheral region. In all cases, those events that survive below the constraint are from totally contained events, on which no constraint is placed. This causes the histograms to remain non-zero in the region $N_{hits} \leq n_0$ or $N_{hits}/\cos\theta \leq n_0$ as seen in Figure 4.6. However, these events are relatively few in number, being less than 2% (3%) of the total reconstructed events for $n_0 = 15$ (20) in Figure 4.6. The constraint $N_{hits}/\cos\theta > 15$ is the most conservative one, with a loss of only about 10% of the reconstructed events and is found to be better than only $N_{hits} > n_0$ requirement.

Different choices of n_0 can be used and the effect of (a) no constraint, (b) $N_{hits} >$

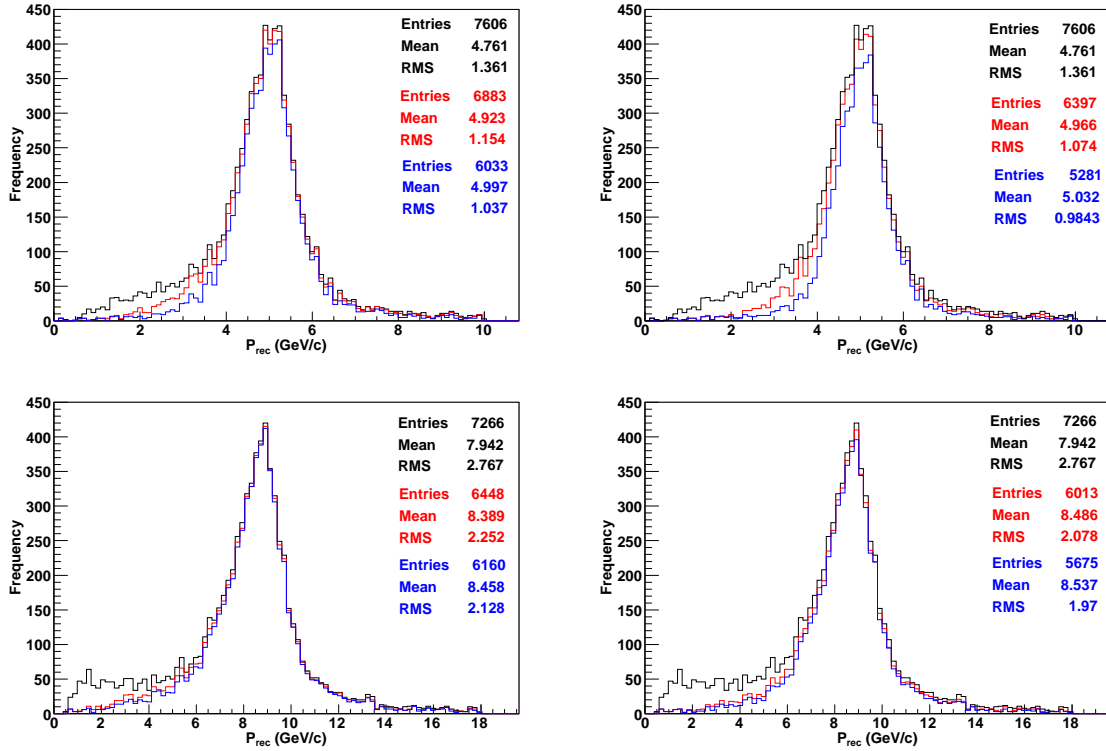


Figure 4.5: Top (bottom) figures show the reconstructed momenta P_{rec} using selection criteria $N_{hits} > n_0$ for partially contained events in the peripheral region with $(P_{in}, \cos\theta) = (5 \text{ GeV}/c, 0.65)$ (top) and $(9 \text{ GeV}/c, 0.85)$ (bottom) with $n_0 = 15$ (20) in the left (right) figure. Fully contained events have no N_{hits} constraint. In each figure, the black curve is without constraints on N_{hits} , red is with $N_{hits}/\cos\theta > n_0$ and blue is for $N_{hits} > n_0$.

15, and (c) $N_{hits}/\cos\theta > 15$ can be seen in the left-hand side of Figure 4.5. The last choice is considered taking into account that a slant-moving muon (in the absence of magnetic field), travels a distance $d/\cos\theta$ in comparison to a vertically upward-going muon of the same momentum that would traverse a distance d . Similar figures on the right use the choice $n_0 = 20$, and is more stringent, causing distributions with correspondingly smaller root-mean-square or square root of the variance (RMS widths) of about 7–8%, but a decrease in the total number of reconstructed events by 10–15%. It was observed that increasing n_0 leads to further removal of well-reconstructed events, visible from the loss of events in the peak apart from just removing the low-energy tails for the lower momentum $P_{in} = 5 \text{ GeV}/c$ for $n_0 = 20$.

The effect of the selection criteria on the reconstruction in the side regions is

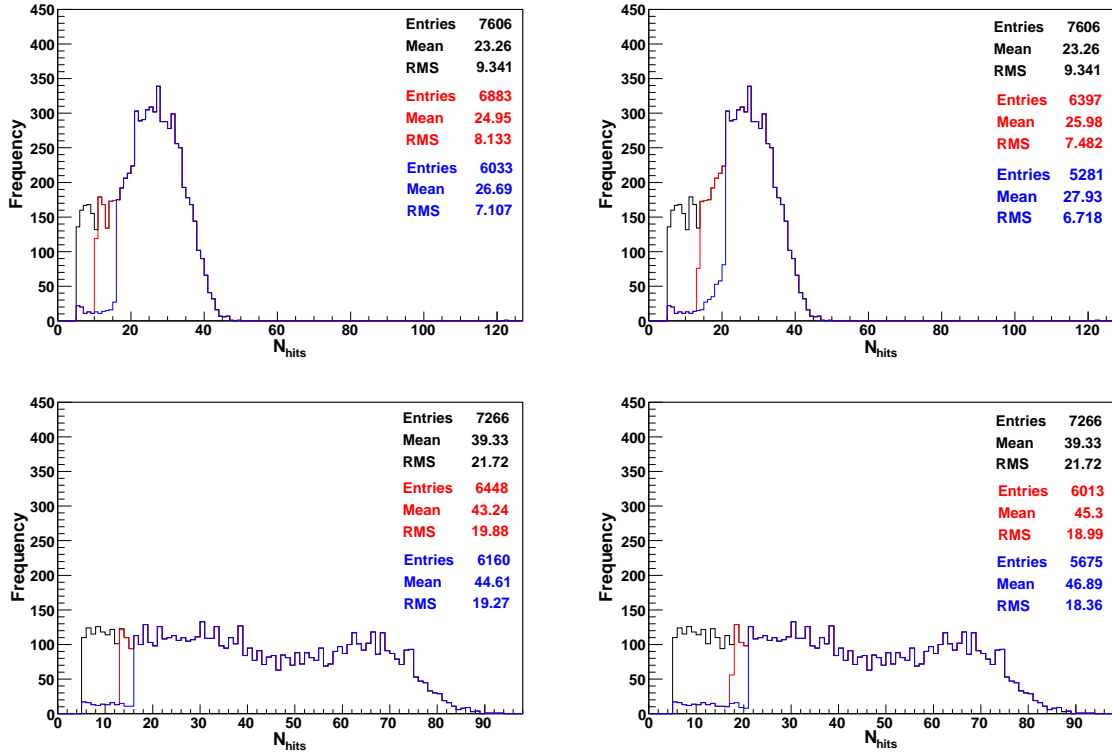


Figure 4.6: Top (bottom) figures show the N_{hits} distributions using selection criteria $N_{hits} > n_0$ for partially contained events in the peripheral region with $(P_{in}, \cos\theta) = (5 \text{ GeV}/c, 0.65)$ (top) and $(9 \text{ GeV}/c, 0.85)$ (bottom) with $n_0 = 15$ (20) in the left (right) figure. Fully contained events have no N_{hits} constraint. In each figure, the black curve is without constraints on N_{hits} , red is with $N_{hits}/\cos\theta > n_0$ and blue is for $N_{hits} > n_0$.

shown in Figure 4.7. The effect on the partially contained events is not as dramatic as in the peripheral region. With the application of N_{hits} selection criteria, there is certainly a decrease in the RMS width of the distribution and in the number of selected events, a larger fraction of events are lost with a number of “good” events being lost from the peak of the distribution as well, unlike in the peripheral region.

The final selection criteria to be used will be guided by the physics study. If the requirement is of good momentum resolution, then $n_0 = 20$ may be appropriate (that is, either $N_{hits} > 20$ or $N_{hits}/\cos\theta > 20$). In the case of $n_0 = 15$, the shape of the distribution is already reasonable so this choice may be used for higher event reconstruction rates instead of precision reconstruction. We used $N_{hits}/\cos\theta > 15$ for our entire analysis as being appropriate and sufficient. It also improves the reconstruction efficiency of large

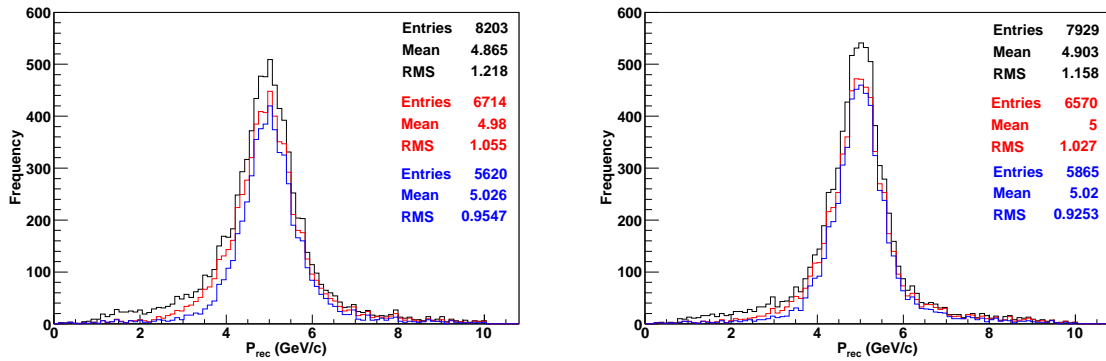


Figure 4.7: The figures show the reconstructed momenta P_{rec} using the selection criteria $N_{\text{hits}} > n_0$ for partially contained events in the side regions 9 (left) and 10 (right) for $(P_{\text{in}}, \cos \theta) = (5 \text{ GeV}/c, 0.65)$ with $n_0 = 15$. Fully contained events have no N_{hits} constraint. In each figure, the black curve is without constraints on N_{hits} , red is with $N_{\text{hits}}/\cos \theta > n_0$ and blue is for $N_{\text{hits}} > n_0$.

angle (small $\cos \theta$) events whose tracks contain fewer hits.

In the next section, we present the results on muon resolution and efficiencies in the peripheral and side regions using these selection criteria described here.

4.4 Muon Response in the Peripheral and Side Regions

4.4.1 Reconstruction Efficiency

The reconstruction efficiency is the ratio of the number of reconstructed events n_{rec} (irrespective of charge) to the total number of events, N_{total} and is given by,

$$\epsilon_{\text{rec}} = \frac{n_{\text{rec}}}{N_{\text{total}}}, \quad (4.3)$$

with error $\delta\epsilon_{\text{rec}} = \sqrt{\epsilon_{\text{rec}}(1 - \epsilon_{\text{rec}})/N_{\text{total}}}$.

Figure 4.8 shows the reconstruction efficiency averaged over ϕ as a function of input momentum for different $\cos \theta$ values in the peripheral and side regions.

4.4. Muon Response in the Peripheral and Side Regions

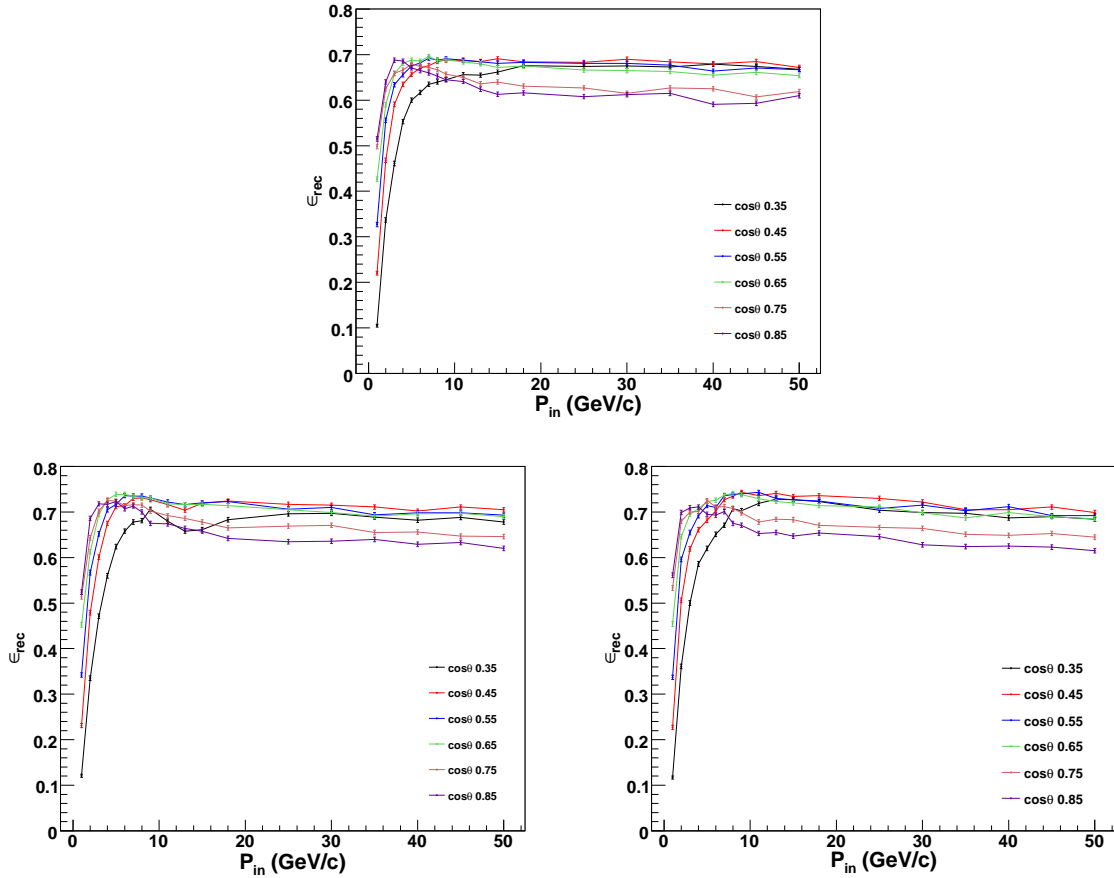


Figure 4.8: Reconstruction efficiency averaged over all ϕ bins as a function of the input momentum P_{in} (GeV/c) for different zenith angles $\cos\theta$ in the peripheral (above), side 9 (below-left) and side 10 (below-right) regions.

The reconstruction efficiency increases for all angles ($\cos\theta$), starting from $P_{\text{in}} = 1$ GeV/c since there is increase in number of hits as the particle crosses more layers. For more slant-angled muons there are just fewer hits, so the efficiency at a given momentum is better for larger values of $\cos\theta$. Also, the reconstruction efficiency of peripheral, side 9 and side 10 region as shown in Figure 4.8 is very similar.

The worsening of the efficiency for $\cos\theta = 0.85$ at higher momenta is spurious and is because of the selection criterion of the reconstruction of exactly one track. At small angles (or large $\cos\theta$), the two portions of a track on either side of a dead space such as a support structure are reconstructed as two separate tracks and are rejected in the present analysis. This problem is solved in the new INO-ICAL code in terms of improved

reconstruction [91]. If these tracks are correctly reconstructed, the efficiency is expected to saturate instead of falling off at these momentum values. Such tracks are not expected to be troublesome in genuine neutrino events, as discussed earlier in section 4.3.

4.4.2 Relative Charge Identification Efficiency

The charge identification (cid) of the particle is important in many studies since it distinguishes muons and anti-muons thus differentiating neutrinos and anti-neutrinos. These particles have different matter effects when they propagate through the Earth and provide sensitivity to the neutrino mass hierarchy. The direction of curvature of the track determines the charge of the particle in the magnetic field. Relative charge identification efficiency is defined as the ratio of the number of events with correct charge identification, n_{cid} , to the total number of reconstructed events, n_{rec} , i.e.,

$$\epsilon_{\text{cid}} = \frac{n_{\text{cid}}}{n_{\text{rec}}}, \quad (4.4)$$

where the errors in n_{cid} and n_{rec} are correlated, so the error in the ratio is calculated as:

$$\delta\epsilon_{\text{cid}} = \sqrt{\epsilon_{\text{cid}}(1 - \epsilon_{\text{cid}})/n_{\text{rec}}}.$$

Figure 4.9 demonstrates the relative charge identification efficiency as a function of input momentum for different $\cos\theta$ values in the peripheral, side region 9 and side region 10. For small momentum, the muon undergoes multiple scattering while propagating in the detector, since the number of layers traversed is small, this may lead to an incorrect reconstructed direction of bending, causing wrong charge identification. Hence the charge identification efficiency is relatively poor at lower energies but improves as the energy increases. The bending due to magnetic field is less at very high input momenta. For partially contained events, only the initial relatively straight portion of the track is contained within the detector; this leads to large momentum uncertainty as well as mis-

4.4. Muon Response in the Peripheral and Side Regions

identification of charge. Overall the relative charge identification efficiency is marginally smaller than in the central region because of the smaller magnetic field.

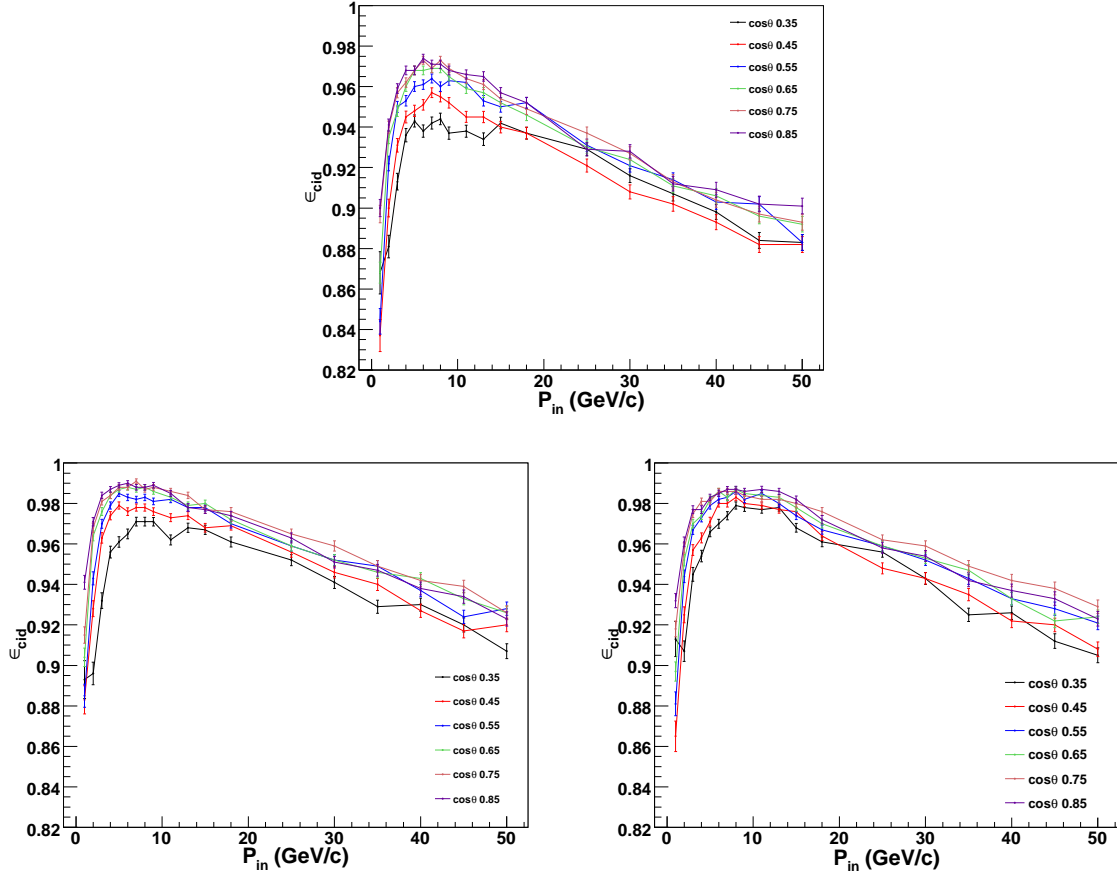


Figure 4.9: Charge identification (cid) efficiency averaged over all ϕ bins as a function of the input momentum P_{in} (GeV/c) for different zenith angles $\cos\theta$ in the peripheral (above), side 9 (below-left) and side 10 (below-right) regions respectively.

4.4.3 Direction (up/down) Reconstruction

The reconstructed zenith angle distributions for $P_{in} = 1$ GeV/c at $\cos\theta = 0.35$ and $\cos\theta = 0.85$ in the peripheral, side region 9 and side region 10 are shown in Figs. 4.10, 4.11 and 4.12 respectively.

From Figure 4.10, it can be seen that there are few events reconstructed in the downward direction (wrong direction) with $\theta_{rec} > \pi/2$. For $P_{in} = 1$ GeV/c with $\cos\theta = 0.35$ (0.85), this fraction is about 0.48 (0.89)% and it drops to a negligible value at higher

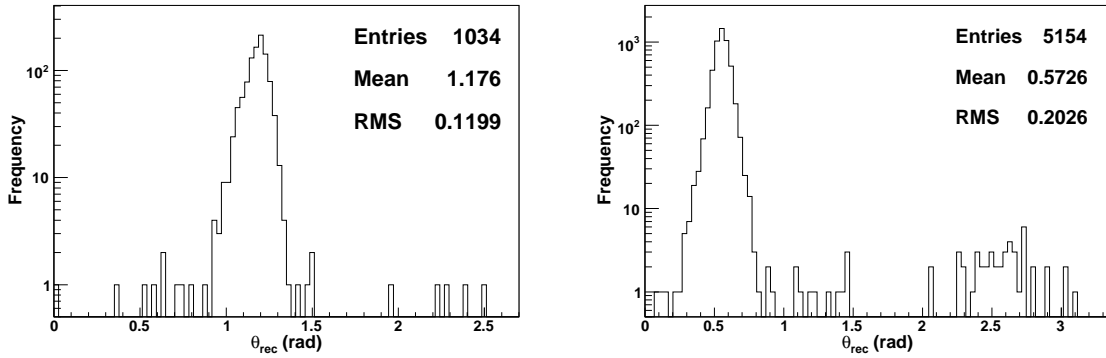


Figure 4.10: Reconstructed zenith angle distributions for $P_{in} = 1$ GeV/c at $\cos \theta = 0.35$ (left) and 0.85 (right) respectively, in the peripheral region. Note that the y-axis scales are different for the two plots.

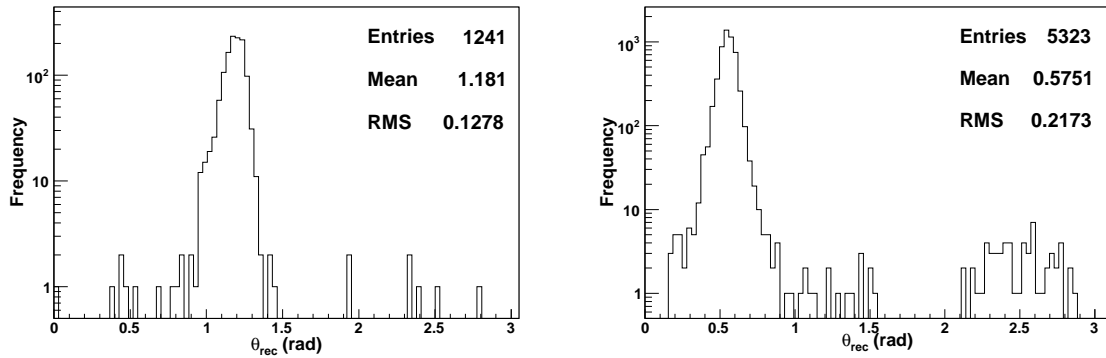


Figure 4.11: Reconstructed zenith angle distributions for $P_{in} = 1$ GeV/c at $\cos \theta = 0.35$ (left) and 0.85 (right) respectively, in the side region 9. Note that the y-axis scales are different for the two plots.

energies for all $\cos \theta$. Similar results are obtained for the side region 9 and side region 10 as can be seen from Figure 4.11 and 4.12. This small fraction also contributes to wrong cid since the relative bending in the magnetic field is measured with respect to the muon momentum direction.

The direction determination depends on the time resolution while the charge identification depends also on the strength of the magnetic field. A 1 GeV/c muon with $\cos \theta \sim 1$ traverses about 12 layers; this corresponds to a time difference between first and last hit of about 4 ns. Since the RPCs have a time resolution of 1 ns, this explains why the fraction of muons whose direction is wrongly determined is small.

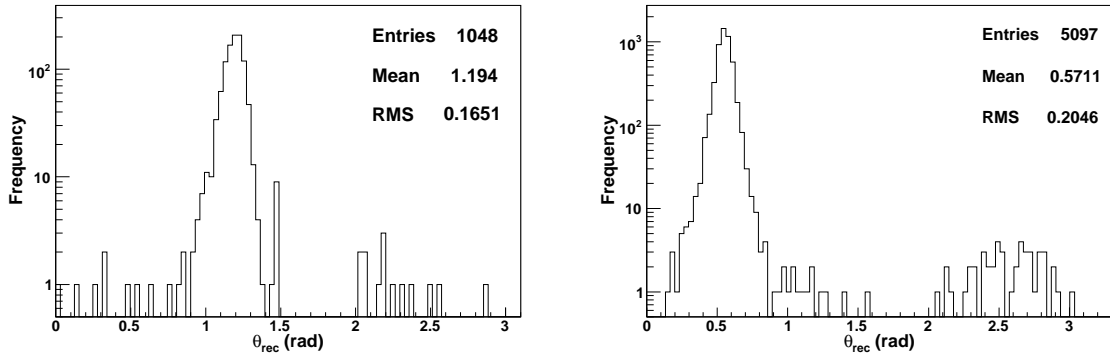


Figure 4.12: Reconstructed zenith angle distributions for $P_{in} = 1$ GeV/c at $\cos \theta = 0.35$ (left) and 0.85 (right) respectively, in the side region 10. Note that the y-axis scales are different for the two plots.

4.4.4 Zenith Angle Resolution

Those events which are successfully reconstructed (for all ϕ) are analysed for their zenith angle resolution. The events distribution as a function of the reconstructed zenith angle θ_{rec} is shown in Figure 4.13 for a sample input $(P_{in}, \cos \theta) = (5 \text{ GeV}/c, 0.65)$ for the peripheral, side 9 and side 10 region respectively.

The angular resolution is good in the three regions and is in fact better than about a degree for the input momenta greater than a few GeV, as seen in Figure 4.14, with the resolution being marginally better in the side regions. Furthermore, the fraction of events reconstructed in the wrong direction (wrong quadrant of $\cos \theta$) is negligibly small, being less than 0.5% for $P_{in} \geq 2 \text{ GeV}/c$.

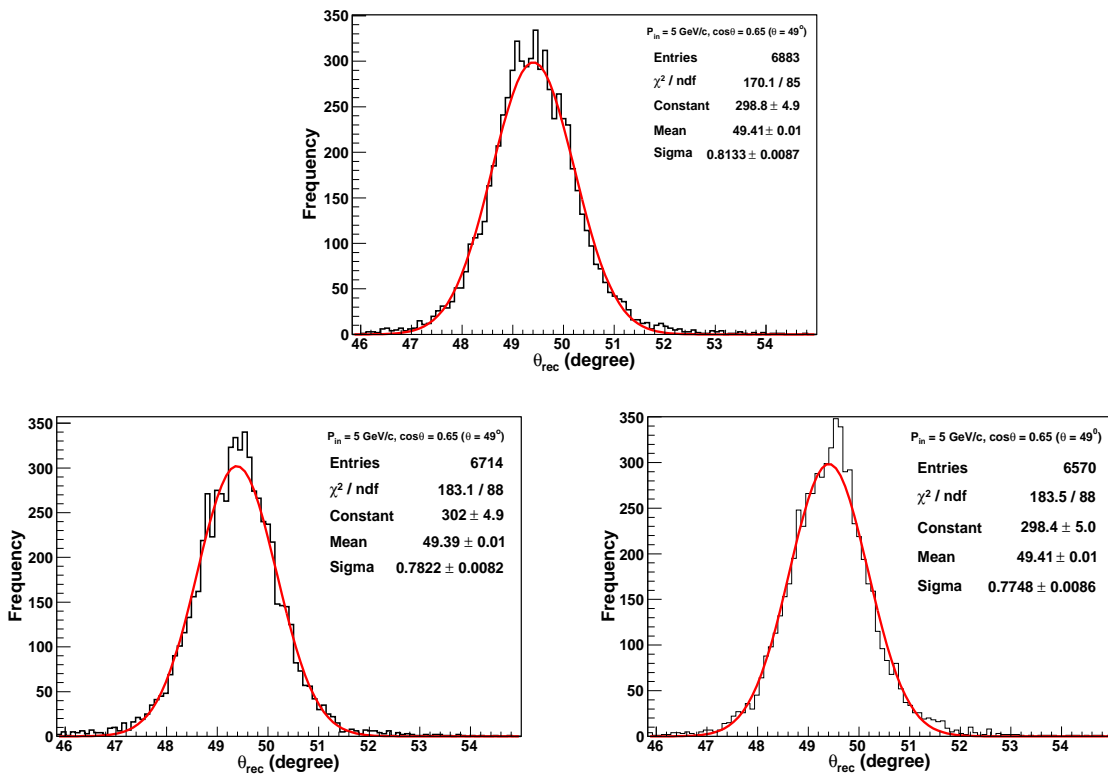


Figure 4.13: Reconstructed distribution θ_{rec} for input $(P_{in}, \cos\theta) = (5 \text{ GeV}/c, 0.65)$ in the peripheral region (above), side region 9 (below-left) and side region 10 (below-right) respectively.

4.4. Muon Response in the Peripheral and Side Regions

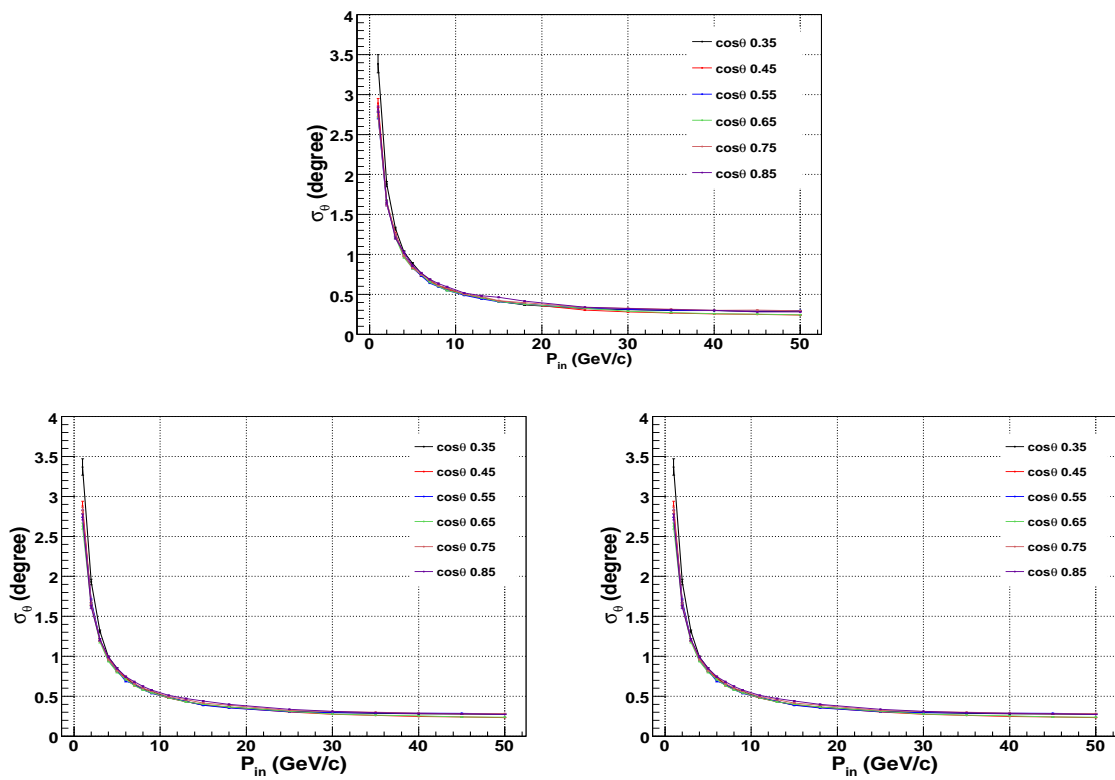


Figure 4.14: Resolution, σ_θ , of reconstructed angle θ_{rec} as a function of the input momentum P_{in} (GeV/c) for different values of input $\cos\theta$ in the peripheral region (above), side region 9 (below-left) and side region 10 (below-right) respectively.

4.4.5 Muon Momentum Response

While the cid efficiency and zenith angle resolution are insensitive to the azimuthal angle ϕ , due to the reasons given above, we analyse the muon momentum response in different ϕ bins. The response is shown in Figure 4.15 for the peripheral region with the constraint $N_{hits}/\cos\theta > 15$ being applied as usual to the partially contained events, for sample input values of $(P_{in}, \cos\theta) = (5 \text{ GeV}/c, 0.65)$.

The histograms in P_{rec} have been fitted with Gaussian functions. The width of each distribution of the four sets differs while the mean remains similar. As expected, ϕ bin III (with most muons exiting the detector from the side) has the smallest number of reconstructed events and the worst resolution. Bin II has the best resolution, while bins I and IV have a similar response of a lower order. This is in contrast to the response in the central region [173] where the reconstruction efficiencies were roughly equal in all ϕ bins.

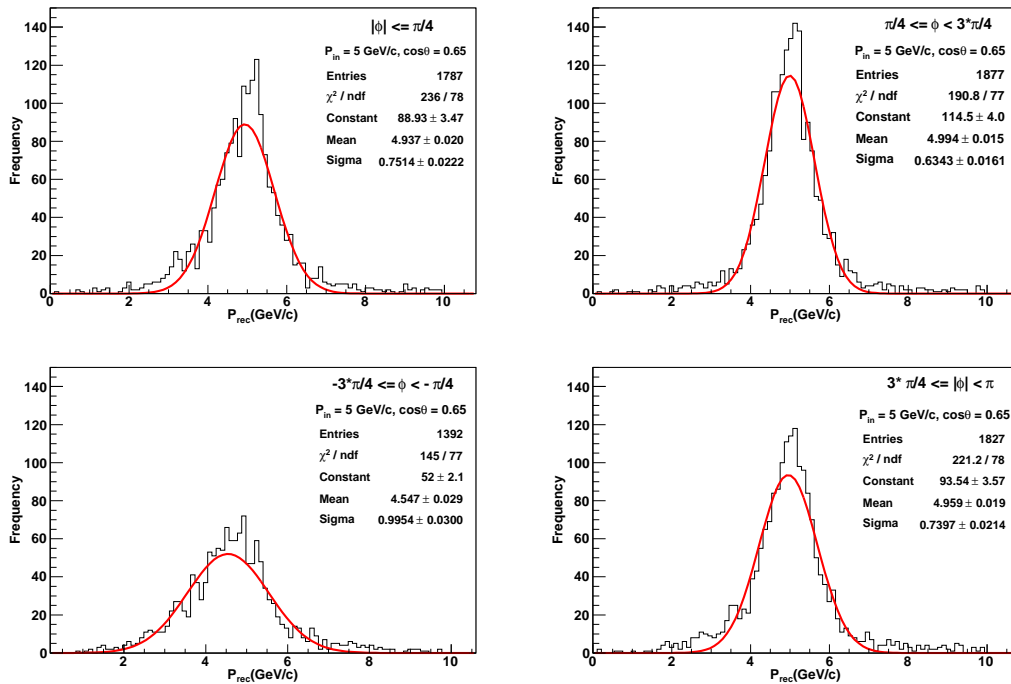


Figure 4.15: Gaussian fits to reconstructed momentum distributions P_{rec} (GeV/c) for muons with fixed energy $(P_{in}, \cos\theta) = (5 \text{ GeV}/c, 0.65)$ in four different bins of azimuthal angle in the peripheral region.

4.4. Muon Response in the Peripheral and Side Regions

Similar histograms are shown in Figure 4.16 for side region 9. As discussed earlier, ϕ bin IV has both the worst reconstruction and the worst resolution, while bin I has the best ones. Here bins II and III are not similar because the side region is not symmetric between these two bins: muons in bin III are more prone to exit the detector and hence the detector response is worse in both efficiency and quality of reconstruction.

The results in side region 10 are shown in Figure 4.17 and is similar to region 9 with interchange of bins I and IV, and bins II and III as can be easily understood from Figure 4.2. But, the overall quality of reconstruction is better in region 10 by about 15% due to the nature of the forces in this region as discussed earlier; (refer to Figure 4.2).

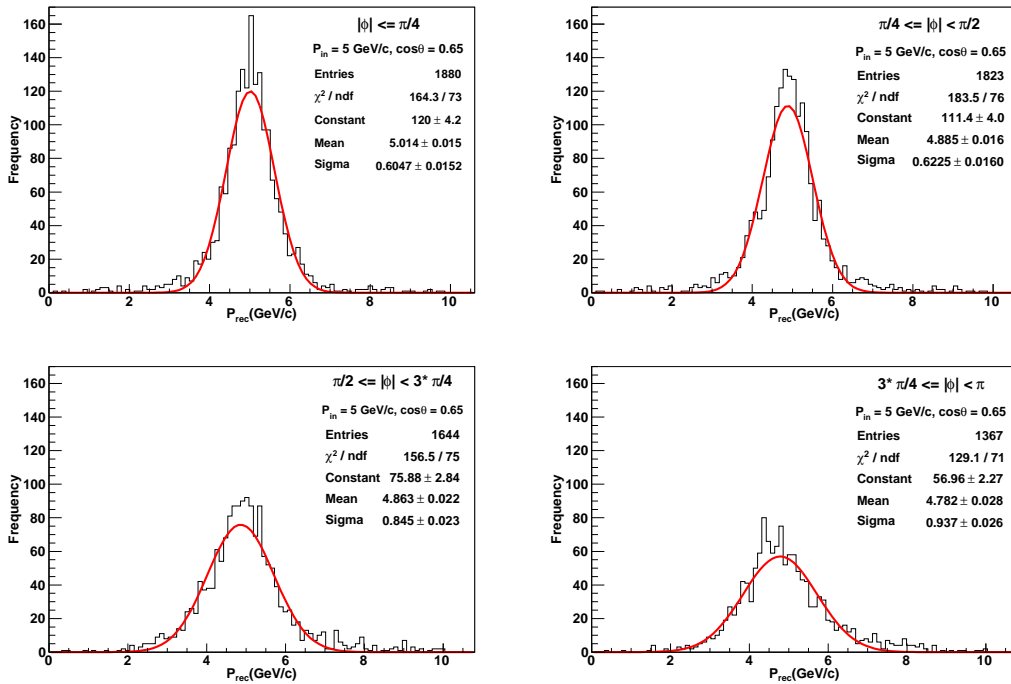


Figure 4.16: Gaussian fits to reconstructed momentum distributions P_{rec} (GeV/c) for muons with fixed energy $(P_{in}, \cos \theta) = (5 \text{ GeV}/c, 0.65)$ in four different bins of azimuthal angle in the side region 9.

Figure 4.18 shows the momentum resolution as a function of P_{in} in the peripheral region for the four ϕ bins using the selection criteria $N_{hits} / \cos \theta > n_0$ with $n_0 = 15$ and 20, for $\cos \theta = 0.65$.

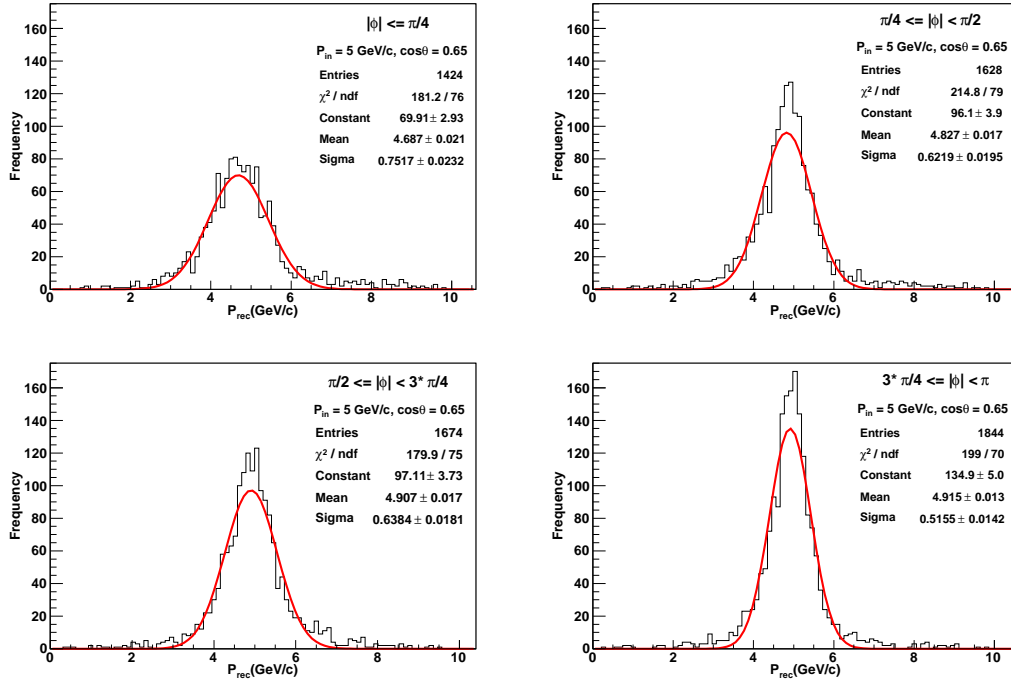


Figure 4.17: Gaussian fits to reconstructed momentum distributions P_{rec} (GeV/c) for muons with fixed energy $(P_{in}, \cos\theta) = (5 \text{ GeV}/c, 0.65)$ in four different bins of azimuthal angle in the side region 10.

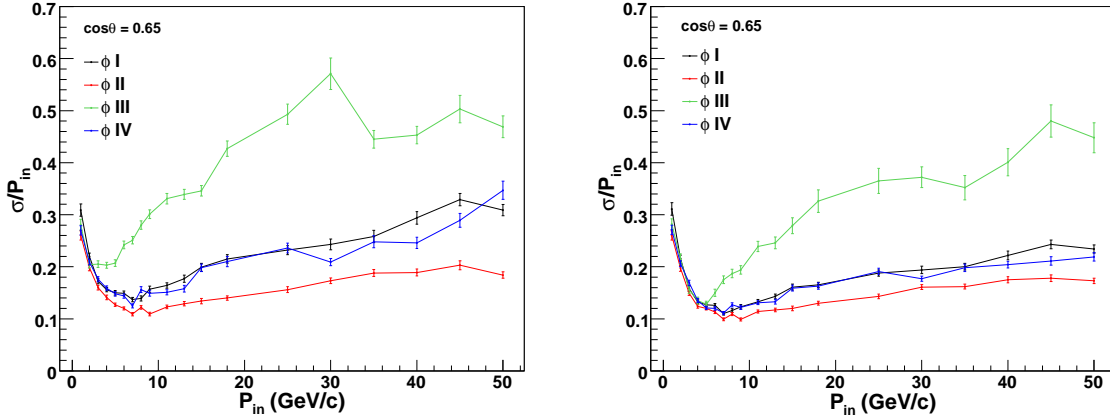


Figure 4.18: Muon resolution in the peripheral region as a function of input momentum P_{in} (GeV/c) for $\cos\theta = 0.65$ in different bins of ϕ with $N_{hits}/\cos\theta > n_0$ cut, where $n_0 = 15$ (20) left (right).

4.4.6 Momentum Resolution as a Function of (θ, ϕ)

Gaussian fits to the reconstructed momentum distribution in these regions give the reconstructed mean and RMS width σ . The momentum resolution (R) is defined from these

4.4. Muon Response in the Peripheral and Side Regions

fits as,

$$R = \sigma/P_{in}, \quad (4.5)$$

$$\text{with error } \delta R = \delta\sigma/P_{in}.$$

Figure 4.19 shows the variation of resolution as a function of P_{in} from 1 to 50 GeV/c for different values of $\cos\theta$ from 0.35 to 0.85 in the different ϕ bins of the peripheral region. In all bins, the momentum resolution improves with the increase of energy upto about $P_{in} \sim 6$ GeV/c as the number of hits increases, but worsens at higher momenta since the particle then begins to leave the detector. This effect is considerable in the ϕ bin III which therefore has the worst resolution while ϕ bin II has the best resolution, as expected from the earlier discussions. In general, the resolution improves for more vertical angles (larger $\cos\theta$) as the number of hits in a track increases.

Figure 4.20 shows similar results for the side region 9. Again, it is observed that for all the angles and energies, ϕ bin I has the best response while the resolutions worsens in bins III and IV. Results in region 10 are similar to those in region 9 with interchange of response in ϕ bins (I, IV) and (II, III), but with a few percent better resolution in all cases, and is shown in Figure 4.21.

The resolution for a given P_{in} is marginally better in the side regions than in the peripheral region due to the somewhat larger and uniform magnetic field. Momentum and angular resolution, reconstruction and cid efficiency in peripheral and side regions is listed in Table 4.1.

Region	Resolution R (%)	ϵ_{rec} (%)	ϵ_{cid} (%)	σ_θ
Peripheral region	15-25	60-70	97	better than a degree
Side region (9 and 10)	11-20	65-72	98	better than a degree

Table 4.1: Momentum and angular resolution, reconstruction and cid efficiency in peripheral and side regions (9 and 10).

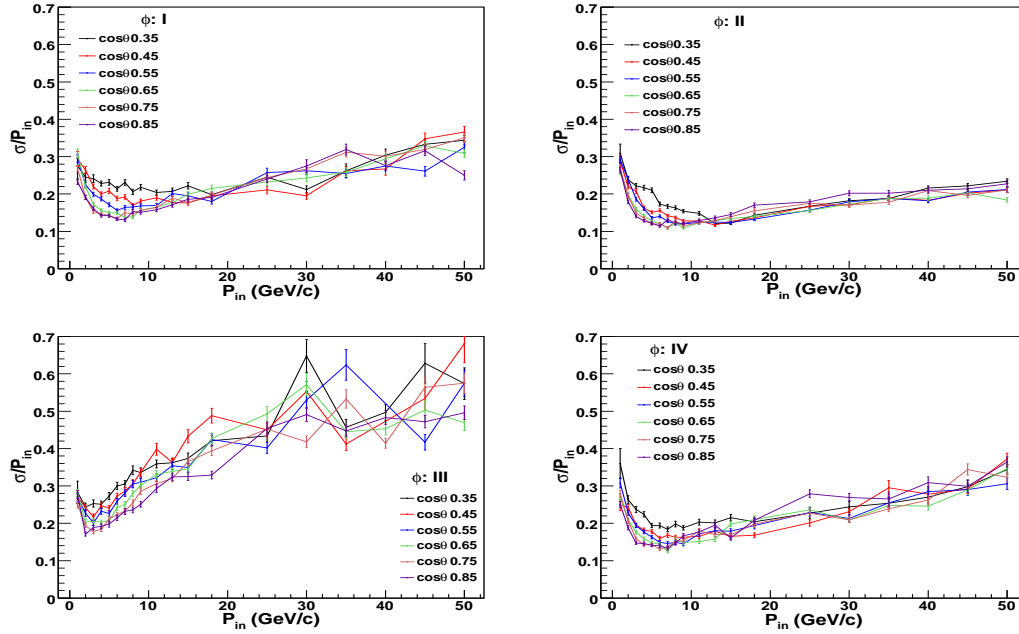


Figure 4.19: Muon resolution in the peripheral region as a function of input momentum P_{in} (GeV/c) for different values of $\cos\theta$ in different bins of ϕ .

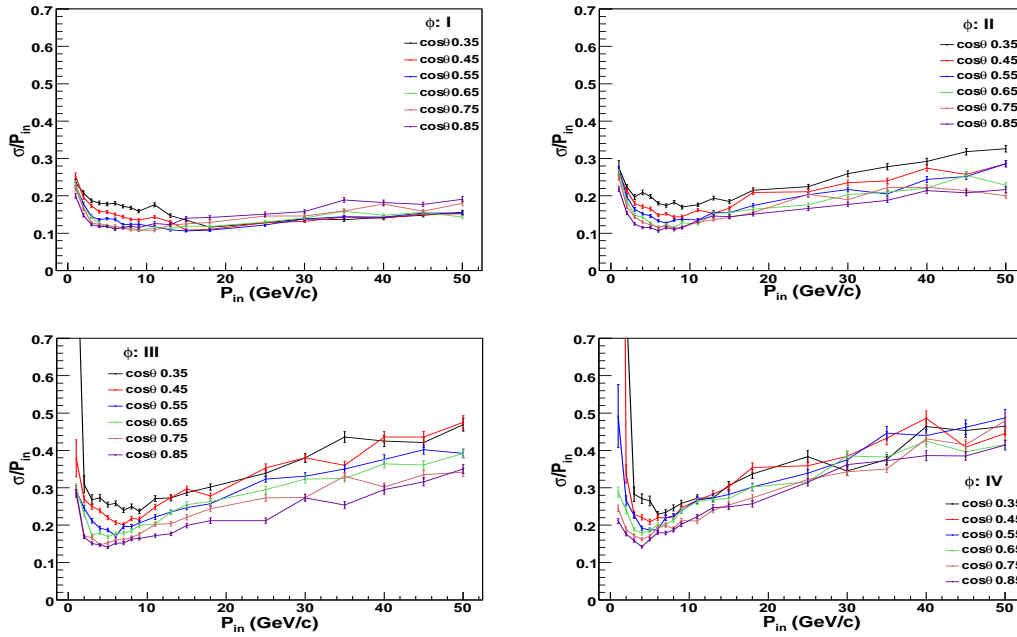


Figure 4.20: Muon resolution in the side region 9 as a function of input momentum P_{in} (GeV/c) for different values of $\cos\theta$ in different bins of ϕ .

4.4. Muon Response in the Peripheral and Side Regions

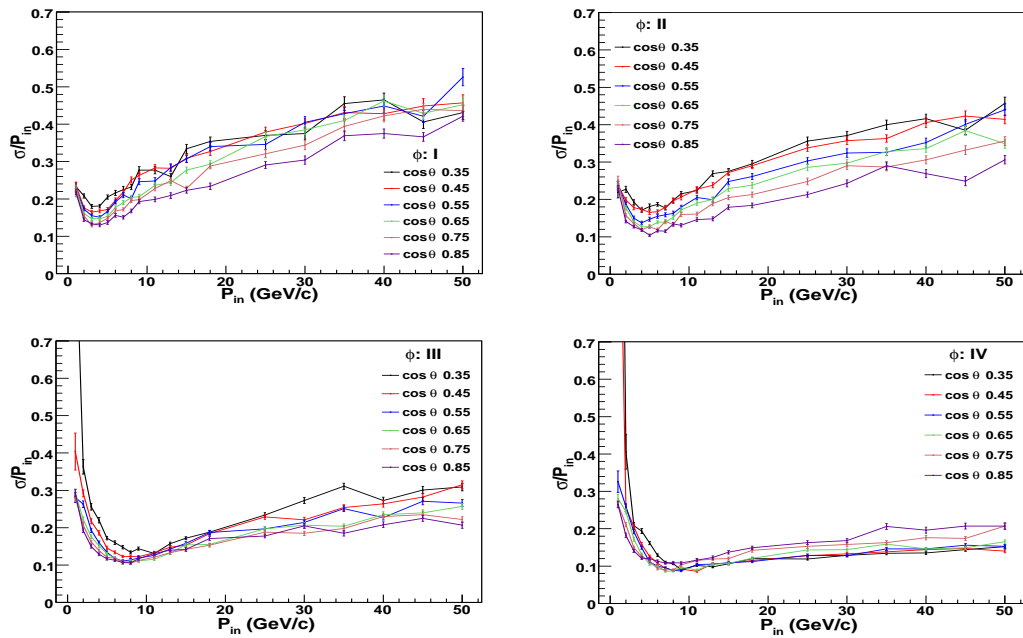


Figure 4.21: Muon resolution in the side region 10 as a function of input momentum P_{in} (GeV/c) for different values of $\cos \theta$ in different bins of ϕ .

4.5 Comparison of Muon Response in Different Regions of ICAL

The response of ICAL to few-GeV muons with respect to both momentum magnitude and direction reconstruction was studied through simulations for muons generated in the central region of ICAL where the magnetic field is largely uniform both in direction and magnitude. For 1-20 GeV/c muons, we obtained an average angle-dependent momentum resolution of 9–14% and an angular resolution of about a degree for few GeVs of the energy range. We obtained reconstruction efficiency of about 80% and a correct charge identification of about 98% in the central regions [173]. A detailed comparison of the response in different regions will be presented in this section.

A comparison of the muon response in the peripheral and side regions with that in the central region [173] is done here. The reconstruction and cid efficiencies in the central region are better than either the peripheral or side region as shown in Figure 4.22 for $\cos\theta = 0.65$, for all choices of selection criteria. But, for input momenta upto $P_{in} \sim 8$ GeV/c, the central and side region cid efficiencies are comparable. The application of tighter selection cuts in order to improve the momentum resolution in the peripheral and side regions (and hence overall resolution of the detector) will further worsen the reconstruction efficiencies in these regions.

Furthermore, the angular resolutions (Figure 4.14) between the peripheral and side regions are similar to those obtained earlier in the central region [173].

The comparison of the ϕ -averaged central, peripheral and side region momentum resolutions as a function of input momentum P_{in} from 1 to 15 GeV/c is shown in Figure 4.23 for $\cos\theta = 0.45, 0.65, 0.85$. No constraint on N_{hits} was applied in central region, only the criterion of a single reconstructed track was applied. The central region gives the best resolution whereas the side region resolutions are only marginally better than those in the peripheral region. Depending on the ϕ bin chosen the resolutions can be

4.5. Comparison of Muon Response in Different Regions of ICAL

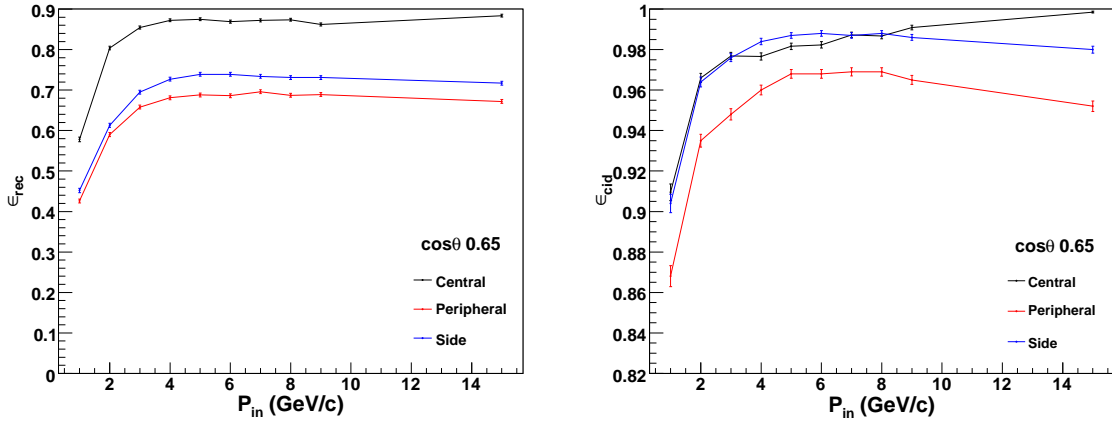


Figure 4.22: Comparison of reconstruction (left) and cid efficiency (right) of central, peripheral and side regions as a function of P_{in} (GeV/c) at $\cos\theta = 0.65$. Note that the y-axis scales are different for the two plots.

further improved in the peripheral and side regions by changing the selection criteria at the cost of reconstruction efficiency. The resolutions in all regions are comparable at low momenta, $P_{in} \leq 3$ GeV/c, because the tracks are fully contained in this case.

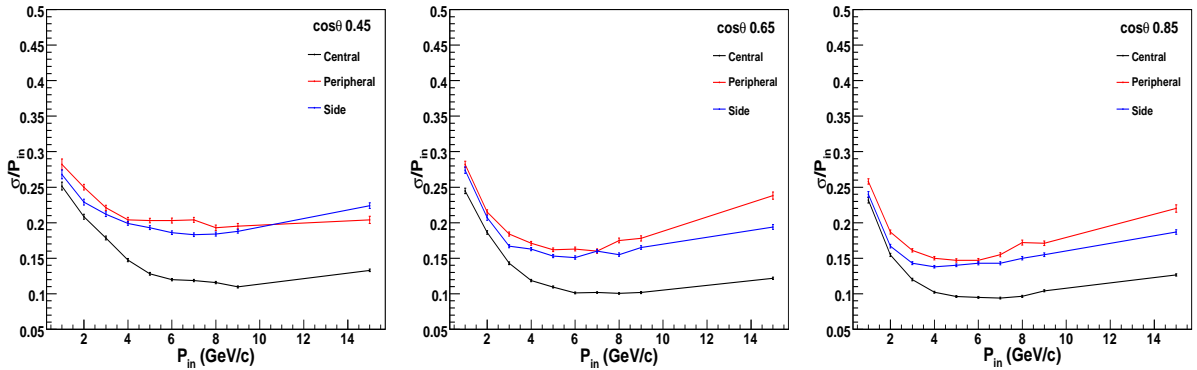


Figure 4.23: Comparison of resolutions in peripheral and side region 9 as a function of the input momentum P_{in} (GeV/c) along with earlier results in the central region [173] for different values of $\cos\theta = 0.45, 0.65, 0.85$.

To summarize, muons were generated in the peripheral and side region of the ICAL detector where the magnetic field is non-uniform in both magnitude and direction and affected by edge effects. A crucial selection criterion on the number of hits

$N_{hits}/\cos\theta > n_0$ for partially contained tracks was applied to get good quality of reconstruction, and $n_0 = 15$ was found to be an optimum choice.

So far, we have considered the reconstruction and response to simulations with mono-energetic muons in ICAL. In the case of real data, when atmospheric neutrinos that interact with (dominantly) the iron in the detector, hadrons will be produced as well, and will leave hits in the detector. Hence the main uncertainties in the reconstruction of muons arise from mis-identification of hadron hits as muon hits (or vice versa) and systematics due to uncertainties in the magnetic field.

In the first case, it has been found [172] that mis-identification of muon hits as hadron hits impacts the hadron energy reconstruction much more than the other way around. The reason for this is mainly because the muon information (both energy/momentum and direction as well as charge identification) is obtained from a Kalman-filter analysis where the possible multiple hits in a layer are averaged to a single hit per layer. Hence, additional hits due to mis-identification of hadron hits does not materially affect the muon reconstruction algorithms. Of course, since the hadron energy is calibrated to the *total* number of hits (excluding those that belong to the muon track), there is a much greater impact on hadron energy reconstruction due to this systematic error. Apart from this is the issue of random hits due to detector noise, and the impact of this on muon reconstruction is expected to be rather low for the same reason.

It should also be noted that the physics studies on upward-going rock muons presented in the next chapter of this thesis deals with the very clean situation of pure muons reaching the detector from neutrino interactions occurring far away in the rock surrounding the detector so that there are no accompanying hadrons in the events.

The more important source of systematic error is due to fluctuations and error in measurement of the (varying) magnetic field. This may have a large impact on the muon simulations since the magnetic field lies at the heart of the muon reconstruction algorithm as well as the ability of ICAL to reconstruct the sign of the muon charge.

4.5. Comparison of Muon Response in Different Regions of ICAL

Very preliminary studies have been conducted by the collaboration on this issue. A large (1/8th of a module, or about 2 kton) prototype is presently under construction and it is expected that studies with this prototype should shed light on this very crucial issue. In addition, it is possible that a (smaller) prototype may be used to validate the simulations by sending various particle beams through it for analysis and calibration. A more detailed analysis lies at present beyond the scope of the present work.

Since the magnetic field and the detector geometry break the azimuthal symmetry, the muon response was analysed in different ϕ bins. A reconstruction efficiency of about 60–70% and a correct charge identification of about 97% of the reconstructed muons was obtained for $P_{\text{in}} \sim 4$ GeV/c and this goes down to about 90% for higher momenta $P_{\text{in}} \sim 50$ GeV/c in both regions. Average (over ϕ) resolutions obtained are between 15–25% over $P_{\text{in}} = 1\text{--}15$ GeV/c in the peripheral region and are marginally better in the side region. A comparison of these results with that obtained in a separate study of the central region shows that the response is the best in the central region as expected. These results are important for precision measurement of neutrino oscillation parameters or the mass hierarchy determination with ICAL. For upward-going or downward-coming cosmic ray muons, only certain ϕ bins are relevant. A good angular resolution of better than a degree (refer to sub-section 4.4.4) for $P_{\text{in}} \geq 4$ GeV/c is obtained in the peripheral and side regions and is comparable to that in the central region. These resolutions and efficiencies can be used for various physics analyses. Upward-going rock muons have been analysed using these resolutions and efficiencies which is described in the next chapter.

Chapter 5

Oscillation Analysis with Upward-going Muons

One of the main goals of the proposed magnetised Iron CALorimeter (ICAL) detector at India-based Neutrino Observatory (INO) is to do precision measurements using atmospheric neutrinos. Atmospheric neutrinos can be either upward-going or downward-coming. Our studies include the oscillation analysis using upward-going muons and finding their significance in INO. This chapter is organized as follows. In Section 5.1, we describe upward-going muon production at the ICAL detector. In Section 5.2, we discuss the data generation for upward-going muons using NUANCE event generator, the detector response for muons, theoretical considerations taken into account while simulating upward-going muons and χ^2 analysis. In Section 5.3, we discuss the results of the simulations analyses—comparison of ICAL data with Super-K, sensitivity to individual parameters, precision measurements and analysis by combining upward-going muon with atmospheric neutrino data.

5.1 Upward-going Muons at ICAL Detector

Upward-going muons, otherwise called rock muons [177] [178] give an independent estimation of the oscillation parameters [73, 74] (also refer to sub-section 1.2.3), despite

the fact that the sensitivity of upward-going muons to the oscillation parameters is lower than contained vertex muons. In any case, an independent estimation utilizing upward-going muons will furnish a consistency check with the contained vertex analysis, that would bring about slight improvement of the overall estimation of oscillation parameters. Consequently, this sort of analysis is useful in any neutrino experiment.

Upward-going muons emerge from the interactions of atmospheric neutrinos with the rock material that surrounds the detector within ~ 200 m. Figure 5.1 demonstrates the generation of upward-going muons at ICAL detector. Neutrinos interacting with rock subsequently produce hadrons and muons. Hadrons get absorbed in the rock while, upward-going muons making an angle θ with the upward or z - direction continue to travel to reach the ICAL detector. Because of its production mechanism, upward-going muons are to be separated from two kind of events. In the first place are those neutrino events that generate muons through interactions inside ICAL detector and which comes under the main studies of ICAL. This background can be removed by considering only those muon tracks which originate from outside of ICAL detector. Second are cosmic [179] ray muon events generated in the Earth's atmosphere that subsequently interact with ICAL. These are the main backgrounds to the rock muon events at the ICAL detector. The first can be removed by requiring that the first hit is in an RPC belonging to the edge layer; the second, by ignoring the downward-coming rock muon events and only considering the upward-going ones, by introducing an angle cut (since there are no cosmic rays from below.)

5.2 Methodology

In this section, we explain the methodology we followed to do the entire simulations analysis. Firstly, we describe the data generation using the NUANCE neutrino generator. Since real data is not available, the NUANCE data is smeared using the resolutions and efficiencies relevant for upward-going muons. These results, which were obtained in the

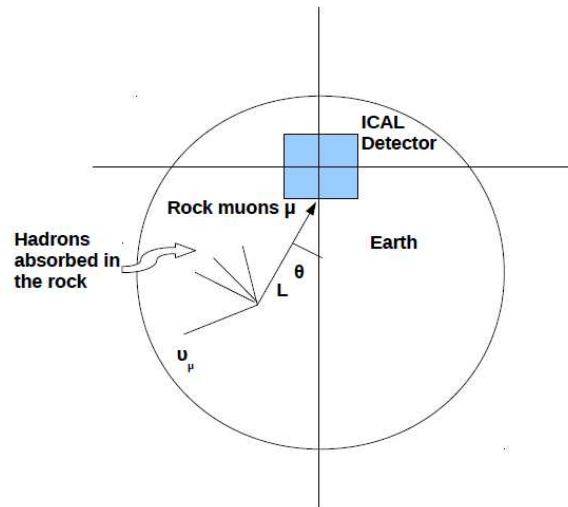


Figure 5.1: Production of upward-going muons at ICAL.

last chapter, are compiled again into a convenient form for use here. These data are then analysed using a χ^2 -minimisation procedure to obtain the sensitivity of these events to neutrino oscillation parameters.

5.2.1 Data Generation

The neutrino event generator NUANCE (Version3.5) [180] is used to generate an exposure of $50 \text{ kt} \times 200 \text{ years}$ of unoscillated upward-going muons in the energy range $0.8\text{--}200 \text{ GeV}$. The atmospheric neutrino fluxes given by Honda et al. [181] at the Super Kamiokande experiment were used. The ICAL detector particulars are characterized inside the NUANCE framework. Just the outer geometry of ICAL is needed as no events are generated inside the detector. The real material in which interactions happen is rock in the present studies, with a density of 2.65 gm/cc . An angle cut of $0^\circ < \theta < 81^\circ$ was applied to cut off cosmic ray backgrounds. The simulations is done in steps as described below.

5.2.2 Nuance Event Generator

NUANCE [180] is a versatile and general purpose neutrino events generator. It simulates neutrino interactions in a medium, for instance water. The list of particles produced in each interaction and their kinematics is saved to a text or binary data file. Passage of particles through the detector material is not included, for that one has to use GEANT4, FLUKA or some other detector simulation software. The simulation is carried out in different stages:

- **Detector geometry:** Since the rock muons are produced from neutrino interactions in rock, no information about the composition of ICAL is required. However, the outer dimensions of the detector are required so that the muons are propagated (with NUANCE itself) upto the appropriate surface of the detector.
- **Cross-sections and rate calculation:** The contributions of various interaction channels of neutrino (or anti-neutrino) with rock, assumed to have $(Z, A) = (11, 22)$, and density of 2.65 g/cc are calculated. Typically, low energy contributions from quasi-elastic and resonance processes produce low energy muons that are unlikely to reach the detector; hence, rock muons arise dominantly from the deep inelastic processes.
- **Event generation:** In this stage the events are generated according to the exposure (in year) specified. The neutrino interaction is simulated further in two steps: primary interaction, which simulates primary neutrino-nucleon interactions depending on the type of nucleus, number of nucleons etc. Processes like pion absorption also takes place in this stage. Quasi-elastic (QE), resonant production (RES), deep inelastic scattering (DIS), coherent/diffractive production and elastic scattering on electrons are the reaction channels simulated in primary vertex (refer chapter 1, section 1.2.2 for more information on these reaction channels.) In the second stage,

the muons from the primary interaction are propagated through the rock up to the detector. This is the most time-consuming part of the calculation.

Muons lose the greater part of their energy in the rock before they reach the detector. The average muon energy loss formula for muons of energy E_μ produced in the rock is given by,

$$\frac{dE_\mu}{dx} = -a - bE_\mu , \quad (5.1)$$

so the energy loss of the muons after the propagation of X g/sq.cm depth is:

$$E_\mu = (E_\mu^0 + \epsilon) \exp(-bX) - \epsilon , \quad (5.2)$$

where $\epsilon = a/b$, E_μ^0 is the initial muon energy, a accounts for ionization losses and b accounts for the three radiation processes: bremsstrahlung, production of electron-positron pairs and photoproduction. We have $\epsilon = a/b \sim 500$ GeV. Note, however, that both a and b depend on E_μ . The event-by-event energy loss of the muons, calculated with the event generator NUANCE [180] is shown in comparison to the linear fit of Equation 5.2 in Figure 5.2. A broad agreement is seen; note that NUANCE uses the correct differential form of the energy loss formula which is very time-consuming, and this is what has been used in the analysis. As mentioned earlier, NUANCE propagates these muons up to the detector surface.

5.2.3 Detector Response for Muons

At this point, these muons should be propagated through the ICAL detector using a simulations package such as GEANT4. Instead, a smearing in muon energy and angle is applied according to the studies described in chapter 4. In that chapter, the response of muons in the different (central, peripheral and side) regions of ICAL was studied and its

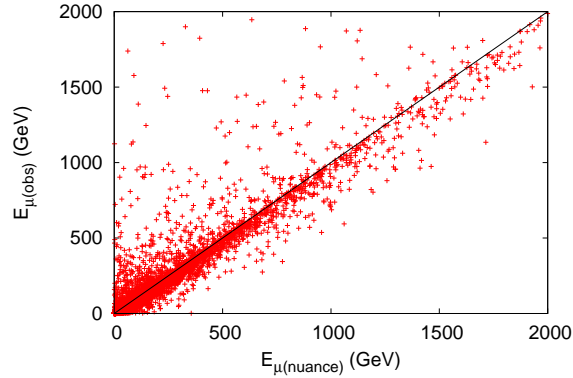


Figure 5.2: E_{μ} calculated from formula Equation 5.2 vs. E_{μ} as calculated by the NUANCE neutrino generator at the ICAL detector.

dependence understood.

For the current study, however it is useful to do a different grouping. This is because over half the rock events have their vertices in the bottom of the detector. The four sides (front, back, left and right) of ICAL together account for the other half events. Hence, we study the response of the bottom face of ICAL to muons. Note that this contains portions of the “central” and “peripheral” regions and so its response is likely to be intermediate between the two.

Using the same procedure as in chapter 4, we obtained resolutions and efficiencies for the bottom part of the entire ICAL. Figure 5.3 clarifies the impact of the same selection criteria ($\chi^2/\text{ndf} \leq 10$, and $N_{\text{hits}}/\cos\theta > 15$) on reconstructed momentum (P_{rec}) in the region. From the figure, at lower energy ($P_{\text{in}} = 5$ GeV/c) the N_{hits} cut does not have significant impact on the momentum distribution as most of the events are fully contained, with a reasonable shape (Gaussian) of the distribution. Then again, the bump at lower energy tail at $P_{\text{in}} = 15$ GeV/c is not as prominent as with the purely peripheral muons analysed in the previous chapter. In addition, the $ntrkt == 1$ constraint is now removed as it eliminated lots of desirable events as shown in Figure 5.4; infact, the constraint $N_{\text{hits}}/\cos\theta > 15$ was found sufficient. Now we discuss the impact of selection criteria on resolutions and efficiencies.

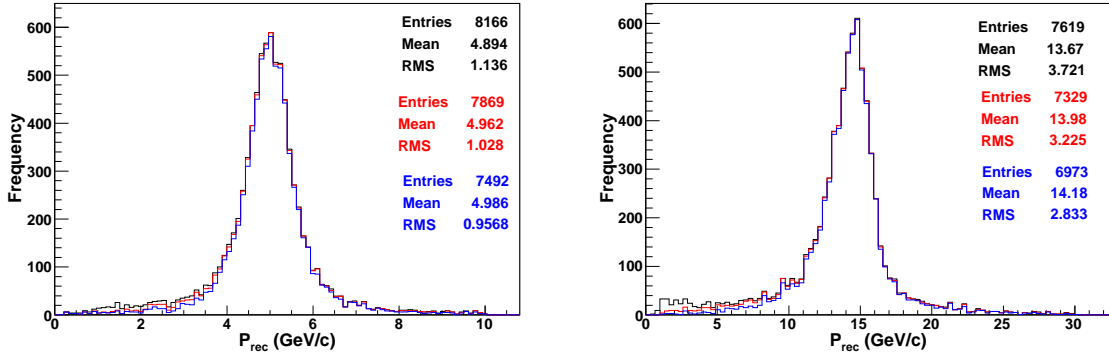


Figure 5.3: The reconstructed momenta P_{rec} using selection criteria $N_{hits} > n_0$ for partially contained events in the bottom region of ICAL at $(P_{in}, \cos\theta) = (5 \text{ GeV}/c, 0.65)$ (left) and $(P_{in}, \cos\theta) = (15 \text{ GeV}/c, 0.65)$ (right). In both figures, the black curve is without constraints on N_{hits} , red is with $N_{hits}/\cos\theta > n_0$ and blue is for $N_{hits} > n_0$; $n_0 = 15$.

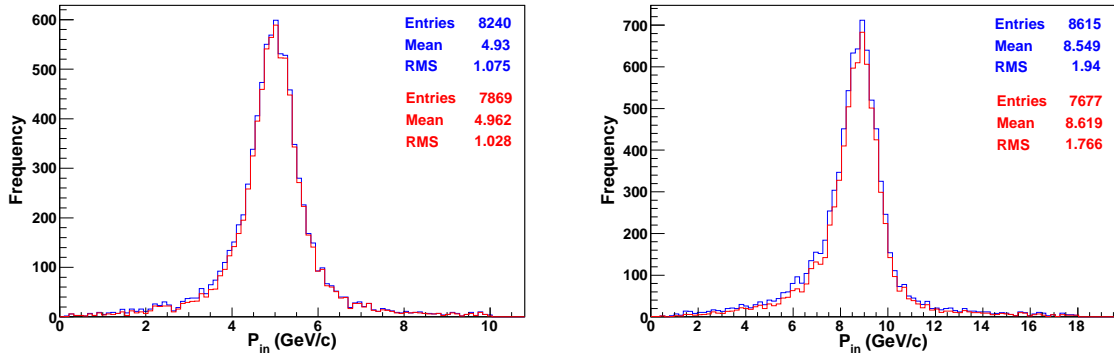


Figure 5.4: The reconstructed momenta P_{rec} with and without $ntrkt == 1$ cut in the bottom region of ICAL at $(P_{in}, \cos\theta) = (5 \text{ GeV}/c, 0.65)$ (left) and $(P_{in}, \cos\theta) = (9 \text{ GeV}/c, 0.65)$ (right). In both figures, the red (blue) curves are with (without) $ntrkt == 1$ cut.

The Figure 5.5 demonstrates the Gaussian fit to the reconstructed momentum distribution P_{rec} (GeV/c) and θ distribution for muons with fixed energy $(P_{in}, \cos\theta) = (5 \text{ GeV}/c, 0.65)$ for $-\pi \leq \phi \leq \pi$ for $N_{hits}/\cos\theta > 15$. The quality of fit will be improved by performing a binned- ϕ analysis as discussed in the previous chapter; however the average resolution obtained in that case will not be different from the resolution of the ϕ -averaged distributions. In Figure 5.6 the muon resolution and θ resolution in the bottom part of ICAL detector is shown (see chapter 4 for the definitions of resolutions and efficiencies). The muon resolution which we get by fitting the muon track is around 12–20% and worsens

at higher energies. The θ resolution is best and is about a degree for few GeV muons. The Reconstruction efficiency is about 70–80% and charge identification (cid) efficiency is around 97% as shown in Figure 5.7. The cid efficiency drops at higher energies because of only the relatively straight initial portion of the track is contained within the detector. We incorporate these values and the Gaussian fits into a set of lookup tables [182] which we use to smear the rock muon data generated by NUANCE over the momentum and direction of the muons.

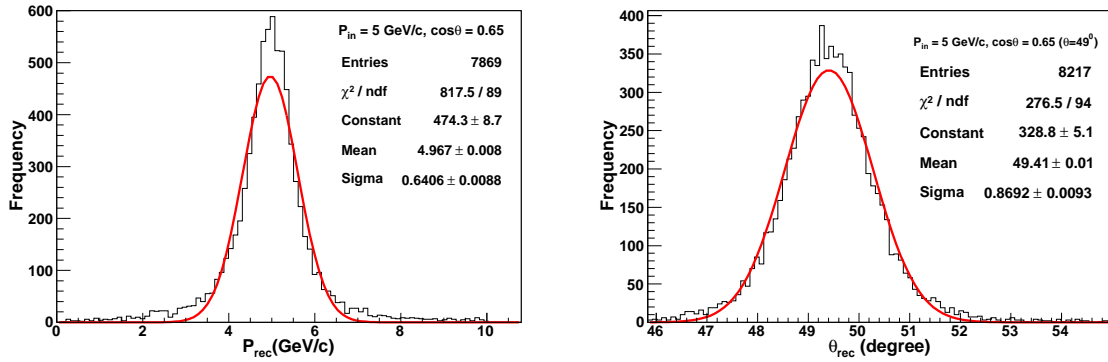


Figure 5.5: Left figure shows Gaussian fit to reconstructed momentum distribution P_{rec} (GeV/c) for muons with fixed energy $(P_{in}, \cos\theta) = (5 \text{ GeV}/c, 0.65)$ bin for $N_{hits}/\cos\theta > 15$. Right figure shows Gaussian fit to θ distribution for muons with fixed energy $(P_{in}, \cos\theta) = (5\text{GeV}/c, 0.65)$ for $N_{hits}/\cos\theta > 15$. In both cases ϕ is uniformly distributed over $-\pi \leq \phi \leq \pi$ (scale is different).

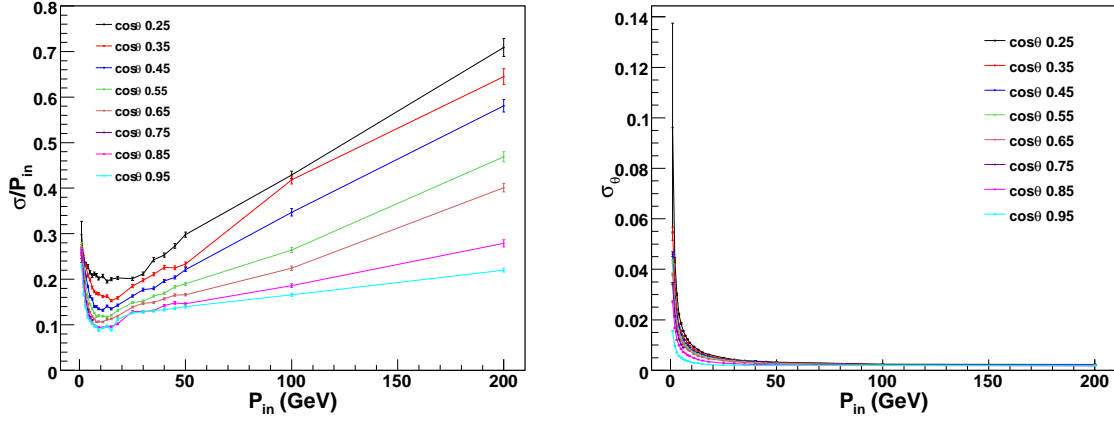


Figure 5.6: Left figure shows muon resolution as a function of input momentum and $\cos\theta$ for $N_{hits}/\cos\theta > 15$. Right figure shows the θ resolution as a function of input momentum and $\cos\theta$. In both cases ϕ is uniformly distributed over $-\pi \leq \phi \leq \pi$ (scale is different).

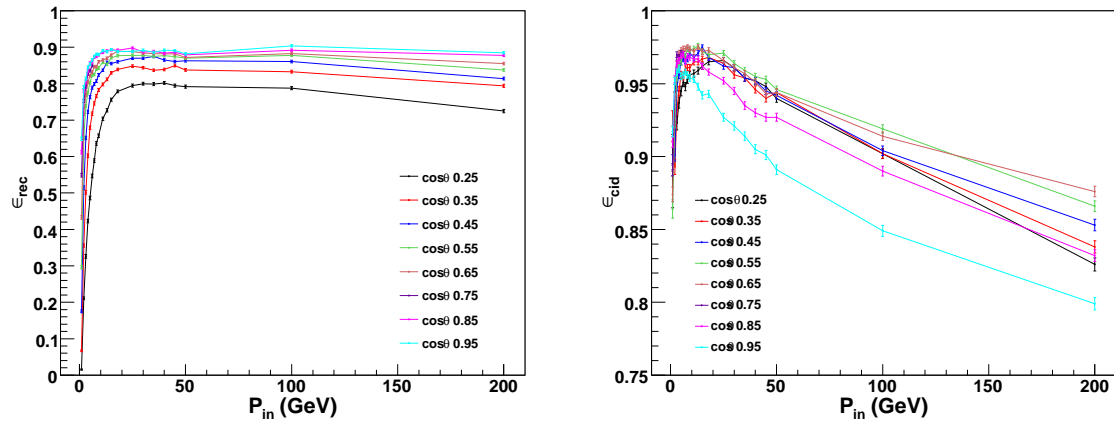


Figure 5.7: Left figure shows reconstruction efficiency for $N_{hits}/\cos\theta > 15$. Right figure shows the charge identification efficiency as a function of P_{in} for different values of $\cos\theta$ and ϕ is uniform over $-\pi \leq \phi \leq \pi$ (scale is different).

5.2.4 Theoretical Considerations

As stated earlier, 200 years of unoscillated upward-going muons were generated using NUANCE. This was scaled to 4.5 years to generate appropriate “data” for comparison with Super-K [33], by suitably turning on neutrino oscillations. Only charge current (CC) ν_μ events were used for the analysis and further they were not passed through Geant4 [90] based INO-ICAL code (containing information of ICAL detector) [173], but smearing in muon energy and angle was applied according to the lookup tables discussed in the previous section. For data generation and oscillation, the set of input parameters taken are, $\theta_{23} = 45^\circ$ ($\sin \theta_{23} = 0.707$), $\Delta m_{32}^2 = 2.4 \times 10^{-3} eV^2$, $\Delta m_{21}^2 = 7.6 \times 10^{-5} eV^2$, $\sin^2 \theta_{12} = 0.304$, $\sin^2 \theta_{13} = 0$ (or 0.1) for 2-flavour (or 3-flavour) [51], $\delta_{cp} = 0$. Then, oscillation is applied as follows.

Both ν_e and ν_μ atmospheric fluxes exist, so both the channels $\nu_\mu \rightarrow \nu_\mu$ and $\nu_e \rightarrow \nu_\mu$ contribute and hence the number of muon events N_μ originating from these two channels is given by,

$$N_\mu = T \times D \times \sigma_{\nu_\mu} \times \left[P_{\mu\mu} \frac{d^2\Phi_\mu}{dE_\nu d\cos\theta_z} + P_{e\mu} \frac{d^2\Phi_e}{dE_\nu d\cos\theta_z} \right], \quad (5.3)$$

where T is the exposure time and D is the number of targets in the detector, $P_{\alpha\beta}$ is the oscillation probability of $\nu_\alpha \rightarrow \nu_\beta$ channel, Φ_μ and Φ_e are fluxes of ν_μ and ν_e respectively, θ_z is the zenith angle of the parent neutrino and is related to the path-length L as,

$$L = \sqrt{(R + L_0)^2 - (R \sin \theta_z)^2} + R \cos \theta_z. \quad (5.4)$$

Here $\theta_z = 0$ relates to the neutrinos coming to the ICAL detector vertically upwards subsequent to navigating a distance L_0 which is the average height over the surface of the earth at which the atmospheric neutrinos are produced and is about 15 km; $\cos \theta_z = -1$

stands for downward-coming and $\cos \theta_z = 1$ is the upward-going neutrinos. Here R is the radius of the Earth. The neutrinos travel a path-length slightly less than L since they do not reach the detector but interact outside it. However, we observe that muons farther than a few 100 m from the detector are stopped in the rock itself, so this difference can be neglected. In order to incorporate oscillations we have utilized re-weighting algorithm, which is a Monte Carlo rejection technique to include the effect of oscillations in an unoscillated set of events. The procedure is as follows: A uniform random number r is generated between 0 and 1 to choose whether an unoscillated ν_μ event survives the oscillations [73]. If $P_{\mu\mu} \geq r$ then we considered this event as a surviving ν_μ event, otherwise it is thought to be changed into a distinct flavor. Similarly, we have used event re-weighting method to get those muon events that are obtained from ν_e . A random number r is generated again between 0 and 1 and if $r < P_{e\mu}$ we consider the event as a ν_μ event, else we dump that event. Events contributing from both the channels are added to get μ^- events and a similar method is utilized to get μ^+ events from $\bar{\nu}$.

Then the oscillated data is binned into smeared muon energy and $\cos \theta$ bins. We binned the data for 2-flavour and 3-flavour analysis differently. For 2-flavour analysis, we have 8 bins of energy and 4 bins of $\cos \theta$ as given in Table 5.1. For 3-flavour analysis, we have 25 bins of energy and 7 bins of $\cos \theta$ as given in Table 5.2. The energy bins were optimised to obtain reasonable number of events in each bin.

Bins in E (GeV)	Bins in $\cos \theta$
1-2	0.2-0.4
2-4	0.4-0.6
4-8	0.6-0.8
8-16	0.8-1
16-32	
32-64	
64-128	
128-256	

Table 5.1: Energy and $\cos \theta$ bins of observed (smeared) muons for 2-flavour analysis.

Since the data sample has proportionately larger component of higher energy events that are not sensitive to oscillations, so we have taken finer bins at lower energy,

Energy range (GeV)	Bin width (GeV)	No. of bins	Bins in $\cos\theta$
1–9	1	8	0–0.15
9–17	2	4	0.15–0.3
17–20	3	1	0.3–0.45
20–40	5	4	0.45–0.6
40–80	10	4	0.6–0.75
80–100	20	1	0.75–0.9
100–200	50	2	0.9–1
200–256	56	1	

Table 5.2: Energy and $\cos\theta$ bins of observed (smeared) muons for 3-flavour analysis.

for $\cos\theta > 0.156$ (angle cut). The energy distribution of muons (E_μ) for different $\cos\theta$ bins is demonstrated in Figure 5.8 and Figure 5.9 for 2-flavour (both μ^+ and μ^- combined) and 3-flavour analysis (of μ^- only) respectively. Tables 5.3, – 5.8 show the unoscillated and oscillated muons (μ^+ and μ^-) for the observed energy and $\cos\theta$ bins. The trend is similar in both cases with the number of events being higher at lower energy and lesser at higher energies. It is seen that in the first $\cos\theta$ bin i.e., 0.2–0.4 there are only few events, reflecting the poorer resolutions and reconstruction efficiencies at large angles, as seen in Figures 5.6 and 5.7. Note that these muons have lost energy in the rock before reaching the detector and so there is a non-trivial correspondence between the momentum of the muon and that of the neutrino which produced it. The energy profile of the neutrinos that survive 3-flavour oscillations is shown in Figure 5.10. It can be seen that there is contribution to events of neutrino energies upto 100 GeV or more. Although events at such high energies are usually suppressed due to the fluxes falling steeply as $E^{-2.7}$, higher energy muons are more likely to survive the propagation in the Earth and this leads to a larger fraction of high energy events in the rock-muon sample.

The number of μ^\pm events observed in a given bin (i, j) of E_μ and $\cos\theta_\mu$ after oscillations, and on including the detector response (smearing of muon energy and angle as well as including reconstruction and cid efficiencies) is given by,

$$N_\mu^{ij} = \epsilon_R^\pm \times [\epsilon_C^\pm \times N_\mu^\pm(E_\mu^i, \cos\theta_\mu^j) + (1 - \epsilon_C^\mp) \times N_\mu^\mp(E_\mu^i, \cos\theta_\mu^j)] \quad , \quad (5.5)$$

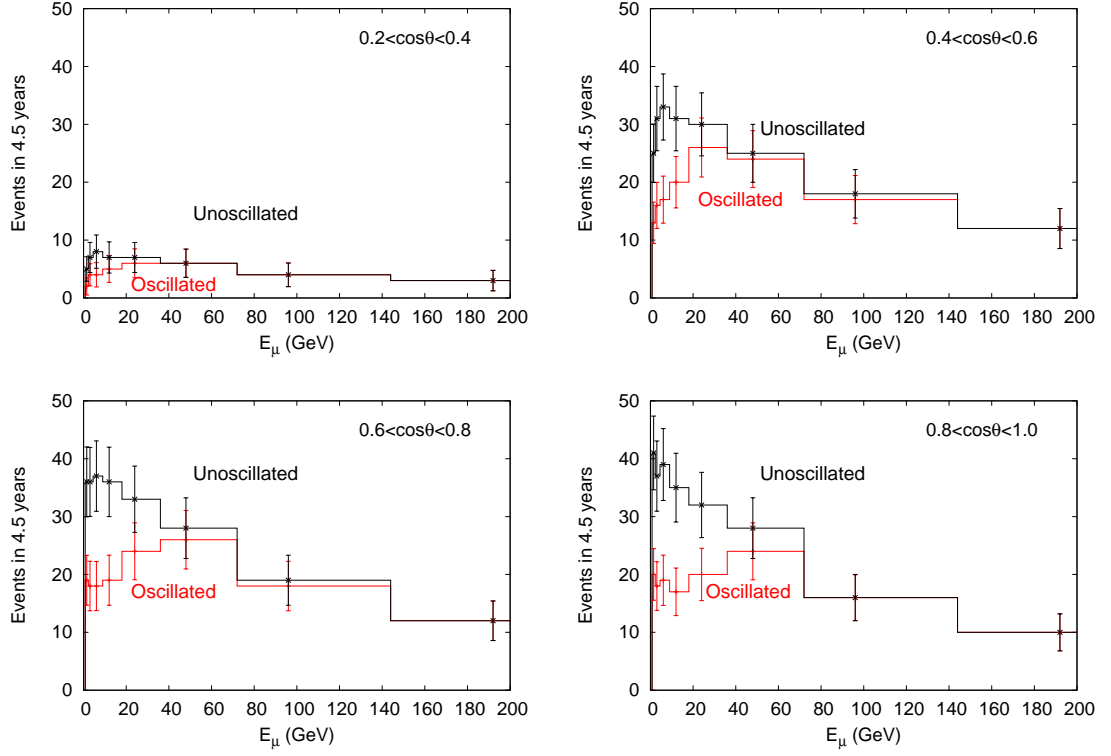


Figure 5.8: Energy distribution of muons (E_μ) for different $\cos\theta$ bins with and without 2-flavour oscillations.

$\cos\theta$ (min)	$\cos\theta$ (max)	E_{min} (GeV)	E_{max} (GeV)	Unosc (μ^-)	Osc (μ^-)	Unosc (μ^+)	Osc (μ^+)
0	0.15	1	2	1	1	0	0
0	0.15	2	3	1	1	0	0
0	0.15	3	4	1	0	0	0
0	0.15	4	5	0	0	0	0
0	0.15	5	6	0	0	0	0
0	0.15	6	7	0	0	0	0
0	0.15	7	8	0	0	0	0
0	0.15	8	9	0	0	0	0
0	0.15	9	11	0	0	0	0
0	0.15	11	13	0	0	0	0
0	0.15	13	15	0	0	0	0
0	0.15	15	17	0	0	0	0
0	0.15	17	20	0	0	0	0
0	0.15	20	25	0	0	0	0
0	0.15	25	30	0	0	0	0
0	0.15	30	35	0	0	0	0
0	0.15	35	40	0	0	0	0
0	0.15	40	50	0	0	0	0
0	0.15	50	60	0	0	0	0
0	0.15	60	70	0	0	0	0
0	0.15	70	80	0	0	0	0
0	0.15	80	100	0	0	0	0
0	0.15	100	150	0	0	0	0
0	0.15	150	200	0	0	0	0
0	0.15	200	256	0	0	0	0

Table 5.3: Oscillated and unoscillated events for the observed energy bin and $0 < \cos\theta < 0.15$ bin.

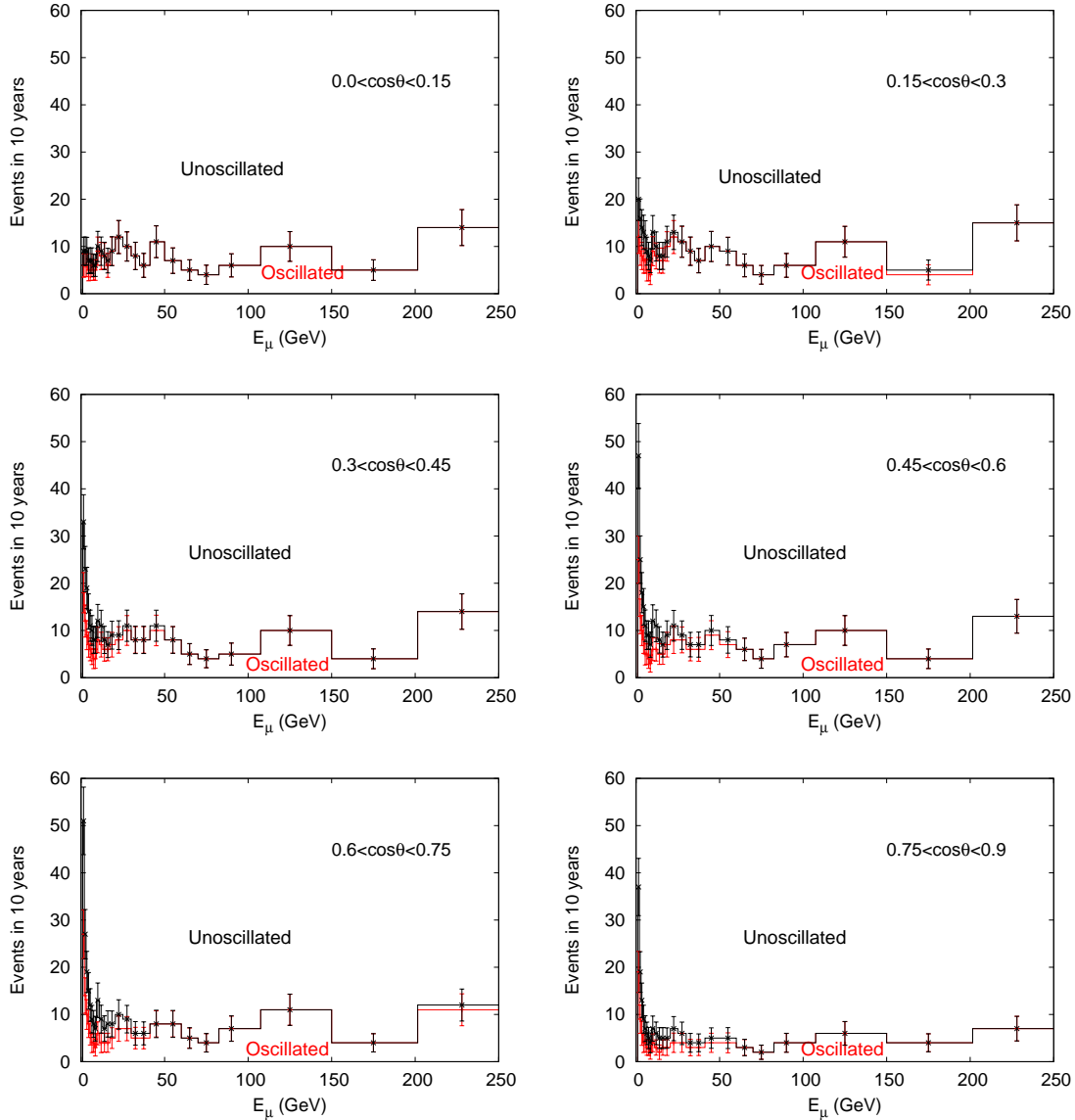


Figure 5.9: Energy distribution of muons (E_{μ^-}) for different $\cos\theta$ bins with and without 3-flavour oscillations.

where N_{μ}^{\pm} are the total number of μ^{\pm} events after detector smearing and oscillations, ϵ_C^{\pm} is the cid efficiency (here $\epsilon_C^+ = \epsilon_C^-$), and ϵ_R is the reconstruction efficiency. Note that ϵ_R and ϵ_C are determined from simulations (refer to sub-sections 4.4.1 and 4.4.2) as functions of the true energy and $\cos\theta$ ($E_{\mu}^t, \cos\theta^t$) of the muons, while $N_{\mu}^{\pm}(E_{\mu}, \cos\theta_{\mu})$ refer to the smeared (or, in the actual experiment, observed) values for the muons. The second term in Equation 5.5 is the contribution of the wrong charge muon due to charge

$\cos \theta$ (min)	$\cos \theta$ (max)	E_{min} (GeV)	E_{max} (GeV)	Unosc (μ^-)	Osc (μ^-)	Unosc (μ^+)	Osc (μ^+)
0.15	0.3	1	2	9	6	5	3
0.15	0.3	2	3	9	6	5	3
0.15	0.3	3	4	9	6	5	3
0.15	0.3	4	5	7	5	4	3
0.15	0.3	5	6	7	5	4	3
0.15	0.3	6	7	7	6	3	2
0.15	0.3	7	8	6	5	3	2
0.15	0.3	8	9	6	5	3	2
0.15	0.3	9	11	10	9	5	5
0.15	0.3	11	13	9	8	5	4
0.15	0.3	13	15	8	8	4	4
0.15	0.3	15	17	7	6	4	3
0.15	0.3	17	20	9	9	4	4
0.15	0.3	20	25	12	12	6	5
0.15	0.3	25	30	10	10	5	5
0.15	0.3	30	35	8	8	4	4
0.15	0.3	35	40	6	6	4	4
0.15	0.3	40	50	11	11	5	5
0.15	0.3	50	60	7	7	3	3
0.15	0.3	60	70	5	5	3	3
0.15	0.3	70	80	4	4	2	2
0.15	0.3	80	100	6	6	3	3
0.15	0.3	100	150	10	10	6	6
0.15	0.3	150	200	5	5	3	3
0.15	0.3	200	256	14	14	9	9

Table 5.4: Oscillated and unoscillated events for the observed energy bin and $0.15 < \cos \theta < 0.3$ bin.

$\cos \theta$ (min)	$\cos \theta$ (max)	E_{min} (GeV)	E_{max} (GeV)	Unosc (μ^-)	Osc (μ^-)	Unosc (μ^+)	Osc (μ^+)
0.3	0.45	1	2	20	12	9	5
0.3	0.45	2	3	16	9	10	5
0.3	0.45	3	4	14	8	6	3
0.3	0.45	4	5	13	7	5	3
0.3	0.45	5	6	12	7	6	3
0.3	0.45	6	7	9	5	5	2
0.3	0.45	7	8	8	5	3	2
0.3	0.45	8	9	7	4	3	2
0.3	0.45	9	11	13	9	6	4
0.3	0.45	11	13	10	8	5	4
0.3	0.45	13	15	8	7	5	4
0.3	0.45	15	17	8	7	4	3
0.3	0.45	17	20	11	10	5	4
0.3	0.45	20	25	13	12	7	6
0.3	0.45	25	30	11	11	5	5
0.3	0.45	30	35	9	9	5	5
0.3	0.45	35	40	7	7	3	3
0.3	0.45	40	50	10	10	6	6
0.3	0.45	50	60	9	9	4	4
0.3	0.45	60	70	6	6	3	3
0.3	0.45	70	80	4	4	2	2
0.3	0.45	80	100	6	6	3	3
0.3	0.45	100	150	11	11	6	6
0.3	0.45	150	200	5	4	3	3
0.3	0.45	200	256	15	15	7	7

Table 5.5: Oscillated and unoscillated events for the observed energy bin and $0.3 < \cos \theta < 0.45$ bin.

mis-identification, while both N_{μ}^+ and N_{μ}^- contain the contributions from $P_{\mu\mu}$ and $P_{e\mu}$ terms of Equation 5.3. The events oscillated according to the parameters mentioned earlier (refer to section 5.2.4) is scaled down to 4.5 or 10 years and labelled as “data”.

Chapter 5. Oscillation Analysis with Upward-going Muons

$\cos \theta$ (min)	$\cos \theta$ (max)	E_{min} (GeV)	E_{max} (GeV)	Unosc (μ^-)	Osc (μ^-)	Unosc (μ^+)	Osc (μ^+)
0.45	0.6	1	2	33	18	15	8
0.45	0.6	2	3	23	12	11	5
0.45	0.6	3	4	19	9	9	4
0.45	0.6	4	5	14	7	7	3
0.45	0.6	5	6	11	6	6	3
0.45	0.6	6	7	10	5	4	2
0.45	0.6	7	8	8	4	5	2
0.45	0.6	8	9	8	4	4	2
0.45	0.6	9	11	12	8	6	3
0.45	0.6	11	13	11	7	5	3
0.45	0.6	13	15	8	6	5	3
0.45	0.6	15	17	7	6	3	3
0.45	0.6	17	20	9	7	4	3
0.45	0.6	20	25	9	8	6	5
0.45	0.6	25	30	11	10	5	4
0.45	0.6	30	35	8	8	5	4
0.45	0.6	35	40	8	8	3	3
0.45	0.6	40	50	11	10	6	5
0.45	0.6	50	60	8	8	4	4
0.45	0.6	60	70	5	5	3	3
0.45	0.6	70	80	4	4	2	2
0.45	0.6	80	100	5	5	3	3
0.45	0.6	100	150	10	10	6	6
0.45	0.6	150	200	4	4	2	2
0.45	0.6	200	256	14	14	7	7

Table 5.6: Oscillated and unoscillated events for the observed energy bin and $0.45 < \cos \theta < 0.6$ bin.

$\cos \theta$ (min)	$\cos \theta$ (max)	E_{min} (GeV)	E_{max} (GeV)	Unosc (μ^-)	Osc (μ^-)	Unosc (μ^+)	Osc (μ^+)
0.6	0.75	1	2	47	25	23	11
0.6	0.75	2	3	25	13	13	6
0.6	0.75	3	4	18	10	10	6
0.6	0.75	4	5	15	8	8	4
0.6	0.75	5	6	11	5	6	3
0.6	0.75	6	7	9	5	5	2
0.6	0.75	7	8	9	4	4	2
0.6	0.75	8	9	7	3	4	2
0.6	0.75	9	11	12	6	6	3
0.6	0.75	11	13	11	6	5	3
0.6	0.75	13	15	8	5	4	3
0.6	0.75	15	17	7	5	3	2
0.6	0.75	17	20	9	7	4	3
0.6	0.75	20	25	11	8	5	4
0.6	0.75	25	30	9	8	5	4
0.6	0.75	30	35	7	6	3	3
0.6	0.75	35	40	7	6	3	3
0.6	0.75	40	50	10	9	6	5
0.6	0.75	50	60	8	7	4	4
0.6	0.75	60	70	6	6	3	3
0.6	0.75	70	80	4	4	3	3
0.6	0.75	80	100	7	7	3	3
0.6	0.75	100	150	10	10	5	5
0.6	0.75	150	200	4	4	2	2
0.6	0.75	200	256	13	13	9	8

Table 5.7: Oscillated and unoscillated events for the observed energy bin and $0.6 < \cos \theta < 0.75$ bin.

The same set is scaled but oscillated according to an arbitrary set of oscillation parameters and referred to as “theory” in this simulation analysis.

$\cos \theta$ (min)	$\cos \theta$ (max)	E_{min} (GeV)	E_{max} (GeV)	Unosc (μ^-)	Osc (μ^-)	Unosc (μ^+)	Osc (μ^+)
0.75	0.9	1	2	51	27	24	12
0.75	0.9	2	3	27	14	12	6
0.75	0.9	3	4	19	10	10	5
0.75	0.9	4	5	15	8	7	3
0.75	0.9	5	6	12	6	6	3
0.75	0.9	6	7	9	4	5	2
0.75	0.9	7	8	8	4	4	2
0.75	0.9	8	9	7	3	3	2
0.75	0.9	9	11	13	6	5	2
0.75	0.9	11	13	9	4	5	2
0.75	0.9	13	15	7	4	3	2
0.75	0.9	15	17	8	4	3	2
0.75	0.9	17	20	8	5	4	2
0.75	0.9	20	25	10	7	6	4
0.75	0.9	25	30	9	7	4	3
0.75	0.9	30	35	6	5	4	3
0.75	0.9	35	40	6	5	3	3
0.75	0.9	40	50	8	8	4	4
0.75	0.9	50	60	8	8	4	4
0.75	0.9	60	70	5	5	3	3
0.75	0.9	70	80	4	4	2	2
0.75	0.9	80	100	7	7	3	3
0.75	0.9	100	150	11	11	6	5
0.75	0.9	150	200	4	4	2	2
0.75	0.9	200	256	12	11	7	7

Table 5.8: Oscillated and unoscillated events for the observed energy bin and $0.75 < \cos \theta < 0.9$ bin.

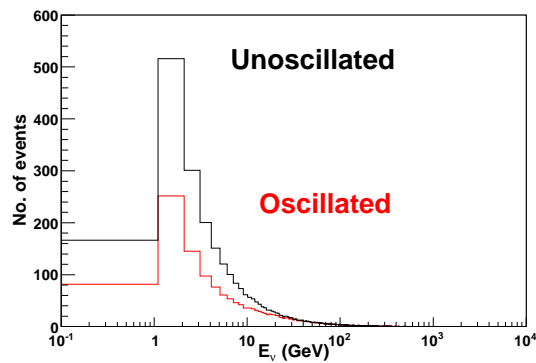


Figure 5.10: Energy profile of the neutrinos surviving 3-flavour oscillations for 10 years of data.

5.2.5 χ^2 Analysis

The two types of measurement errors are statistical errors and systematic errors. Statistical errors arise from random quantum processes and are given by the standard deviation of the sampling distribution of a statistic. On the other hand, systematic errors usually come from the measuring instruments and the techniques followed to do the observations. The reason for these errors are: if there is something wrong with the instrument or its data handling system, or the instrument is wrongly used by the experimenter. While comparing data with theory, systematic effects also arise due to uncertainties in the theory. The accuracy of measurements is often reduced by systematic errors. We use the pull method for the treatment of systematic errors in the χ^2 analysis; the idea of using it [50] is to parametrize the systematic errors in terms of a set of variables say ξ , called pulls, which are then treated on the same footing as the other parameters of the model.

The χ^2 analysis includes the “data” binned as specified in Tables 5.1, 5.2 with the addition of systematic uncertainties [50]. Different χ^2 analysis (a statistical method to assess the goodness of fit between a set of observed values and the ones expected theoretically) are performed. First of all, the μ^\pm events are combined to get the total events in each bin so that the charge identification information is not used:

$$\chi^2 = \sum_{i,j} \left(\frac{N_{ij}^{th} (1 + \sum_{k=0}^5 \pi_{ij}^k \xi_k) - N_{ij}^{ex}}{\sigma_{ij}^{stat}} \right)^2 + \sum_{k=0}^5 \xi_k^2 . \quad (5.6)$$

Here N_{ij}^{th} , N_{ij}^{ex} are the theoretically predicted and observed “data” in E_μ and $\cos \theta$ bins, π_i^j are the systematic errors defined below, ξ_j are the pull variables. For this analysis we have defined Gaussian χ^2 with σ_{ij}^{stat} , the statistical errors, defined as $\sqrt{(N_{ij}^{ex})}$.

The set of systematic uncertainties [50] considered for our analysis are a flux normalisation error of 20%, 10% error on cross-sections, 5% error on zenith angle dependence of flux, and an energy dependent tilt error, which is described as follows. The event

spectrum is calculated with the predicted atmospheric neutrino fluxes and with the flux spectrum shifted as,

$$\Phi_\delta(E) = \Phi_0(E) \left(\frac{E}{E_0} \right)^\delta \simeq \Phi_0(E) \left(1 + \delta \ln \frac{E}{E_0} \right). \quad (5.7)$$

The different parameters are, $E_0 = 2$ GeV, $\delta = 1\sigma$ systematic tilt error, which is taken as 5%. In addition, an overall systematic of 5% has been included to account for uncertainties such as those arising from the reconstruction of the muon energy and direction, due to uncertainties in the magnetic field used in the Kalman filter, as discussed in the previous chapter. In total, there are 5 systematic uncertainties. For the simple 2-flavour analysis, we considered a single normalisation error of 20%. Better sensitivity was found to be obtained when the μ^+ and μ^- events were separately considered. While the systematic errors were taken to be the same as before, there are now 10 pulls, 5 for each charge sign. Since the events in each bin are now smaller, we use the Poissonian definition of χ^2 (refer to [73]):

$$\chi_\pm^2 = \sum_{i=1} \sum_{j=1} \left[2 \left(N_{ij}^{th}(\mu^\pm) - N_{ij}^{ex}(\mu^\pm) \right) - 2N_{ij}^{ex}(\mu^\pm) \ln \left(\frac{N_{ij}^{th}(\mu^\pm)}{N_{ij}^{ex}(\mu^\pm)} \right) \right]; \quad (5.8)$$

$$\chi^2 = \chi_-^2 + \chi_+^2 + \sum_{k=1}^{10} \xi_k^2, \quad (5.9)$$

where,

$$N_{ij}^{th}(\mu^\pm) = N_{ij}(\mu^\pm) \left(1 + \sum_{k=1}^{10} \pi_{ij}^k \xi_k \right). \quad (5.10)$$

Here N_{ij}^{th} , N_{ij}^{ex} are the theoretically predicted data and observed data in given bins $(E_\mu, \cos\theta)$, and N_{ij} is the number of events without the systematic errors defined in Equation 5.5. π_{ij}^k are the systematic errors and ξ_k are the pull variables. The χ_\pm^2 are

independently minimised, first over the pulls for a given set of oscillation parameters, and then over the oscillation parameters themselves.

Till now, this analysis is an extension of the simulations analysis of the atmospheric neutrinos (contained) events to the rock muon events. However, it was found that further improvement in the sensitivity to the oscillation parameters can be obtained with the addition of an extra pull that constrains the $\nu_\mu/\bar{\nu}_\mu$ flux ratio. Since this therefore relates N_μ^+ and N_μ^- , the χ^2 can no longer be written as a simple sum over the N_μ^+ and N_μ^- contributions. We have,

$$\chi_\pm^2 = \sum_{i=1} \sum_{j=1} \left[2 \left(N_{ij}^{th}(\mu^\pm) - N_{ij}^{ex}(\mu^\pm) \right) - 2N_{ij}^{ex}(\mu^\pm) \ln \left(\frac{N_{ij}^{th}(\mu^\pm)}{N_{ij}^{ex}(\mu^\pm)} \right) \right]; \quad (5.11)$$

$$\chi^2 = \chi_-^2 + \chi_+^2 + \sum_{k=1}^{11} \xi_k^2, \quad (5.12)$$

where,

$$N_{ij}^{th-} = N_{ij}^- \left(1 + \sum_{k=1}^5 \pi_{ij}^k \xi_k^- - \pi_6 \xi_6 \right); \quad (5.13)$$

$$N_{ij}^{th+} = N_{ij}^+ \left(1 + \sum_{k=1}^5 \pi_{ij}^k \xi_k^+ + \pi_6 \xi_6 \right), \quad (5.14)$$

where ξ_k^\pm are the original set of 5 pulls each for μ^\pm and ξ_6 is the 11th pull that incorporates the constraint on the $\nu_\mu/\bar{\nu}_\mu$ flux ratios. Since $P_{e\mu}$ is small everywhere, we ignore the ν_μ/ν_e flux uncertainty. Then the 11th pull's effect can be understood by writing the ratios (momentarily ignoring the other pulls):

$$\frac{N^-}{N^+} = \frac{N_0^-(1 - \pi_6 \xi_6)}{N_0^+(1 + \pi_6 \xi_6)} \simeq \frac{N_0^-}{N_0^+} (1 - 2\pi_6 \xi_6) . \quad (5.15)$$

Hence a 5% uncertainty in this ratio is incorporated by taking $\pi_6 = 2.5\%$. Finally, the whole data is marginalised over the 3σ range of $\sin \theta_{23}$, Δm_{32}^2 and θ_{13} given in Table 5.9 and a prior on $\sin^2 2\theta_{13}$:

$$\chi^2 = \chi^2 + \left(\frac{\sin^2 2\theta_{13}(true) - \sin^2 2\theta_{13}}{\sigma_{\sin^2 2\theta_{13}}} \right)^2 ; \quad (5.16)$$

Parameter	Min. limit	Max. limit
$\sin \theta_{23}$	0.6	0.812
Δm_{32}^2	2.1×10^{-3}	2.6×10^{-3}
θ_{13}	7.671	9.685

Table 5.9: 3σ range of $\sin \theta_{23}$, Δm_{32}^2 and θ_{13} for marginalisation.

where $\sigma_{\sin^2 2\theta_{13}}$ is the 1σ error for the corresponding neutrino parameters which is taken to be 8% in this analysis. In order to determine χ_{min}^2 , the minimization of χ^2 is done over all three parameters θ_{23} , Δm_{32}^2 and θ_{13} keeping the other parameters fixed at their input values. For $\Delta\chi^2$ plots, we fixed two parameters; one is θ_{13} (always fixed) and the other is either Δm_{32}^2 or θ_{23} , which depends on the parameter we want to find. For $\Delta\chi^2$ vs $\sin^2 \theta_{23}$, Δm_{32}^2 is fixed and for $\Delta\chi^2$ vs Δm_{32}^2 , θ_{23} is fixed. We did not fix any parameter for contour analysis (as described in next section) and let θ_{23} , Δm_{32}^2 and θ_{13} vary over this 3σ allowed ranges.

5.3 Results of the Simulations Analyses

We begin with the simplest 2-flavour analysis. Since there are no matter effects, the muon events were not separated according to their charge and a Gaussian χ^2 minimisation was performed. Determination of the two dimensional confidence region of the two oscillation parameters $(\Delta m_{32}^2, \sin^2 \theta_{23})$ is done by minimising $\Delta\chi^2$ around the best fit value. We assumed $\Delta\chi^2 = \chi_{min}^2 + A$ to obtain contour plots, where χ_{min}^2 is the minimum value of χ^2 for each set of oscillation parameters and values of A are taken as 2.30, 4.61 and 9.21 corresponding to 68%, 90% and 99% confidence levels respectively for two degrees of freedom.

For 2-flavour analysis, Figure 5.11 shows 90 % CL contour of ICAL for 4.5 years data simulation in comparison with Super-K [183] data. For Super-K, $\sin^2 2\theta_{23} \geq 0.765$, $\Delta m_{32}^2 = (1.2 - 4.3) \times 10^{-3} eV^2$. For ICAL, $\sin^2 2\theta_{23} \geq 0.771$, $\Delta m_{32}^2 = (1.48 - 3.7) \times 10^{-3} eV^2$, so ICAL has similar sensitivity as Super-K for the same exposure.

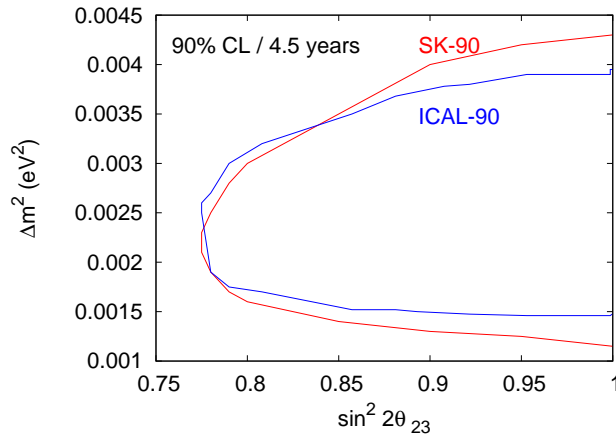


Figure 5.11: 90 % CL allowed contour of ICAL with 4.5 years of simulated data in comparison with the same contour obtained from 4.5 years data at Super-K, in the $\Delta m_{32}^2 - \sin^2 2\theta_{23}$ parameter space of 2-flavour oscillation analysis.

The oscillation results for 3-flavour analysis are shown in the next series of plots. Since the oscillation probabilities are now sensitive to matter effects, we consider the N_{μ}^+ and N_{μ}^- events separately. In order to have a more realistic analysis, we also include

systematic errors through the 5 pulls described earlier and use the Poissonian definition of χ^2 given in Equations 5.10 and 5.16. In Figure 5.12, ICAL detector's data is compared with Super-K [183] data for 4.5 years. For Super-K: $\sin^2 2\theta_{23} \geq 0.79$ and for ICAL : $\sin^2 2\theta_{23} \geq 0.69$ whereas Δm_{32}^2 is comparable for both ICAL and Super-K detector for 90% C.L contour. Right plot shows precision reach expected at ICAL in the $\sin^2 \theta_{23} - \Delta m_{32}^2$ plane for 4.5-years with the exposure of 50 kt detector. Since our three-neutrino analysis should be sensitive to the octant of θ_{23} [184], [185] therefore we choose $\sin^2 \theta_{23}$ instead of $\sin^2 2\theta_{23}$.

Figure 5.13 shows the precision reach expected at ICAL in the $\sin^2 \theta_{23} - \Delta m_{32}^2$ plane for 10-years with the exposure of 50 kt detector. Left plot shows the comparison of precision results when μ^+ and μ^- data are combined, or kept separate. It is seen that the cid capability of ICAL improves the sensitivity in both Δm_{32}^2 and $\sin^2 \theta_{23}$. Right plot shows the effect of including the constraint on the μ^+/μ^- flux ratio, using the definitions of χ^2 from Equations 5.14 and 5.16. Although inclusion of yet another systematic error tends to worsens the sensitivity here an improvement in the sensitivity is noticed with the addition of this pull to the earlier 10 systematic uncertainties. This is because this pull prevents the overall normalisations of μ^+ and μ^- events from varying independently as would have been the case earlier and thus acts like a constraint.

Also, because of the true value of $\sin^2 \theta_{23} = 0.5$, the contours are symmetric about $\sin^2 \theta_{23} = 0.5$ value. The values away from 0.5 would make the contours asymmetric and would result in some sensitivity to the octant of θ_{23} . We do not discuss this further here.

5.3.1 Sensitivity to Individual Parameters

We now study the individual sensitivities. For this, all parameters other than the one under study are varied within their 3σ ranges and the calculation is repeated. Here $\Delta\chi^2 = 1,4,9$, gives the 1σ , 2σ and 3σ allowed values for the parameter. Figure 5.14 shows $\Delta\chi^2$ as a function of Δm_{32}^2 using Δm_{32}^2 (true) = $2.4 \times 10^{-3} eV^2$ and $\sin \theta_{23} = 0.707$ with N_μ^+

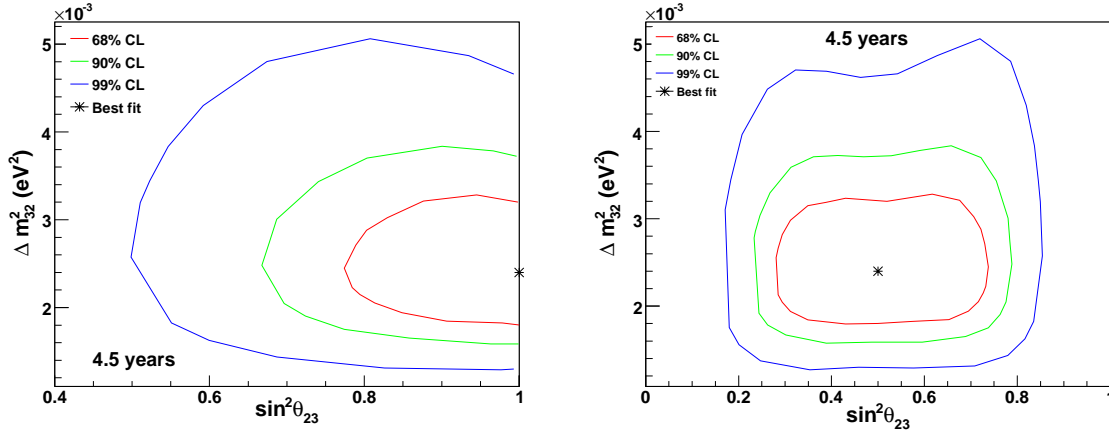


Figure 5.12: Left plot shows the allowed parameter space as a function of Δm_{32}^2 and $\sin^2 2\theta_{23}$ for simulations at ICAL with input values $\Delta m_{32}^2 = 2.4 \times 10^{-3} eV^2$ and $\sin^2 \theta_{23} = 0.707$. Right plot shows the precision reach expected at ICAL in the $\sin^2 \theta_{23} - \Delta m_{32}^2$ plane for 4.5-years running of the 50 kton detector.

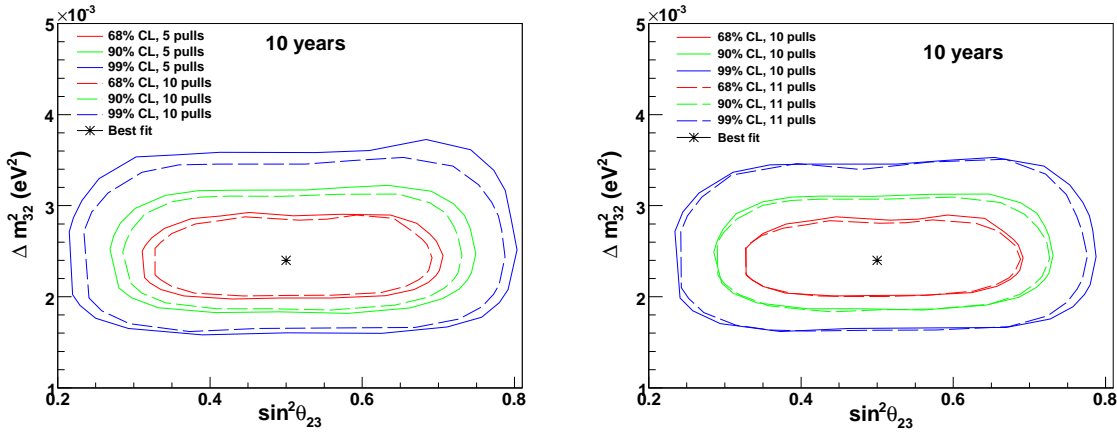


Figure 5.13: The precision reach expected at ICAL in the $\sin^2 \theta_{23} - \Delta m_{32}^2$ plane for 10-years with 50 kton detector. The left plot shows the comparison of precision results when μ^+ and μ^- events are combined and analysed (so no cid capability is assumed) and when they are kept separate. The latter shows better sensitivity. The right plot compares the effect of including the additional constraint on the μ^+/μ^- charge ratio. The sensitivity, especially on θ_{23} marginally improves.

and N_{μ^-} events considered together and separately. As with the 2nd contour, the analysis with cid efficiency included and separating N_{μ^+} and N_{μ^-} events gives a better sensitivity. Figure 5.14 also shows a similar plot for $\Delta\chi^2$ as a function of $\sin^2 \theta_{23}$ using $\Delta m_{32}^2 = 2.4 \times 10^{-3} eV^2$ and $\sin \theta_{23}$ (true) = 0.707, with similar improvement in the cid-dependent

analysis.

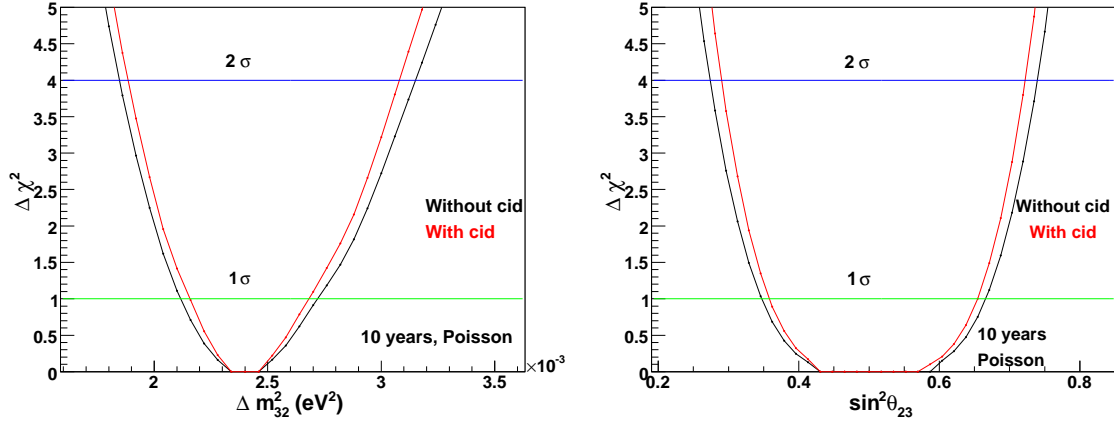


Figure 5.14: Left plot shows comparison of 5 systematic (black) with 10 systematic (red) for $\Delta\chi^2$ as a function of Δm_{32}^2 . Right plot shows comparison of 5 systematic (black) with 10 systematic (red) for $\Delta\chi^2$ as a function of $\sin^2\theta_{23}$.

We now consider the effect of the 11th pull. Figure 5.15, shows comparison of the sensitivities when μ^+ and μ^- events are combined (black), when considered separately (red) and when the additional 11th pull on the flux ratios is included (blue). All plots are for $\Delta\chi^2$ as a function of Δm_{32}^2 (left) and $\sin^2\theta_{23}$ (right) using Δm_{32}^2 (true) = $2.4 \times 10^{-3} \text{ eV}^2$ and $\sin\theta_{23} = 0.707$, for 10-year simulations with 50 kton detector. It is observed that the addition of one constraint with 10 systematic uncertainties improves overall sensitivity, but more to Δm_{32}^2 .

5.3.2 Precision Measurements

The precision on the oscillation parameters is given by:

$$\text{Precision} = \frac{P_{max} - P_{min}}{P_{max} + P_{min}}. \quad (5.17)$$

The parameters, P_{max} and P_{min} are the maximum and minimum values of the concerned oscillation parameters at a given confidence level. From Tables 5.10 and 5.11

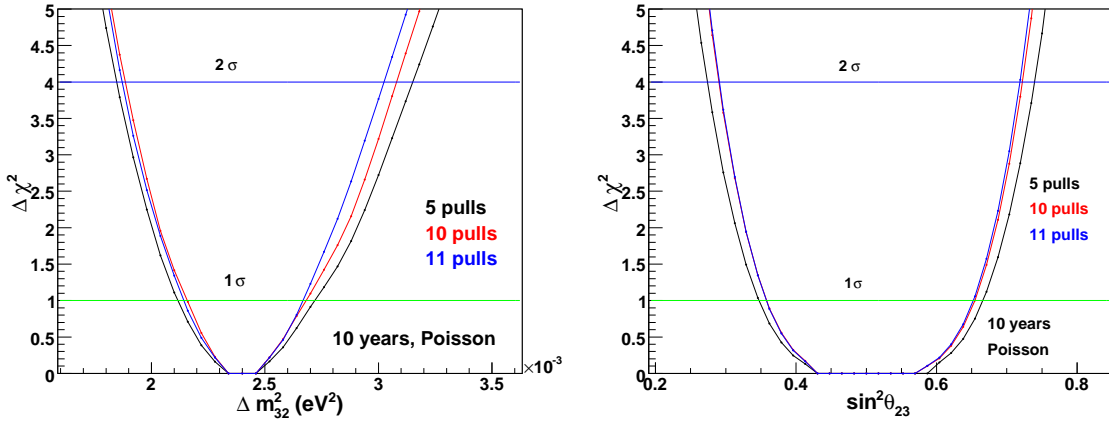


Figure 5.15: Sensitivity to Δm_{32}^2 (left) and $\sin^2 \theta_{23}$ (right) with different analysis: combining μ^+ and μ^- data so without cid is done (black curve), retaining them separately, with cid (red curve) and further including the 11th pull (blue curve).

we conclude that the addition of 10 systematic uncertainties along with one constraint together improves the capability of ICAL detector for the estimation of oscillation parameters significantly.

Precision			
Confidence level	5 pulls(%)	10 pulls(%)	10 pulls along with one constraint(%)
1 σ	38.8	35.7	35.5
2 σ	47.2	43.8	42.9
3 σ	57.7	54.1	52.4

Table 5.10: ICAL's capability for measuring the atmospheric mixing angle $\sin^2 \theta_{23}$ with a precision of at 1 σ , 2 σ and 3 σ confidence levels respectively.

Precision			
Confidence level	5 pulls(%)	10 pulls(%)	10 pulls along with one constraint(%)
1 σ	19.3	18.1	17.3
2 σ	27.8	25.6	25.4
3 σ	40	36.6	36.7

Table 5.11: ICAL's capability for measuring the atmospheric mass squared difference Δm_{32}^2 with a precision of at 1 σ , 2 σ and 3 σ confidence levels respectively.

5.3.3 Combining with Atmospheric Neutrino Analysis

The main goal of ICAL is to study sensitivity of atmospheric neutrinos to neutrino oscillation parameters. The bulk of these events are those where the neutrino interacts inside the

detector, so that the energy and angle of the muon are directly correlated to that of the initiating neutrino. We call these the “atmospheric neutrino” events. In this chapter, we have analysed the events when the atmospheric neutrinos interact in the rock surrounding the detector so that the muon undergoes energy loss before it reaches the detector. For this reason, these so-called “rock muon” events are not as sensitive to the oscillation parameters as the atmospheric neutrino events. However, neutrino experiments being low count rate experiments, we wish to consider all possible events to obtain maximum sensitivity.

Figure 5.16 shows the effect of including the rock events with atmospheric neutrino events analysed with the same 10 systematic uncertainties [186] using Δm_{32}^2 (true) = $2.4 \times 10^{-3} eV^2$ and $\sin \theta_{23} = 0.707$ for 10-years with 50 kton detector.

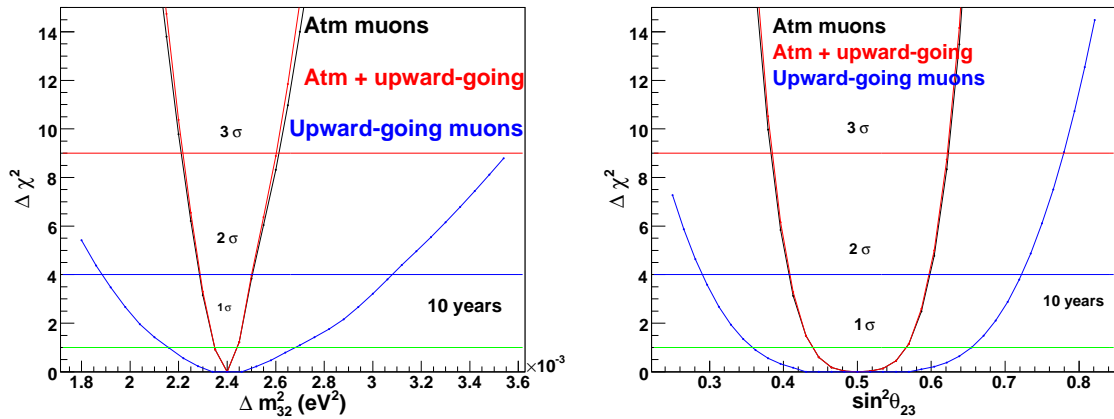


Figure 5.16: Left plot shows comparison of atmospheric muons (black) with combined atmospheric and upward-going muons (red), upward-going muons (blue) with 10 systematic uncertainties for $\Delta\chi^2$ as a function of Δm_{32}^2 . Right plot shows comparison of atmospheric muons (black) with combined atmospheric and upward-going muons (red), upward-going muons (blue) with 10 systematic uncertainties for $\Delta\chi^2$ as a function of $\sin^2 \theta_{23}$.

An improvement can be observed with the addition of upward-going muons to atmospheric muons. While this improvement is marginal, it is important to understand that the bulk of the contribution to these events are from high energy neutrinos as can be seen from Figure 5.10; hence these events explore a different kinematic range than the so-called “atmospheric neutrino” events that are produced by direct interaction of neutrinos in the

detector. In addition, these events are produced mainly through deep-inelastic scattering, where the cross-section uncertainties are smaller. We have chosen to retain the same systematic errors as for the main analysis; hence our results are somewhat conservative. Finally, these rock muon events will come “for-free” when the main atmospheric neutrino events are being acquired, and it is therefore necessary to analyse them and their contribution to our understanding of neutrino oscillation parameters.

To summarize, upward-going muons [187] originate from the interactions of atmospheric neutrinos within the rock material around the detector and carry signatures of neutrino oscillation. To analyse these events, the resolutions and efficiencies for ICAL were generated with vertex at the bottom part of the detector. The three neutrino flavor mixing with earth matter effect was considered and the marginalised $\Delta\chi^2$ analysis has been performed. The different systematic uncertainties were included and the results were compared with Super-K detector for 4.5 years of data. The analysis was also done for 10 years of 50 kton exposure of INO-ICAL detector, with an additional constraint in the μ^+/μ^- flux ratio apart from the usual 10 systematic uncertainties. Addition of upward-going muons to atmospheric muons improves the sensitivity, but is useful from different considerations as they explore a different kinematic region of atmospheric neutrino fluxes.

Chapter 6

Summary and Conclusions

The proposed Iron CALorimeter is contemplated as a detector for atmospheric muon neutrinos. At ICAL detector, muon tracks and hadron showers are reconstructed to produce neutrinos that we aimed to study and hence the studies related to muon and hadron reconstruction are crucial. ICAL detector has good energy, direction resolution and reconstruction and charge identification, timing resolution and has a wide range of energy (E) and path-length (L) travelled by muons. The ICAL detector will have a modular structure of total size 48 m \times 16 m \times 14.5 m having mass of 50 kt volume. The detector consists of a stack of 150 horizontal layers with iron plates sandwiched between Resistive Plate chambers (RPCs) which act as active detector elements. The ICAL detector will be magnetized with the magnetic field of about 1.3–1.5 Tesla. The magnetising power of ICAL will make it distinguish μ^- and μ^+ and hence can solve mass hierarchy problem. Along with that INO-ICAL aims to observe precise measurement of the oscillation parameters, evidence for matter effects, determine the sign of the mass-squared difference Δm_{32}^2 involved in atmospheric neutrino oscillations, CP violation in the leptonic sector, sterile neutrinos and probe non-standard effects beyond neutrino oscillations such as such as non-standard interactions (NSIs) to accommodate sub-leading effects in neutrino flavour transitions.

We worked on three different problems, namely, RPCs performance, detector re-

sponse and physics analysis with upward-going muons. These three analysis are linked to each other and are presented in that order. In our first analysis, we optimised and characterised glass RPC parameters. We began our work with selecting the electrode material for RPC. So we procured glass samples from different manufacturers. We initiated the characterisation of glass samples from manufacturers Asahi, Saint Gobain and Modi with the help of various facilities. We compared their physical properties and no significant difference was found in the density measurements. For electrical properties, we measured bulk resistivity and was found to be of the order of 10^{11} Ω -cm. For optical properties, we performed UV transmission test and Asahi and Saint Gobain glass showed better UV-VIS transmittance over Modi glass. Various elements were observed in the glass samples after WD-XRF and PIXE analysis, such as, those with high Z are mostly responsible for degrading the quality of the glass. On the basis of these properties we conclude that Asahi and Saint Gobain were better than Modi glass sample (refer to section 3.2). Then, we calibrated four gases (Freon(R134a), Isobutane, Argon and SF_6) used for our analysis. Our studies include two gases (avalanche mode), three gases (avalanche mode) and streamer mode with gas proportion as mentioned in section 3.3. Fabrication and characterisation of scintillator detectors of different widths, 1.8 cm, 2.5 cm and 3.8 cm, was done. Plateauing study was done in order to find operating voltages of the attached PMTs to the scintillator paddles and efficiency of more than 95% was obtained (refer to Figure 3.17). Before RPC testing, fabrication of pick-up panels of different strip width size, 1.8 cm, 2.8 cm and 3.8 cm was done using standardized procedure as laid down by the INO-ICAL collaboration. Then, the fabrication of RPCs of Asahi, Saint Gobain and Modi glass was done with standardized procedure. Efficiency and cross-talk measurements were done using these fabricated scintillator paddles, pick-up panels and RPCs. We observed that the addition of third gas either SF_6 or argon improves the efficiency and reduces the cross-talk. A shift of threshold voltage was observed with the decrease in the strip width size. For each combination of different strip widths with different RPCs, we obtained the best results

(cross-talk measurements) for Asahi and Saint Gobain glass with strip widths 2.8, 3.8 cm in the avalanche mode (three gases). The efficiency for these RPCs is greater than 90% (refer to Table 3.6). Cross-talk for Asahi glass RPC is $\approx 12\%$ and 20% for strip widths 2.8 and 3.8 cm respectively and $\approx 30\%$ and 20% for Saint Gobain glass RPC with strip widths 2.8 and 3.8 cm respectively (refer to Figure 3.39, Table 3.7). We measured the efficiency of RPC stack too and this was found to be greater than 90% (refer to Figure 3.44).

Our second part of analysis is a simulations study of the response of ICAL to muons (refer to chapter 4). For this, we simulated the muons using GEANT-based INO-ICAL code. Muons were propagated in the peripheral and side regions with the magnetic field non-uniform in both magnitude and direction which are further effected by edge effects, i.e., they are partially contained events (refer to Figure 4.2). Selection criteria were applied on the number of tracks as the muon scattered due to passage through support structure, causing more than one track. Thus, this cut ensured to take into account only one track. As the magnetic field and the detector geometry break the azimuthal symmetry so we analysed muons in different ϕ bins in all the regions. The binning scheme is different for both peripheral and side regions but side and central region ϕ bins are same. A cut on number of hits, $N_{hits}/\cos\theta > n_0$ was applied for partially contained tracks to get good efficiency. The nhits cut with $N_{hits}/\cos\theta > 15$ was considered to take into account the slant-moving muons and showed the best momentum resolutions (refer to Figure 4.18). We obtained average (over ϕ) momentum resolutions between 15–25% for $P_{in} = 1$ –15 GeV/c in the peripheral region, whereas side region resolutions are marginally better because of the uniform magnetic field in this region. A comparison was made to results obtained in a separate analysis in the central region (refer to section 4.5). For $P_{in} \geq 4$ GeV/c, a reconstruction efficiency of about 60–70% and a correct charge identification of about 97% was obtained and this decreased to about 90% for higher momenta $P_{in} \sim 50$ GeV/c in both peripheral and side regions. An angular resolution better than a degree for $P_{in} \geq 4$ GeV/c is obtained in the peripheral and side regions and is observed to be same

in all the regions (refer to section 4.5). Hence, we observed the ICAL detector will have good response to muons, with well-reconstructed direction and good charge identification capability which are the basic ingredients for solving the mass hierarchy problem and making precision measurements on neutrino oscillation parameters.

In the third part of our analysis we performed an oscillation analysis with simulated upward-going muons (refer to chapter 5). The estimation of oscillation parameters of upward-going muons provides an independent check on overall sensitivity and further improves the overall measurement of oscillation parameters. Upward-going muons or rock muons arise from the charged current interactions of atmospheric muon neutrinos with the rock material surrounding the detector. These muons carry a significant signature of oscillation. We extended our earlier study on muon response in ICAL to obtain the resolutions and efficiencies when vertex of the event (here single muon) is taken at the bottom part of the ICAL detector and used them for upward-going analysis. We generated 200 years of data with NUANCE neutrino generator. Input parameters taken for data generation are, $\theta_{23} = 45^\circ$ ($\sin \theta_{23} = 0.707$), $\Delta m_{32}^2 = 2.4 \times 10^{-3} eV^2$, $\Delta m_{21}^2 = 7.6 \times 10^{-5} eV^2$, $\sin^2 \theta_{12} = 0.304$, $\sin^2 \theta_{13} = 0$ (or 0.1) for 2-flavour (or 3-flavour), $\delta_{cp} = 0$. Angle cut of $0^\circ < \theta < 81^\circ$ was applied to cut off cosmic ray backgrounds. Only CC ν_μ events were taken for analysis which were not passed through the ICAL detector via INO-ICAL code. Data is oscillated using re-weighting algorithm and binned into 25 energy and 7 $\cos \theta$ bins. The whole data is then scaled down to 4.5 years or 10 years. Marginalisation was applied for $\Delta\chi^2$ analysis over three parameters θ_{23} , Δm_{32}^2 and θ_{13} . Five different sets of systematic uncertainties were taken including overall normalisation of fluxes and cross sections, zenith angle uncertainty and tilt uncertainty (individually for neutrinos and anti-neutrinos). The ICAL detector simulations results were compared with Super-K detector data for 4.5 years. In a different analysis, 10 years of 50 kton of detector was used, and the sensitivity was found to improve with 10 systematic uncertainties along with one additional new constraint. The constraint was applied to the ratio of the neutrino to anti-

neutrino fluxes, which is much better known than the individual fluxes themselves. The addition of upward-going muons to the atmospheric muons further improves the overall sensitivity (refer to section 5.3).

Hence our studies establish that ICAL will be a good detector with good muon energy and direction detection capability and excellent charge identification. In addition, neutrino experiments being low count-rate experiments, it is useful to study neutrino oscillations through a completely independent (although less sensitive) process such as upward-going rock muons.

Future Outlook

It is possible to improve the understanding of muon response by further studying its dependence on the variation in magnitude and direction of the magnetic field. Effect of local variations and even temporal fluctuations need to be thoroughly studied. Some preliminary studies of cosmic ray muon detection in small RPC stacks (without iron plates and hence without magnetic field) have been carried out. A 1/8th scaled prototype of one module of ICAL (2 kton mass) is currently under construction. A direct future work is to apply the results we have obtained for muon resolution to study cosmic ray muons in this prototype. It will also be possible to validate our understanding of the different regions of ICAL using this prototype. This is crucial to optimise the fiducial volume of the detector.

On the experimental side, further studies of RPC stability and efficiency must continue to be carried out so that the characteristics of the RPCs used in the ICAL detector, when finally built, will be of consistently high standards.

Appendix A: Detector Simulation Framework

The INO-ICAL detector simulation is based on Geant4 [90] toolkit, thus is modular and flexible. It consists of the ICAL detector information, which can be modified as needed, the types of interaction which the charge particles undergo in the detector volume. The simulations are run with a set of input parameters and the output generated is in the form of rootuple, based on ROOT analysis framework [188]. INO-ICAL code [173] consists of four main components which are particle generation, simulation, digitization, reconstruction and then the output is used for analysis to get the results. The description of the simulation framework is given as:

- *Neutrino event generation (Geant4/NuanceV3.5 [180]):* Particles that results from a random interaction of a neutrino with matter using theoretical models are generated with the neutrino event generator NuanceV3.5. The outputs are the reaction channels or processes, vertex information, energy and momentum of all the particles.
- *Event simulation (Geant4):* Particles propagated through the matter are simulated. The outputs are the position and time of the particles at their interaction point in the detector, also it gives the energy deposited and momentum information.
- *Event digitization (Geant4):* The detector efficiency and noise to the hits are added. The output from the event simulation are digitized.
- *Event reconstruction:* Track finding and fitting are done so that the outputs are the energy and momentum (magnitude and direction) of initial neutrino.

Our analysis used the step from generation to reconstruction.

Appendix B: Muon Simulation Framework in ICAL

Muons being minimum ionizing particles and most sensitive to ICAL detector leave long and clean tracks in it. The muon momentum can be reconstructed either by curvature of its track or by path length method. The upward-going muons can be discriminated from downward-coming muons by the precise (ns) response time of RPC which is essential to be determined as both carry different oscillation signatures. The direction of curvature of the track is used to determine the charge of muon thus distinguishing ν_μ and $\bar{\nu}_\mu$ interactions. On the other hand, hadrons leave shower in the detector so their energy is determined from the total number of hits [172]. For multiple tracks, the track reconstructed closest to the vertex is considered as the muon track. The reconstruction of muon track is based on a Kalman filter algorithm [174] that considers the magnetic field. This algorithm works in the following steps:

Hit and track generation: When muon passes through the RPC, it produces a “hit” in the detector which has some x or y values as per the information from pick-up strip, a z-value from the layer information, and a time stamp t. Then the hit information is digitised with the strip width information considered in such a way that the spatial resolution in the horizontal plane is of the order of cm and in the z direction its of the order of mm (due to the gas gap). The R & D work on RPCs [160] have given information on cross-talk which has been incorporated into the analysis (refer to chapters 3 and 4). Also, the x and y strip information are independent and the possible pairs of nearby x and y hits in a plane are combined to form a cluster. A set of clusters further generated in a few successive layers are known as a tracklet.

The track finder: The basic elements for the track finder algorithm are clusters. Muons leave around one hit per layer while traversing (~ 1.6 , on average) whereas hadrons and electrons produce showers leaving several hits per layer. Considering the cross-talk also (which produces more than one hit in a plane for muons too), the separation/rejection of

hadronic showers is done by an algorithm that puts a cut on the total number of hits in a given RPC module.

The track finder algorithm utilizes a curve fitting algorithm which finds tracklets by further finding clusters in three adjacent planes. When there is no hit (due to inefficiency) in a given plane then finder considers the adjoining planes as well. Adjacent tracklets are combined to form the tracks and then the iterations are done in order to find the longest possible tracks [189]. The timing information averaged over the timing values of x and y in a plane gives the direction (up/down) of the track. The finder also separate the tracks as “shower-like” or “muon-like”. In case of muon-like tracks it must have at least 5 hits in the event and then the clusters in a layer are averaged to produce a single hit per layer with x, y and timing information which are sent to the track fitter for further analysis. So for a nearly vertical muon, a minimum momentum of about $0.4 \text{ GeV}/c$ is required ($0.4/\cos\theta$ in the absence of the magnetic field) below which no track is fitted.

The track fitter: The fitting of tracks is done with Kalman-filter based algorithm which depends on the bending of the tracks in the magnetic field. Each track is recognized by a starting vector $X_0 = (x, y, dx/dz, dy/dz, q/p)$ containing the position of the earliest hit (x, y, z) as recorded by the finder, with the charge-weighted inverse momentum q/p taken to be zero. As the tracks are virtually straight at the beginning, the initial track direction is measured by using the first two layers. Then using Kalman-filter algorithm and the information on the local magnetic field along with the geometry and composition of the matter through which the particle propagates, this initial state vector is then extrapolated to the next layer. This extrapolation considers noise due to multiple scattering [190] and energy loss in matter (iron) as per Bethe formula [191]. Then a comparison is done of the extrapolated point with the actual location of a hit in that layer and the process is iterated.

The fit parameters: The iteration process gives the best fit to the track. The extrapolation of track is done to another half-layer of iron to find the vertex of the interaction.

Then the best fit value of the momentum at the vertex is returned as the reconstructed momentum (both in magnitude and direction). While q/p calculates the magnitude of the momentum at the vertex, the direction is measured using dx/dz and dy/dz , which yield $\cos\theta$ and ϕ . We used only those fits for which the quality of fit is better than $\chi^2/ndf < 10$. Then each muon track is further analysed to identify its direction, charge and momentum as discussed in chapter 4.

Appendix C: Smearing Options in INO-ICAL Geant Code

In real detector a particle can be found anywhere, so in simulations study we choose to smear the particle co-ordinates to get more realistic results. Smearing of vertex, energy, zenith angle and azimuthal angle is required to generate events in INO-ICAL geant code [173]. We generated muons in two ways, firstly, fixed vertex events; with just small smearing ± 10 cm and a fixed vertex. Secondly, muons having vertex which depends on the different regions (central, peripheral or side regions) with smearing in such a way that the vertex spreads covering almost entire region say, peripheral region [176].

There are two options to smear the co-ordinates. Gaussian or uniform smearing for energy, vertex, zenith angle and azimuthal angle and can be done in a file that is required to for generating the events. The following commands are used to smear the co-ordinates.

```
/Ical0/gun/ensmear enerSmear  
/Ical0/gun/thsmear thetaSmear  
/Ical0/gun/phsmear phiSmear  
/Ical0/gun/vxsmear vxSmr  
/Ical0/gun/vysmear vxSmr  
/Ical0/gun/vzsmear vxSmr
```

Gaussian smearing is when,

- $\text{enerSmear} \geq 0$ with $\text{sigma} = \text{enerSmear}$ in GeV.
- $\text{thetaSmear} \geq 0$ with $\text{sigma} = \text{thetaSmear}$ in milliradian.
- $\text{phiSmear} \geq 0$ with $\text{sigma} = \text{phiSmear}$ in milliradian.
- $\text{vxSmr} \geq 0$ with $\text{sigma} = \text{vxSmr}$ in cm.
- $\text{vySmr} \geq 0$ with $\text{sigma} = \text{vySmr}$ in cm.

-
- $vzSmr \geq 0$ with $\sigma = vzSmr$ in cm.

Uniform smearing is when,

- $enerSmear < 0$ then, uniformly smeared in range $ener - enerSmear$ to $ener + enerSmear$ in GeV.
- $thetaSmear < 0$ then, uniformly smeared in range $theta - thetaSmear$ to $theta + thetaSmear$ in milliradian.
- $phiSmear < 0$ then, uniformly smeared in the range $phi - phiSmear$ and $phi + phiSmear$ in milliradian.
- $vxSmr < 0$ then, uniformly smeared in the range $vx - vxSmr$ and $vx + vxSmr$ in cm.
- $vySmr < 0$ then, uniformly smeared in the range $vy - vySmr$ and $vy + vySmr$ in cm.
- $vzSmr < 0$ then, uniformly smeared in the range $vz - vzSmr$ and $vz + vzSmr$ in cm.

For our analysis, we uniformly smeared vertex, θ and ϕ .

Bibliography

- [1] W. N. Cottingham and D. A. Greenwood *An Introduction to the Standard Model of Particle Physics*, 2nd Ed., Cambridge University Press, (2007).
- [2] S. Glashow: Nucl. Phys. 22, 579 (1961); S. Weinberg: Phys. Rev. Letter. 19, 1264 (1967); A. Salam in Elementary Particle Theory, Nobel Symp. N. 8, ed. by N.Svartholm, Aspenasgarden, Stockholm, 367 (1968).
- [3] M. Herrero, *The Standard Model*, arXiv:hep-ph/9812242v1 (3 Dec 1998).
- [4] P. Langacker, *Introduction to the Standard Model and Electroweak Physics*, arXiv:hep-ph/0901.0241 (2009).
- [5] D. H. Perkins, *Introduction to High Energy Physics*, 4th Ed., Addison-Wesley Publishing Company Inc., (2000).
- [6] D. Griffiths, *Introduction to Elementary Particles*, 2nd Ed., WILEY-VCH (2008).
- [7] CMS Collaboration, *Observation of a new boson at a mass of 125 GeV with the CMS experiment at the LHC*, Phy. Lett. B 716 (1), 30–61, arXiv:hep-ex/1207.7235 (2012).
- [8] ATLAS Collaboration, *Observation of a new particle in the search for the Standard Model Higgs boson with the ATLAS detector at the LHC*, Phy. Lett. B 716 (1), 1–29, arXiv:hep-ex/1207.7214v2 (2012).
- [9] <https://en.wikipedia.org/wiki/Quark>

-
- [10] W. B. Rolnick. *The fundamental Particles and Their Interactions*, 1st Ed., Addison - Wesley Publishing Company, (1994).
- [11] Solveig Skadhauge, *Probing CPT violation with atmospheric neutrinos* Nucl. Phys. B 639 (1–2), 281–289 (2002).
- [12] R. N. Mohapatra et al., *Theory of neutrinos: A White Paper*, arXiv:hep-ph/0510213v2, 2 Dec 2005.
- [13] Y. Fukuda et al., (Super-Kamiokande Collaboration), Phys. Rev. Lett. 82, 2430 (1999); 86, 5651 (2001).
- [14] B. Aharmim et al., (SNO Collaboration) Phys. Rev. D 70, 093014, arXiv:hep-ex/0407029 (2004).
- [15] M. B. Smy et al., (Super-Kamiokande Collaboration), Phys. Rev. D 69, 011104, arXiv:hep-ex/0309011 (2004).
- [16] S. N. Ahmed et al., (SNO Collaboration), Phys. Rev. Lett. 92, 181301, arXiv:nucl-ex/0309004 (2004).
- [17] J. Yoo et al., (Super-Kamiokande Collaboration), Phys. Rev. D 68, 092002, arXiv:hep-ex/0307070 (2003).
- [18] B. T. Cleveland et al., *Astrophys. J.* 496, 505 (1998); *Nucl. Phys. B (Proc. Suppl.)* 38, 47 (1995).
- [19] W. Hampel et al., (Gallex Collaboration), Phys. Lett. B 447, 127 (1999).
- [20] J. N. Abdurashitov et al., (SAGE Collaboration), Phys. Rev. C 60, 055801 (1999).
- [21] M. Altmann et al., (GNO Collaboration), Phys. Lett. B 490, 16, arXiv:hep-ex/0006034 (2000).

-
- [22] H. V. Klapdor-Kleingrothaus, A. Dietz, L. Baudis, G. Heusser, I. V. Krivosheina, S. Kolb, B. Majorovits and H. Pas et al., *Eur. Phys. J. A* 12, 147, arXiv:hep-ph/0103062 (2001).
- [23] N. Ackerman et al., (EXO-200 Collaboration), *Phys. Rev. Lett.* 107, 212501, arXiv:nucl-ex/1108.4193 (2011).
- [24] W. Pauli, Offener Brief an die Gruppe der Radioaktiven bei der Gauvereins-Tagung zu Tbingen, (Open letter to the group of radioactive people at the Gauverein meeting in Tbingen), 1930.
- [25] G. Danby et al., *Phys. Rev. Lett.* 9, 36 (1962).
- [26] DONuT, K. Kodama et al., *Phys. Lett. B* 504, 218, arXiv:hep-ex/0012035 (2001).
- [27] Gernot Eder, *Terrestrial neutrinos*, Elsevier - *Nucl. Phys.*, Volume 78, Issue 3, 657-662, April 1966.
- [28] IceCube Collaboration, *Evidence for High-Energy Extraterrestrial Neutrinos at the IceCube Detector*, *Science* 342, 1242856, arXiv:astro-ph.HE/1311.5238 (2013).
- [29] M. S. Athar et al., *India-based Neutrino Observatory: Project Report Volume I*, <http://www.ino.tifr.res.in/ino/OpenReports/INOReport.pdf> (2006).
- [30] Super-Kamiokande, J. P. Cravens et al., *Phys. Rev. D* 78, 032002 (2008).
- [31] T. J. Haines et al., *Phys. Rev. Lett.* 57, 16 (1986).
- [32] Kamiokande-II, K.S. Hirata et al., *Phys. Lett. B* 205, 416 (1988).
- [33] Y. Ashie et al., (Super-Kamiokande Collaboration), *Phys. Rev. Lett.* 93, 101801, arXiv:hep-ex/0404034v1 (2004).
- [34] Super-Kamiokande, Y. Fukuda et al., *Phys. Rev. Lett.* 81, 1562, arXiv:hep-ex/9807003 (1998).

-
- [35] Super-Kamiokande, Y. Fukuda et al., Phys. Rev. Lett. 82, 2644, arXiv:hep-ex/9812014 (1999).
- [36] Super-Kamiokande, Y. Fukuda et al., Phys. Lett. B 433, 9, arXiv:hep-ex/9803006 (1998).
- [37] Super-Kamiokande, Y. Fukuda et al., Phys. Lett. B436, 33, arXiv:hep-ex/9805006 (1998).
- [38] W. W. M. Allison et al., Phys. Rev. D 72, 052005 (2005).
- [39] M. H. Ahn et al., (K2K Collaboration), Phys. Rev. D 74, 072003, arXiv:hep-ex/0606032 (2006).
- [40] K. Eguchi et al., (KamLAND Collaboration), Phys. Rev. Lett. 90, 021802, arXiv:hep-ex/0212021 (2003).
- [41] S. N. Ahmed et al., (SNO Collaboration), Phys. Rev. Lett. 92, 181301, arXiv:nucl-ex/0309004 (2004).
- [42] SNO, Q. R. Ahmad et al., Phys. Rev. Lett. 87, 071301 (2001).
- [43] SNO, A. L. Hallin, Prog. Part. Nucl. Phys. 64, 199 (2010).
- [44] B. Pontecorvo, Sov. Phys. JETP 7, 172 (1958).
- [45] Z. Maki, M. Nakagawa and S. Sakata, Prog. Theor. Phys. 28, 870 (1962).
- [46] S. M. Bilenky and B. Pontecorvo, Phys. Rept. 41, 225 (1978).
- [47] B. Pontecorvo, Sov. Phys. JETP 26, 984 (1968); Zh. Eksp. Teor. Fiz. 53, 1717 (1967).
- [48] F. P. An et al., (Daya Bay Collaboration), *Search for a Light Sterile Neutrino at Daya Bay*, Phys. Rev. Lett. 113, 141802 (2014).

-
- [49] D. Indumathi et al., *Neutrino oscillation probabilities: Sensitivity to parameters*, arXiv:hep-ph/0603264v2, 13 April 2006.
- [50] Michele Maltoni, M.C. Gonzalez-Garcia et. al., *Atmospheric neutrino Oscillations and new Physics* Phys. Rev. D 70, 033010, arXiv:hep-ph/0404085v1 (2004).
- [51] J. K. Ahn et al., (RENO Collaboration) *Observation of Reactor Electron Antineutrino Disappearance in the RENO Experiment*, Phys. Rev. Lett. 108, 191802, arXiv:hep-ex/1204.0626 (2012).
- [52] F. P. An et al., (DAYA BAY Collaboration) *Observation of electron-antineutrino disappearance at Daya Bay*, Phys. Rev. Lett. 108, 171803, arXiv:hep-ex/1203.1669 (2012).
- [53] J. Schechter, J. W. F. Valle, Phys. Rev. D 25, 2951 (1982); E. Takasugi, Phys. Lett. B149, 372 (1984).
- [54] M. Goldhaber, L. Grodzins, and A. W. Sunyar, *Helicity of Neutrinos*, Physical Review 109, 1015-1017, doi:10.1103/PhysRev.109.1015 (1958).
- [55] Lee Grodzins, *Measurement of Helicity*, Progress in Nuclear Physics 7, 163–241 (1959).
- [56] G. T. Zatsepin et al., *Upper limit of the spectrum of cosmic rays*, ZHETF Pis'ma 4, No. 3, 114–117, 1 August 1966.
- [57] D. D. Stancil et al., *Demonstration of communication using neutrinos*, Mod. Phys. Lett. A 27, 1250077, arXiv:hep-ex/1203.2847v2 (2012).
- [58] https://en.wikipedia.org/wiki/Cosmic_ray/
- [59] Adarkar, H. et al., *Experimental evidence for GUT proton decay UHEOCU-98-01*, arXiv:hep-ex/0008074.

-
- [60] K. Eguchi et al., (KamLAND Collaboration), Phys. Rev. Lett. 90, 021802, arXiv:hep-ex/0212021 (2003).
- [61] M. H. Ahn et al., (K2K Collaboration), Phys. Rev. Lett. 90, 041801, arXiv:hep-ex/0212007 (2003).
- [62] Y. Fukuda et al., (Super-Kamiokande Collaboration), Phys. Rev. Lett. 81, 1562, arXiv:hep-ex/9807003 (1998).
- [63] S. Fukuda et al., (Super-Kamiokande Collaboration), Phys. Rev. Lett. 85, 3999, arXiv:hep-ex/0009001 (2000).
- [64] W. W. M. Allison et al., (Soudan-2 Collaboration), Phys. Lett. B 449, 137, arXiv:hep-ex/9901024 (1999).
- [65] M. Ambrosio et al., (MACRO Collaboration), Phys. Lett. B 478, 5 (2000).
- [66] M. Ambrosio et al., (MACRO Collaboration), Phys. Lett. B 566, 35, arXiv:hep-ex/0304037 (2003).
- [67] M. Sanchez et al., (Soudan 2 Collaboration), Phys. Rev. D 68, 113004, arXiv:hep-ex/0307069 (2003).
- [68] M. Honda and T. Kajita, K. Kasahara, S. Midorikawa, Phys. Rev. D 52, 4985 (1995).
- [69] V. Agrawal et al., Phys. Rev. D 53, 1314-1323 (1996).
- [70] L. V. Volkova, Yad. Fiz. 31, 1510 (1980); Sov. J. Nucl. Phys. 31, 784 (1980).
- [71] A. V. Butkevitch, L. G. Dedenko and I. M. Zhelenznykh, Yad. Fiz. 50, 90 (1989); Sov. J. Nucl. Phys. 50, 142 (1989).
- [72] Choji Saji, *Study of upward-going muons in Super-Kamiokande*, PhD thesis, Niigata University, <http://www-sk.icrr.u-tokyo.ac.jp/sk/pub/sajithesis.pdf> (2002).

-
- [73] T. Thakore, A. Ghosh, S. Choubey and A. Dighe, *The Reach of INO for Atmospheric Neutrino Oscillation Parameters*, JHEP **1305**, 058, arXiv:hep-ph/1303.2534 (2013).
- [74] A. Ghosh, T. Thakore and S. Choubey, *Determining the Neutrino Mass Hierarchy with INO, T2K, NOvA and Reactor Experiments*, JHEP **1304**, 009, arXiv:hep-ph/1212.1305 (2013).
- [75] C. L. Bennett et al., *Astrophys. J.* **583**, 1 (2003).
- [76] C. Kraus et al., *Eur. Phys. J. C* **40**, 447, arXiv:hep-ex/0412056 (2005).
- [77] V. M. Lobashev et al., *Phys. Lett. B* **460**, 227 (1999).
- [78] A. Osipowicz et al., (KATRIN Collaboration), *KATRIN: A next generation tritium beta decay experiment with sub-eV sensitivity for the electron neutrino mass*, arXiv:hep-ex/0109033.
- [79] L. Baudis et al. (Heidelberg-Moscow Collaboration), arXiv:hep-ex/9902014, *Phys. Rev. Lett.* **83**, 41 (1999).
- [80] K. S. Hirata, et al., (Kamiokande-II Collaboration), *Phys. Rev. D* **38**, 448 (1988).
- [81] M. Apollonio et al., (CHOOZ Collaboration), *Eur. Phys. J. C* **27**, 331, arXiv:hep-ex/0301017 (2003).
- [82] T. Akiri et al., (LBNE Collaboration), arXiv:hep-ex/1110.6249 (2010).
- [83] D. S. Ayres et al., (NOvA Collaboration), arXiv:hep-ex/0503053 (2005).
- [84] MINOS Collaboration, *The MINOS Detectors Technical Design Report*, NUMI-L-337, FERMILAB-DESIGN-1998-02, Experiment: FNAL-E-0875 (1998).
- [85] ALEPH, DELPHI, L3, OPAL, and SLD Collaborations, and LEP Electroweak Working Group, and SLD Electroweak Group, and SLD Heavy Flavour Group, *Phys. Reports* **427**, 257 (2006).

-
- [86] C. Athanassopoulos, et al., (LSND Collaboration), Phys. Rev. Lett. 81, 1774 (1998); Phys. Rev. C 58, 2489 (1998).
- [87] T. K. Gaisser, *The Cosmic-ray Spectrum: from the knee to the ankle*, JOP: Conference Series 47, 15-20 (2006).
- [88] Bietenholz, Wolfgang et al., *Cosmic Rays and the Search for a Lorentz Invariance Violation*, Phys. Rept. 505, 145-185, arXiv:hep-ph/0806.3713, DESY-08-072 (2011).
- [89] Takaaki Kajita, Arthur B. McDonald, *Metamorphosis in the particle world*, The Nobel Prize in Physics 2015, http://www.nobelprize.org/nobel_prizes/physics/laureates/2015/press.pdf, 6 October 2015.
- [90] GEANT4 Collaboration, S. Agostinelli et al. *Geant4: a simulation toolkit*, Nucl. Instrum. Meth. **A 506**, 250–303, <http://geant4.cern.ch> (2003).
- [91] Kolahal Bhattacharya, et al., (INO Collaboration), *Error propagation of the track model and track fitting strategy for the iron calorimeter detector in India-based neutrino observatory*, Computer Physics Communications (Elsevier) **185** (12) 3259–3268, (2014).
- [92] G. Charpak et al., Nucl. Instrum. Meth. 62, 217 (1968).
- [93] G. L. Bruno, Ph.D. Thesis, (2000–2001).
- [94] J. Keuffel, Phys. Rev. 73, 531 (1948).
- [95] Christian Lippmann, *Detector Physics of RPCs*, Ph.D. Thesis, (2003).
- [96] V. Parchomchuk et al., Nucl. Instrum. Meth. 93, 269 (1971).
- [97] Y. Pestov, Nucl. Instrum. Meth. 196, 45 (1982).
- [98] Y. Pestov, Proc. Intl. Winter Meeting on Nucl. Phys., Bormio, Italy, (1998).

-
- [99] A. Arefiev et al., Nucl. Instrum. Meth. A 348, 318 (1994).
- [100] Infolytica Corp., *Electromagnetic field simulation software*,
<http://www.infolytica.com/en/products/magnet/>.
- [101] R. Santonico and R. Cardarelli, Nucl. Instrum. Meth. 187, 377 (1981).
- [102] R. Cardarelli et al., Nucl. Instrum. Meth. A 263, 20 (1988).
- [103] R. Cardarelli et al., Nucl. Instrum. Meth. A 382, 470 (1996).
- [104] C. C. Bueno et al., Proc. Intl. Nucl. Atlantic Conf., Brazil, (2007).
- [105] K. Abe et al., Nucl. Instrum. Meth. A 455, 397 (2000).
- [106] R. Cardarelli et al., Nucl. Instrum. Meth. A 333, 399 (1993).
- [107] P. Fonte, Nucl. Instrum. Meth. A 456, 6 (2000).
- [108] P. Fonte, IEEE Trans. on Nucl. Sci. 49, 881 (2002).
- [109] W. R. Leo, *Techniques for Nuclear and Particle Physics Experiments*, 2nd Ed.,
Narosa Publ. House, (1995).
- [110] A. Blanco, et al., Nucl. Instrum. Meth. A 513, 8 (2003).
- [111] CMS Collaboration, Technical Proposal, CERN-LHCC-94-38, 1994; CMS Collaboration, JINST 3, S08004 (2008).
- [112] L3 Collaboration, Nucl. Instrum. Meth. A 456, 113 (2000).
- [113] BaBar Collaboration, Nucl. Instrum. Meth. A 479, 1 (2002).
- [114] M. Yamaga et al., Nucl. Instrum. Meth. A 456, 109 (2000).
- [115] YBJ-ARGO Collaboration, Nucl. Instrum. Meth. A 562, 92 (2006); *ibid.*, 588, 7 (2008).

-
- [116] OPERA Collaboration, OPERA Proposal CERN/SPSC 2000-028, (2008); Nucl. Instrum. Meth. A 602, 631 (2009).
- [117] Yuguang Xie et al., Nucl. Instrum. Meth. A 599, 20 (2009).
- [118] Jiawen Zhang et al., Nucl. Instrum. Meth. A 540, 102 (2005).
- [119] ALICE Collaboration, Nucl. Instrum. Meth. A 604, 301 (2009).
- [120] A. Antonelli et al., Nucl. Instrum. Meth. A 337, 34 (1993).
- [121] E. Gorini, Nucl. Instrum. Meth. B 23A, 249 (1991).
- [122] G. Bressi, Nucl. Instrum. Meth. A 261, 449 (1987).
- [123] M. Ambrosio, Scientifica Acta 13, 245 (1998).
- [124] T&T Collaboration, Nucl. Instrum. Meth. A 344, 350 (1994).
- [125] G. Agnetto et al., Nucl. Instrum. Meth. A 359, 596 (1995).
- [126] AUGER Collaboration, Proc. 3rd Int. Workshop on RPCs and Related Detectors, Pavia, (1995).
- [127] C. Aramo, Scientifica Acta 13, 257 (1998).
- [128] ALICE Collaboration, *ALICE Technical Design Report of the Time-of-Flight System (TOF)*, CERN-LHCC 2000-12 (2000).
- [129] ATLAS Collaboration, *ATLAS Muon Spectrometer: Technical Design Report*, CERN-LHCC 97 - 22 (1997).
- [130] A. Aloisio et al., Nucl. Instrum. Meth. A 535, 265 (2004).
- [131] CMS Muon Collaboration, CERN/LHCC 97-32, (1997).
- [132] CMS Collaboration, JINST S08004, (2008).

-
- [133] LHCb Collaboration, CERN-LHCC-2001-010, (2001).
- [134] A. Bizzeti et al., LHCb Note, LHCb-2001/027, (2001).
- [135] A. N. Akindinov et al., Nucl. Instrum. Meth. A 533, 74 (2004).
- [136] M. Bogomilov et al., Proc. Workshop on RPCs and Related Detectors, Coimbra, Portugal, (2001).
- [137] M. Bogomilov et al., Nucl. Instrum. Meth. A 508, 152 (2003).
- [138] STAR TOF Collaboration, *Proposal for a Large Area Time of Flight System for STAR*, http://www.star.bnl.gov/~uanlj/MTDreview2010/TOF_20040524.pdf (2004).
- [139] B. Bonner et al., Nucl. Instrum. Meth. A 508, 181 (2003).
- [140] Byungsik Hong, Nucl. Instrum. Meth. A 602, 644 (2009).
- [141] Diego Gonzalez Diaz, *Research and developments on timing RPC's application to the ESTRELA detector of the HADES experiment at GSI*, Ph.D. Thesis, (2006).
- [142] D. Belver et al., Nucl. Instrum. Meth. A 602, 687 (2009).
- [143] A. Schuttauf et al., Nucl. Instrum. Meth. A 602, 679 (2009).
- [144] JingboWang et al., Proc. Workshop on RPCs and Related Detectors, GSI, Germany, (2010).
- [145] Daniel Bemmerer et al., Proc. Workshop on RPCs and Related Detectors, GSI, Germany, (2010).
- [146] P. Picchi and F. Pietropaolo, ICGF RAP. INT. 344/1997, Torino 1997 (CERN preprint SCAN-9710037).
- [147] T. Tabarelli de Fatis, Eur. Phys. J. C 24, 43 (2002).

-
- [148] Sergio Palomares-Ruiz , S.T. Petcov, Nucl. Phys. B 712, 392–410, arXiv:hep-ph/0406096 (2005).
- [149] R. Gandhi, P. Ghoshal, S. Goswami, P. Mehta and S. Uma Sankar, Phys. Rev. Lett. 94, 051801, arXiv:hep-ph/0411252 (2005).
- [150] Raj Gandhi et al., *Mass Hierarchy determination via future Atmospheric Neutrino Detectors*, arXiv:hep-ph/0707.1723v2, 6 Sep 2007.
- [151] Abhijit Samanta, *The mass hierarchy with atmospheric neutrinos at INO*, arXiv:hep-ph/0610196v3, 29 Jan 2009.
- [152] S. Choubey and P. Roy, Phys. Rev. D 73, 013006 (2005).
- [153] A. Datta et al., *Atmospheric neutrinos as a probe of CPT violation*, Phys. Rev. Lett. B 597, arXiv:hep-ph/0312027 (2004).
- [154] K. Nakamura et al., *Neutrino Properties: Particle Data Group*, JP G 37, 075021, (2010).
- [155] H. Murayama and T. Yanagida, Phys. Lett. B 520, 263 (2001).
- [156] A. S. Joshipura and S. Mohanty, Phys. Lett. B 584, 103 (2004), arXiv:hep-ph/0310210; A. S. Joshipura and S. Mohanty, *Constraining long-range leptonic forces using iron calorimeter detectors*, PRL Preprint, October 2004.
- [157] J. A. Grifols and E. Masso , Phys. Lett. B 579, 123 (2004).
- [158] R. Santonico, R. Cardarelli, Nucl. Instrum. Meth. A 187, 377 (1981).
- [159] R. Santonico, R. Cardarelli, Nucl. Instrum. Meth. A 263, 20 (1988).
- [160] B. Satyanarayana, *Design and Characterisation Studies of Resistive Plate Chambers*, Ph.D thesis, Department of Physics, IIT Bombay, PHY-PHD-10-701, (2009).

-
- [161] H. Czyrkowski, et al., Nucl. Instrum. Meth. A 419, 490 (1998).
- [162] K. K. Meghna, et al., Journal of Instrumentation 7, P10003 (2012).
- [163] <http://www.ammrf.org.au/myscope/spm/background>.
- [164] <http://kids.britannica.com/comptons/art-167800>.
- [165] A. Mengucci, A. Paoloni, M. Spinetti, L. Votano, Nucl. Instrum. Meth. A 583, 264 (2007).
- [166] M. Cwoik, W. Dominik, M. Gorski, J. Krolikowski, Nucl. Instrum. Meth. A 508, 38 (2003).
- [167] M. A. Lie-Hua, et al., Chinese Physics C 34 (8), 1116 (2010).
- [168] M. Salim, R. Hasan, N. Majumdar, S. Mukhopadhyay, B. Satyanarayana, JINST 7, P11019 (2012).
- [169] K. Abe, et al., Nucl. Instrum. Meth. A 455, 397 (2000).
- [170] Sarika Bhide, V. M. Datar, Satyajit Jena, S. D. Kalmani, N. K. Mondal, G. K. Padmashree, B. Satyanarayan, R. R. Shinde, P. Verma, Pramana - Journal of Physics 69 (6), 1015 (2007).
- [171] V. M. Datar, Satyajit Jena, S. D. Kalmani, N. K. Mondal, P. Nagaraj, L. V. Reddy, M. Saraf, B. Satyanarayan, R. R. Shinde, P. Verma, Nucl. Instrum. Meth. A 602, 744 (2009).
- [172] M. M. Devi et al., *Hadron energy response of the Iron Calorimeter detector at the India-based Neutrino Observatory*, JINST **8** P11003, [arXiv:1304.5115] (2013).
- [173] A. Chatterjee et al., *A Simulations Study of the Muon Response of the Iron Calorimeter detector at the India-based Neutrino Observatory*, JINST **9** P07001, [arXiv:1405.7243] (2014).

-
- [174] R. E. Kalman, *A new approach to linear filtering and prediction problems*. Journal of Basic Engineering **82** (1) 35–45, (1960).
- [175] Meghna, K.K., *Performance of RPC detectors and study of muons with the Iron Calorimeter detector at INO*, Ph.D thesis, submitted to Homi Bhabha National Institute (HBNI) (2015).
- [176] R. Kanishka et al., *Simulations study of muon response in the peripheral regions of the Iron Calorimeter detector at the India-based Neutrino Observatory*, JINST **10** P03011, [arXiv:1503.03369] (2015).
- [177] A. Habig et al., *Measurement of the flux and zenith-angle distribution of upward through-going muons by Super-Kamiokande*, arXiv:hep-ex/9812014v2, 18 March 1999.
- [178] Y. Ashie et al., *A Measurement of Atmospheric Neutrino Oscillation Parameters by Super-Kamiokande-I*, arXiv:hep-ex/0501064v2, 15 Jun 2005.
- [179] T. Stanev, *High Energy Cosmic Rays*, Springer-Praxis, Berlin (2003).
- [180] D. Casper, *The Nuance neutrino physics simulation, and the future*, Nucl. Phys. Proc. Suppl. **112** 161–170, [arXiv:0208030] (2002).
- [181] M. Honda T. Kajita, K. Kasahara and S. Midorikawa, Phys. Rev. D **70**, 043008, arXiv:astro-ph/0404457 (2004).
- [182] R. Kanishka et al., *Oscillation Analysis of Upward-going Muons in ICAL Detector at India-based Neutrino Observatory* to be submitted to JHEP.
- [183] Kazunori Nitta, *Neutrino Oscillation Analysis of Upward Through-going and Stopping Muons in Super-Kamiokande*, PhD thesis, Department of Physics, Osaka University, <http://www-sk.icrr.u-tokyo.ac.jp/sk/pub/nitta.pdf> (2003).

-
- [184] V. Barger, R. Gandhi, P. Ghoshal, S. Goswami, D. Marfatia, S. Prakash, S. K. Raut and S U. Sankar, Phys. Rev. Lett. 109, 091801, arXiv:hep-ph/1203.6012 (2012).
- [185] D. Indumathi, M. V. N. Murthy, G. Rajasekaran and N. Sinha, Phys. Rev. D 74, 053004, arXiv:hep-ph/0603264 (2006).
- [186] Lakshmi S Mohan, *Precision measurement of neutrino oscillation parameters at INO ICAL*, Ph.D. Thesis, submitted to Homi Bhabha National Institute (HBNI) (2015).
- [187] M. Ambrosio et al., *Measurement of the atmospheric neutrino-induced upgoing muon flux using MACRO*, arXiv:hep-ex/9807005v1, 7 July 1998.
- [188] R. Brun et al., *Root: An Object-Oriented Data Analysis Framework*, User's Guide: 5.26, Dec 2009.
- [189] J.S. Marshall, *A study of muon neutrino disappearance with the MINOS detectors and the NuMI neutrino beam*, Ph.D. Thesis, University of Cambridge (2008).
- [190] E.J. Wolin and L.L. Ho, *Covariance matrices for track fitting with the Kalman filter*, Nucl. Instrum. Meth. A 329, 493 (1993).
- [191] PARTICLE DATA GROUP Collaboration, J. Beringer et al., *Review of Particle Physics (RPP)*, Phys. Rev. D 86, 010001, <http://pdg.lbl.gov> (2012).

List of Publications

- A. Chatterjee, K.K. Meghna, R. Kanishka, T. Thakore et al., *A Simulations Study of the Muon Response of the Iron Calorimeter detector at the India-based Neutrino Observatory*, JINST **9** P07001, [arXiv:1405.7243] (2014).
- R. Kanishka et al., *Simulations study of muon response in the peripheral regions of the Iron Calorimeter detector at the India-based Neutrino Observatory*, JINST **10** P03011, [arXiv:1503.03369] (2015).
- Kanishka Rawat, Vipin Bhatnagar, D. Indumathi, *Study of Muon Resolution in the INO-ICAL Detector*, presented a poster in ASIA-EUROPE-PACIFIC SCHOOL OF HIGH-ENERGY PHYSICS: AEPSHEP-2012, Fukuoka, Japan, 14 to 27 October.
- Oral presentation on *How muons are reconstructed in different regions of ICAL* and poster presentation on *A Simulations Study of the Response of ICAL Detector to Muons* in XVth neutrino conference NUFACT2013, Beijing, China, Proceedings will be published online in Open Access Journal of Physics: Conference Series (JPCS), which is part of IOP (Institute of Physics) Conference Series.
- Kanishka Rawat, Vipin Bhatnagar, D. Indumathi *MUON RESPONSE IN THE INO-ICAL*, presented in National Workshop on Contemporary Trends in High Energy Physics and Instrumentation - 2014, Panjab University, Chandigarh, India, accepted paper, to be published in Pramana journal.
- Kanishka Rawat, Vipin Bhatnagar, D. Indumathi *Oscillation Sensitivity with Upward-going Muons in ICAL at India-based Neutrino Observatory (INO)*, presented poster in XVIth International Workshop on Neutrino Factories and Future Neutrino Facilities, NuFact2014, University of Glasgow, 25-30 August 2014, will be published online in Proceedings of Science (PoS) <http://pos.sissa.it>.

-
- Kanishka Rawat, Vipin Bhatnagar, Gurpreet Kaur Cheema, D. Indumathi *Characterisation of Glass for RPCs of India-based Neutrino Observatory*, poster presented in ICCMP 2014, Shimla, 4 - 6 Nov 2014.
 - Kanishka Rawat, Vipin Bhatnagar, D. Indumathi, *Oscillation Studies with Upward-going Muons INO-ICAL*, presented poster in XXI DAE-BRNS High Energy Physics Symposium 2014, IIT-Guwahati, 8-12 December 2014, accepted paper, to be published in springer.com <http://www.springer.com/in/book/9783319256177>.
 - Kanishka Rawat, Vipin Bhatnagar, D. Indumathi, *Efficiency and Cross-talk Studies of RPCs*, 59th DAE-BRNS symposium on nuclear physics, BHU, Varanasi, 8-12 December 2014, published online at <http://www.sympnp.org/proceedings/59/G12.pdf>.

Talks/Posters Presented

- Presentation: Kanishka Rawat, Vipin Bhatnagar, *Simulation and Study of Resistive Plate Chambers for INO Experiment*, Collaboration meeting - Jan 2011, Madurai, India.
- Paper: Kanishka Rawat, Vipin Bhatnagar, *Study of Resistive Plate Chamber for INO-ICAL experiment*, presented in 5th CHAndigarh Science CONgress - Feb 2011, Chandigarh, India.
- Presentation: Kanishka Rawat, Vipin Bhatnagar, *Momentum and Theta Resolution*, Collaboration meeting - July 2011, Kolkata, India.
- Presentation: Kanishka Rawat, Vipin Bhatnagar, *Software Validation using Muons and VICE*, Collaboration simulation meeting - November 2011, TIFR Mumbai, India.
- Poster: Vipin Bhatnagar, Jyoti Bala, Kanishka Rawat, *Hough transform: serial and parallel implementations*, to be published in DAE Symposium on Nuclear Physics - 2011.

-
- Paper: Kanishka Rawat, Vipin Bhatnagar, *Study of Muon resolution in the INO-ICAL experiment*, presented in 6th CHAndigarh Science CONgress (CHASCON) - Feb 2012, Panjab University, Chandigarh, India.
 - Presentation: Kanishka Rawat, Vipin Bhatnagar, D. Indumathi, *Muon Analysis in the Region of Changing Magnetic Field*, Collaboration meeting - Feb 2012, BARC, Mumbai, India.
 - Presentation: Kanishka Rawat, Vipin Bhatnagar, D. Indumathi, *Study of Up-Going Muons at INO-ICAL Experiment*, Collaboration meeting - Feb 2012, BARC, Mumbai, India.
 - Poster: Vipin Bhatnagar, Jyoti Bala, Kanishka Rawat, *Track Finding in INO-ICAL Detector using Hough Transform*, Workshop of frontiers of nuclear and particle physics - March 2012, Aligarh Muslim University, Aligarh, India.
 - Poster: Vipin Bhatnagar, Jyoti Bala, Kanishka Rawat, *Track Finding in INO-ICAL Detector using Hough Transform*, National symposium on particles, detectors and instrumentation - March 2012, TIFR, Mumbai, India.
 - Presentation: Kanishka Rawat, Vipin Bhatnagar, D. Indumathi, *Muon Analysis in Changing Magnetic Field*, Collaboration meeting, Theni, India, August 2012.
 - Presentation: Kanishka Rawat, Vipin Bhatnagar, D. Indumathi, *First look at the up-going muons*, Collaboration meeting, Theni, India, August 2012.
 - Poster: Kanishka Rawat, Vipin Bhatnagar, D. Indumathi, *Study of Muon Resolution in the INO-ICAL Detector*, 2012 ASIA-EUROPE-PACIFIC SCHOOL OF HIGH-ENERGY PHYSICS: AEPSHEP-2012, Fukuoka, Japan, 14 to 27 October 2012.
 - Paper: Kanishka Rawat, Vipin Bhatnagar, D. Indumathi, *Muon Analysis in the Peripheral Region of INO-ICAL*, XX DAE-BRNS High Energy Physics Symposium, Visva-Bharati, Santiniketan, January 13-18, 2013.

-
- Paper: Kanishka Rawat, Vipin Bhatnagar, D. Indumathi, *Oscillation Sensitivity with Up-going Muons in ICAL at India-based Neutrino Observatory (INO)*, XX DAE-BRNS High Energy Physics Symposium, Visva-Bharati, Santiniketan, January 13-18, 2013.
 - Presentation: Kanishka Rawat, Vipin Bhatnagar, D. Indumathi, *OSCILLATION SENSITIVITY with UP-GOING MUONS in ICAL at INO* presented in 7th CHAndigarh Science CONgress (CHASCON) - March 2013, Panjab University, Chandigarh, India.
 - Presentation: Kanishka Rawat, Vipin Bhatnagar, D. Indumathi, *Muon Analysis in the Peripheral Region of INO-ICAL*, Collaboration meeting, BARC, Mumbai India, 5-7 March 2013.
 - Presentation: Kanishka Rawat, Vipin Bhatnagar, D. Indumathi, *A Study of Up-going Muons in ICAL at India-based Neutrino Observatory (INO)*, Collaboration meeting, BARC, Mumbai India, 5-7 March 2013.
 - Presentation: Kanishka Rawat, Vipin Bhatnagar, D. Indumathi, *A Study of Up-going Muons in ICAL at India-based Neutrino Observatory (INO)*, Double Beta Decay and Neutrinos (DBD 2013), IIT-Ropar and Panjab University, 20-21 April 2013.
 - Presentation: Kanishka Rawat, Vipin Bhatnagar, D. Indumathi, *Muon Analysis in Peripheral and Side Region*, MKU, Madurai, 13-15 Sep 2013.
 - Presentation: Kanishka Rawat, Vipin Bhatnagar, D. Indumathi, *A Study of Up-going Muons in ICAL at India-based Neutrino Observatory (INO)*, MKU, Madurai, 13-15 Sep 2013.
 - Poster: Kanishka Rawat, Vipin Bhatnagar, D. Indumathi *MUON RESPONSE in ICAL DETECTOR at INO*, presented in 8th CHAndigarh Science CONgress - Feb

2014, Chandigarh, India.

- Poster: Kanishka Rawat, Vipin Bhatnagar, D. Indumathi *A STUDY OF MUON RESPONSE IN THE INO-ICAL DETECTOR*, presented in Multi Disciplinary National Conference in Emerging Trends in Basic & Applied Sciences - March 2014, DAV Jalandhar.
- Poster: Kanishka Rawat, Vipin Bhatnagar, D. Indumathi *MUON RESPONSE IN THE INO-ICAL*, presented in National Workshop on Contemporary Trends in High Energy Physics and Instrumentation - 2014, Panjab University, Chandigarh, India.
- Presentation: Kanishka Rawat, Vipin Bhatnagar, D. Indumathi, *Characterisation of Glass for RPC*, VECC, Kolkata 3-5 April 2014.
- Poster: Kanishka Rawat, Vipin Bhatnagar, D. Indumathi, *Muon Response in ICAL Detector at India-based Neutrino Observatory*, Department of Physics, Panjab University, Chandigarh, 13-15 May 2014.
- Poster: Kanishka Rawat, Vipin Bhatnagar, D. Indumathi *Oscillation Sensitivity with Upward-going Muons in ICAL at India-based Neutrino Observatory (INO)*, XVIth International Workshop on Neutrino Factories and Future Neutrino Facilities, NuFact2014, University of Glasgow, 25-30 August 2014.
- Presentation: Kanishka Rawat, Vipin Bhatnagar, D. Indumathi *Efficiency and Cross-talk Studies of RPCs*, INO Collaboration Meeting IICHEP, Madurai, 18-20 Sept 2014.
- Poster: Kanishka Rawat, Vipin Bhatnagar, Gurpreet Kaur Cheema, D. Indumathi *Characterisation of Glass for RPCs of India-based Neutrino Observatory*, ICCMP 2014, Shimla, 4 - 6 Nov 2014.
- Poster: Kanishka Rawat, Vipin Bhatnagar, D. Indumathi, *Oscillation Studies with*

Upward-going Muons INO-ICAL, XXI DAE-BRNS High Energy Physics Symposium 2014, IIT-Guwahati, 8-12 December 2014.

- Presentation: Kanishka Rawat, Vipin Bhatnagar, D. Indumathi, *Efficiency and Cross-talk Studies of RPCs*, DAE symposium on nuclear physics, BHU, Varanasi, 8-12 December 2014.
- Presentation: Kanishka Rawat, Vipin Bhatnagar, D. Indumathi *Efficiency and Cross-talk Studies of RPCs*, INO Collaboration Meeting IIT, Chennai, 2 - 4 April 2015.
- Presentation: Kanishka Rawat, Vipin Bhatnagar, D. Indumathi *A Study of Upward-going Muons in ICAL INO*, INO Collaboration Meeting, IIT, Chennai, 2 - 4 April 2015.

Conferences/Schools Attended

- Workshop on Synergy between High Energy and High Luminosity Frontiers - 2011, TIFR, Mumbai, India.
- 5th CHAndigarh Science CONgress (CHASCON) - 2011, Panjab University, Chandigarh, India.
- Seventh International Workshop on Neutrino - Nucleus Interactions in the Few - GeV Region, March 2011.
- 8th SERC-EHEP School - 2011, VECC, Kolkata, India.
- Frontiers in high energy physics, Lecture series at IMSc - 2011, in celebration of Prof. G Rajasekharan's 75th birthday, IMSc, Chennai, India.
- 6th CHAndigarh Science CONgress (CHASCON) - 2012, Panjab University, Chandigarh, India.

-
- Workshop on frontiers of nuclear and particle physics - 2012, Aligarh Muslim University, Aligarh, India.
 - National symposium on particles, detectors and instrumentation - 2012, TIFR, Mumbai, India.
 - An international school: ASIA-EUROPE-PACIFIC SCHOOL OF HIGH-ENERGY PHYSICS: AEPSHEP-2012, Fukuoka, Japan, 14 to 27 October 2012.
 - Frontiers in high energy physics Symposium, The Institute of Mathematical Sciences (IMSc), Dec 10-13, 2012.
 - XX DAE-BRNS High Energy Physics Symposium, Visva-Bharati, Santiniketan, January 13-18, 2013.
 - 7th CHAndigarh Science CONgress (CHASCON) - 2013, Panjab University, Chandigarh, India.
 - National conference on Double Beta Decay and Neutrinos (DBD 2013), IIT-Ropar and Panjab University, Chandigarh.
 - 8th CHAndigarh Science CONgress (CHASCON) - 2014, Panjab University, Chandigarh, India.
 - **Multi Disciplinary National Conference in Emerging Trends in Basic & Applied Sciences - March 2014, DAV Jalandhar. Bagged best paper award.**
 - National Workshop on Contemporary Trends in High Energy Physics and Instrumentation - 2014, Panjab University, Chandigarh, India.
 - International Workshop on Unification and Cosmology after Higgs Discovery and BICEP2, Department of Physics, Panjab University, Chandigarh, 13-15 May 2014.

-
- An International Conference on Condensed Matter Physics (ICCMP) 2014, Shimla, 4 - 6 Nov 2014.
 - 59th DAE-BRNS symposium on nuclear physics, BHU, Varanasi, 8 - 12 December 2014.